Simultaneous Hydrogen Generation and Separation by Plasmolysis

A thesis
submitted to The University of Sheffield for the degree of
Doctor of Philosophy in Faculty of Engineering

By

Fahad Rehman

The University of Sheffield
Department of Chemical and Biological Engineering

January 2015

Acknowledgements

First and foremost I would like to express my sincere thanks and gratitude to my research supervisor Professor William B. J. Zimmerman for his advice, support and encouragement throughout research work. This thesis and the related published articles couldn't have been possible without him.

I would also like express my sincere thanks and gratitude to all my sponsors COMSASTS Institute of Information Technology, Pakistan, The University of Sheffield, UK, and Professor William B. J. Zimmerman.

I am thankful to all technical staff of mechanical and electrical workshops of department of chemical and biological engineering. Especially, Mr. Andy Patrick, Stuart Richards, Mark McIntosh, Mr. Keith Penny and Mr. Mark Jones who provided the technical support in fabricating the custom made research equipment and helped in day to day equipment problems.

I also would like to thanks sincerely Dr. Dmitriy Kuvshvinov, Dr. Wameath Abdul Majeed, Mr. Thomas David Holmes, Mr. Gareth James David Medley and Mr. Yining Liu for their support and collaborative work and other group members.

Finally this work couldn't have been possible without the support, love, patience and continuous encouragement of my family, especially my wife (***Mrs. Saba Fahad Rehman***), my mother ***(Mrs. Tallat Rehman)*** and prayers of my father ***(late Mr. Atta-ur-Rehman)***. It is to my family I dedicate this work.

Summary

The research was dedicated to develop a method for simultaneous production and separation of hydrogen by integrating micro-plasma technology with fluidic oscillation for microbubble generation. Several types of chemical pathways have been identified for water vapour dissociation. A homogenous chemical kinetics model is proposed for hydrogen production by water vapour plasmolysis using a plasma micro-reactor. The time scale (τ) to reach steady state hydrogen production was found to be approximately 10^{-2} s. The concentration of hydrogen was found to increase with the increase in electron number density. However, the time scale to reach steady state production of hydrogen was found to decrease with the increase in electron number density. A dielectric barrier discharge- corona hybrid discharge reactor has been built for hydrogen production. Water vapour plasma is characterised for basic plasma characteristics such as electron, excitation, rotational, vibrational temperatures, electron number density and Debye length by optical emission spectroscopy under non-thermal equilibrium conditions. The values of electron, excitation, rotational, vibrational temperatures, electron number density and Debye length were estimated to be 0.77 *eV*, 0.53 *eV*, 0.067 *eV*, 0.062 *eV*, 1.76 x 10^{17} m^{-3} and 3.24 µm respectively. Hydrogen was preliminary estimated by gas chromatography. However, it was not possible to quantify hydrogen by GC because of the build-up of pressure inside plasma micro-reactor. Hydrogen quantification by GC is described in chapter 5. By measuring the decomposition rate of water vapours along with argon gas, energy yield and cost of hydrogen production were calculated to be 20 g/kWh and 0.305 m^3/kWh. A short experimental investigation has been presented to identify peaks in emission spectrum in the range of 317-400 nm. The operational parameters of plasmolysis were optimised using ozone generation by air plasma instead of hydrogen generation. A detailed discussion on the use of ozone generation for optimisation studies is given in chapter 5. Operational parameters such as flow rate and pressure of gas, material, type and configuration of electrodes, frequency and total power applied to the plasma micro-reactor was optimised. The optimum conditions of plasmolysis were found to be 1 l min^{-1} of air, 0.2 bar*g,* 28 kHz and 70 W. However, the material, type and the configuration of electrodes used in the current study do not significantly affect the

plasmolysis efficiency. A novel approach, based on difference of solubilities of hydrogen and oxygen in water, for separation of hydrogen and oxygen has been identified. Fluidic oscillation by fluidic oscillator has been proposed as a cost effective method to produce microbubbles for the separation of hydrogen and oxygen. Volumetric mass transfer coefficient ($K_l a$) for steady flow and oscillatory flow has been measured using an air-water system. The use of air-water system, instead of H_2-O_2 system, to determine $K_l a$ has been discussed in chapter 5. $K_l a$ was measured for 40-100 l min^{-1} of air. At each flow rate, $K_l a$ using oscillatory flow was found to be significantly higher than the $K_l a$ using steady state flow. Maximum improvement in $K_l a$ was found to be approximately 55% at 60, 90 and 100 l min^{-1}. Bubble size distribution has been measured by acoustic bubble spectrometry. The number density of microbubbles was found to be significantly higher for oscillatory flow than the steady state flow. Finally the applicability of reactive separation has been assessed on water vapour plasmolysis by experimental investigations. Preliminary estimates of $K_l a$ (1.9 x 10^{-3} s^{-1}) and τ (10^{-2} s) suggest that the reactive separation could be applied on plasma-chemical processes. Conclusions and recommendations for future study have been proposed in the end.

Table of Contents

List of Figures

List of Tables

Chapter 1

Introduction

1.1 Foreword

Energy and environmental sustainability is one of the greatest challenges faced by the world today. Fossil fuels have been the main source of the energy and oil remains the major fuel consumed (33.1%) (BP, 2013). The major consumption of the oil is in the transport sector. World primary energy consumption, though at slower rate of 2.6%, has still risen by 1.8% in 2012. It requires hundreds of millions of years to form fossil fuels (coal, oil and gas) and human species have already consumed it so much that reserves to production ratio (R/P-proven reserves/current rate of production) of oil is 52.9 years, gas is 55.7 years and coal is 109 years only (BP, 2013). Although new reserves for fossil fuels are discovered each year and the time frame for complete depletion of fossil fuel is still unpredicted. However, the other fact is that, 80% of the world energy in 2001 was produced from fossil fuel utilisation (Das and Veziroğlu, 2001) and in 2013 the total energy share of fossil was 86.8% (33% oil, 23.9% gas, 29.9% coal) (BP, 2013). This ever increasing consumption of fossil fuel is expected to increase because of increasing population and economic growth. The other major problem associated with consumption of fossil fuels is the emission of carbon dioxide and other greenhouse gases (GHGs). Increasing concentration of GHGs in atmosphere has contributed to the abnormal climate changes (Solomon et al., 2007). Subsequently, a long term solution for both sustainable energy and environmental protection is needed. However, currently there exists no "perfect solution" to this problem. All the current efforts are driven in the direction of fossil fuel independent, clean and environmental friendly energy sources. It could be a single energy source or more likely a mix of several energy sources which will be complimentary to each other. One of the options is to use an energy carrier other than electricity such as hydrogen. Hydrogen can be stored more readily than electricity (Kroposki et al., 2006). Hydrogen has been on the scene as an alternative of the fossil fuels for approximately two centuries (Dixon, 2007). A Hydrogen economy could offer advantages both in terms of reduction in GHGs and as an alternative fuel which will eventually reduce the consumption rate of fossil fuels. Hydrogen fuel produced by a renewable energy source such as wind or solar is totally green and renewable (Dixon, 2007). Almost 95% (600 billion m^3 at STP per year) of the hydrogen produced is captive (with in the vicinity

of its application). Amount of hydrogen traded or sold "over the fence" is only 3 million tonnes to the users adjacent to the production site (Mueller-Langer et al., 2007). Renewable energy, in this regard, is expected to play a major role in the global energy mix. Due to ever increasing energy demand efforts are carried out to maximise the renewable share in the energy consumption. The share of individual primary energy sources in meeting the final energy needs in near future has been suggested in **Table 1-1** where hydrogen share in the future energy mix is expected to be significantly higher than today (Balat and Kırtay, 2010).

Table 1-1 Expected contribution of energy mix (%) in future (Balat and Kırtay, 2010)

Source of Energy	1998 (%)	2025 (%)	2050 (%)
Fossil Fuels	88	62	29
Nuclear Fuels	10	2	2
Hydrogen from solar energy	-	7	31
Electricity from solar energy	-	11	16
Heat from solar energy	-	18	22
Energy from solar energy	2	25	35
Hydrogen	-	11	34

As reported by National Renewable Energy Laboratory *"to fully realise the benefits of a hydrogen economy, hydrogen must be produced cleanly, efficiently and affordably from domestically available renewable resources"* (NREL, 2004). For the development of the hydrogen economy, it is very important to develop hydrogen production processes which could produce hydrogen efficiently, at minimum cost (so that it may compete with fossil fuels for power generation and in the transport sector) and should be environmental friendly (Mueller-Langer et al., 2007). In addition, problems like economical production, separation of H_2/O_2 mixture and storage are the barriers still to overcome.

Conventionally, 90% hydrogen has been produced by steam methane reforming (SMR) which requires natural gas as fuel (Das and Veziroğlu, 2001). Hydrogen production by

plasmolysis has been considered as an expensive method (Bockris et al., 1985). In addition to this, separation of hydrogen and oxygen is another problem to be addressed. The current study is focused on economical production of hydrogen. A novel scheme for separation of hydrogen and oxygen is proposed.

1.2 Hypothesis

The project is based on two hypotheses**.**

1. Hydrogen can be produced at comparable costs to the common method (electrolysis) and substantially more energy efficiently than conventional plasmolysis; electrolysis has been considered more energy efficient than the plasmolysis to produce hydrogen. However, using micro-plasma technology it is possible to increase the efficiency of plasmolysis.

2. Reactive separation is applicable on plasma-chemical processes- Reactive separation could improve the energy efficiency and yield by the use of plasma micro-reactors integrated with microbubble separation technologies if the time scale for reaction (τ) and separation ($K_l a$) are similar or separation faster than reaction. Since both could be interfacially controlled processes on microbubbles, the former a plausible hypothesis. If reaction is mixing controlled, then whether internal mixing is faster than separation is potentially individually controllable for both processes. Reactive separation is the engineering exploitation of Le Chatelier's principle, where the preferential removal of oxygen by interfacial mass transfer can provide an additional Gibbs free energy driver towards products.

1.3 Aims of the project

The aim of this study is to produce microbubble mediated hydrogen using micro-plasma reactor utilising less power than the conventional plasma reactors. It was done in following steps:

1. Formulation of the kinetic model for water vapour plasmolysis
2. Generation of self-sustained water vapour plasma

3. Characterisation of water vapour plasma. This involves measurement of electrical and optical plasma parameters like electron, excitation, vibrational and rotational temperatures
4. Optimisation of operational parameters
5. Separation of hydrogen
6. Application of reactive separation over water vapour plasma

In this study, it has been proposed that two steps of production and separation could be carried out simultaneously. First, hydrogen was produced by water vapour plasmolysis and in second step, separation of hydrogen and oxygen mixture was achieved by the virtue of the difference in their solubilities in water. Oxygen is twenty five fold (one order of magnitude higher) more soluble in water than hydrogen. The product gases from the plasma micro-reactor will be fed into a water column in the form of bubbles. Oxygen will be preferentially dissolved in water as the bubbles rise in water. A tall enough water column will yield hydrogen rich gas when the bubbles will burst at the water surface. There are various common chemical and bio-processes having oxygen requirement. For instance, yeast production is oxygen starved and has little dissolved oxygen (DO) in the liquid. Biological wastewater treatment is the most common industrial process with an oxygen requirement that could be integrated with hydrogen from waste steam/heat production. Alternatively fresh water could be recycled in order to maintain constant (DO) level in the water column. Water vapour plasma has been characterised by optical emission spectroscopy (*OES*) for electrical and optical properties. Optimisation of operational parameters has been studied. Microbubble mediated mass transfer by oscillatory flow has been identified as a separation technique. Finally the applicability of reactive separation on plasma-chemical processes was assessed.

1.4 Organisation of thesis

This section describes the organisation of thesis and how each chapter is related to complete each objective described above.

Chapter 1 is dedicated towards stating the problem. A short analysis is carried out at the energy mix of the current scenario and future demands of sustainable and clean

energy sources. Role of hydrogen in future energy mix is explained and need to produce hydrogen by cheap methods is identified.

Chapter 2, as a first step, is dedicated to establish understanding of related subjects and applied principles. A brief review on current methodologies to produce hydrogen is described and problems associated with them are discussed. Basic plasma science is reviewed and principles applied in this study are discussed. Different methods of generating hydrogen by utilising plasma have been given. A detailed review on hydrogen production by water vapour plasmolysis and a brief comparison with electrolysis is discussed. Kinetics of ozone formation and its decomposition in water is studied in detail. Separation methodologies for hydrogen from oxygen and other plasmolysis product is studied briefly. Separation of hydrogen by using microbubbles have been discussed in detail. Finally, reactive separation and its possible application on plasma-chemical processes are studied.

Based on the understanding of plasma chemistry in chapter 2 a kinetic model is proposed in chapter 3. Rationale for kinetic modelling has been discussed. The model was developed to understand the kinetics of formation of hydrogen by dissociating water vapours using plasma micro-reactor. Time scales for steady state hydrogen production is identified. Different mechanisms of water vapour plasmolysis for hydrogen production have been examined to find the dominating reaction pathways. The effect of varying electron density on concentration and time scale to reach steady state production of hydrogen and other species are studied.

Chapter 4 encompasses the experimental design and procedure used in the current study. Equipment used, experimental design and procedures adopted to achieve the aims and objectives of the study are reported. Experimental procedures for water vapour plasmolysis, optical emission spectroscopy of water vapour plasma and a short investigation on identification of optical emission spectral peaks is given. Based on the kinetics of formation of ozone given in chapter 2 and kinetic modelling of hydrogen production studied in chapter 3, rationale of use ozone generation (instead hydrogen generation) for optimisation of operational parameter of plasmolysis is discusses. Experimental procedures for optimisation studies are reported. Based on the discussion on the separation of hydrogen using microbubbles in chapter 2 and

considering the low flow rates of steam and gases used in the current study, the rationale of using air water system to produce microbubbles to study volumetric mass transfer coefficient ($K_l a$) is discussed. Experimental procedure to produce microbubbles using oscillatory flow and steady flow have been reported. To assess the applicability of reactive separation on water vapour plasmolysis, similar procedure for microbubble generation, as mentioned above, however at lower flow rates and with a different type of diffuser was adopted to measure $K_l a$ and bubble size density for both oscillatory and steady flow. A new type of plasma micro-reactor was designed for reactive separation of water vapour plasmolysis experiment and the procedure is reported.

Chapter 5 contains results from experiments conducted in chapter 4 and their detailed analysis. Water plasma has been characterised for its electrical and optical properties. Hydrogen was preliminary estimated by gas chromatography. However, it was not possible to quantify hydrogen by GC because of the build-up of pressure inside plasma micro-reactor. Energy yield and cost are calculated by measuring decomposition rate of water vapours. Different parameters like electron density, Debye length, electron, excitation, rotational and vibrational temperatures are calculated. The possible phenomenon producing optical emission spectral peaks in the range of 317 – 400 nm is discussed. Operational parameters of water vapour plasmolysis are optimised using ozone generation. Flow rate and pressure of the air, power and frequency of the discharge, length, configuration and different types of electrode materials are studied for optimisation. Mass transfer by microbubbles is determined by measuring Kla. Bubble size was determined using acoustic bubble spectrometer (ABS) to determine the effect of fluidic oscillation on mass transfer. Oxygen separation efficiency is reported. Application of reactive separation is assessed using the reaction time scale calculated in chapter 3 (by kinetic modelling) and $K_l a$ calculated. Ozone production is also used to analyse the affects of changing positions for plasma ignition on plasma micro-reactor to assess the application of reactive separation on plasma-chemical processes.

Conclusions from the current research and recommendations for future work are given in chapter 6.

Chapter 2

Literature Survey

2.1 Preface

The purpose of this chapter is to review the fundamental understanding of the engineering processes and scientific principles underpinning the research work presented in this thesis. The necessities for producing hydrogen economically by water vapour plasmolysis have been identified. The chapter starts with a concise review of conventional hydrogen production technologies such as (SMR) and gasification etc. The associated problems with conventional technologies have been discussed. A whole section is dedicated to reviewing plasma science and relevant applications to the current study. Different types of plasma have been discussed in order to identify the potential types of plasma which could be used in the experiments. Different characteristics and parameters of plasma have been studied to be used in experimental work. Several studies have been reviewed for hydrogen production by utilising different types of plasma, feedstock, reactors and power sources e.g., pulse power and efficiency (in some cases) is presented. A brief comparison of plasmolysis and electrolysis is carried out. Electrolysis has been chosen as a reference for comparison because both plasmolysis and electrolysis involve direct use of electricity. The kinetics of ozone formation and its decomposition in aqueous solutions have been discussed as ozone formation has been used for optimising the operational parameters of plasmolysis. Different methods for separating hydrogen from oxygen have been discussed. Finally, reactive separation and its application on plasma-chemical reactions has been studied.

This chapter has been divided into seven sections. In the second section conventional hydrogen production technologies such as reforming, gasification etc., are described. A concise review of plasma science, basic principles and processes, different types of plasmas, summary of hydrogen production by plasma utilising different methodologies and a brief comparison of plasmolysis and electrolysis has been studied in section three. The fourth section entails formation of ozone kinetics and its decomposition in aqueous solution. Methodologies for separating hydrogen from oxygen has been discussed in fifth section. Sixth section deals with reactive separation. Conclusions are given in seventh section.

2.2 Hydrogen production technologies

Hydrogen has got the potential to address the current energy and climate challenges human race face today. The technologies like steam methane reforming, coal gasification and electrolysis have demonstrated the production of hydrogen at the commercial level. Electrolysis and plasmolysis integrated with the renewable energies could make hydrogen economy totally green. In the subsequent section a summary of the hydrogen production technologies is given**.**

2.2.1 Reforming

Commercially, hydrogen is produced by different technologies. However, almost 90% of hydrogen produced commercially is by the process of steam reforming (Das and Veziroğlu, 2001) and the rest of it is produced by coal gasification (Simpson and Lutz, 2007). Reforming processes are divided in three types depending upon the type of the oxidising material being used (steam or oxygen) and presence of catalyst (Larminie et al., 2003). These are known as steam reforming, partial oxidation (non-catalytic and catalytic) and autothermal reforming. Methane is an obvious choice for fuel because of its availability and excellent combustion properties (Stefanidis and Vlachos, 2010). Methane is reacted over a heated catalyst, usually Ni, with steam. The reaction is carried out over a very high temperature range (900-1200 K) and pressure range (5-25 bar). (Simpson and Lutz, 2007, Rostrup-Nielsen and Rostrup-Nielsen, 2002, Joensen and Rostrup-Nielsen, 2002). Hydrogen is separated from H_2O and CO_2 by three steps: pressure swing adsorption to separate to CO_2 followed by condensation of H_2O and membrane separation of H_2. Pressure swing adsorption is a mature technology and gives very high purity (>99%). A detailed study of membrane technologies for hydrogen separation is given in (Adhikari and Fernando, 2006).

Although the reforming of methane represents the major technology to produce hydrogen at the moment, however, it utilises natural gas as feedstock which means hydrogen thus produced is neither green (because it would involve emission of GHGs) nor sustainable (because of fossil fuel reserves are limited). The major component of the price of hydrogen (52-68%) is the cost of the input natural gas for larger plants. While for smaller plants the price of natural gas contributes about 40% towards the

total cost. The remaining cost is attributed towards the capital investment. Based on the assumption of natural gas price as 7 US$/GJ production cost of hydrogen from SMR ranges from 1.50 US$/kg at large scale facilities (1.2 Gg/d) to about 3.75 US$/kg at 500 kg/d facility. Details of cost of hydrogen production is discussed in (Balat and Kırtay, 2010).

2.2.2 Hydrogen from biomass

Hydrogen can generally be produced from a variety of biomass by thermo-chemical and biological processes (Guoxin et al., 2009). Thermo-chemical processes involve gasification, pyrolysis and liquefaction while biological processes involve direct biophotolysis, indirect photolysis, biological water-gas shift reaction, photo fermentation and dark fermentation.

A difference in the gaseous products for different thermo-chemical cycles is shown in equations (2-1) to (2-3) (Demirbaş, 2002a). A summary of biomass energy content and hydrogen yield of different thermo-chemical processes is shown in **Table 2-1** (Demirbaş, 2002a).

Pyrolysis of biomass $\longrightarrow$ $H_2 + CO_2 + CO$+ Hydrocarbon gases (2-1)

Catalytic steam reforming of biomass $\longrightarrow$ $H_2 + CO_2 + CO$ (2-2)

Gasification of biomass $\longrightarrow$ $H_2 + CO_2 + CO + N_2$ (2-3)

Table 2-1 Summary of the structural and elemental composition and higher heating values of the biomass samples (Demirbaş, 2002a)

Processes	**H_2 yield (%)**	**H_2 contents/biomass energy content (%)**
Pyrolysis + catalytic reforming	12.6	91
Gasification +shift reaction	11.5	83
Biomass + steam + except heat (theoretical maximum)	17.1	124

2.2.2.1 Gasification

Basu and Kushal (2009) have studied biomass gasification in fluidised bed detail . The reaction kinetics and gasification processes has also been studied in detail elsewhere

(Rajvanshi, 1986). Biomass can be gasified with steam using a suitable catalyst like, transition metal based, nickel or calcined dolomite to convert carbonaceous materials to gases like H_2, CO, CO_2, CH_4, light hydrocarbons, char and Tar. Catalysts play a very important role in the gasification process. They not only improve the quality of the products and conversion efficiency but can also eliminate the tar content as well (Basu and Kaushal, 2009, Balat and Kırtay, 2010).

Although gasification is considered as more environmentally friendly than the direct combustion of biomass, it is a process which converts the fuel to low calorific gas which carries net energy loss. Further transformation to synthetic natural gas and liquid fuels reduces the net energy perhaps to 30% of the original heat content (Balat, 2006). Also, the hydrogen yield is inherently low due to the low hydrogen content of the biomass feedstock (roughly 6% by mass), by comparison the ~25% hydrogen content of methane. More than half of the hydrogen from thermo-chemical conversion of biomass comes from water splitting in the steam reforming step; the energy content of the feedstock is an inherent limitation on the process. Energy content of the biomass is further lowered because of the fact that it contains relatively high oxygen which is incombustible (Balat and Kırtay, 2010).

2.2.2.2 Coal gasification

Coal is the most abundant and widely distributed fuel in the world but the emission of GHGs and other pollutants has forced societies to look for green energy production processes (Lee and von Gunten, 2010). Coal gasification offers a great potential not only for CO_2 sequestration but also reduction of other pollutants like NOx and SOx (Lee and von Gunten, 2010). The composition of the product gas can be controlled by varying parameters such as coal composition and its rank, particle size, gasifying agents and operational parameters such as temperature and pressure (Collot, 2006).

One inherent advantage of using coal as feedstock over the biomass is its composition. Biomass has 50 wt% carbon and 45 wt% oxygen which may be argued to be good because it reduces the amount of oxygen required for gasification but this reduces the calorific value of the gases produced from biomass by diluting it. On the other hand, coal, depending on its grade, has 65-80% carbon and 5-20% oxygen (Prins et al., 2007).

Coal gasification is relatively independent from the price of fuel that is coal which is relatively cheap, US$ 10-12 GJ^{-1}, and if the coal price is changed by 25% the hydrogen cost would be changed by US$ 0.05 kg^{-1}.The major cost component of coal gasification is its plant cost which is quite expensive (Balat et al., 2009).

The severe conditions of gasification cause major problems in the gasifier. Feed injectors, refractory bricks or protective liners and instruments such as thermocouple involving in gasifier have very low life time depending upon how aggressive are the conditions in the gasifier. All these problems reduce the mean operative time of the gasifier and another gasifier unit is desirable for continuous operation as >97% of the availability of the gasifier is of paramount importance which could be provided but this put serious implications to the cost of the plant (Clayton et al., 2002).

2.2.2.3 Pyrolysis

Pyrolysis is a process in which organic matter of the feedstock is thermally degraded in a total absence of added oxidising agents which results in a complex volatile phase and carbonaceous char containing inorganic components (Demirbaş, 2002b) as shown above in equation 2-1. Transition metals based catalyst produce gas with high initial hydrogen concentration. Carbon based catalysts offer advantage over transition metal based catalyst that is they are not deactivated by the carbon soot (Muradov, 1998). Cost of biomass pyrolysis was estimated to be in range of US$ 8.86/GJ to US$ 15.52/GJ depending on the facility size and biomass type (Ni et al., 2006).

Energy from biomass in the form of gasification, pyrolysis, steam reforming or direct combustion still faces some severe limitations like seasonal availability and high cost of handling. Process limitations like corrosion, pressure resistance and tar production, still requires extensive research. Although, SMR and coal gasification, to some extent, are cheaper sources for producing hydrogen, nevertheless, these are fossil fuel based hydrogen production technologies which are not renewable at all. A typical SMR plant produces 0.3-0.4 million cubic meters of CO_2 per day which is directly exhausted in the atmosphere per 1 million m^3 of H_2 per day (Muradov and Veziroğlu, 2005). This creates a serious environmental concern about this technology. It has been reported that CO_2

sequestration will add about 25-30% to the cost of producing hydrogen by SMR (Balat and Kırtay, 2010).

2.2.3 Thermocyclic methods

Direct thermal decomposition of water does not proceed spontaneously below 2500 K. However, there are methods/processes in which water passing through a series of chemical reactions can be decomposed well below the temperature required for the thermal decomposition. These methods are known as thermocyclic methods. These processes involves series of steps with different chemicals participating in the reactions but only water and energy are inputs, and the only products are hydrogen and oxygen along with waste heat while the chemicals used in the cycles are recovered at the end of the process. A well-known example is shown in equations (2-4)-(2-6).

$$H_2O + CH_4 \longrightarrow CO + 3H_2 \qquad (2\text{-}4)$$

$$CO + 2H_2 \longrightarrow CH_4 + \frac{1}{2} O_2 \qquad (2\text{-}5)$$

Overall reaction $$H_2O + CH_4 + \text{heat} \longrightarrow H_2 + \frac{1}{2} O_2 + CH_4 \qquad (2\text{-}6)$$

More than three hundred different water splitting cycles could be found from literature (Kothari et al., 2004). Most of these require significantly lower temperature than 2500 K. However, all of them require higher operating pressures. Different processes have been reported with thermal efficiency ranging from 17.5% to as high as 75.5% with requirement of relatively low temperatures of around 600-1673 K. High temperature, high pressure and corrosive conditions require materials which could withstand these conditions for longer period of time. However it is thought that better understanding of the relationship between thermal efficiency, thermodynamic wastes in the process and capital cost could increase the overall efficiency (Kothari et al., 2004, Holladay et al., 2009) .

2.2.4 Electrolysis

In electrolysis, water is split with electricity to produce hydrogen and oxygen. Electrolysis is a commercially mature process. However, It does not contribute significantly (0.1-0.2%) in world's hydrogen production (Šingliar, 2007). An electric

current is passed through a electrolytic cell to split water into the products. The electrodes in electrolytic cells are separated by a diaphragm, usually asbestos (Zeng and Zhang, 2010, Grigoriev et al., 2006). This barrier prevents the quick mixing of the solution while allowing the exchange of the ions. Overall reactions could be written as equation (2-7):

$$2H_2O \xrightarrow{\text{electricity}} 2H_2 + O_2 \qquad (2\text{-}7)$$

This reaction could be carried out by using different types of electrolytes i.e., liquid solid polymer and ion conducting ceramics (Mueller-Langer et al., 2007). This reaction requires 39 kWh of electricity to produce one kg of hydrogen at 25^{o}C and 1 atm (Šingliar, 2007). Electrolysers are usually run at a cell voltage of 1.8 to 2.2 V and temperature is usually in between 70-80 ^{0}C (Lumanauw, 2000). This set of conditions gives 68-80% efficiency. Based on the type of electrolyte used in the process, three different electrolytic processes have been developed which are alkaline water electrolysers (Zeng and Zhang, 2010, Grigoriev et al., 2006), proton exchange membrane (PEM) electrolysers (Papagiannakis, 2005) and solid oxide electrolytic cells (SOEC) (Udagawa et al., 2007).

There is a big argument on the clean nature of this technology because the electricity required to produce hydrogen still comes from fossil fuels. So there will be net burning of fossil fuel to generate electricity which finally produces the hydrogen. It could be concluded that hydrogen production via water electrolysis could only be consider as a zero greenhouse emission process if the source of the electricity is also a zero greenhouse emission process i.e., renewable. An example of this could be the generation of hydrogen by nuclear power, wind power and solar power (Šingliar, 2007). At the moment suitable materials for both electrolyser and separator are available. These materials are not expensive but their long term stability (wear and tear over the several years) is yet to be proven. Energy efficiency of the electrolysis will be discussed in later part of this section 2.39.

2.3 Fundamentals of plasma and applied principles

Plasma is originated from the Greek word "πλασσειν "which means mold. Langmuir was the first in 1929 who used plasma as a word to describe an arc discharge in which

the densities of ions and electrons are high but substantially equal (Langmuir, 1929). In a more rigorous way plasma could be defined as a *quasi-neutral gas of charged and neutral particles characterised by a collective behaviour.* Plasma could be referred as a gas which, instead of having molecules, have an almost equilibrium mixture of positive and negative ions. Plasma is characterised by three fundamental parameters which are particle density "*n*" (particle/m^3), temperature of species (eV or K) and steady state magnetic field (Tesla) (Bellan, 2006). Other parameters like Debye length etc., could be derived from these three fundamentals characteristics.

Plasma essentially contains two types of species: electron and heavy gas particles. Motion of particles in plasma can cause local concentrations of positive and negative electric charges to develop. As a result these local charge concentrations can develop long range columbic fields which could affect the motion of the particle away from them. Local charge concentrations are confined in a volume of specific dimension known as Debye length in the plasma. Debye length is a distance scale over which charge imbalance could spontaneously exist. For plasma to be sustainable dimensions of the overall plasma system should be greater than the Debye length. This is termed as characteristics length. Outside these tiny volumes of order tens of micrometres, density of positive ion is equal to that of negative ions/electrons and that is why plasma is considered quasi neutral (Lieberman and Lichtenberg, 2005).

$$\lambda_{De} = \left(\frac{\varepsilon_0 T_e}{e n_0} \right)^{1/2} \tag{2-8}$$

Or

$$\lambda_{De}(cm) \approx 743 \sqrt{T_e / n_e} \tag{2-9}$$

Where, λ_{De} is Debye length, ε_0 is vacuum permittivity, T_e is electron temperature, e is electronic charge, n_0 is number density of particles and n_e is the electron number density. For an ionised gas to exhibit as plasma, it is necessary that $\lambda_{De} << L$ where L is characteristic length of the discharge. When this condition is met, as discussed

above, local concentrations of charges may occur in the plasma which is shielded out by Debye shielding effect over distances smaller than the Debye length.

The rate of reactions occurring in plasma is dependent on the number of electron having sufficient energy to carry out the reaction. This is explained by a term known as electron energy distribution function (EEDF). The EEDF is actually the probability density for an electron to have sufficient kinetic energy known as mean electron energy (ε) to carry out the reactions. Since this function is largely dependent on the energy, it could be concluded that applied electric fields play an important role in determining this function. It also depends on the type of gas used for plasma generation. The reaction rate constant is an integral factor that includes information about the EEDF and depends on temperature or, precisely, the mean energy of the particles involved in the reaction.

Various transport variables obey the same single type of partial differential equation which is given in terms of a transport property ϕ.

$$\frac{\partial \rho \phi}{\partial t} + \nabla . \overrightarrow{\Gamma_\phi} = S_\phi \tag{2-10}$$

Where, S_ϕ is source term and $\vec{\Gamma} = \rho \vec{\upsilon}_\phi - \lambda_\phi \nabla_\phi$.

$\vec{\Gamma}$ is a combination of two different transport mechanisms; convective and diffusive. The convective term $\rho \vec{\upsilon} \phi$ is characterised by a convective bulk velocity $\vec{\upsilon}$ and the diffusion term is a function of the diffusion coefficient λ_ϕ. In plasma studies, this equation can be extended to the following relation (Hartgers et al., 2005);

$$\frac{\partial f_\phi \rho \vec{c}_\phi \phi}{\partial t} + \nabla . \left(f_\phi \rho \overrightarrow{c_\phi} \phi \right) - \nabla . \left(\lambda_\phi \nabla_\phi \right) = s_\phi \tag{2-11}$$

Where, f_ϕ is an adjustment parameter, $\vec{c}_\phi$ is the generalised velocity and λ_ϕ is the diffusion coefficient. Both of these coefficients have no direct bearing on the ordinary velocity and diffusion coefficient.

2.3.1 Ionisation processes

One key process in plasma is ionisation, which converts neutral atoms into electrons and positive ions. Ionisation processes are found to be different in various plasma-chemical systems and are categorised as follows (Fridman and Kennedy, 2004, Fridman, 2008) :

1. Direct ionisation by electron impact
2. Stepwise ionisation by electron impact
3. Ionisation by collision of heavy particle
4. Photo ionisation
5. Surface ionisation

2.3.2 Elementary plasma-chemical reactions of positive ions

Positive ions are considered very important in plasma-chemical processes as their exothermic reactions with neutrals make their contribution significant because they involve very little change in the activation energy. Different mechanisms occurring in recombination reactions of positive ions with electrons are (Fridman and Kennedy, 2004, Fridman, 2008, Lieberman and Lichtenberg, 2005):

1. Dissociative electron-ion recombination
2. Three body electron-ion recombination
3. Radiative electron recombination

2.3.3 Elementary plasma-chemical reactions of negative ions

Negative ions are involved in important reactions in plasma. They undergo the reactions in the following ways (Fridman and Kennedy, 2004, Fridman, 2008, Lieberman and Lichtenberg, 2005):

1. Dissociative electron attachment
2. Three body electron attachment
3. Destruction of negative ions
4. Recombination of negative and positive ions

2.3.4 Minimum breakdown voltage

To breakdown the gas for plasma ignition, a threshold amount of voltage termed as "breakdown-voltage" (V_b) must be exceeded.

V_b is a function of electrode spacing and pressure at which gas flows (Schutze et al., 1998).

$$V_b = \frac{B(p \cdot d)}{\ln[A(p \cdot d)] - \ln[\ln(1 + 1/\gamma_{sec})]} \tag{2-12}$$

Where A and B are constants determined experimentally and γ_{sec} is the secondary electron emission coefficient of cathode. Values of A and B for different set of conditions for E/p ratio for water vapours and several other gases are given in (Fridman and Kennedy, 2004). Where, E is applied electrical field and p is the pressure at which gas flows. This could be explained with the help of the "Paschen Curve" in the **Figure 2-1**. Breakdown voltage is a function of pd number. Where d is the inter-electrode distance.

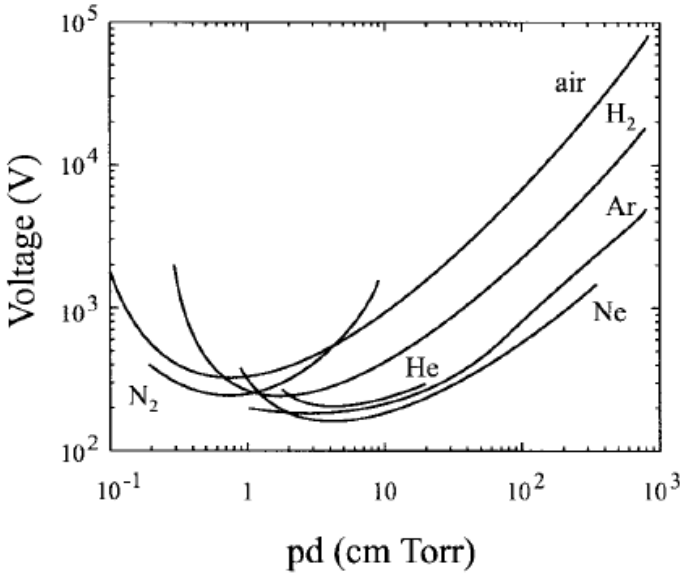

Figure 2-1 Breakdown potential in various gases as a function of the pressure and the inter-electrode distance for plane-parallel electrode

2.3.5 Types of plasma

Plasma can be classified in different types depending upon electron energy level, electronic density and temperature which alter the properties of plasma. These changes are governed by the source and amount of the energy supplied. **Figure 2-2**

shows the different types of the plasmas according to electron number density and electron temperature. Water vapour plasma is found in glow discharge region.

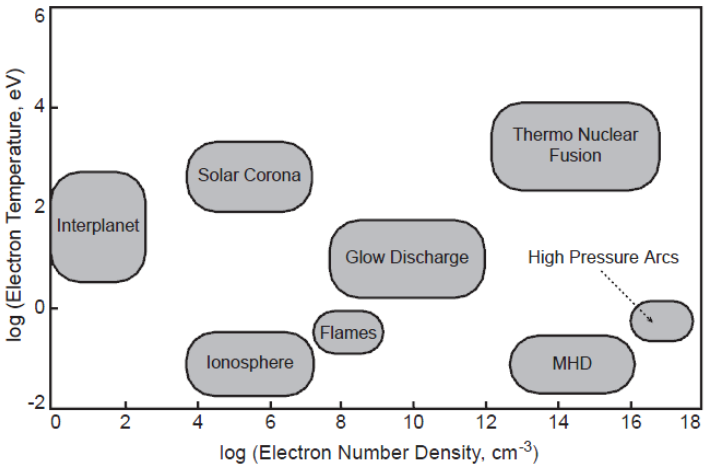

Figure 2-2 Plasma temperature and densities (Fridman, 2008)

Typical classification is made on the basis of the local thermodynamic equilibrium of the plasma. Plasma could be stated as high temperature (thermal) plasma and cold (non-thermal) plasma (Petitpas et al., 2007). Plasma could be classified into two major types of discharges in this regard (Tendero et al., 2006, Bellan, 2006).

1. Local thermodynamic equilibrium plasmas (LTE)
2. Non-local thermodynamic plasmas (Non-LTE)

In LTE plasmas, transitions and chemical reactions are governed by collisional process and radiative process does not play an important role. LTE plasmas are micro-reversible having reversible processes to balance all the types of collisions occurring e.g., excitation/dexcitation, ionisation/recombination etc. In LTE plasmas, electron temperature (T_e) is found to be in equilibrium with the gas temperature (T_g) which could range from tens of *eV* to hundreds of *eV*. However, in non-thermal plasma, the electron temperature can reach 1-10 *eV* while gas temperature can be as low as room temperature. Electrons, due to their very small sizes, can absorb energy quickly and attain temperatures in the range of tens of thousands. However, large gas particles/ions tend to stay at quite low temperature usually in the range of 300-325 K. There may also be a situation where the ions have different temperature from each other. Especially in the presence of magnetic field, the ions would be characterised by

two different temperatures regarding the movement of ions either in parallel or perpendicular to the magnetic field.

Hydrogen can be obtained from both types of the plasma but non-thermal plasma has been found to be more energy efficient because much of the heat in the thermal plasma is utilised in just heating the particles (Petitpas et al., 2007).

Non-thermal plasma could be further classified into several types. This classification is based on many factors including mechanism of plasma generation, pressure applied and electrode geometry. The major classifications are as follows;

1. Direct current glow discharges
2. Corona discharges
3. Dielectric barrier discharges
4. Inductively coupled radio frequency discharges (ICP-RF) radio frequency discharges
5. Capacitively coupled radio frequency discharges (ICP-RF)

2.3.5.1 Direct current glow discharges

When constant voltages are applied between electrodes at very low pressure, a continuous current flows through the discharge which gives rise to the glow discharge. This type of the discharge is characterised by a particular glow (e.g., fluorescent tubes) caused by the excited atoms and excited species. These kinds of discharges are operated under very low pressure (>10 mbar) usually in a flat electrode geometry. Applied voltages are usually in the range of 300-1500 V which may be increased in to several kV in different applications while current is generally in the mA range. The electrons, in glow discharge, are highly energetic producing effective collisions. Low pressure DC glow discharge can be divided into four regimes according to current-voltage behaviour as shown in **Figure 2-3**. The first one is dark or Townsend discharge which occurs prior to the spark ignition. Second one is normal glow in which the voltage remains constant or decrease very slightly with the current. Abnormal flow is the third region where the voltage increases with the current and the fourth one is the arc discharge where plasma is found to become highly conductive (Schutze et al., 1998). Electrodes play an essential role in the sustainability of this type of discharges.

Glow discharges are not suitable for chemical synthesis because of their low pressure characteristics.

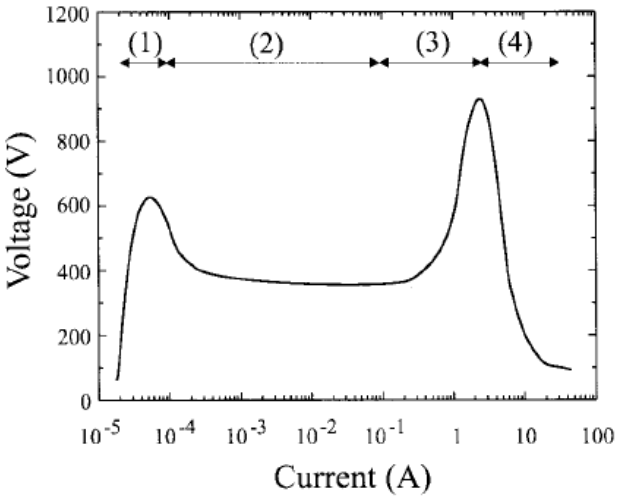

Figure 2-3 Current-Voltage characteristic of a low power DC glow discharge at 1 torr (Schutze et al., 1998)

2.3.5.2 Corona Discharges

This type of discharges could be initiated using asymmetric electrode geometries like a pointed wire electrode with a plate one. It could be imagined as a line of pins fastened to a hollow pipe at one end and protruding from the other end through tiny holes. The feed gas enters the chambers and passes through the holes and provides a local atmosphere around the corona points (Laroussi, 2002). It is also said that it creates a crown around the wire which is why it is called as corona discharge. Small radius of curvature at the top of the wire results in a high electric field which is required for ionising the neutral atoms. Cathode is in the form of a wire at very high negative potential. Due to this negative potential, positive ions are accelerated towards the cathode where secondary electron are emitted and accelerated into the plasma. This moving front of electrons can reach up to 10 *eV*. This is followed by a tail of lower energy electrons (~1 *eV*) which is called streamers. Plasma could be ignited in the range of 2-5 kV and produces extremely small current 10^{-10}-10^{-5} A. Above higher current value of 10^{-5}A, voltage rapidly increases with current and generation of micro-arcs or streamers may occur. A maximum voltage has been recorded at the current values of about 5 x 10^{-4}A where arcing starts (Schutze et al., 1998). Corona discharges are inhomogeneous and could be operated at atmospheric pressure. In pulse mode operation, pulse time is usually shorter than the time for arc formation which implies

that when each pulse ends, the discharge extinguishes before it becomes too conductive (Tendero et al., 2006). Density of the species is decreased very rapidly from 10^{13} cm^{-3} to 10^{9} cm^{-3} with the distance from the electrode. The electron temperature within the plasma averages about 5 *eV*. Corona discharges, having pulsed power source, are nowhere in equilibrium both with respect to temperature and chemistry. This is because of the short nature of the pulse. If the source is not pulsed, it would result in build-up of heat giving rise to thermal emission and finally into an arc discharge. Major applications of corona discharges are stack gas treatment facilities where it is employed for the removal of dust particles or destruction of the volatile compounds from the paint or water purification industry.

2.3.5.3 Dielectric Barrier Discharges (DBDs)

A dielectric layer within the discharge zone in between the two electrodes covering at least on electrode differentiates the DBD discharges from other types of plasmas. Usually it is operated under high pressure with an oscillating voltage providing operational sustainability at kilohertz frequencies. DBDs are usually ignited by means of a sinusoidal or pulsed power source (Tendero et al., 2006). Gas composition, voltage and frequency determine the discharge to be filamentary or glow. DBDs are powered by AC voltage of 1-100 kV with the frequency ranging from few Hz to MHz. Distance between electrodes depends upon the application and could be 0.1 mm in plasma displays to several cm in CO_2 lasers (Kogelschatz et al., 1999). Under high pressure in small gaps between electrodes, this discharge operates in a regime called streamer regime (micro-discharges) characterised by narrow discharge filaments. At atmospheric pressure, the current filaments in DBDs in streamer region have an electron density in the range of 10^{12}-$10^{17}$$cm^{-3}$ and is very short lived (Barni et al., 2005). DBDs could be produced in two different types of configurations namely volume discharge (*VD*) and surface discharge (*SD*). The basic difference is the configuration of the electrodes. In *VD*, the plasma is sustained between parallel electrodes and is distributed over the electrode surface. The number of micro discharges/period is proportional to the amplitude of the voltage. In *SD,* discharges are sustained in number of surface electrodes on dielectric layer and a counter electrode on the opposite side (Gibalov and Pietsch, 2000).

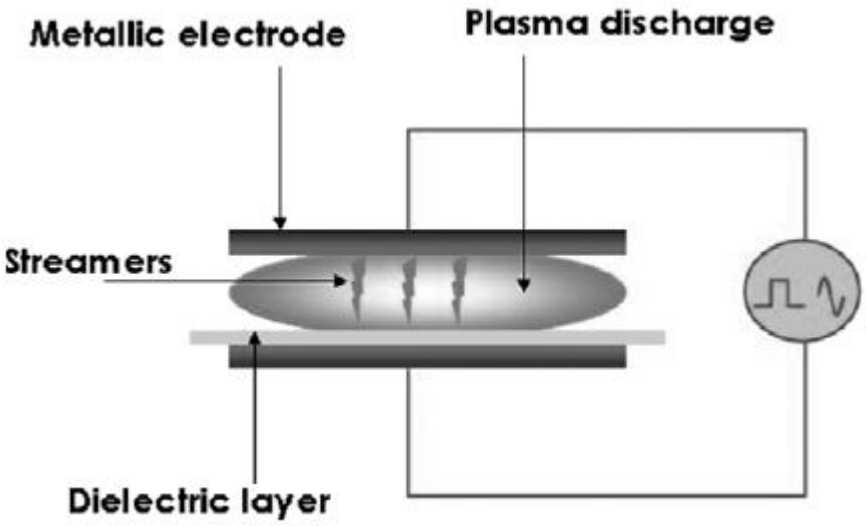

Figure 2-4 Principle of dielectric barrier discharge (Tendero et al., 2006)

Significant role is played by dielectric layer that;

1. Limits the discharge current. Arcing is avoided between the two electrodes which allow applying either continuous or pulsed mode.
2. Distributes the irregular streamers on the electrode surface which results in homogenous treatment.

DBDs are known to be flexible with respect to geometrical shape, operational parameters of the reactors and the type of the gas/mixture which could be used as feed. DBDs offer another advantage in terms of the scaling up which is very straight forward (Sarmiento et al., 2007).

2.3.5.4 Inductively coupled radio frequency discharges (ICP-RF)

ICP's are intrinsically three dimensional (3-D) while the micro-fabrication techniques are essentially (2-D). This is why this type of discharge is not considered very much in this literature survey.

2.3.5.5 Capacitively coupled radio frequency discharges (CCP-RF)

In CCPs discharges electric energy is coupled with the plasma discharge with the use of its sheaths and the two electrodes. This happens when one of the electrodes is nonconductive as in case of spectro-chemical analysis of non-conducting materials or for the deposition of dielectric films. The electrodes are gradually covered with insulating material which results in the charge up of electrodes due to the

accumulation of positive and negative charges eventually extinguishing the plasma. This problem is sorted by applying an alternating voltage making each electrode alternating positive and negative. Charge thus accumulated would be partially neutralised by the next half cycle having with opposite charge. This type of discharge is characterised by very high frequencies and low operating pressure. Frequency usually ranges between (1 MHz-100 MHz) with 13.56 MHz being most commonly used. This is done to achieve non equilibrium conditions. Frequency should be tuned in such a way that it is high enough so that half the period of the alternating voltages is less than the time during which the insulator charges up. Otherwise shorter frequencies may yield a series of short lived discharges with electrodes successively taking opposite polarities instead of quasi-continuous discharges (Lozano-Parada, 2007). Electron density could range from 10^{9}-$10^{10}cm^{-3}$ and may be increased to $10^{11}cm^{-3}$ with the increase in frequency.

Typical examples of non-thermal atmospheric pressure plasmas are corona discharges and DBDs (Kim et al., 2006). Corona discharges are considered suitable for various industrial processes as this type of discharges generates a high concentration of radicals. However, continuous corona discharges have a very low power which is unacceptable for many applications. Voltages could be increased to raise the power level, but this leads to corona transition into arcs. Arcing could be prevented by covering one or both electrodes with dielectric material or by creating corona discharge with pulse-periodic mode (Fridman et al., 2005). By introducing a dielectric layer, the discharge current is limited, arcing could be avoided between two electrodes, and a homogenous discharge could be created (Sarmiento et al., 2007). Therefore, many DBD-corona hybrid reactors have been designed to overcome these difficulties and take advantage of both high concentration of radicals in corona discharges and homogeneity of plasma discharge at higher power in DBDs (Kim et al., 2006). Based on the above discussion, in the current study, a DBD-corona hybrid discharge reactor was used. it is discussed in details in chapter 4.

2.3.6 Water vapour plasmolysis

Plasma could be generated from electrical energy by transforming it to kinetic energy of electrons which is then transformed into molecular excitations and to kinetic energy

of heavy particles (Bockris et al., 1985). High efficiency and productivity of chemical reactions has raised interest in the hydrogen production in non-equilibrium plasma. This high specific productivity is the advantage of plasma-chemical methods over any other electrical hydrogen method e.g., electrolysis (Givotov et al., 1981). Plasmolysis can produce hydrogen 1000 times more than the conventional electrolysis process with same size of electrolyser because of its volumetric nature. This is due to the fact that using plasma activation energy barrier of transition states could be overcome easily because of multiple excited species. However, the energy efficiency of the plasma-chemical reaction is thought to be same as the electrolytic and thermo-catalytic (Fridman, 2008) systems. Hydrogen production by water vapour plasmolysis has always been viewed as an expensive route, with estimates of 50% efficiency with conventional plasma reactors (Bockris et al., 1985), trailing behind electrolysis and about on par with thermo-chemical cycles.

Cumulative dependence of energy efficiency of H_2O dissociation on energy input is usually calculated for different specific mechanisms of the process with experimental results. Most of the discharge energy is thought to be transferred to vibrational excitation of plasma-chemical water dissociation. This is why it is considered to play an important role in water dissociation (Fridman, 2008). Vibrational excitation stimulated dissociation of water molecules in plasma follow three major steps:

1. Electron impact excitation cause the excitation of lower vibrational levels of water molecule
2. Excitation of higher vibrational level of H_2O
3. Decomposition of highly vibrationally excited molecules H_2O^* starts as a chain reaction (2-13 - 2-18)

Water vapour dissociation by vibrational excitation has been thought to follow the given mechanism (2-13 - 217) (Bockris et al., 1985):

$$H_2O^* + H_2O \longrightarrow H + OH + H_2O \quad (2\text{-}13)$$

$$H + H_2O^* \longrightarrow H_2 + OH \quad (2\text{-}14)$$

$$OH + H_2O^* \longrightarrow H_2O_2 + H \quad (2\text{-}15)$$

$$OH + H_2O \longrightarrow H_2 + HO_2 \quad (2\text{-}16)$$

$$HO_2 + H_2O \longrightarrow H_2O_2 + OH \quad (2\text{-}17)$$

$$H + OH + H_2O \longrightarrow H_2O + H_2O \quad (2\text{-}18)$$

Major products of the water dissociation by vibrational excitation mechanism are molecular H_2 and H_2O_2. H_2O_2 is unstable under typical plasma conditions and decomposes yielding H_2O and O_2. The reactions 2-16 & 2-17 have very poor kinetics because of the large activation barrier they have to overcome. In a separate study (Fridman, 2008) another chain termination by three body recombination reaction (2-18) has been proposed. Another mechanism which could lead to the propagation of dissociation by vibrational excitation is as follows:

$$OH + H_2O^* \longrightarrow H_2 + HO_2 \qquad \Delta H = 2.1\, eV/molecule \quad (2\text{-}19)$$

$$HO_2 + H_2O^* \longrightarrow H_2O_2 + OH \qquad \Delta H = 1.1\, eV/molecule \quad (2\text{-}20)$$

The total energy efficiency of the water molecule dissociation by this method is governed by three major factors namely excitation factor η_{ex}, relaxation factor η_{rel} and chemical factor η_{chem}. The detail of these factors and how they affect the water vapour plasmolysis is discussed by Fridman (2008). Also, mechanism of water vapour plasmolysis is discussed in detail in section 3.2 of chapter 3. In the following section different hydrogen production studies have been summarised.

2.3.7 Review of previous hydrogen generation methods by plasma

Water vapours were used as feedstock for hydrogen production using two methods (Givotov et al., 1981). High frequency (H.F) and ultra high frequency (U.H.F) discharges and a non-self-sustained discharge stimulated by a relativistic electron beam was used for water vapour plasmolysis. Maximum energy efficiency was found to be 40% which was less than the predicted theoretical efficiency of 50-70% . A two stage plasma reactor involving carbon dioxide dissociation as first step was proposed to increase the energy efficiency (Givotov et al., 1981).

$$CO_2 \longrightarrow CO + \frac{1}{2}O_2 \qquad \Delta H = 2.9\ eV/molecule \quad (2\text{-}21)$$

$$CO + H_2O \longrightarrow CO_2 + H_2 \qquad \Delta H = -0.4\ eV/molecule \quad (2\text{-}22)$$

However, this process requires the separation of CO and O_2 in the intermediate stages.

A novel method for methane reforming utilising pulsed corona discharge has been used for hydrogen generation (Mutaf-Yardimci et al., 1998). Pulsed corona discharge acted as a catalyst and its effect could be seen as promotion in hydrogen generation. Energy efficiency of 350% for 16% conversion was observed.

Liu et al. (2003) produced hydrogen from methanol using corona discharge at room temperature and found that methanol conversion increased from 0.196 to 0.284 $mol.hr^{-1}$ with increase in water concentration from 1.0%-16.7%.

Production of anomalous hydrogen from an aqueous solution using conventional plasma electrolysis has been reported by Mizuno et al. (2002). In their study, continuous generation of the hydrogen greater than the predicted by Faraday's Law was found to occur after certain conditions of temperature, current density, input voltage and electrode surface was achieved and in some observations hydrogen produced was 80 times higher than predicted by normal Faraday's law. The power efficiency ranges between 93-103% and current efficiency varied between 0.98~1.1.

Dielectric barrier discharge has been used to decompose methane to produce hydrogen and carbon by Boutot et al. (2004). Authors claimed the process to be greener as compare to SMR, insensitive to catalyst, inherently load following, safe, low temperature and an atmospheric operation. However, energy efficiency has not been reported.

Microwave plasma induced partial oxidation has been used to reform of kerosene oil and methane with air and oxygen by atmospheric pressure microwave discharge plasma by Babaritskii et al. (2004). They found that the energy input in the form of plasma is 1.3-1.6 times as effective in the enhancement of kerosene conversion compare with thermal energy input.

Paulmier and Fulcheri (2005) studied non-thermal plasma reforming for hydrocarbon and found reformer efficiency in auto thermal mode reached 12.3% and in steam reformer it reached 26%.

Hydrogen was produced by plasma electrolysis by placing metal electrodes above the liquid surface by Chaffin et al. (2006). This method is suggested to remove the cost of the electrolytes and catalysts of conventional electrolytic processes. However, energy efficiency has not been reported.

Plasma was used to catalyse the reaction between water vapours and sulphur dioxide by Koo and Lee (2007). The process has been claimed to produce hydrogen with a voltage $1/8^{th}$ of the voltage utilised by conventional electrolysis method.

In another study (Sarmiento et al., 2007), hydrocarbon and alcohols in mixtures were reformed with carbon dioxide and water. Methane was converted up to 70% into CO and H_2 without transforming into higher hydrocarbons while alcohols (methanol and ethanol) were converted 100% to the same products with very high flow rates than that of methane.

Hydrogen was produced via steam reforming in an atmospheric pressure microwave plasma by Jasinski et al. (2008). Hydrogen production rate and the corresponding energy efficiency were up to 225 g of H_2 per hour and 85 g per kWh^{-1} respectively and are considered as better than steam methane reforming and electrolysis.

Magnetically enhanced radio frequency plasma source has been used to decompose water vapours to produce hydrogen by Nguyen et all. (2009). Hydrogen production was found to increase linearly with rf-power without the application of the axial magnetic field. However, with the application of the magnetic field hydrogen production reaches its maximum value at 500 W and then saturates with rf power.

The rate of formation of H_2 and H_2O_2 from decomposition of pure water has been studied by Burlica et al. (2010). The energy yield of H_2 and H_2O_2 in Ar were 45% and 20% of the thermodynamic limit respectively. When air was used as a carrier gas, formation of both H_2 and H_2O_2 was found to decrease while formation of nitrates was dominant.

More recently, the thermodynamics of the steam reforming of ethanol using cold plasma conditions using "Density Functional Theory" has been studied Wang et al. (2010). The results showed that the only thermodynamics barrier for the production of

H_2, CO, CH_4 and CH_3CHO is the dissociation of ethanol and steam molecules which is considered as rather easy to be done under clod plasma conditions.

A discussion on energy efficiency of different hydrogen production technologies is done in section 5.2.9 and comparison of energy yields of different hydrogen production technologies is given in **Table 5-4**.

2.3.8 Plasma micro-reactors

Plasma processes are considered as a capital and power intensive to sustain a plasma discharge. This is a consequence of the large gap distance between electrodes requiring high voltage differences to support a steady state plasma. The large distance is maintained to avoid the recombination of active species near the walls of the reactor. However, micro-plasmas require much less energy to sustain plasmas at atmospheric pressures. Scaling down plasma reactors to micro-channels has shown capability of producing plasma at much lower power voltages than the conventional plasma reactors (Lozano-Parada, 2007). This could be explained on the basis of the reduced electric field or *E/n* ratio where *E* is applied electric field strength and *n* is the gas number density. Mean kinetic energy of the plasma discharges is the unique function of this ratio. It should be noted that despite scaling down of conventional plasmas discharges, *E/n* should be kept constant to have similar discharge properties. The trick here is that decreasing the distance between the electrodes in capacitive coupled discharges to the micron-scale increases the electric field strength thereby voltage and hence power required to have a sustainable plasma discharge is lowered. Due to this reason, it is possible to sustain micro-plasmas at substantially lower power which results in lower operation cost. Reducing distance, however, requires finding a pressure regime in which plasma discharges could be described in terms of continuum nature of the conservation equations. This means an increase in the working pressure (e.g., 1 bar) to preserve the continuum character of the conservation equations. The operation at elevated pressures eliminates the use of expensive vacuum pumps and gives micro-plasmas another economical advantage over conventional plasma systems (Lozano-Parada, 2007).As mentioned above breakdown voltage of the gas (V_b), according to Paschen law, is given as a function of pd number where p is the pressure

of the gas and d is inter-electrode distance as shown in the **Figure 2-1**. The values of V_b for helium and argon gases are 125 V and 70 V respectively over an inter electrode distance of 1 mm at atmospheric pressure (Moravej et al., 2004). These sorts of voltages are easily and safely available at laboratory scale. Lozano-Parada and Zimmerman (2010) have shown the production of ozone from a plasma micro-reactor at 170 V AC which is much lower than the kilovolts used in conventional plasma reactors.

2.3.9 Plasmolysis versus electrolysis

The efficiency of water vapour plasmolysis has been considered low (~40%). Electrolysis has been considered as a better option for mass production of hydrogen on the basis of its higher proposed efficiency (~85%) which may lead up to 100% by increasing the voltage. It has been suggested that electrolysis may be the efficient way of utilising it (Bockris et al., 1985). National Renewable Energy Laboratories (Johanna, 2004) has published a report on different scale of hydrogen production by electrolysis. The energy efficiency of the electrolysis has been defined as;

$$Energy\ \ Efficiency\ = \frac{Higher\ \ heating\ \ value\ of\ \ H_2}{Energy\ \ conusption\ by\ \ electrlysi\,s\ per\ kg\ of\ \ H_2} \qquad (2\text{-}23)$$

The higher heating value is taken assuming electrolysis of liquid water. Energy efficiency of the different electrolysis system of different scales has been found to range from 56-73%. This report clearly differentiates the energy efficiency of standalone electrolyser and entire electrolysis system. It is further clarified by an example that a specific electrolyser "Stuart IMET 1000" requires 46.8 kWh/kg of H_2. Dividing heat of formation of hydrogen (39 kWh/kg of H_2) with the energy requirement yields and energy efficiency of 83% based on HHV which is approximatley equal to what has been previously reported (Bockris et al., 1985). However, when the energy requirement of the rectifier and auxiliaries are included the energy requirement jumps to 53.5 kWh/kg of H_2 reducing an efficiency of 73%. According to the report there are two major factors in fixing H_2 cost. If plant is relatively big, it is the electricity that plays the major role and if plant size is small; capital cost becomes the limiting factor.

Another implication is relatively short life of electrolyser stack ranging between 5-15 years.

Production of hydrogen by water vapour plasmolysis looks even more advantageous, as steam in this study is considered to be produced from waste heat sourced from the plants which could be find easily in chemical plants or power generation plant and does not require additional energy for steam generation. Secondly, scaling down to micro-fluidics system is anticipated to require much less power. Micro-plasma reactors, along with their lower power requirement, offer another advantage of better control over the process than the conventional processing. This is possible because use of microfluidics can tailor fluid dynamics through high but brief field gradients which are spatially precise and electronically controlled (Rehman et al., 2012, Zimmerman, 2011). Another advantage of hydrogen production by plasmolysis is the separation of hydrogen from the product gases. This could be solved again taking help from micro-fluidics using microbubble dynamics. There is significant difference in solubilities of oxygen and hydrogen in water with oxygen being 25 fold more soluble than the hydrogen. Product gases entering in the form of microbubbles in a tall column of water will yield hydrogen rich gas from the top.

Considering the above discussion and recent developments in plasma technology, it is envisaged that water vapour plasmolysis could potentially be a cheaper way of producing hydrogen. Integration of waste heat, to produce steam with plasma micro-reactor technology may increase process efficiency. Secondly low capital cost and maintenance of plasma micro-reactors may be the biggest attraction. Multiplexing plasma micro-reactors (Lozano-Parada and Zimmerman, 2010) could increase the production of hydrogen which could be substantially cheaper than electrolysis stacks in terms of capital outlay for a given scale production facility.

2.4 Kinetics of ozone formation

In the current study, ozone generation has been used to optimise the operational parameters of plasmolysis instead of hydrogen. Based on the similarities of kinetics of formation of ozone and hydrogen, the rationale for using ozone for optimisation studies has been discussed in detail in section 5.3.1 in chapter 5. So, it is of great importance to understand the kinetics of ozone formation.

Ozone was first identified by its characteristic odour during water electrolysis (Schönbein, 1837) and few years later, Siemens (1857) proposed a novel type of electrical gas discharge which could generate ozone from air or oxygen flowing at atmospheric pressure (Rubin, 2001, Kogelschatz et al., 1999). Kinetics of ozone formation both from oxygen and air has been studied extensively (Hadj-Ziane et al., 1992, Kossyi et al., 1992, Eliasson and Kogelschatz, 1991, Lozano-Parada and Zimmerman, 2010, Yagi and Tanaka, 1979, Kogelschatz et al., 1997, Fridman, 2008)

The most important kinetic pathway in ozone formation is the dissociation of an oxygen molecule in to excited oxygen states (2-24[a] and 2-24[b]). This is followed by a three body recombination reaction (2-25). The third body role could be played by O_2 or O_3 in air plasmas. Along with O_2 and O_3, N_2 could also work as third body in air plasmas.

$$e + O_2 \longrightarrow e + O_2\left(A^3\textstyle\sum_u^+\right) \longrightarrow e + O\,(^3P) + O\,(^3P) \qquad (2\text{-}24^a)$$

$$e + O_2 \longrightarrow e + O_2\left(A^3\textstyle\sum_u^-\right) \longrightarrow e + O\,(^1D) + O\,(^3P) \qquad (2\text{-}24^b)$$

$$O(^3P) + O_2 + M \longrightarrow O_3^* + M \longrightarrow O_3 + M \qquad (2\text{-}25)$$

O_3* is an excited/transient ozone species. Reactions (2-24)-(2-25) are the generally accepted mechanism, however, much more complex mechanistic models are proposed for ozone formation in air (Eliasson and Kogelschatz, 1991). Ozone formation from air as a feedstock has additional complexity due to generation of nitrogen-containing reactive intermediate and product species. NO, NO_2, N_2O, NO_3, N_2O_5, N^+ and N_2^+ are just few examples of species which could be present in air plasma. However, under conventional ozone synthesis from air only N_2O and N_2O_5 could be detected in addition to ozone in an air plasma (Eliasson and Kogelschatz, 1991).

Ionic reactions do not contribute significantly towards the formation of ozone. There is an optimum micro-discharge strength for ozone production. This strength is characterised by the ratio of concentrations of oxygen atoms to oxygen molecules $[O]/[O_2]$ in the micro-discharge channel or energy deposited in the micro-discharge channel. For oxygen plasma, stronger microdischarges start favouring the unwanted

reactions as shown in (2-26)-(2-28), where an optimised ratio of an order of 10^{-3} has been proposed (Eliasson and Kogelschatz, 1991).

$$O + O + M \longrightarrow O_2 + M \quad (2\text{-}26)$$

$$O + O_3^* \longrightarrow 2O_2 \quad (2\text{-}27)$$

$$O + O_3 \longrightarrow 2O_2 \quad (2\text{-}28)$$

The presence of moisture can alter the kinetics. The increased moisture content also increases the surface conductivity of the dielectric materials. This increased surface conductivity enhances the ability of dielectric materials to conduct charges and hence leads to strong micro-discharges (Fridman, 2008). The strong micro-discharges produce higher concentration of atomic oxygen which favours side reactions as stated above. For an optimised O_3 production, air has to be dried "completely" to a dew point of -60 ^{o}C. Ozone formation is poisoned by moisture because of the formation of additional OH and HO_2 (2-29)-(2-30) (Fridman, 2008). NO and NO_2 produced in this case react with OH to form HNO_2 and HNO_3 respectively as shown in (2-31) and (2-32) (Pinart et al., 1996, Kogelschatz, 2003) and related species.

$$OH + O_3 \longrightarrow HO_2 + O_2 \quad (2\text{-}29)$$

$$HO_2 + O_3 \longrightarrow OH + O_2 + O_2 \quad (2\text{-}30)$$

$$OH + NO \longrightarrow HNO_2 \quad (2\text{-}31)$$

$$OH + NO_2 \longrightarrow HNO_3 + O_2 + O_2 \quad (2\text{-}32)$$

For air plasmas, higher power densities tend to produce nitrogen oxides. In this case NO and NO_2 could also be formed along with N_2O. Surprisingly, the ozone concentration in air plasma is higher than what could be expected from an oxygen content (21%) of air which could possibly be explained on the basis of additional processes (2-33)-(2-36) releasing oxygen atoms along with (2-24[a])-(2-24[b]). (Eliasson and Kogelschatz, 1991, Kogelschatz, 2003, Fridman, 2008)

$$N + O_2 \longrightarrow NO + O \quad (2\text{-}33)$$

$$N + NO \longrightarrow N_2 + O \quad (2\text{-}34)$$

$$N_2 (A^3 \sum_u^+) + O_2 \longrightarrow N_2O + O \quad (2\text{-}35)$$

$$N_2 (A^3 \sum_u^+, B^3 \prod_g) + O_2 \longrightarrow N_2 + 2O \quad (2\text{-}36)$$

2.4.1 Ozone decomposition in water

Ozone, in the current study, has been quantified using a chemical method (Bader and Hoigné, 1981). Therefore, it is very important to understand how ozone is decomposed in aqueous solutions. Ozone is unstable in water (half life of 15 minutes at 25^{o}C). Ozone decay in natural water is characterized by initial fast reactions followed by slow first order kinetics (Von Gunten, 2003). Also, decomposition of ozone is sensitive to temperature, type of organic matter and pH of the solution in which it is injected (Tomiyasu et al., 1985, Von Gunten, 2003, Hoigné, 1998). Higher temperatures above 800^{o}C favour nitrogen oxide formation which suppress ozone synthesis (Fridman, 2008). Ozone diluted in air is unstable at higher temperatures hence there is a chance for ozone decomposition in the plasma zone if the temperature is high (Fridman, 2008). Ozone dissolved in water decomposes by following two different chemical pathways. Some fraction of ozone produced reacts directly with the solute (Potassium indigo trisulfonate in the current study) in water and the rest of the ozone may first decomposes into $\dot{OH}$ radicals which would than react with the solute/organic matter (Hoigne and Bader, 1976). Ozone decomposition mechanisms have been studied extensively and the generally accepted mechanism (Staehelin and Hoigne, 1982, Forni et al., 1982, Buehler et al., 1984) is such that where one mole of ozone would produce one mole of $\dot{OH}$ during propagation reaction. Either direct reaction of potassium indigo trisulfonate with ozone or indirect decomposition of the potassium indigo trisulfonate by $\dot{OH}$, it can be assumed that one mole of ozone will react with one mole of indigo salt.

Table 2-2 indicates comparison of basic operational parameters of industrial scale ozone generators. The data in **Table 2-2** has been presented to emphasise the difference between the operational parameters of conventional ozone generation and the current study. Detailed discussion on this topic is done in chapter 5.

Table 2-2 Comparison of different types of industrial ozone generators (Fridman, 2008)

Ozone Generator	Feed	T_{dew} (^oC)	d (mm)	V (kV)	f (Hz)	$D_{thickness}$ (mm)	η (kWh/kg)
Otto	Air	-40	3.1	7.5-20	50-500	3-5	10.2
Tubes	Air	-60	2.5	15-19	60	2.5	7.5-10.0
Tubes	Oxygen	-60	2.5	15-19	60	2.5	3.75-5.0
Lowther	Air	-60	1.25	8-10	2000	0.5	6.3-8.8
Lowther	Oxygen	-60	1.25	8-10	2000	0.5	2.5-5.5

Where, T_{dew} is dew point of air, d inter-electrode distance, V is voltage, f is frequency, $D_{thickness}$ is the thickness of dielectric barrier and η is energy cost

2.5 Separation of hydrogen from product gases

Despite having more specific productivity over other electrical hydrogen production methods such as electrolysis (Givotov et al., 1981), separation of the product gases (hydrogen and oxygen) of water vapour plasmolysis has remained an unsolved problem. In the following section separation of the hydrogen from product gases will be discussed by different methods.

2.5.1 Hydrogen separation technologies

There are several techniques available for hydrogen separation and purification such as membrane separations, pressure swing absorption (PSA) and cryogenics. Both PSA and cryogenic distillation can give high purity hydrogen but are energy intensive processes (Adhikari and Fernando, 2006). One of the solutions is to use a membrane to separate hydrogen and oxygen. Membranes can also provide high purity of hydrogen, as an alternative to PSA or cryogenic process at relatively lower energy consumption (Cheng et al., 2002). In the current study, the product stream will have more than one component (hydrogen, oxygen, un-decomposed steam, and argon) compared with direct plasmolysis of water where product stream would contain only hydrogen and oxygen. Although membranes presents a viable option, there are particular limitations. For example, metallic membranes such as Pd-based give very high purity hydrogen but they are very expensive. Ceramic membranes present relatively less expensive option but they are brittle. Polymeric membranes are not brittle and the cheapest option to use. However, they are known to plasticise in the presence of moisture (Basu et al., 2010). Their separation efficiency has been found to reduce with the moisture content present in the feed. Presence of a large amount of

un-decomposed steam reduces permeability of hydrogen and hence separation efficiency will be reduced (Wang et al., 2013). Separation of hydrogen from such mixture of gases may require more than one membrane or a custom made membrane for this job which would increase the cost of the overall plasmolysis system. The separation problem could be solved by taking help from microfluidics using microbubble dynamics as discussed in the following section.

2.5.2 Separation by microbubbles

A novel approach based on microbubble separation is proposed to separate hydrogen from the other gas mixtures. As **Figure 2-5** shows there exists more than an order of magnitude difference between solubility of hydrogen and oxygen in water at all temperatures. The proposed separation scheme exploits this difference, to separate hydrogen from oxygen. Water vapours along with Ar will be decomposed in a plasma micro-reactor as sown in **Figure 2-6.** Argon being inert would not participate in the water vapour plasmolysis and would leave the plasma micro-reactor without any chemical transformation. Un-decomposed steam would condense once it comes in contact with water. A bubble would essentially contain argon, oxygen and hydrogen in it at this stage. As products would rise in the form of bubbles in a column filled with water, oxygen would preferentially dissolve in water while bubbles containing hydrogen and argon would keep on rising. If hydrogen is to be used on a plant on as intermediate energy storage then conversion by a fuel cell will result in the argon in the off-gases, hence naturally separated and recycled. If the hydrogen is to be used as a chemical intermediary, say for reducing biofuels to drop-in fuels, then if it is a liquid drop-in fuel, the argon will stay in the gaseous phase and again be recycled automatically.

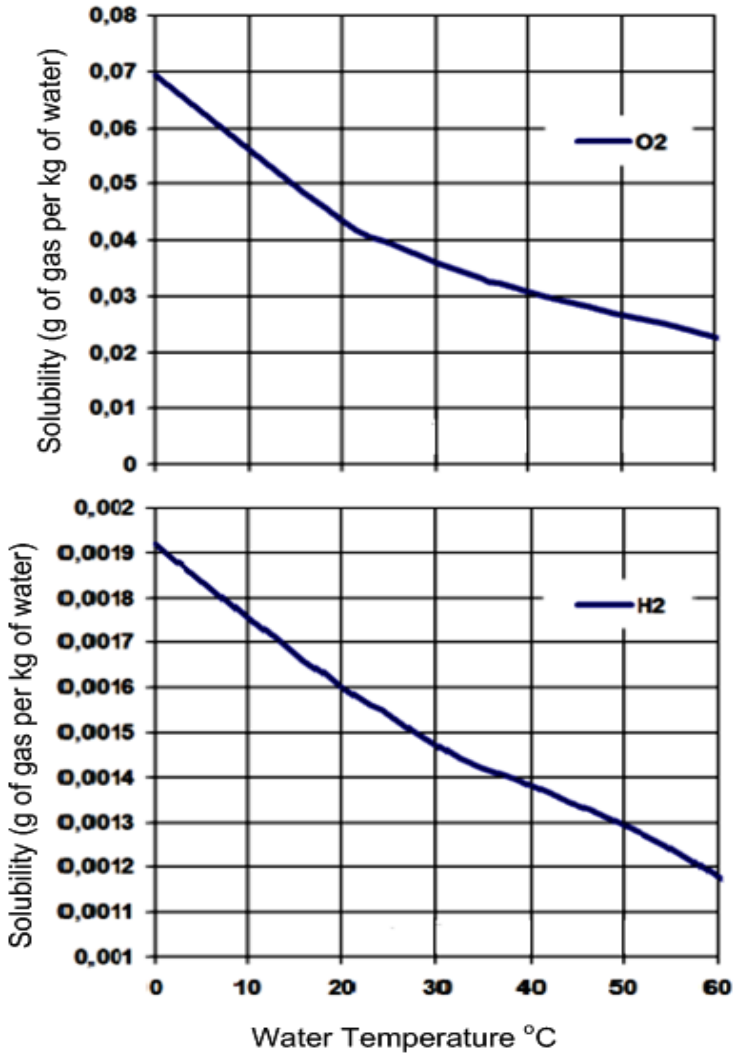

Figure 2-5 Solubility of hydrogen and oxygen at different temperatures (ToolBox, 2014)

A DO probe would then be required to continuously monitor level of DO in the water column. Fresh water could be circulated in the column in order to make process continuous. The oxygen rich water could be utilised elsewhere in the plant for applications like feeding an algae or some other microorganism in a bioreactor. A change in the value of $K_l a$ in this regard could indicate efficient mass transfer by a microbubble generation technique.

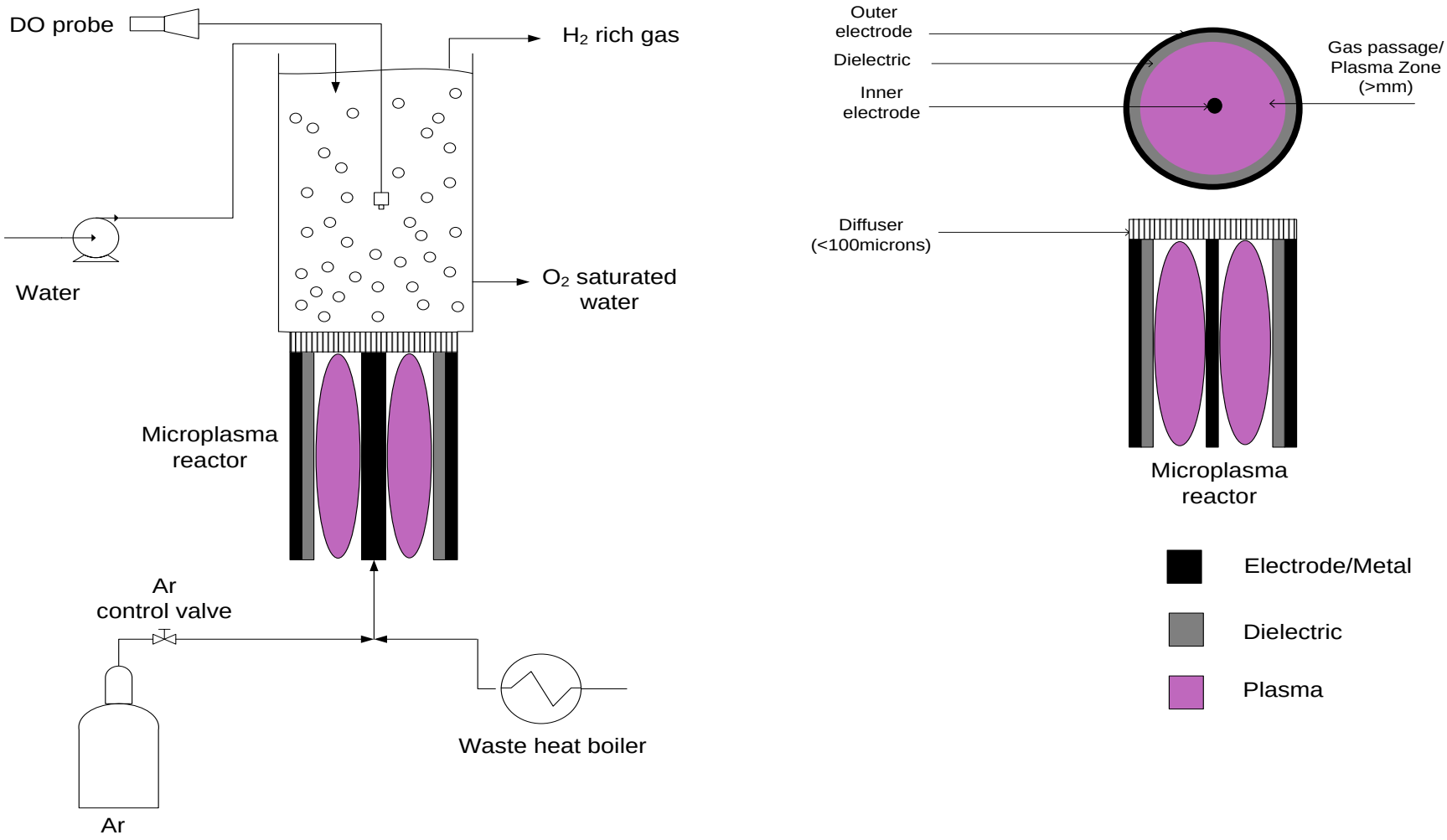

Figure 2-6 Experimental plan for simultaneous production and separation of hydrogen

An efficient and cost effective method to generate microbubbles out of the product gases would than hold the key for taking full advantage of proposed microbubble separation process. It becomes equally important to measure the number density of microbubbles produced as the separation of the gases would depends upon it.

The following discussion is based on the identification, understanding and utilisation of a method to produce microbubbles economically.

2.5.3 Microbubble generation

Although fine pore diffusers are almost ubiquitous at industrial scale bubble generation and utilisation processes like wastewater treatment, the fine pore diffusers working alone as nozzles are not sufficing to produce microbubbles (200-800 µm). Conventional diffusers/nozzles use steady flow to produce fine bubbles on order of 1-2 mm. These bubbles on average are an order of magnitude larger than the pore size. This could be explained on the basis of dynamics of bubble formation. There are two forces responsible for bubble formation. First, wetting force of the liquid around the bubble and second is buoyancy force of the bubble responsible for its rise. A bubble starts to grow when gas passes through a pore. The bubble will keep on growing until the buoyant force overcomes the liquid wetting of the surface (surface tension). Bubble breaks off from the surface and rise up at the velocity based on buoyancy force (Zimmerman et al., 2008). Usually this break off size comes at an order of magnitude higher than the pore size. This could be explained on the basis of Young-Laplace Law which governs the relation between radius of the bubble and pressure difference (ΔP) across the gas-liquid interface. The bubbles growing in the diffuser pores are subjected to instability which make all the bubble growth concentrate at few pores where the size of the bubble could be larger than the size of the pore (Tesař, 2012) . These bubbles then coalesce to produce even bigger bubbles. The coalescence could occur because of polydispersity of the bubble size and irregular space between the bubbles. The other reason for not forming smaller bubbles from very fine porous materials is the channelling in diffuser material which has been shown in Figure 1 (a) of (Zimmerman et al., 2008). In that case the bigger bubble formed provides the path of least resistance and hence all the air would go through this path. This is mainly due to

the non-uniformity in the pores on the diffuser surface. This variation in the pore size leads to a non-uniform gas distribution. These fine bubbles are subjected to a high buoyancy force hence rising rapidly and reducing the resident time. In addition, the surface area to volume ratio of the fine bubbles is also low relative to microbubble which reduces the mass transfer across the gas liquid interface. On the contrary microbubbles offers high surface to mass ratio, hence increase the mass transfer across the gas liquid boundary (Al-Mashhadani et al., 2011).

Surface wetting properties of diffuser are also found to be of great importance. A hydrophobic surface would make gas spread over a larger area than the pore size. This induces a secondary force which holds the bubble to the surface increasing the buoyant force required to dislodge the bubble and hence bubble volume to overcome it. On the other hand hydrophilic surfaces have a thin film between the bubbles and pore surface, so, the hydrophobic gas (air for example) does not stick to the solid surface. Bubbles in this case seem to shoot out like bullets from the pores in the diffuser contrary to the slow pushing out from the diffuser pores (Zimmerman et al., 2011).

As mentioned earlier that conventionally microbubble generation relies on the instabilities shown in Figure 1 in Zimmerman et al., (2008). However, with fluidic oscillations, bubbles could be released from the surface when they form a hemispherical cap which is the smallest possible shape in which bubble could be formed in the strong adverse effects of the surface tension at higher curvatures. Again, this could be explained by looking at the mechanism of bubble formation. There are two phases in bubble formation namely stable phase and unstable phase corresponding to the pressure difference (ΔP) across gas-liquid interface. When a gas is passed through a porous medium/diffuser, a bubble starts to grow with infinite radius of curvature since the interface is a flat plane. Bubble starts to grow big with more gas filling in the bubble. As more gas enters in the bubble, radius of the interface starts to decrease with the increase in the ΔP across the interface following the Young-Laplace law. This is the first stable phase. This is, however, only true for the stage when the bubble has not acquired the hemispherical shape. The second phase of the bubble formation starts when the bubble has reached the hemispherical shape. The bubble

volume keeps growing with increase in the radius which diminishes the ΔP across the interface. Hence the bubble size would keep on growing until the volume of the bubble is such that buoyancy forces overcome the surface tension of the liquid. Consequently a bigger bubble is formed. However, oscillatory flow, does not allow the bubble go past the hemispherical shape due to instabilities caused by pulsations. Using oscillatory flow to produce microbubbles suggests to break bubble off at a critical point at which the bubble could occur. At this critical point the bubble keeps on growing in size if no external force is present to break off the bubble or the bubble might also collapse as the point at which a bubble could be formed has not been reached yet. This kind of fluidic oscillation could be achieved by mechanical means or by fluidic oscillator having no moving parts (Zimmerman and Tesar, 2013).

Usually the microbubbles are produced by three different methods (Zimmerman et al., 2008). Most common method involves compressing the air to a relatively higher pressure (~6 bars) and then releasing through a specially designed nozzle. This method is based on cavitation principle and could produce bubbles as small as nanobubbles. However, high power densities are required for the generation of smaller bubble by this method. Microbubbles could also be produced by the use of ultrasound. Ultrasound is used to induce cavitation locally at points of extreme rarefaction in the standing ultrasonic waves. Again, it involves usage of high power for the microbubble generation. The third method involves oscillating the fluids which could be achieved either by mechanical vibrations or using fluidic oscillator (Zimmerman and Tesar, 2013). The fluidic oscillator is based on the Coanda effect. The tendency of a fluid to attach itself to a vertical wall/ structure and bend away from the initial direction of flow is known as the Coanda effect (Reba, 1966, Freire et al., 2002). The fluidic oscillator offers potentially cheapest means to oscillate the fluid with no moving part. The fluidic oscillator consists of two components. The first one is the amplifier shown in right hand side of **Figure 2-7 (A)**. The amplifier is composed of cavities in a number of computer numerical control (CNC) machined Perspex plates. The second component is a feedback loop which connects the two control terminals of the amplifier as shown in left hand side of **Figure 2-7 (B)**. The pressure difference between the terminals generates the flow in the loop which causes the main air flow from the inlet to switch

from one attachment wall to the opposite one under the Coanda effect (Zimmerman et al., 2008).

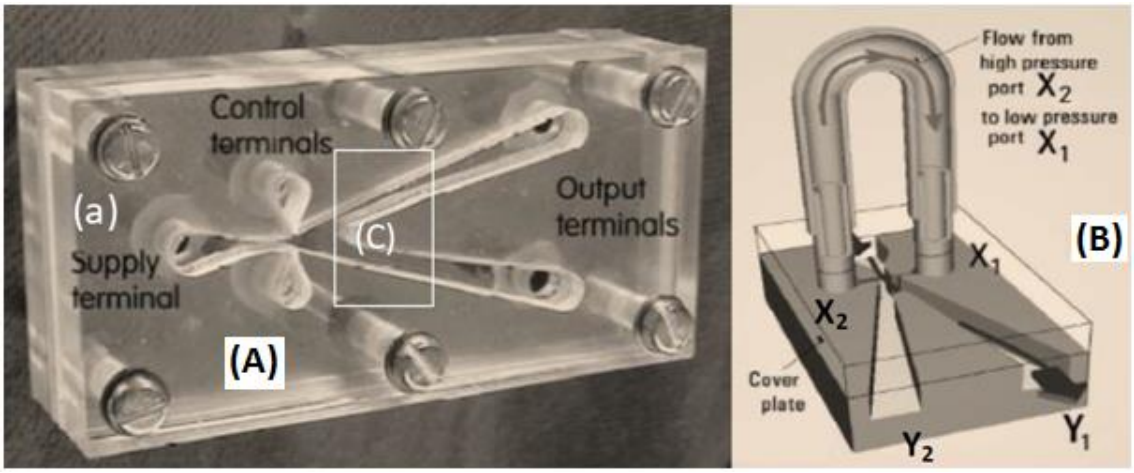

Figure 2-7 Fluidic oscillator and how fluid switches channel based on Coanda effect

2.6 Reactive separation

"Cheating chemical equilibrium" is something which chemical engineers have learned well in last few decades. Changing the equilibrium and pushing the reactions to completion is the art behind this science. Integrating the reaction stage and separation stage in one single process unit lead towards significant savings in the capital and running costs (Schembecker and Tlatlik, 2003). According to the Le Chatelier's principle, chemical equilibrium could be shifted by changing the concentration of the reactants or products, temperature and pressure of the system. Equilibrium is shifted in the direction so as to minimize the effect of change. Therefore if the products or one of the products are simultaneously removed from the system as they are being produced, equilibrium will shift in the forward direction and hence more reactants would combine together to restore the equilibrium increasing overall conversion of the system. For reactive separation, a defined window of operation is needed for chemical reaction, physical separation and the design of the apparatus. The economic advantages from reactive separation could only be exploited when the windows of these operations overlap with each other (Schembecker and Tlatlik, 2003). The economic benefits could be related to the reduction of the raw materials used, simplification of production cycles, energy integration and/or by getting higher rates of conversion and improvements in selectivity.

Reactive separation is one of the principles applied in the current project. For hydrogen production by water vapour plasmolysis, it is of great interest to see that if chemical engineering principles of reactive separation could be applied to it effectively. It is worth noting that plasma reactions, unlike chemical reactions, do not follow well-defined mechanisms. Ozone production from oxygen has more than hundred different pathways involving different species of oxygen producing ozone as a net product (Kossyi et al., 1992, Eliasson and Kogelschatz, 1991) and same has been found in case of hydrogen where more than hundred reactions have been identified to participate in kinetics of hydrogen formation (Rehman et al., 2012). As discussed in section 2.5.2 that product gases would come out in the form of microbubbles which would be dissolved in water. Oxygen having higher solubility would dissolve preferentially in water leaving hydrogen rich bubble to rise in water column. The volumetric mass transfer coefficient of product gases will then be deciding factor to see whether the reactive separation is possible or not. In order for the reactive separation to occur the volumetric mass coefficient of products or one of the product (oxygen and or hydrogen) will have to be greater than the time scale for hydrogen generation. If products of the water vapour plasmolysis are dissolved in water faster than they are produced in the plasma micro-reactor it can shift the equilibrium towards the forward direction. Time scale of the plasmolysis has been estimated by solving the kinetics model while the time scale of dilution of hydrogen/oxygen/ (products) could be obtained by measuring volumetric mass transfer coefficient. Comparing both values would indicate whether reactive separation is effective or not in yield enhancement.

2.4 Summary

This chapter is dedicated to review literature for the related subjects which is utilised in the current study. The fact that the major hydrogen production technologies like SMR and coal gasification depend upon fossil fuel and hence not green indicates the need of developing new processes which could generate hydrogen independent of fossil fuel. It has been identified that there still remains niche for a process for hydrogen production by water vapour plasmolysis. Lower principle cost of plasmolysis and recent developments in the field of plasma shows that hydrogen could be produced by water vapour plasmolysis economically. Kinetics of ozone formation has been studied for the optimisation of plasma micro-reactor. Review of separation technologies for hydrogen indicates that hydrogen could be separated from product using microbubbles. Reactive separation has been reviewed in order to assess its potential application the current study.

Chapter 3

Kinetic Modelling of Water Vapour Plasmolysis

3.1 Preface

The chapter comprises homogeneous chemical kinetics modelling of water vapour plasmolysis. A stream of pure water vapour was considered as feedstock. Different pathways of decomposition such as, dissociation reactions, dissociative attachment of electron, dissociative ionisation reactions, ionisation reactions and dissociative excitation reactions were included along with the other pathways for different species produced and consumed with in plasmolysis. The chapter is organised as follows: In section 2, a kinetic model has been developed, assuming the plasmolysis of water vapour in a plasma micro-reactor similar to that used in (Lozano-Parada and Zimmerman, 2010) having channel width of 800 μm and characteristic length of 1 cm of plasma zone. In section 3, the model results are analysed and discussed. Time scales for different species to reach steady state concentration has been evaluated. Effect of varying electron density over the concentration and evolution time for different species is monitored. Important pathways affecting the overall kinetics of water vapour plasmolysis have been identified. Based on the findings by kinetic modelling, a reaction mechanism of water vapour plasmolysis has been proposed. In section 4, summary of the chapter is given.

3.2 Rationale for kinetic modelling of water vapour plasmolysis

A chemical kinetics model was developed for water vapour dissociation flowing at atmospheric pressure under nonthermal plasma conditions . The kinetics modelling was studied to understand the chemistry of hydrogen formation by water vapour plasmolysis. The kinetics study is applied to the plasma micro-reactor design described in the next chapter. The reaction time scale obtained from kinetics modelling would serve three purposes. Firstly, the period of oscillation of an AC plasma source could be tuned such that the power is only supplied for the required reaction time scale. A detailed discussion on this is given in section 3.3. Secondly, if the diameter of the plasma micro-reactor is fixed, an estimation of the required length of the plasma micro-reactor could be made. Thirdly, the reaction time scale could be used to assess the applicability of reactive separation on water vapour plasmolysis in the latter part of the thesis. The effects of parameters like electron density on the concentration of hydrogen can be monitored as well. The kinetics modelling can therefore be considered as the first step towards hydrogen production by water vapour plasmolysis.

3.2 Kinetic model

Plasma-chemical processes have been applied to different feedstocks including water in liquid and vapour state (Givotov et al., 1981, Maehara et al., 2006, Nguyen et al., 2009, Burlica et al., 2010), methanol (Mutaf-Yardimci et al., 1998, Xi Zhen et al., 2003, Sarmiento et al., 2007, Rico et al., 2009), ethanol (Wang et al., 2010, Yan et al., 2008) and different hydrocarbons such as methane (Boutot et al., 2004, Sarmiento et al., 2007, Jasinski et al., 2008, Paulmier and Fulcheri, 2005) and kerosene oil (Babaritskii et al., 2004). Most of the plasma studies reported (Givotov et al., 1981, Maehara et al., 2006, Nguyen et al., 2009, Bockris et al., 1985, Avtaeva et al., 2010) have been carried out at very low pressure. Recently, some experimental studies have shown the conversion of hydrocarbons to hydrogen by plasma at atmospheric pressure (Sobacchi et al., 2002, Paulmier and Fulcheri, 2005). This study models the plasmolysis at atmospheric pressure, with the effect of atmospheric pressure incorporated through initial number density of water vapours.

Many efforts have been made to model water/ water vapour plasma for different purposes. From the study of a single type of plasma-chemical reaction such as electronic and ionic collision with the water vapour (Dolan, 1993), to overall kinetics models for water vapour have been investigated (Bockris et al., 1985, Fridman, 2008, Avtaeva et al., 2010). Dissociative excitation of water by an electron impact has been studied (Beenakker et al., 1974). The electron beam (0-1000 *eV*) was incident on a gas phase (water vapour and a gas- He and N_2). The authors concluded that the hydroxyl radicals excited in the $A^2\sum^+$ state are originated from excitation of both singlet and triplet states of the water molecule. A more complex mathematical model for the chemical reactions occurring in water in discharge channels have been proposed Mededovic et al., (2008) as well. The discharge channel was divided into two zones, namely, the core zone having diameter of 10 µm and recombination zone having diameter of 200 µm. The model explains the molecular hydrogen evolution in submerge discharges and describes the stoichiometric generation of H_2, O_2 and H_2O_2. More recently a zero dimensional model (well mixed homogeneous reactor) for low density non-stationary gas discharge in water vapours has been proposed by Avtaeva et al., (2010). The authors have studied the water vapour plasma at very low pressure (133-150 Pa) and found that the major positive and negative species were H_3O^+ and OH^- respectively.

Water vapour plasmolysis by vibrational excitation (as discussed in section 2.3.6 in **chapter 2**) and dissociative electron attachment depending upon energy distribution has been discussed by Fridman (2008). **Figure 3-1** explains the electron energy distribution through different pathways in water vapour plasma. It can be seen that eighty percent of the energy is absorbed in a vibrational excitation channel which is dominant at lower electron energy levels (< $1\,eV$). For typical electron temperatures 3-5 eV in nonthermal plasmas (Lozano-Parada and Zimmerman, 2010), most energy is absorbed in a dissociative attachment channel. The direct route of water vapour plasmolysis is as follows (Fridman, 2008);

$$H_2O \longrightarrow H_2 + \frac{1}{2} O_2 \qquad \Delta H = 2.6\,eV/molecule \qquad (3\text{-}1)$$

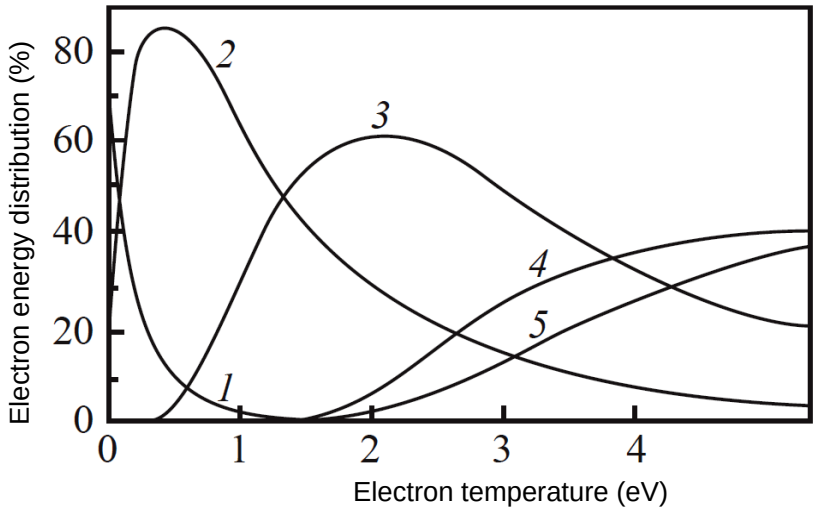

Figure 3-1 Electron energy distribution between excitation, dissociation and ionisation channels in water vapours for : (1) elastic scattering (2) vibrational excitation (3) dissociative attachment (4) electron excitation (5) (Fridman, 2008)

Hydrogen and hydroxyl radicals are the primary species produced when the water molecule is decomposed (Medodovic and Locke, 2009). The reaction representing the production of atomic hydrogen and hydroxyl radical (dissociation reaction) can be written as follows (Lukes et al., 2008a, Medodovic and Locke, 2009, Shirafuji et al., 2009).

$$H_2O + e^- \longrightarrow H + OH + e^- \qquad (3\text{-}2)$$

Several processes are initiated in the non-thermal plasma including a high electric field, intense ultraviolet radiation, overpressure shock waves and most important of all, formation of reactive species like hydroxyl-OH, hydrogen atom-H and oxygen atom-O. H and OH are associated with primary chemical activity in water discharges (Lukes et al., 2008a). After being produced in a plasma discharge, these species could then react with each other to form molecular products (Mededovic et al., 2008, Lukes et al., 2008a) and other species such as hydroperoxyl-HO_2 (Locke et al., 2006). Eighteen different pathways of water molecule dissociation by electrons impact have been reported by Avtaeva et al. (2010). The types of reaction included were momentum transfer, ionisation, dissociative ionisation, dissociative attachment, dissociation and dissociative excitation. However, Dolan (1993) has dropped the dissociative attachment reactions producing negative species (OH^-, H^- and O^-) due to their small cross sections (1-6x$10^{-18}$$cm^2$ $molecule^{-1}$) which peak at electron energies of 6-12 eV . It is further reported that the rate of negative ions production by these reactions is very

low and produces less than 1% products at 100 eV . Dolan (1993) has also pointed out a few dissociative attachment of electron pathways which may occur in water vapour plasma but have lower probability and relative higher energy requirement. However, considering the energy distribution in **Figure 3-1** (Fridman, 2008), the mechanism of water vapour plasmolysis by dissociative attachment of electron, producing OH and H^-, was also included in the model to analyse the effect of its co-existence with other dissociation reactions. Dissociative attachment of electron in water plasmolysis could play an important role because more than 60% of the discharge electron energy could be utilised in this mechanism at slightly higher electron temperature $T_e \geq 1.5$ *eV.* It is worth noting here that the electron temperatures of 1.5-4 eV have been reported in water plasmas for hydrogen generation (Nguyen et al., 2009). The dissociative attachment of electron mechanism of water vapour plasmolysis is initiated by reaction 3-3 (Bockris et al., 1985, Fridman, 2008);

$$H_2O + e^- \longrightarrow OH + H^- \qquad (3\text{-}3)$$

This dissociative attachment results in the loss of the electron which has a very high electron energy threshold ($\geq 30\,eV$). Unlike the dissociation pathway which produces OH and H, the initiation step produces OH and H^-. The H^- radical formed here combines with an electron through electron detachment process eliminating the negative charge on H^- and thus producing H and an extra electron. This process is only feasible if the above mentioned reaction (3-3) is followed by the given reaction (3-4).

$$H^- + e^- \longrightarrow H + e^- + e^- \qquad (3\text{-}4)$$

The electron produced by the electron detachment would then able to participate in the initiation reaction with another water molecule, thus starting a chain reaction and by doing so one electron is able to participate in the reaction many times making process energy effective. The rate constant for detachment process is very fast ~10^{-6} $cm^3\,s^{-1}$. This chain mechanism (3-3 and 3-4) is initiated by ionisation of water molecules while it could be terminated by an ion-ion recombination reaction (3-5),

$$H^- + H_2O^+ \longrightarrow H_2 + OH \qquad (3\text{-}5)$$

or by fast ion-molecular reaction (3-6).

$$H^- + H_2O \longrightarrow H_2 + OH^- \quad (3\text{-}6)$$

The energy efficiency of water plasmolysis through dissociative attachment of electron mechanism depends upon the length of the chain "μ" that is how many times an electron can take part in dissociative attachment reaction.

Electron collisions with water molecules (H_2O) are known to excite rotational, vibrational and electronic levels of water molecules to H_2O^* (Itikawa and Mason, 2005). However, the effect of H_2O^* on the rate of reactions including H_2O is not yet studied (Avtaeva et al., 2010) and to the best of our knowledge this piece of information could not be found. Although, kinetic data for the formation and decomposition of excited molecules of H_2^* is available (Hagelaar et al., 2000), there exists no information on the formation of excited H_2^* molecules by electron impact with water molecules (Itikawa and Mason, 2005). Oxygen emission lines in water spectra have been reported in different studies (Sato, 2008, Lukes et al., 2008a, Shih and Locke, 2010b). Production of O($3p\ ^3P$) and O($3p\ ^5P$) has been reported by the electron impact reaction with a water molecule (Lukes et al., 2008a).

$$e^- + H_2O \longrightarrow O(3p\ ^3P) + H_2 + e^- \quad (3\text{-}7)$$

$$e^- + H_2O \longrightarrow O(3p\ ^5P) + H_2 + e^- \quad (3\text{-}8)$$

The transition $(O\,3p\ ^3P - 3s\ ^3S^0)$ produces an emission line at 844 nm while emission line at 777 nm is produced by the transition $(O\,3p\ ^5P - 3s\ ^5S^0)$. However, both routes mentioned above require higher electron energy (~17 eV) than the dissociation pathway of water into H and OH (Reaction 1 in **Table 3-1**) (Lukes et al., 2008a). That is why both of these reactions are not considered in the model. At this point it is worth mentioning that a delicate balance between the production and consumption of each species must be sought such that the overall products of the plasmolysis remain in agreement to the experimental results /published literature.

Waste heat could be utilised to produce steam for hydrogen production from nonthermal plasmas. Typically a waste heat boiler could be utilised to produce low quality steam such as considered in the current study. Demineralised water is used for

the steam production which shall have very little impurities. Also, when water is vaporised any impurity (salts) would remain behind in waste heat boiler so no impurity would enter in the plasma reactors. This is the rationale for neglecting impurities in the model.

3.2.1 Initial conditions

Water vapours and electrons are the only precursors as only these two species enter the system as starting reactants. The number density of every other species is set to zero. The number density of water vapour was calculated using the ideal gas law at slightly above its boiling point and atmospheric pressure. At the given values of temperature and pressure, number density for water vapours was found to be at 1.925 x 10^{25} m^{-3}. Results using number density of water vapours calculated by the Van der Waals equation are shown in Appendix I. The initial number density of seed electrons is very low, approximately 1 x 10^{6} m^{-3} (due to cosmic radiation). However value of equilibrium electron density varies in different studies. The value of electron density as high as in the order of 10^{20} m^{-3} has been reported by Zhang et a.l 2007. Lower values of order of 10^{17} m^{-3} has also been reported in experimental investigation by Abdul Majeed et al. (2011). However, equilibrium electron densities found in nonthermal plasmas like DBD (10^{18}-10^{21} m^{-3}) (Nehra et al., 2008) were used to set the initial electron concentrations as advised by Professor Siméon Cavadias of Laboratoire de Génie des Procédés Plasmas et Traitement des Surfaces / ENSCP/ UPMC (Private communication, 2012) to help the convergence of the numerical solution. A general range of electron density was chosen to study the kinetic behaviour of water vapour plasmolysis over that range.

3.2.1.1 Electron temperature

As discussed earlier, EEDF is the probability for an electron to have sufficient kinetic energy known as mean electron energy "ε" (eV) to carry out the reactions. So under a high applied electric field, an electron would have higher mean electron energy to carry out a particular reaction. Since the current simulation was run under constant values of electron density which is a function of applied electric field, electron energy could be assumed to have a constant value (have reached equilibrium value). Before

deciding a value for the electron temperature in the plasmas, it is very important to understand the discharge physics which governs this value. As discussed in **chapter 2** the breakdown voltage depends on the pressure "p" of the gas and inter-electrode distance "d" of the plasma micro-reactor. If pd number is small (usually in low pressure plasmas) the breakdown follows classical Townsend mechanism. However if f pd number is large (usually in high/atmospheric pressure plasma-under current set of conditions), instead of following the Townsend breakdown mechanism, streamer breakdown initiates (Lozanskii, 1976, Kunhardt and Byszewski, 1980, Eliasson and Kogelschatz, 1991). The streamer, in this case becomes self-propagating because of the presence of high concentration of space charge at the head of electron avalanche and the resulting high eignfield causes the breakdown to occur in a single transit. A moderately homogenous conducting channel having low electric field filled with charged and excited particles are left behind this high energy streamer. The effective reduced field in this mechanism is significantly higher than the reduced electric field in classical Townsend breakdown. In this case, energy loss by elastic collisions of electrons with neutrals is not significant because of considerably high energies (~5 *eV*) and limited lifetime of electrons (Eliasson and Kogelschatz, 1991). Since water vapour plasmolysis has been studied at atmospheric pressure in the current modelling work, the breakdown of water vapours is thought to occur by streamer initiation.

It is worth noting that electron temperature in DBDs (at high pressure) have been reported in the range of 1-10 *eV* (Eliasson and kogelschatz, 1991, Schutze et al., 1998). Previous modelling studies (Lozano-Parada and Zimmerman, 2010), of nonthermal plasmas at atmospheric pressure has also reported electron temperature in the range of 3-5 *eV*. Experimental investigations have also found the electron temperature to vary between 1.5-4 *eV* in water vapour plasma (radio frequency plasma) for hydrogen generation (Nguyen et al., 2009). In the light of above discussion and, since, the current study focuses on utilising low power plasma, the lower limit of electron temperature of 3 *eV* has been chosen for simulation work.

3.2.1 Implementation of kinetic model

The kinetic model has been implemented using COMSOL Multiphysics™- Reaction Engineering Laboratory (REL). This package provides an automatic sensing of stiff systems and an adaptive time stepping algorithm with relative tolerance set to 10^{-6} (Lozano-Parada and Zimmerman, 2010). It is presumed that the water vapour concentration is fixed in a hypothetical reactor at the ideal gas molar level and the electron density is set by the electric field. If the reactor is supposed to be well-mixed (dominated kinetically), then every reaction in the kinetic scheme (**Table 3-1)** contributes mass action law terms to the kinetics model with rate constants (including Arrhenius temperature dependence), with number densities corresponding to the species incorporated in this study and given in **Table 3-2**. The rate equations for the reactions given in **Table 3-1** can be solved to make a model of intrinsic chemical kinetics for the concentration of the species (Lozano-Parada and Zimmerman, 2010) given in **Table 3-2**. To get steady state concentration of molecular hydrogen (C_{H_2}) the overall equation could be written as follows (3-21);

$$\left[\frac{dC_{H_2}}{dt}\right] = k_6 n_e n_7 + k_{23} n_1 n_{14} + k_{30} n_1 n_{15} + k_{35} n_1 n_{13} - k_{37} n_{14} n_2 - k_{40} n_2 n_{15} - k_{41} n_2 n_{20} +$$
$$k_{44} n_1^{\,2} m + k_{45} n_7 n_1 - k_{54} n_2 m - k_{63} n_8 n_2 + k_{66} n_{38} n_1 + k_{70} n_4 n_7 + k_{88} n_{31} n_4 + k_{92} n_{31} n_8 +$$
$$k_{94} n_{25} n_4 + k_{99} n_{16} n_4 + k_{102} n_{31} n_9 - k_{113} n_2 n_4 - k_{114} n_2 n_{26} - k_{115} n_3 n_2^2 + k_{126} n_e n_9 + k_{128} n_e n_8 +$$
$$k_{136} n_e n_5 - k_{148} n_2 n_{29} - k_{149} n_2 n_{25} + k_{150} n_{31} n_1 - k_{153} n_{25} n_2 + k_{164} n_{35} n_7$$

Where n_i is the symbol used for the species given in **Table 3-2** and subscript "i" represents different indices given to the different species. "k_i" is the rate constant for the reactions given in **Table 3-1** with subscript "i" represents different indices given to the reactions. The kinetic model does not account for the losses at the electrode surfaces. The electrons accelerated by the electric field collide with water vapours as shown in the reaction initiation step (Reactions 1-13 in **Table 3-1)**.

Table 3-1 Kinetic scheme of plasma-chemical reactions considered in the current model

Sr. No.	Reactions	Rate constant (*K*) ($m^3.mole^{-1}.sec^{-1}$, $m^6.mol^{-1}.sec^{-1}$)	Ref.
Dissociation Reactions			
K_1	$e^- + H_2O \longrightarrow H + OH + e^-$	9.978E+07	S[a], A[b]
Momentum Transfer Reaction			
K_2	$e^- + H_2O \longrightarrow e^- + H_2O$	3.65776E+11	A[b]
Ionisation Reaction			
K_3	$e^- + H_2O \longrightarrow 2e^- + H_2O^+$	2.990E+05	A[b]
Dissociative Ionisation Reactions			
K_4	$e^- + H_2O \longrightarrow 2e^- + OH + H^+$	6.992E+01	A[b]
K_5	$e^- + H_2O \longrightarrow 2e^- + H + OH^+$	3.268E+02	A[b]
K_6	$e^- + H_2O \longrightarrow 2e^- + H_2 + O^+$	3.094E+00	A[b]
K_7	$e^- + H_2O \longrightarrow 2e^- + H_2^+ + O$	2.37E-09	A[b]
Dissocitive Attachment Reactions			
K_8	$e^- + H_2O \longrightarrow H^- + OH$	3.706E+07	F, A[b]
Dissocitive Excitation			
K_9	$e^- + H_2O \longrightarrow H + O^*(2^1S_0) + e^-$	3.938E+04	A[b]
K_{10}	$e^- + H_2O \longrightarrow H + OH^*(A) + e^-$	4.132E+06	A[b]
K_{11}	$e^- + H_2O \longrightarrow OH + H\ (n=2) + e^-$	3.021E+02	A[b]
K_{12}	$e^- + H_2O \longrightarrow OH + H\ (n=3) + e^-$	4.604E01	A[b]
K_{13}	$e^- + H_2O \longrightarrow OH + H\ (n=4) + e^-$	7.184E+00	A[b]
Neutral-Neutral Reactions			
K_{14}	$OH + OH \longrightarrow H_2O_2$	1.02E+07	S[a]
K_{15}	$OH + O_3 \longrightarrow HO_2 + O_2$	4.46E+04	S[a]
K_{16}	$OH + HO_2 \longrightarrow H_2O + O_2$	6.63E+07	S[a]
K_{17}	$OH + H_2O_2 \longrightarrow HO_2 + H_2O$	1.02E+06	S[a]

K_{18}	$O + O_2 \longrightarrow O_3$	8.43E+03	S[a]
K_{19}	$O + HO_2 \longrightarrow OH + O_2$	3.37E+07	S[a]
K_{20}	$H + O_3 \longrightarrow OH + O_2$	1.69E+07	S[a]
K_{21}	$H + HO_2 \longrightarrow H_2O + O$	1.69E+06	S[a]
K_{22}	$H + HO_2 \longrightarrow OH + OH$	3.91E+07	S[a]
K_{23}	$H + HO_2 \longrightarrow O_2 + H_2$	3.91E+07	S[a]
K_{24}	$HO_2 + HO_2 \longrightarrow H_2O_2 + O_2$	9.64E+05	S[a]
K_{25}	$OH + OH \longrightarrow H_2O + O$	8.91E+05	M[a]
K_{26}	$OH + M \longrightarrow H + O + M$	$f \times (4.09\times10^{-9} \exp^{(-416kJ/RT)})$	M[b]
K_{27}	$O + O + M \longrightarrow O_2 + M$	$f \times (9.26\times10^{-34}(T/298)^{-1})$	M[b]
K_{28}	$OH + O \longrightarrow O_2 + H$	$f \times (4.55\times10^{-12}(T/298)^{0.40}\exp^{(49.64kJ/RT)})$	M[b]
K_{29}	$O+OH \longrightarrow HO_2$	$f \times (2.69\times10^{-10}\exp^{(-0.26kJ/RT)})$	M[b]
K_{30}	$H + OH \longrightarrow O + H_2$	$f \times (6.86\times10^{-14}(T/298)^{2.80}\exp^{(16.21kJ/RT)})$	M[b]
K_{31}	$O_2 + OH \longrightarrow HO_2 + O$	$f \times (3.7\times10^{-11}\exp^{(-220)})$	M[b]
K_{32}	$OH + OH \longrightarrow 2O + 2H$	$f \times (`4.09\times10^{-9}\exp^{(-416kJ/RT)})$	M[b]
K_{33}	$H_2O_2 + O \longrightarrow HO_2 + OH$	$f \times (1.42\times10^{-12}(T/298)^{2}\exp^{(-16.31kJ/RT)})$	M[b]
K_{34}	$H_2O_2 + H \longrightarrow OH + H_2O$	$f \times (4.01\times10^{-11}\exp^{(-16.63kJ/RT)})$	M[b]
K_{35}	$H_2O_2 + H \longrightarrow HO_2 + H_2$	$f \times (8\times10^{-11}\exp^{(-33.26kJ/RT)})$	M[b]
K_{36}	$H_2O_2 + O_2 \longrightarrow 2HO_2$	$f \times (9\times10^{-11}\exp^{(-166kJ/RT)})$	M[b]
K_{37}	$HO_2 + H_2 \longrightarrow H_2O_2 + H$	$f \times (5\times10^{-11}\exp^{(-109kJ/RT)})$	M[b]
K_{38}	$HO_2 + M \longrightarrow H + O_2 + M$	$f \times (2.41\times10^{-8}(T/298)^{-1.1}8\exp^{(-2031)})$	M[b]
K_{39}	$O_2 + H + M \longrightarrow HO_2 + M$	$f \times (1.94\times10^{-32}(T/298)^{-1})$	M[b]
K_{40}	$OH + H_2 \longrightarrow H_2O + H$	$f \times (2.97\times10^{-12}(T/298)^{1.21}\exp^{(-19.71kJ/RT)})$	M[b]
K_{41}	$O + H_2 \longrightarrow OH + H$	$f \times (3.44\times10^{-13}(T/298)^{2.67}\exp^{(-26.27kJ/RT)})$	M[b]
K_{42}	$O + H_2O \longrightarrow OH + OH$	$f \times (668\times10^{-13}(T/298)^{2.60}\exp^{(-63.52kJ/RT)})$	M[b]
K_{43}	$OH + OH + M \longrightarrow H_2O_2 + M$	3.13E+06	H
K_{44}	$H + H + M \longrightarrow H_2 + M$	$g \times (6.04\text{x}10\text{-}33\ (T/298)^{-1})/6.04\text{e-}33$	M[b], D

K_{45}	$H_2O + H \longrightarrow H_2 + OH$	f x (1.58×10^{-11} $(T/298)^{1.20}$ $\exp^{(79.90}$ [KJ/mole]/RT))	N
K_{46}	$O + H_2O \longrightarrow HO_2 + H$	3.98068E-37	N
K_{47}	$HO_2 + H_2O \longrightarrow OH + H_2O_2$	1.00091E-13	N
K_{48}	$H+OH+ H_2O \longrightarrow H_2O + H_2O$	3E-33	N
K_{49}	$H_2O + O_2 \longrightarrow HO_2 + OH$	2.51647E-40	N
K_{50}	$H_2O + O_3 \longrightarrow H_2O_2 + O_2$	7.1673E-05	N
K_{51}	$HO_2 + O_3 \longrightarrow OH + 2O_2$	$1.4x10^{-20}exp^{(-600x8.6xE-05/T)}$	A[b]
K_{52}	$H + O_2 + H_2O \longrightarrow HO_2 + H_2O$	2.321E+05	A[b]
K_{53}	$H + O_2 \longrightarrow HO_2$	1.084E+06	A[b]
K_{54}	$H_2 + M \longrightarrow H + H + M$	8.15E-50	M[c]
K_{55}	$H + O + M \longrightarrow OH + M$	1.232E-02	M[c]
K_{56}	$H + OH + M \longrightarrow H_2O + M$	25.544E+05	M[c]
K_{57}	$H+O_2 + M \longrightarrow HO_2 + M$	7.379E+03	M[c]
K_{58}	$H_2O_2 + M \longrightarrow OH + M$	1.295E-15	M[c]
K_{59}	$O_3 + M \longrightarrow O_2 + O + M$	4.450E-05	M[c]
K_{60}	$O_3 + O \longrightarrow O_2 + O_2$	2.219E+07	M[c]
K_{61}	$H + O_3 \longrightarrow OH + O_2$	1.600E+07	M[c]
Charge Transfer Reactions			
K_{62}	$H_2O^+ + H_2O \longrightarrow H_3O^+ + OH$	f x 0.5E-09	F,A[b],A[a]
K_{63}	$H_2O^+ + H_2 \longrightarrow H_3O^+ + H$	8.431E+08	A[b]
K_{64}	$H_2O^+ + O_2 \longrightarrow O^+_2 + H_2O$	9.033E+07	A[b]
K_{65}	$OH^+ + H_2O \longrightarrow H_2O^+ + OH$	1.807E+09	A[b]
K_{66}	$OH^+ + H \longrightarrow O^+ + H_2$	f x ($4.9x10^{-16}exp^{(-0.36/T)}$)	A[b] ,S[b]
K_{67}	$OH^+ + O \longrightarrow O^+ + OH$	f x ($1.6x10^{-16}exp^{(-0.44/T)}$)	A[b]
K_{68}	$H^+ + H_2O \longrightarrow H_2O^+ + H$	1.807E+09	A[b]
K_{69}	$H^+_2 + O_2 \longrightarrow HO_2^+ + H$	1.144E+09	A[b]

K_{70}	$H^+_2 + H_2O \longrightarrow H_2O^+ + H_2$	2.168E+09	A^b
K_{71}	$H^+_2 + H_2O \longrightarrow H_3O^+ + H$	2.047E+09	A^b
K_{72}	$O^+ + H_2O \longrightarrow H_2O^+ + O$	1.403E+09	A^b
K_{73}	$OH^+ + O_2 \longrightarrow O_2^+ + OH$	1.204E+08	A^b
K_{74}	$O_2^+ + H_2O \longrightarrow H_2O_3^+$	1.325E+09	A^b
K_{75}	$H_2O_3^+ + H_2O \longrightarrow H_3O^+ + OH + O_2$	1.807E+08	A^b
K_{76}	$H_2O_3^+ + H_2O \longrightarrow H_4O_2^+ + O_2$	1.144E+09	A^b
K_{77}	$H_4O_2^+ + H_2O \longrightarrow H_5O_2^+ + OH$	6.022E+08	A^b
K_{78}	$e^- + O_2 \longrightarrow e^- + O_2$	f x (4.7E-8)$T_e^{0.5}$	L
K_{79}	$OH^- + O_3 \longrightarrow OH + O^-_3$	6.02E+08	K
K_{80}	$O^- + O_3 \longrightarrow O_3^- + O$	3.19E+02	L
Ion Electron Detachment Reaction			
K_{81}	$H^- + e^- \longrightarrow H + e^- + e^-$	f x 1E-06	N
K_{82}	$O^- + e^- \longrightarrow O + e^- + e^-$	1.74E+04	L
Mutual Nueteralisation Reactions			
K_{83}	$H^- + H^+ \longrightarrow H + H$	f x 3.9E-07	F,A^b
K_{84}	$O^- + O^+ \longrightarrow O + O$	1.807E+11	F, A^b
K_{85}	$O^- + O_2^+ \longrightarrow O + O_2$	6.022E+10	F, A^b
K_{86}	$O_2^- + O_2^+ \longrightarrow O_2 + O_2$	f x 4.2E-07	F, A^b
K_{87}	$O_2^- + O^+ \longrightarrow O_2 + O$	f x 2E-07	F, A^b
K_{88}	$H^- + H_2^+ \longrightarrow H + H_2$	4.035E+10	F, A^b
K_{89}	$H^- + O^+ \longrightarrow H + O$	1.861E+11	F, A^b
K_{90}	$H^- + OH^+ \longrightarrow H + OH$	1.861E+11	A^b
K_{91}	$H^- + H_2O^+ \longrightarrow H + H_2O$	1.855E+11	A^b
K_{92}	$H^- + H_2O^+ \longrightarrow H_2 + OH$	f x 1E-07	F
K_{93}	$O^- + H^+ \longrightarrow O + H$	1.861E+11	A^b
K_{94}	$O^- + H_2^+ \longrightarrow O + H_2$	1.355E+11	A^b

K_{95}	$O^- + OH^+ \longrightarrow O + OH$	6.323E+10	A[b]
K_{96}	$O^- + H_2O^+ \longrightarrow O + H_2O$	6.203E+10	A[b]
K_{97}	$OH^- + OH^+ \longrightarrow OH + OH^*(A)$	6.564E+10	A[b]
K_{98}	$OH^- + H^+ \longrightarrow OH + H$	1.861E+11	A[b]
K_{99}	$OH^- + H_2^+ \longrightarrow OH + H_2$	1.355E+11	A[b]
K_{100}	$OH^- + O^+ \longrightarrow OH + O$	6.323E+10	A[b]
K_{101}	$OH^- + H_2O^+ \longrightarrow OH + H_2O$	6.142E+10	A[b]
K_{102}	$H^- + H_3O^+ \longrightarrow H_2 + H_2O$	1.855E+11	A[b]
K_{103}	$O^- + H_3O^+ \longrightarrow H + O + H_2O$	6.142E+10	A[b]
K_{104}	$OH^- + H_3O^+ \longrightarrow 2H_2O$	6.082E+10	A[b]
K_{105}	$H^- + O_2^+ \longrightarrow H + O_2$	1.831E+11	A[b]
K_{106}	$OH^- + O_2^+ \longrightarrow OH + O_2$	5.420E+10	A[b]
K_{107}	$H^- + H_2O_3^+ \longrightarrow HO_2 + H_2O$	1.825E+11	A[b]
K_{108}	$O^- + H_2O_3^+ \longrightarrow O_3 + H_2O$	5.179E+10	A[b]
K_{109}	$OH^- + H_2O_3^+ \longrightarrow O_2 + OH + H_2O$	5.058E+10	A[b]
Ion-Molecule Reactions			
K_{110}	$H_3O^+ + 2H_2O \longrightarrow H_3O^+.H_2O + H_2O$	6.53E+08	A[a]
K_{111}	$H_3O^+.H_2O + 2H_2O \longrightarrow H_3O^+.(H_2O)_2 + H_2O$	8.34E+08	A[a]
K_{112}	$H_3O^+.(H_2O)_2 + 2H_2O \longrightarrow H_3O^+.(H_2O)_3 + H_2O$	8.71E+08	A[a]
K_{113}	$H_2^+ + H_2 \longrightarrow H_3^+ + H$	1.264E+09	S[b]
K_{114}	$H_2 + O^-_2 \longrightarrow OH^- + OH$	2.41E+07	K
K_{115}	$H^+ + 2H_2 \longrightarrow H_3^+ + H_2$	1.12E+07	H[b]
Dissociative Electron-Ion Recombinaiont Reactions			
K_{116}	$e^- + H_2O^+ \longrightarrow H + OH$	$f \times (0.66\times10^{-13}(0.01/T_e))$	A[a], A[b]
K_{117}	$e^- + H_3O^+ \longrightarrow H + H_2O$	$3.15\times10^{-7}(300/T_e)^{0.5}$/ 2.05E+12	A[a]
K_{118}	$e^- + H_3O^+.H_2O \longrightarrow H + H_2O + H_2O$	$2.5\times10^{-6}(300/T_e)^{0.5}$/ 1.63E+13	A[a]

K_{119}	$e^- + H_3O^+.(H_2O)_2 \longrightarrow H + 3H_2O$	$4.5x10^{-6}(300/T_e)^{0.5}$/ 2.93E+13	A^a
K_{120}	$e^- + H_3O^+.(H_2O)_3 \longrightarrow H + 4H_2O$	$6.5x10^{-6}(300/T_e)^{0.5}$/ 4.23E+13	A^a
K_{121}	$e^- + H_3O^+ + H_2O \longrightarrow H + H_2O + H_2O$	9.79E+12	A^a
K_{122}	$e^- + H_3O^+.(H_2O) + H_2O \longrightarrow H + 3H_2O$	9.79E+12	A^a
K_{123}	$e^- + H_3O^+.(H_2O)_2 + H_2O \longrightarrow H + 4H_2O$	9.79E+12	A^a
K_{124}	$e^- + H_3O^+.(H_2O)_3 + H_2O \longrightarrow H + H_2O$	9.79E+12	A^a
K_{125}	$e^- + e^- + H_2O^+ \longrightarrow e^- + H_2O$	7.26E+25	A^a,F
K_{126}	$e^- + H_3O^+ \longrightarrow H_2 + OH$	f x 2E-07	F
K_{127}	$e^- + H_2O^+ \longrightarrow 2H + O$	fx2E-07	F
K_{128}	$e^- + H_2O^+ \longrightarrow H_2 + O$	$f \times (0.3x10^{-13}(0.01/T_e))$	A^b
K_{129}	$e^- + OH^+ \longrightarrow O^*(2^1S_0) + H$	$f \times (0.6x10^{-14}/T_e^{0.5})$	A^b
K_{130}	$e^- + O_2^+ \longrightarrow 2O$	$f \times (2x10^{-14}(0.026/T_e)^{0.5})$	A^b
K_{131}	$e^- + H_2O_3^+ \longrightarrow 2O + H_2O$	$f \times (3x10^{-13}(0.026/T_e)^{0.5})$	A^b
K_{132}	$e^- + H_4O_2^+ \longrightarrow H + H_2O + OH$	1.204E+12	A^b
K_{133}	$e^- + H_5O_2^+ \longrightarrow H + 2H_2O$	$f \times (2.4x10^{-12}(0.026/T_e)^{0.08})$	A^b
K_{134}	$e^- + O^+ \longrightarrow O$	$f \times (2.7x10^{-19}(T_e)^{-0.7})$	A^b
K_{135}	$2e^- + H_3O^+ \longrightarrow H + H_2O + e^-$	$f \times (7\ x10^{-39}(T_e)^{-4.5})$	A^a, A^b
K_{136}	$e^- + H_3^+ \longrightarrow H_2 + H$	$f \times (9.75x10^8\ T_e^{0.5})$	S^b
K_{137}	$e^- + H_2^+ \longrightarrow H + H$	$f \times (5.66x10^8 Te^{0.5})$	S^b
K_{138}	$e^- + H^+ \longrightarrow H$	$f \times (2.62x10^{13} T_e^{0.5})$	S^b
K_{139}	$e^- + O_2 \longrightarrow O^- + O$	$f \times (1.07E\text{-}9 * Te^{-1.391} * \exp(-6.26/T_e))$	L
K_{140}	$e^- + O_2 + O \longrightarrow O_2^- + O$	3.62E+04	L
K_{141}	$e^- + O_3 \longrightarrow O^- + O_2$	2.93E+08	L
K_{142}	$e^- + HO_2^+ \longrightarrow O_2(\Delta) + H$	$f \times (1E\text{-}14/T_e^{0.5})$	A^b
K_{143}	$e^- + O_2 \longrightarrow O + O(^1D) + e^-$	3.55E+00	L
K_{144}	$e^- + O_2^+ \longrightarrow O + O(^1D)$	9.89E04	L
K_{145}	$e^- + O_2^+ \longrightarrow 2O$	7.65E03	L

K_{146}	$e^- + O_2^+ + O_2 \longrightarrow 2O$	3.62E-03	L
Associative Detachment Reactions			
K_{147}	$OH^- + HO_2 \longrightarrow H_2O + O_2 + e^-$	6.023E+08	K
K_{148}	$H_2 + O_3^- \longrightarrow H_2O + O_2 + e^-$	6.023E+08	K
K_{149}	$H_2 + O^- \longrightarrow H_2O + e^-$	3.61380E+08	K
K_{150}	$H^- + H \longrightarrow H_2 + e^-$	9.033E+07	F, A[b]
K_{151}	$H^- + O_2 \longrightarrow HO_2 + e^-$	7.26E+08	F, A[b]
K_{152}	$O^- + O \longrightarrow O_2 + e^-$	9.03E+07	F, A[b]
K_{153}	$O^- + H_2 \longrightarrow H_2O + e^-$	3.613E+08	F, A[b]
K_{154}	$O^- + O_2 \longrightarrow O_3 + e^-$	4.145E+04	F, A[b]
K_{155}	$O_2^- + O \longrightarrow O_3 + e^-$	f x 3E-10	F
K_{156}	$OH^- + O \longrightarrow HO_2 + e^-$	9.03E+08	K,F, A[b]
K_{157}	$OH^- + H \longrightarrow H_2O + e^-$	6.022E+08	K,F, A[b]
K_{158}	$O_2^- + O_2 \longrightarrow O_2 + O_2 + e^-$	f x 2.2E-18	F
K_{159}	$O^- + O_2^+ \longrightarrow 3O$	1.27E+10	L
Excited Species Reactions			
K_{160}	$O(^1D) + O_3 \longrightarrow O_2 + O_2$	1.99E+08	S[a]
K_{161}	$O(^1D) + H_2O \longrightarrow OH + OH$	1.14E+08	S[a]
K_{162}	$O(^1D) + H_2 \longrightarrow H_2 + O$	1.927E+18	H[a]
K_{163}	$O(^1D) + H_2O \longrightarrow H_2O + O$	1.204E+16	H[a]
K_{164}	$O(^1D) + H_2O \longrightarrow H_2 + O_2$	6.023E+15	H[a]
K_{165}	$O^- + O^*(2^1S_0) \longrightarrow O_2 + e^-$	9.033E+07	A[b]
K_{166}	$OH^- + O^*(2^1S_0) \longrightarrow HO_2 + e^-$	9.033E+08	A[b]
K_{167}	$O^*(2^1S^0) + H_2O \longrightarrow O + H_2O$	2.168E+08	A[b]
K_{168}	$O^*(2^1S^0) + H_2O \longrightarrow OH + OH$	1.506E+08	A[b]
K_{169}	$O^*(2^1S^0) \longrightarrow O + h\upsilon$	4.215E+25	A[b]
K_{170}	$O_2(\Delta) + O_2 \longrightarrow O_2 + O_2$	f x (4.1E-23 $*T^{0.8}$)	H[a]

K_{171}	$O_2(\Delta) \longrightarrow O_2$	1.81E+04	A^b
K_{172}	$OH^*(A) \longrightarrow OH$	800ns	A^b
K_{173}	$H^- + H^+ \longrightarrow H + H^*(n=2)$	4.21E+03	A^b
K_{174}	$H^- + H^+ \longrightarrow H + H^*(n=3)$	7.83E+03	A^b
K_{175}	$H^*(n=2) \longrightarrow H + h\nu$	$1.6\,ns$	A^b
K_{176}	$H^*(n=3) \longrightarrow H^*(n=2) + h\nu$	$10.2\,ns$	A^b
K_{177}	$H^*(n=4) \longrightarrow H^*(n=2) + h\nu$	$33.7\,ns$	A^b

f= 6.02x10^{17}, **g**= 3.62404x10^{35}, **T**= Gas temperature, **T_e**= Electron temperature,
S^a for (Shirafuji et al., 2009), S^b for (Salabas et al., 2004), M^a for (Mededovic et al., 2008), M^b for (Medodovic and Locke, 2009), M^c for (Mukasa et al., 2011), A^a for (Aleksandrov et al., 2007), A^b for (Avtaeva et al., 2010), H^a for (Herron, 2001), H^b for (Hagelaar et al., 2000), K for (Kosarev and Starikovskii, 2000), N for (NIST, 2011), F for (Fridman, 2008), D for (Dixon et al., 1962) and L for (Lieberman and Litchenberg, 2005).

Table 3-2 Neutral, excited, positive and negative species and their respective symbols considered in the model

Positive ions	Symbol	Neutral Species	Symbol	Excited Species	Symbol	Negative species	Symbol
H_2O^+	n_8	H_2O	n_7	$O^*(2^1S_0)$	n_{39}	OH^-	n_{16}
OH^+	n_{38}	OH	n_{15}	O(1D)	n_{35}	O^-	n_{25}
H_3^+	n_5	H_2	n_2	$OH^*(A)$	n_{17}	H^-	n_{31}
H_2^+	n_4	H	n_1	$H^*(n=2)$	n_{54}	O_2^-	n_{26}
H^+	n_3	HO_2	n_{14}	$H^*(n=3)$	n_{55}	O_3^-	n_{29}
O^+	n_{32}	H_2O_2	n_{13}	$H^*(n=4)$	n_{44}	e^- (Electron)	n_e
O^+_2	n_{33}	O	n_{20}	$O_2(\Delta)$	n_{50}		
HO_2^+	n_{45}	O_2	n_{19}				
H_3O^+	n_9	O_3	n_{27}				
$H_2O_3^+$	n_{46}	m	M				
$H_4O_2^+$	n_{47}						
$H_5O_2^+$	n_{48}						
$H_3O^+.H_2O$	n_{10}						
$H_3O^+.(H_2O)_2$	n_{11}						
$H_3O^+.(H_2O)_3$	n_{12}						

3.3 Analysis and discussion

Figure 3-2 and **Figure 3-3** show the time scale to reach 99% of H_2 and O_2 concentration is less than 0.01 s. It is worth noticing again that the number density of water vapours

has been set to account for the effect of atmospheric pressure. At atmospheric pressure ambipolar diffusion dominates the diffusion mechanism. Under these conditions the value of ambipolar diffusivity is around 10^{-5} m^2s^{-1} and is assumed to be same for ions and heavy gas particles (Lozano-Parada and Zimmerman, 2010). The time scale for such plasma to diffuse a length of 1 mm will be $\sim \tau_{ambipolar} =$ 100 ms which is an order of magnitude 10^{-1}s slower than the reaction time $\tau_{reaction}$ (model results). Therefore the reaction would be completed long before the ions could reach the wall of the reactor (Lozano-Parada and Zimmerman, 2010). So, in a continuous process, the time in which electric field is switched on, where $\tau_{reaction} < \tau_{ambipolar}$, the residence time in the micro-reactor could be set such that $\tau_{reaction} = \tau_{residence}$ by choosing a suitable combination of superficial velocity and characteristic length of reactor (Butterworth, 2010). This implies an AC plasma source such that its period of oscillation is approximately equal to reaction time- $T_{ac} \sim \tau_{reaction}$. As mentioned earlier, ozone has been successfully produced at 170 V AC with a frequency of 100 Hz (Lozano-Parada and Zimmerman, 2010). The kinetic model results of $\tau_{reaction} < \tau_{ambipolar}$ also validates the assumption of not considering the extinction processes on the wall as the reaction would have completed long before ion or gas particles could likely reach the electrode surface. Considering this discussion and the reaction time scale for water vapour plasmolysis, it could be stated that hydrogen can reliably be produced by water vapour plasmolysis at much lower voltage and frequency thereby improving the efficiency (Bockris et al., 1985) and reducing the cost associated with plasmolysis.

A typical optical emission spectra showing different species (H, OH, O etc.,) along with their corresponding wavelengths can be found in literature (Shih and Locke, 2010b). Avtaeva et al., (2010) has reported a wide band of wavelength between (390-550 nm) referring it to be radiation of H_2O molecule $(\tilde{C} \rightarrow \tilde{A})$ and weak emission in the range of 540-588 nm which is most likely due to H_2*.

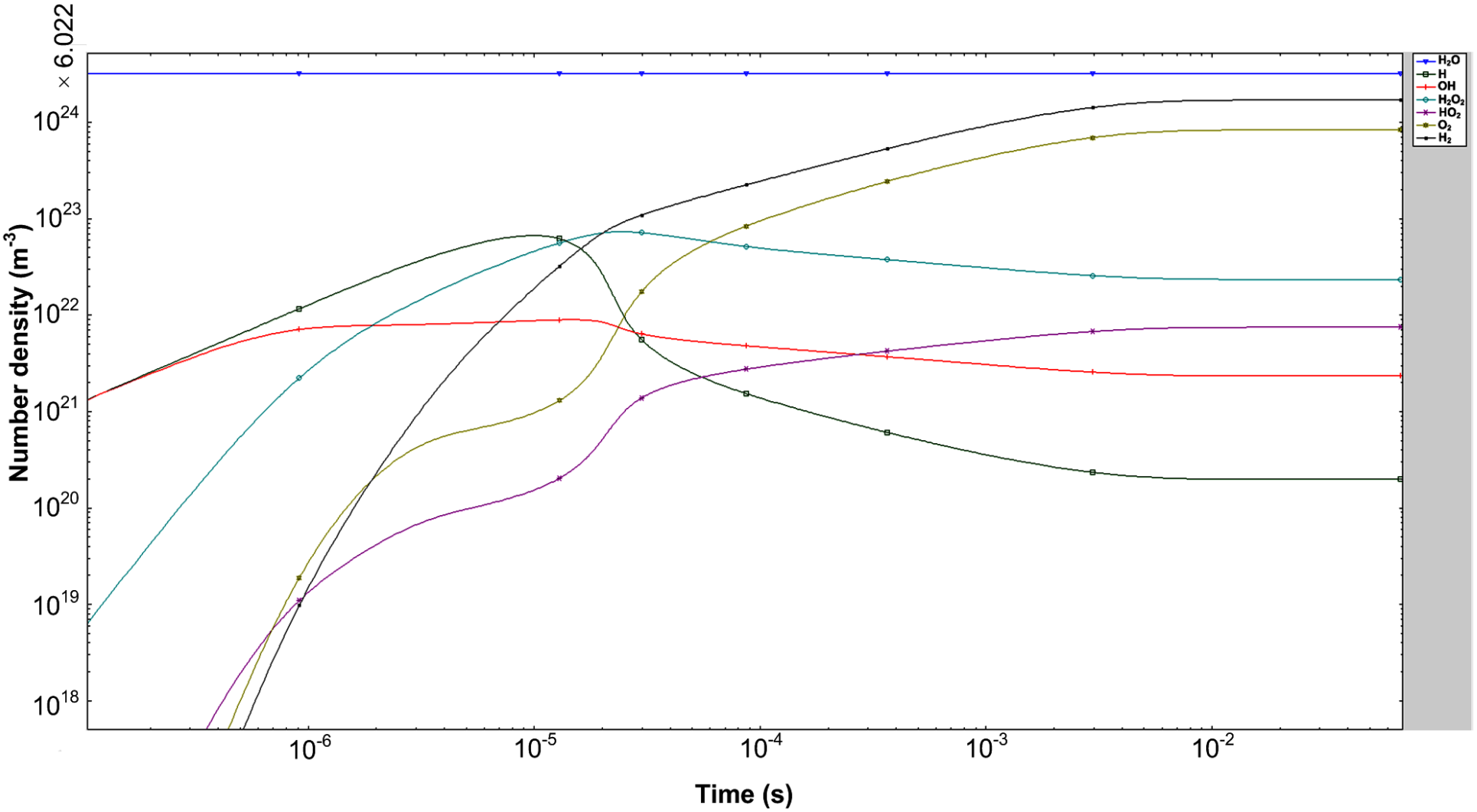

Figure 3-2 Number densities of H_2, O_2, H_2O_2, HO_2, OH and H w. r. t evolution time without dissociative attachment mechanism at electron number density of 10^{21} m^{-3}

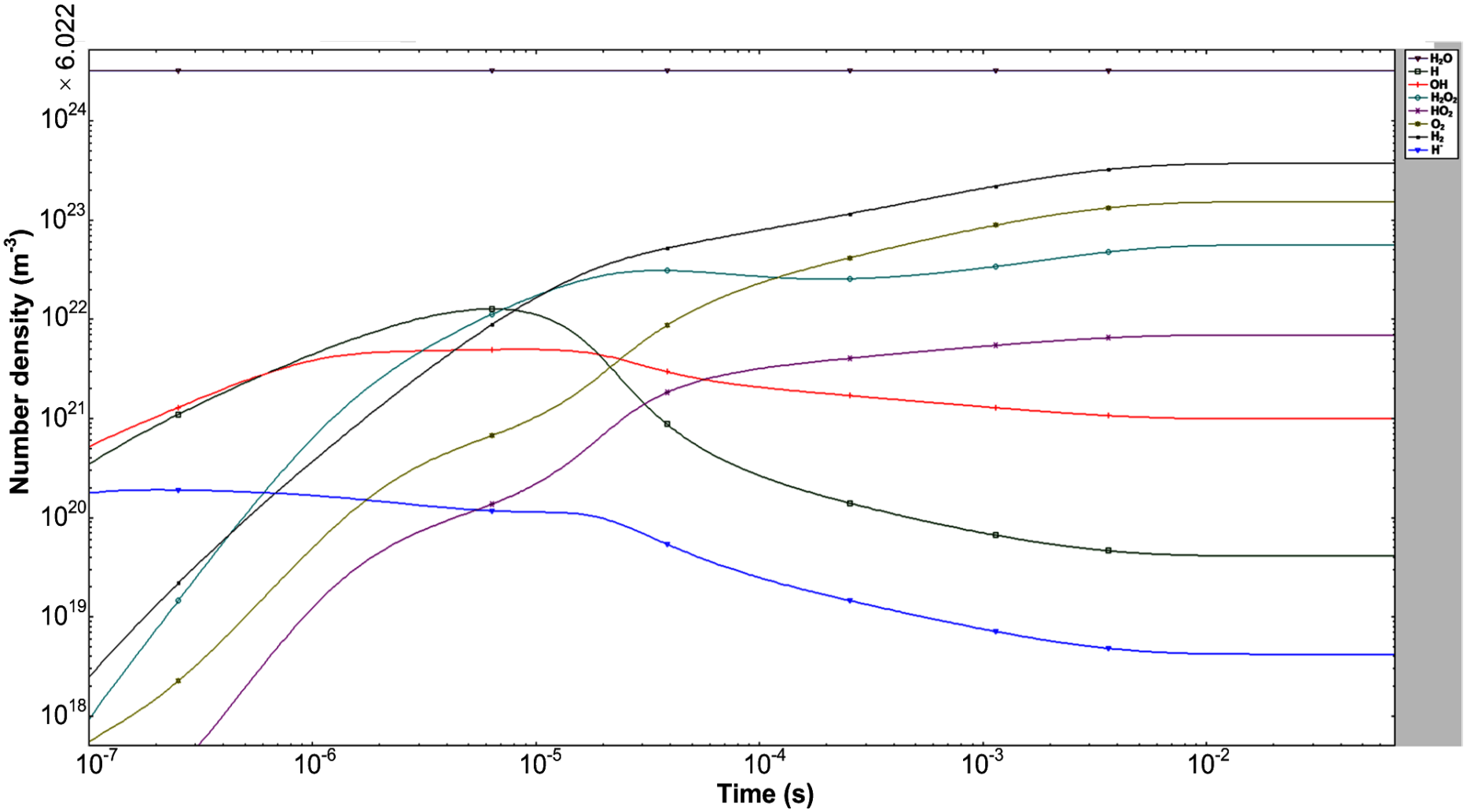

Figure 3-3 Concentration profiles of H_2, O_2, H_2O_2, HO_2, OH and H w. r. t evolution time with dissociative attachment mechanism at electron number density of 10^{21} m^{-3}

As discussed earlier, the model was analysed with and without the addition of dissociative electron attachment mechanism. REL allows selecting or deselecting any reaction from the reaction scheme and observing its effects on number density and time of evolution of different species. Mechanistic steps (reaction no. 8, 81 and 92) of dissociative attachment were introduced in kinetic scheme presented in **Table 3-1** to see its effects on the types and concentration of species produced and reaction time scales. **Figure 3-2** shows the kinetic curves of H_2, O_2, H_2O_2, HO_2, OH and H without dissociative attachment mechanism (water vapour plasmolysis is initiated by dissociation mechanism reaction 1 in **Table 3-1**) and **Figure 3-3** shows the kinetic curves of the above given species when dissociative attachment mechanism of electron was used as primary reaction to break water vapour by electron impact. The dominant step in this plasmolysis system was found to be dissociation reaction (Reaction 1). The threshold electron energy for electron impact dissociation of water to form H and OH is 5.1 *eV* (Itikawa and Mason, 2005, Lukes et al., 2008a). **Table 3-3** summarises the threshold energies for electron impact dissociation pathways of water molecule. Under non-LTE conditions or at lower electron energies (as in current study) the dissociation channel given as reaction-1 in **Table 3-1** and **Table 3-3** is most likely to dominate the kinetics because of lower energy requirement (Kregar et al., 2009). A detailed discussion on important pathways present in water vapour plasmolysis is done at later in this section.

Table 3-3 Electron impact dissociation pathways of water molecule (Itikawa and Mason, 2005, Lukes et al., 2008a)

Sr. No.	Reaction	Threshold Energy (*eV*)
1	$e^- + H_2O \longrightarrow OH + H + e^-$	5.1
2	$e^- + H_2O \longrightarrow O^*(^1D) + H_2(X) + e^-$	7.0
3	$e^- + H_2O \longrightarrow OH^*(A) + H(^1S) + e^-$	9.15
4	$e^- + H_2O \longrightarrow O^*(^1S) + H_2(X) + e^-$	9.22
5	$e^- + H_2O \longrightarrow O^*(^3P) + 2H + e^-$	9.51
6	$e^- + H_2O \longrightarrow O^*(3S^3S^o) + H_2(X) + e^-$	14.56
7	$e^- + H_2O \longrightarrow OH^*(A) + H^*(n=2) + e^-$	15.3
8	$e^- + H_2O \longrightarrow OH^*(A) + H^*(n=3) + e^-$	17.19

Figure 3-2 shows the steady state number density of 9.64 x 10^{24} m^{-3} of H_2 is produced. When the reaction 1 was deselected from the reaction scheme, a drop of 98.75% in the number density of H_2 was observed. Dissociative attachment was found to be the other important step in water vapour plasmolysis. When the model was run with dissociative electron attachment mechanism (Reaction 8), number density of H_2 (produced by dissociation pathway-reaction 1) dropped from 9.64 x 10^{24} m^{-3} to 2.41 x 10^{24} m^{-3}. Deselecting other pathways of electron impact water vapour breakdown (ionisation reactions, dissociative ionisation reaction and dissociative excitation reaction) included in the current study does not seem to affect the kinetics as no significant difference in the number densities of species or reaction time scale was observed. This reveals that dissociation reaction and dissociative attachment reaction are the main pathways of water vapour plasmolysis under conditions of the present study.

However, a general trend of the concentration profiles is found to be similar in both mechanisms. H_2 and O_2 are the major products along with traces of H_2O_2. Twice as much H_2 is produced as O_2. The profile of H_2 is apparently following two slopes. In the first regime the reaction rate increases rapidly and then gradually slows down before reaching steady state at just before 10^{-2}s. From the lower number densities involved in the first regime, it is likely that only the second regime and slope are important in producing substantial amount of hydrogen (Lozano-Parada and Zimmerman, 2010). The profile of O_2, however, after being evolved shows a slight dip in number density at 10^{-5}s and then rises to reach steady state at about the same time as H_2.

The number density of H_2O_2 drops after its evolution and reaches steady state at 8 x 10^{-3}s in absence of dissociative attachment mechanism. H_2O_2 is an unstable molecule under typical plasma conditions. However, it could be produced as a stabilised product in water plasma at low temperature especially if the process is carried out at supersonic flows (Fridman, 2008). H_2 has been shown to produce at double the rate of H_2O_2 (Kirkpatrick and Locke, 2005) but their study was carried out in an aqueous phase. However, the current model is based on vapours, so a very low number density of H_2O_2 is found to be present in the product stream. The low predicted number density of H_2O_2 could be neglected, however it is being discussed because reactions

involving H_2O_2 were found to affect the overall kinetics of the process and same is true for HO_2, OH and H. Production of OH and H radicals has been shown by optical emission spectroscopy while H_2 and H_2O_2 have been detected by chemical methods (Lukes et al., 2008a).

At every increasing value of electron concentration, hydrogen (H) atoms are produced at higher number density and then drop rapidly as it combines with HO_2 to form hydrogen H_2 and O_2 (Reaction 23 in **Table 3-1**). It was thought that the recombination of hydrogen atoms (H + H) would be the major source of H_2 generation (Reaction 44 in **Table 3-1**).

$$H + H + M \longrightarrow H_2 + M \quad (44)$$

Where M is the third body. However, this recombination reaction is a third order reaction (Dixon-Lewis et al., 1962, Larkin and Thrush, 1965), is temperature dependent, and has a very small rate constant (~10^{-33} $cm^3 molecules^{-1}$) (Medodovic and Locke, 2009, Avtaeva et al., 2010). Since the temperature in the current study is low, H-H recombination reaction does not seem to affect the overall kinetics. Medodovic and Locke (2009) has proposed the formation of H_2 by H-H recombination reaction (Reaction 44 in **Table 3-1**) in the core zone and 21% of the hydrogen in recombination zone was thought to be produced by the reaction of H and OH (Reaction 30 in **Table 3-1**).

$$H + OH \longrightarrow O + H_2 \quad (30)$$

The value of rate constant of H-H recombination reaction (Reaction 44 in **Table 3-1**) given in the core zone is not applicable in the current model as the temperature (2500 - 7000 K) in the said study (Medodovic and Locke, 2009) in the core zone was very high. The rate constant of reaction between H and OH (Reaction 30 in **Table 3-1**) in the recombination zone is temperature dependent and does not contribute significantly at lower temperatures. Atomic oxygen O has also been produced but is not included in the present analysis as its number density was very low (below $10^{17} m^{-3}$). However, its production is evident in water discharges (Lukes et al., 2008b). One noticeable difference about the addition of the dissociative electron attachment mechanism

(Reaction 8 in **Table 3-1**) was the emergence of H^- (n31) along with H and OH in **Figure 3-3** showing it to be other significant water vapour decomposition pathway along with dissociation reaction (Reaction 1 in **Table 3-1**).

Figure 3-4 shows the number densities of different species as a function of electron number density. With an increase in the electron density, number density of all species is increased. With every value of electron density, number density of H_2 was found to be double than that of O_2. The addition of dissociative electron mechanism caused a decrease in the number density of all species. However, the number density of H was found to be most affected. This is because H is directly produced in dissociation reaction (Reaction 1 in **Table 3-1**). However, in the dissociative electron attachment mechanism H is produced by ion-electron detachment process (Reaction 81 in **Table 3-1**).

$$H^- + e^- \longrightarrow H + e^- + e^- \qquad (81)$$

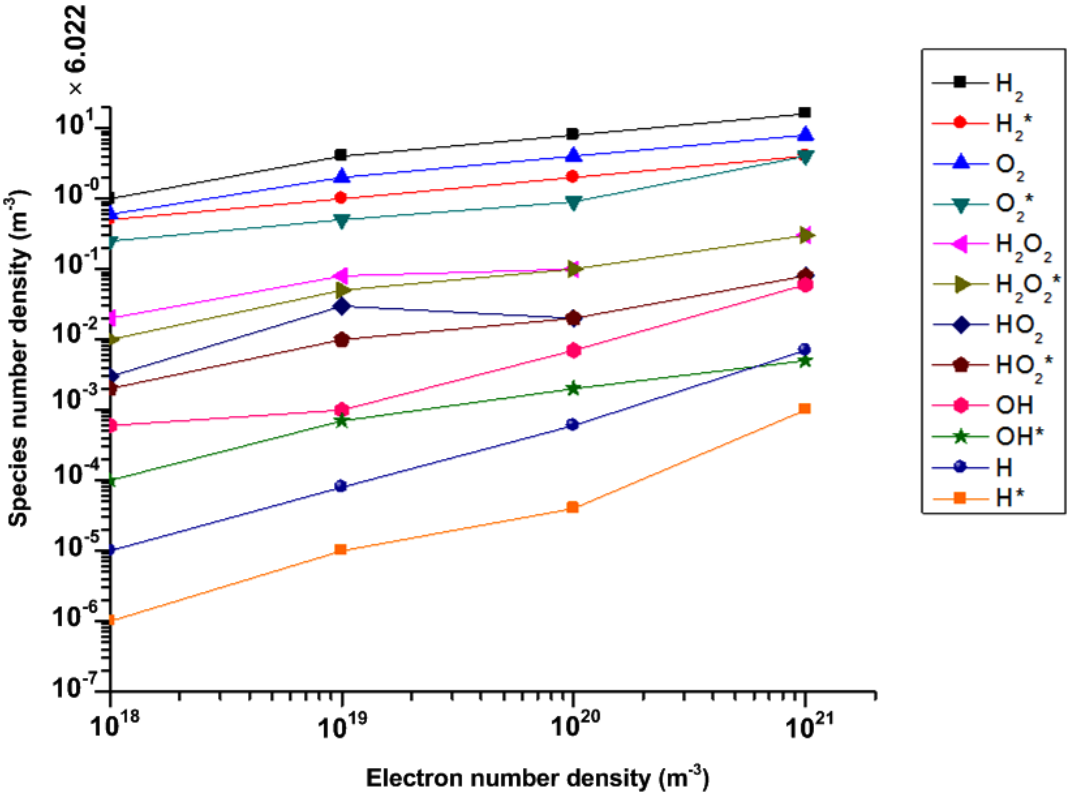

Figure 3-4 shows number density of H_2, O_2, H_2O_2, HO_2, OH and H (without the addition of dissociative electron attachment mechanism) and H_2*, O_2*, H_2O_2*, HO_2*, OH* and H*(with dissociative attachment mechanism)

Figure 3-5 shows the time of evolution of different species as a function of electron number density. With the increase in electron number density, the evolution time for each species was decreased. The time scale to reach steady state with dissociative electron attachment mechanism was similar to the corresponding time scale of different species in the absence of dissociative electron attachment.

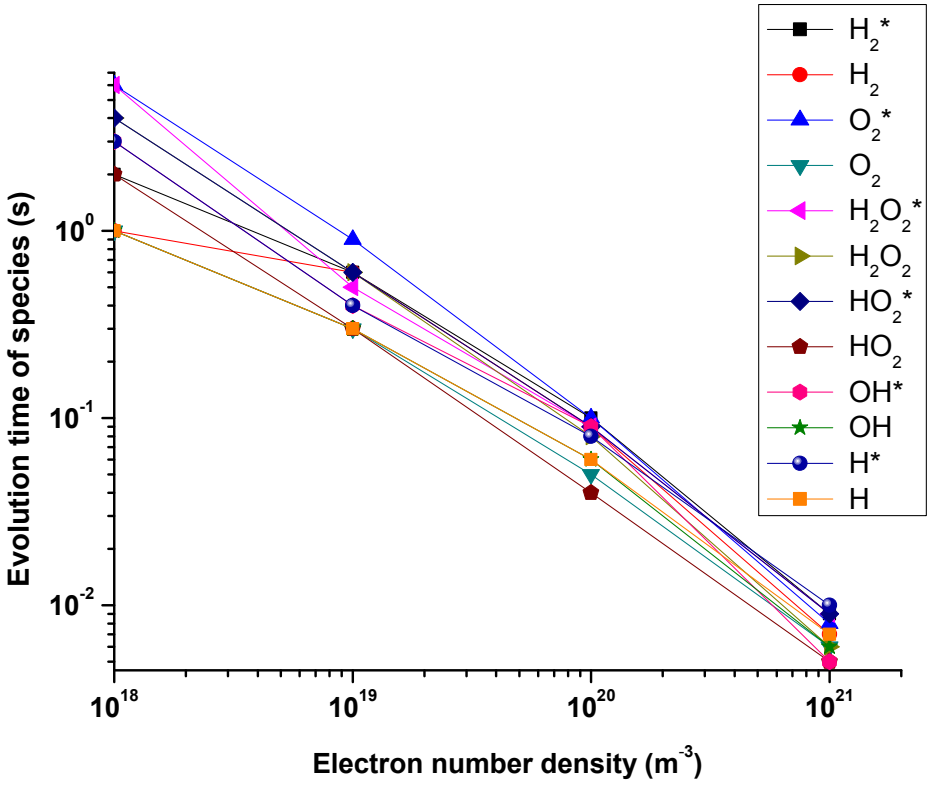

Figure 3-5 Evolution time H_2, O_2, H_2O_2, HO_2, OH and H (without the addition of dissociative attachment mechanism) and H_2*, O_2*, H_2O_2*, HO_2*, OH* and H*(with dissociative attachment mechanism)

As discussed earlier, REL allows the user to select or deselect any reaction from the reaction scheme and observe its effects on the number density and time of evolution of different species. The effect of every reaction on the number density of different species and their time of evolution was observed by deselecting the respective reaction from the reaction scheme. This was done for the whole range of electron densities (10^{18}-10^{21} m^{-3}) and in both mechanisms (dissociation and dissociative attachment of electron). Same reactions were found to affect the number densities of H_2, O_2 and H_2O_2. Reaction numbers given in following discussion refer to the corresponding reaction numbers in **Table 3-1**.

Reaction-1 was found to be the major source of production of H and OH. This could be explained on the basis of relatively larger cross sectional area (0.7 x 10^{-16} cm^2) of producing OH in ground state by this pathway compared with other pathways of creating OH, having smaller cross sectional area (0.09 x10^{-16} cm^2), in excited state such as reaction-10 (Kregar et al., 2009). The other source of OH was found to be reaction-22. When dissociative electron attachment mechanism was introduced, H^- was also produced along with H and OH. The number density of H, in this case, was controlled by reaction-81. Amongst every reaction producing H_2, reaction-23 was found to be the most significant one and for all values of electron densities (10^{21}-10^{18}) m^{-3}, it was the major source of H_2 and O_2 production. By deselecting reaction-23, the number density of H_2 was reduced from 9.64 x 10^{24} m^{-3} to 4.22 x 10^{23} m^{-3}. Along with reaction-1, the number density of O_2 was affected by reaction-28 as well.

$$H + HO_2 \longrightarrow H_2 + O_2 \quad (23)$$

$$OH + O \longrightarrow O_2 + H \quad (28)$$

As reaction-23 was deselected H_2O_2 became the primary product. The number density of H was found to increase as well as it is not consumed anymore in the reaction. The increase in the number density of H_2O_2 can be explained on the basis of excess of H and HO_2 available once reaction-23 is deselected. These excessive H and HO_2 combine together in reaction-22 to form OH which consequently reacts in recombination reaction (Reaction-14) to form H_2O_2 and hence a sharp increase in number density of H_2O_2 is observed.

$$H + HO_2 \longrightarrow OH + OH \quad (22)$$

$$OH + OH \longrightarrow H_2O_2 \quad (14)$$

Reaction-24 was found to affect the number density of H_2O_2 and this could also explain the increase in H_2O_2 as reaction-23 was deselected. In reaction-24, HO_2 recombines with itself to produce more H_2O_2, again, deselecting reaction-23 means more of HO_2 are available to participate in the reaction-24 to produce more H_2O_2.

$$HO_2 + HO_2 \longrightarrow H_2O_2 + O_2 \quad (24)$$

By deselecting reaction-22, the number density of OH was dropped to 3.01 x 10^{21} m^{-3} from 6.02 x 10^{21} m^{-3}showing a drop of 50% in the concentration of OH. However, a slight increase was also noticed in the number density of H_2 and O_2. This is because the increased availability of H and HO_2 to participate in the reaction-23 to form H_2 and O_2. Reaction-14 was found to be a key step in forming H_2O_2 by recombination of OH-OH (Shih and Locke, 2010a). By deselecting reaction-14 from the kinetic scheme, the number density of H_2O_2 was dropped to 6.02 x 10^{20} m^{-3} from 6.02 x 10^{22} m^{-3}.

$$OH + OH \longrightarrow H_2O_2 \qquad (14)$$

Reaction-24 produces both H_2O_2 and O_2. However, deselecting reaction-24, did not show any significant change in the O_2 concentration, while, almost 20% of H_2O_2 was found to decrease for all values of electron density. The major source of production of HO_2 was found to be the reaction between OH and H_2O_2 (Reaction 17).

$$OH + H_2O_2 \longrightarrow HO_2 + H_2O \qquad (17)$$

Deselecting reaction-17 reduced the number density of HO_2. Consequently the number density of both O_2 and H_2 was decreased. There was an increase in the number density of H_2O_2 showing that reaction-17 is the major reaction consuming H_2O_2. Based on these observations, a mechanism is proposed in **Table 3-4**.

Table 3-4 Mechanism of water vapour plasmolysis to produce H_2

Reaction no. according to Table 3-1	Reactions	Process explanation
1	$H_2O + e^- \longrightarrow H + OH + e^-$	Water vapours are decomposed by dissociation reaction and/or dissociative electron attachment. Water vapours are decomposed to form H, H^- and OH. H^- would further participate in dissociative electron attachment mechanism as discussed previously.
8	$H_2O + e^- \longrightarrow H^- + OH$	
14	$OH + OH \longrightarrow H_2O_2$	OH combines together to form H_2O_2**.** Reaction-24 is also another important pathway which can produce H_2O_2. However, reaction-14 has been found to affect H_2O_2 production the most.
24	$HO_2 + HO_2 \longrightarrow H_2O_2 + O_2$	
17	$OH + H_2O_2 \longrightarrow HO_2 + H_2O$	H_2O_2 combines with OH to form HO_2 and water molecule.
23	$H + HO_2 \longrightarrow H_2 + O_2$	This HO_2 reacts with H atom to produce H_2 andO_2.

3.4 Summary

Dissociation reaction and dissociative electron attachment were found to dominate the water vapour breakdown processes. This was observed to be true for the whole range of electron densities selected. Both time scales and number densities reached their respective highest values of n_{H_2} = 9.64 x 10^{24} m^{-3} and $\tau_{reaction}$= 10 ms at a maximum electron density of 10^{21} m^{-3}. Time scales for reaching 99% percent of H_2 produced was found to be ~10 ms. This shows scope for economical H_2 production through plasma micro-reactors. This was found in agreement with (Lozano-Parada and Zimmerman, 2010). The time scales found to reach steady state hydrogen production is an essential parameter for plasma micro-reactor design which is carried out in next chapter. With every value of initial electron number density, the number density of H_2 was found to be double that of O_2. The dissociation reaction (Reaction 1) was found to dominate the water vapour breakdown yielding an equilibrium number density of H_2 (9.64 x 10^{24} m^{-3}). The other important kinetic step was found to be dissociative attachment of electrons (Reaction 8). Number density dropped from 9.64 x 10^{24} m^{-3} to 2.41 x 10^{24} m^{-3} of H_2 when dissociative electron attachment was used as primary reaction of electron impact water vapour dissociation. However, its addition introduced H^- radicals into the system which in turn control the production of H by electron detachment with electron. Recombination of H-H atom was not found to be responsible for the production of H_2. H_2 was found to be produced mainly by the reaction between H and HO_2. By performing a detailed kinetic analysis major steps influencing the overall kinetics of water vapour plasmolysis were found. Based on these findings, a simplified process is proposed.

Chapter 4

Experimental Design and Procedure

4.1 Preface

This chapter is dedicated towards experimental design and procedures followed in the current study. The chapter consists of two sections. The first chapter deals with the introduction of the chapter. In second section, details of materials and methods of all experiments have been given. Section two has been further divided into four subsection. In the first subsection experimental methods for generating water vapour plasma, its electrical and optical electrical characterisation, and identification of optical emission spectral peaks in the range of 317-400nm is given. Experimental methods for optimisation of operational parameters of plasmolysis have been studied in second subsection. Experiments regarding separation of hydrogen by microbubbles have been given in third subsection. Applicability of reactive separation has been assessed experimentally in fourth subsection.

4.2 Materials and methods

Different configurations of plasma micro-reactors were fabricated and tested in order to find the optimum design which could be used for sustainable water vapour plasma generation, its characterisation, feasibility study of hydrogen production and assessment of reactive separation.

The water vapour plasma was generated in a rectangular capillary of 1mm width. Electrodes were cut from aluminium sheet in rectangular shape. The electrodes were pasted, using an adhesive (araldite), on opposite sides of the capillary tube such that the overlapping distance between them is about 1cm. The assembly was sandwiched between glass slides by using the adhesive as shown in **Figure 4-1**. One end of the capillary tube was used as inlet and the other was used as the outlet. This arrangement was simple and easy to use. For preliminary experiments, water vapour plasma was ignited at 3.6 kV at 37kHz. However, it was difficult to control the adhesive thickness between electrode and capillary tube making plasma inhomogeneous at some places. Because of the fragile nature of capillary tubes, the reactor kept breaking.

Figure 4-1 Capillary plasma micro-reactor

The disk reactor originally used for ozone production (Lozano-Parada, 2007) was used for generating water vapour plasma as shown in **Figure 4-2**. The disk reactor was micro-fabricated, so it offered better control on the process. It is more robust than the

capillary reactor. The outlet of the disk reactor has small slits at the perimeter which meant the product from water vapour plasmolysis would come out in the form of bubbles. However, glass wafers of 120 μm thickness were used as dielectric material. Again, it was difficult to control the thickness of adhesive to paste glass wafer on electrodes. Non-uniform layer of adhesive means the distance between the electrodes cannot be kept constant. This increases the chance of arcing as most of the current would pass through to the point where the distance between two electrodes is minimum and hence arcing can occur at that point. Drilling a hole to be used as water vapour inlet on the glass wafer was difficult as well. Laser drilling could be used to accomplish the job but it increases the principle cost of the plasma micro-reactor.

Figure 4-2 Disk plasma micro-reactor

Preliminary experimental results identified the need of designing a new plasma micro-reactor to achieve the objectives of the current study. Looking into preliminary reactor designs and discussion done in section 2.3.5 in **chapter 2**, a DBD-corona hybrid discharge reactor was designed as discussed in next section.

4.2.1 H_2 production by water vapour plasmolysis and its characterisation

A custom made high voltage power source (Entwicklung Leistungselectronic, Germany) was used to ignite the plasma. The power source was designed to give voltage up to 12 kV with frequency ranging from 20 kHz to 40 kHz. The power supply was equipped with manual control knobs to control voltage, current and frequency. It also has two digital LCDs to monitor voltages and current values. No matching network has been provided in the device due to limited frequency range. A T-shaped borosilicate glass reactor was designed and built with 7 mm outer diameter and 4.88 mm inner diameter. A stainless steel circular rod of diameter 2.40 mm was used as the driven

electrode. **Figure 4-3** shows the schematic representation of plasma micro-reactor. The configuration produced a flow channel of 2.48 mm with a radial gap of 1.24 mm. An Aluminium sheet of thickness 0.5 mm and 2 cm long was wrapped around the reactor and used as ground electrode. **Figure 4-4** shows the DBD-corona hybrid discharge reactor used in the experimenters.

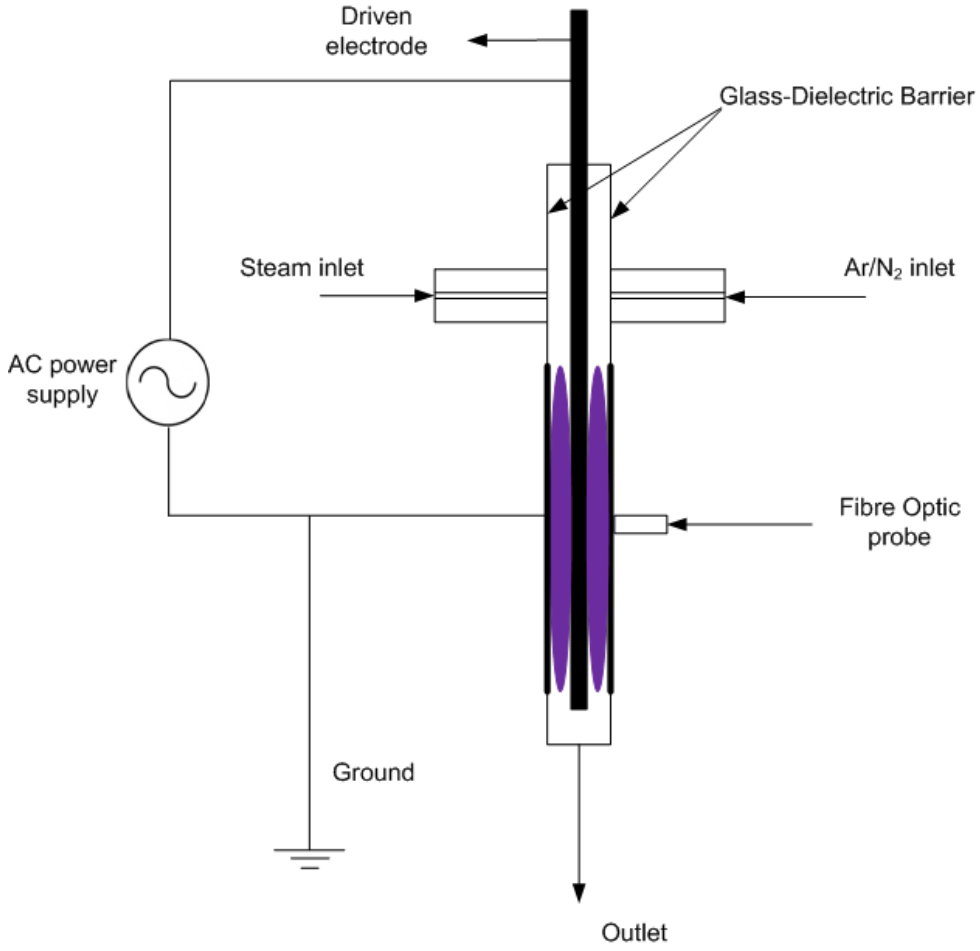

Figure 4-3 Schematic representation of DBD-Corona hybrid discharge reactor used in experiments

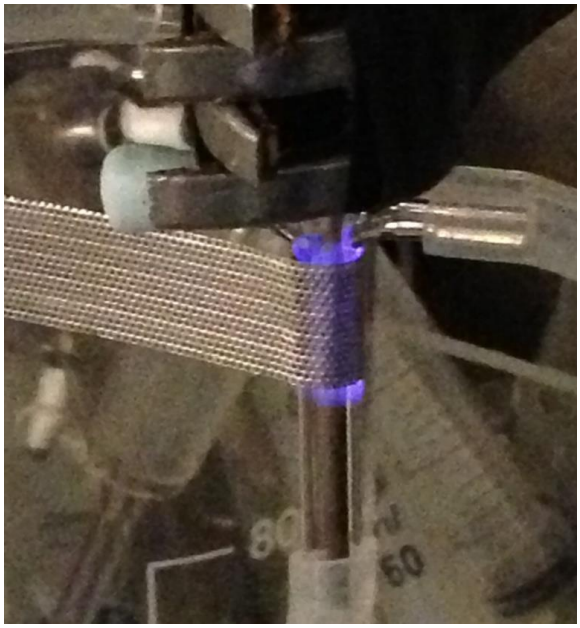

Figure 4-4 DBD-Corona hybrid reactor used in experiments

A 3 mm hole in the centre of the ground electrode was drilled to serve as a window for data acquisition. A holder was attached with the plasma micro-reactor to support fibre optic probe for data acquisition as shown in **Figure 4-5**.

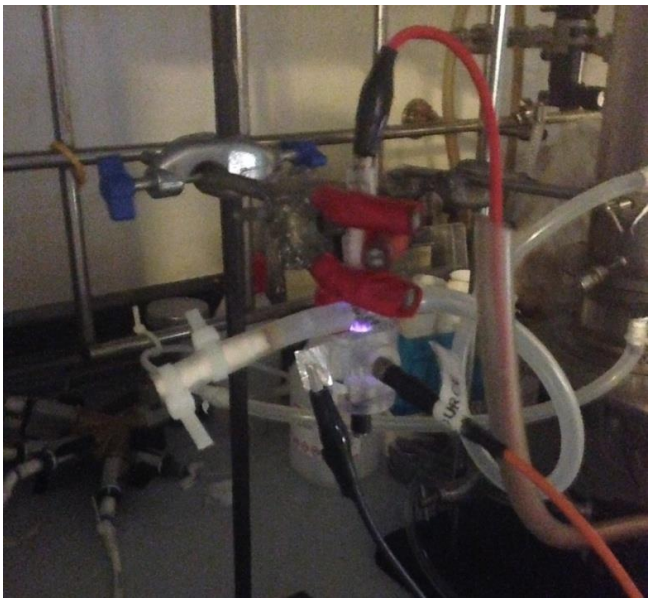

Figure 4-5 Fibre optic probe and holder attached to DBD-Corona hybrid discharge reactor

Three different sets of experiments were performed. In the first set of experiments water vapour plasma was characterised. In part 1, only water vapours were run through the reactor. Flow rate of water vapour was set to 2 ml min^{-1} at 1 atm. Power

was supplied from the above mentioned power source to obtain steam plasma. This was followed by the injection of argon gas at 10 ml min^{-1} from the other side of the reactor. Lastly, Argon gas was replaced by 10 ml min^{-1} of nitrogen into the reactor along with steam. The gases (Ar and N_2) have been injected through an inlet opposite to that used for steam in order to prevent condensation. Both argon and nitrogen were 99.998% pure and purchased from BOC.

In second set of experiments, water vapour decomposition was monitored by connecting a set of condensers to the outlet of the reactor. The experiment was run for ten minutes and steam condensate was collected in a measuring cylinder. The experiment was repeated with injection of argon gas and water vapour decomposition rate was monitored. Decomposition products were analysed using both online and offline GC. An empirical model was generated by applying an experimental plan according to the second order central composite rotatable design (Cochran and Cox, 1992) to study the effects of steam and argon flow rates on the decomposition rate. A detailed discussion on the statistical model is done in section 5.2.9 in chapter 5.

A third set of experiments was carried out to explore the identity of the peaks in the optical emission spectrum in the range of 317-400 nm. Two experiments were carried out separately. In the first experiment, plasma was ignited in a glass tube (9cm ID) filled with demineralised water. Two bungs were fitted at each end having two Al electrodes as shown in **Figure 4-6**. An inter-electrode gap of approximately 1 mm was maintained. In the second experiment, glass chip was treated with Ar plasma. The contact angle for demineralised water with glass chip was measured before and after experiment by First Ten Angstrom tensiometer using the sessile drop method.

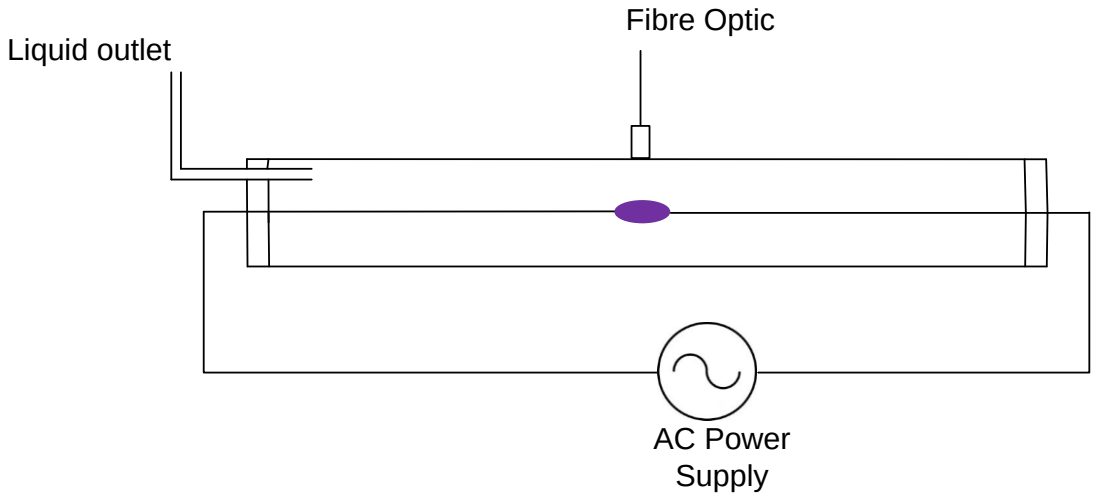

Figure 4-6 Schematic representation of reactor used for the optical emission spectral peaks

A high voltage probe and digital oscilloscope (ADC-212, Pico Technology Limited) was used to measure the applied voltage and to generate voltage and frequency output signals. The plasma current was measured by a calibrated digital current clamp meter (UNI-T, UT 201) (Abdul-Majeed et al., 2011).

The experiments were started with an initial voltage of 2.2 kV and gradually increased upto 4 kV. Optical emission spectra were obtained by a fibre optic cable which was connected to an (Ocean Optics USB 2000) spectrometer (monochromator and detector). The spectral data obtained were analysed by Spectral Suite software (Ocean Optics). This spectrometric system has 0.3-1.5 nm $FWHM$ resolution, 600 lines grating density blazed at 300 nm and 25µm slit width. The spectrometric parameters, integration time and boxcar width, were 1000 ms and 2 respectively. All spectral data was recorded at 4 kV, 16 mA and 36.74 kHz.

4.2.2 Optimisation of operational parameter of plasmolysis using ozone generation

Operational parameters of plasmolysis were optimised using ozone generation instead of hydrogen generation. It is assumed that the kinetics of formation of ozone from air plasma and hydrogen from water vapour plasma are similar. Hence, a plasma micro-reactor optimised for ozone generation would work equally good for hydrogen generation as well. A detailed discussion on the justification of this assumption is done in section 5.3.1 in chapter 5.

Plasma was ignited and sustained by the same power supply used in section 4.2.1. **Figure 4-7** shows the schematic representation of reactor. However, the dimensions of DBD-corona hybrid discharge reactor was reduced in order to get the radial flow channel down to micron scale (external diameter of reactor = 7.0 mm and internal diameter = 3.40 mm). A circular rod of diameter 2.40 mm was used as the driven electrode. The configuration produced a flow of channel 1.20 mm with a radial gap of 0.6 mm. Brass, stainless steel 316 (SS) and aluminium (Al) rods of the same thickness were used in turn as the driven electrodes. Four different materials were used as outer electrodes in turn. These materials were aluminium sheet, aluminium tape, a squared holes stainless steel mesh (mesh 1) and punched holes stainless steel sheet (mesh 2).

The ozone concentration was measured using the indigo solution decolourisation method proposed by Bader and Hoigné (1981). The method was chosen because it is very sensitive to change in ozone concentration, fast, precise, specific, easy to handle and recommended for kinetics measurements and studies of ozonation processes (Bader and Hoigné, 1981). It involves making a stock solution of potassium indigo trisulfonate and then diluting it with 1 litre deionised water to make a standard solution.

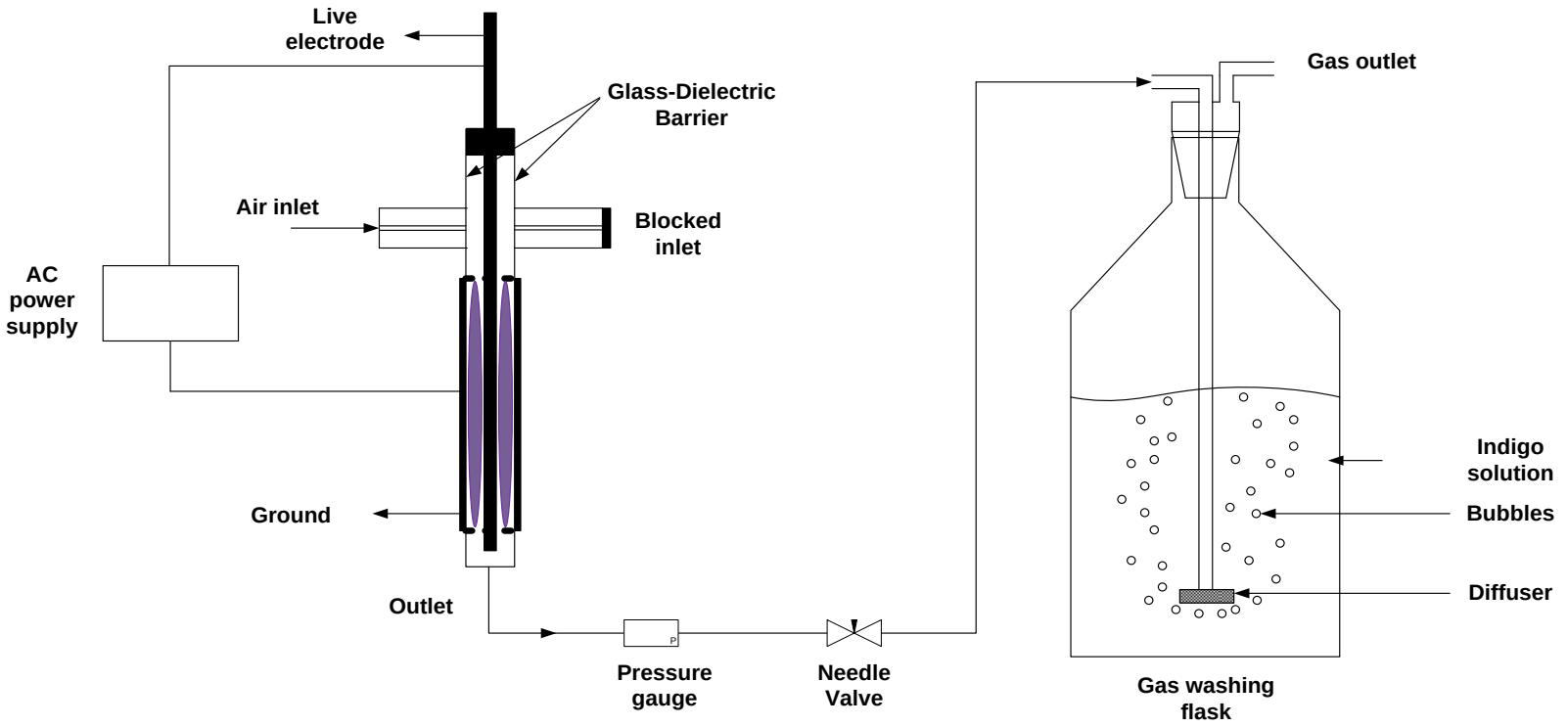

Figure 4-7 Experimental set up of the T-shaped DBD-corona hybrid reactor for optimisation experiments

To test the solution, 1 ml of stock solution diluted with 99 ml of water should give an absorption value of 0.20 ± 0.010 cm^{-1} at 600 nm.

The stock solution is stored in cold and dark conditions because of its sensitivity to light and temperature. Standard solution was prepared by taking 20 ml of stock solution, 10 g of sodium dihydrogen phosphate and 7 ml of concentrated phosphoric acid (85% v/v) and diluting it with deionised water to make a total volume of 1 litre. Phosphoric acid and sodium dihydrogen phosphate were used as buffers in order to keep the pH around 2. This is essential as at lower pH values, the amines are protonated and all of the ozone is assumed to react with C=C. The structural formula of potassium indigo trisulfonate is shown in **Figure 4-8**.

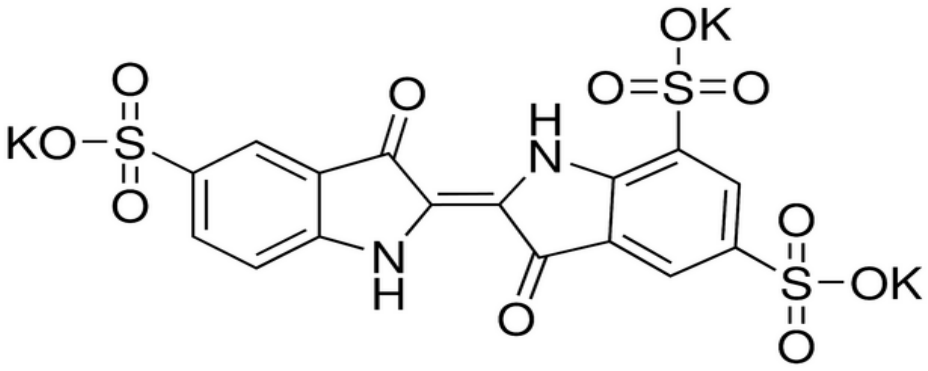

Figure 4-8 Structural formula of potassium indigo trisulfonate

150 ml of the indigo solution was used in each experiment. The plasma was switched on for 20 seconds. Air was blown through the gas washing flask for 2 minutes after the power was switched off. This was done to allow all the ozone to react with the indigo solution. The samples were taken from the gas washing flask and analysed for absorption at 600 nm (Bader and Hoigné, 1981) using a Hach Lange (DR 2800) spectrophotometer. Each experiment was run for 20 seconds except for the experiments with 4.8 kV which were run for 15 seconds as the solution was getting decolourised in 18 seconds. For experiments to optimise pressure, a needle valve was used to maintain air pressure between 0.2-1 gauge pressure (bar*g*) inside the reactor. A Bourdon gauge was used to monitor the pressure.

All experiments were repeated three times and a standard deviation was used to estimate the standard error.

4.2.3 Separation of hydrogen by microbubbles

Air was used to produce microbubbles and the changes in DO concentrations were monitored to calculate $K_l a$. The rationale for using air-water system to generate microbubbles has been discussed in section 5.4.1. $K_l a$ was studied for oscillatory flow and compared with steady state flow in the range of 40-100 l min^{-1}.

Two different sets of experiments were carried out to determine $K_l a$ and to measure the bubble size distribution. In the first set of experiment $K_l a$ of air in to water was measured. **Figure 4-9** shows schematic representation of the experimental rig used.

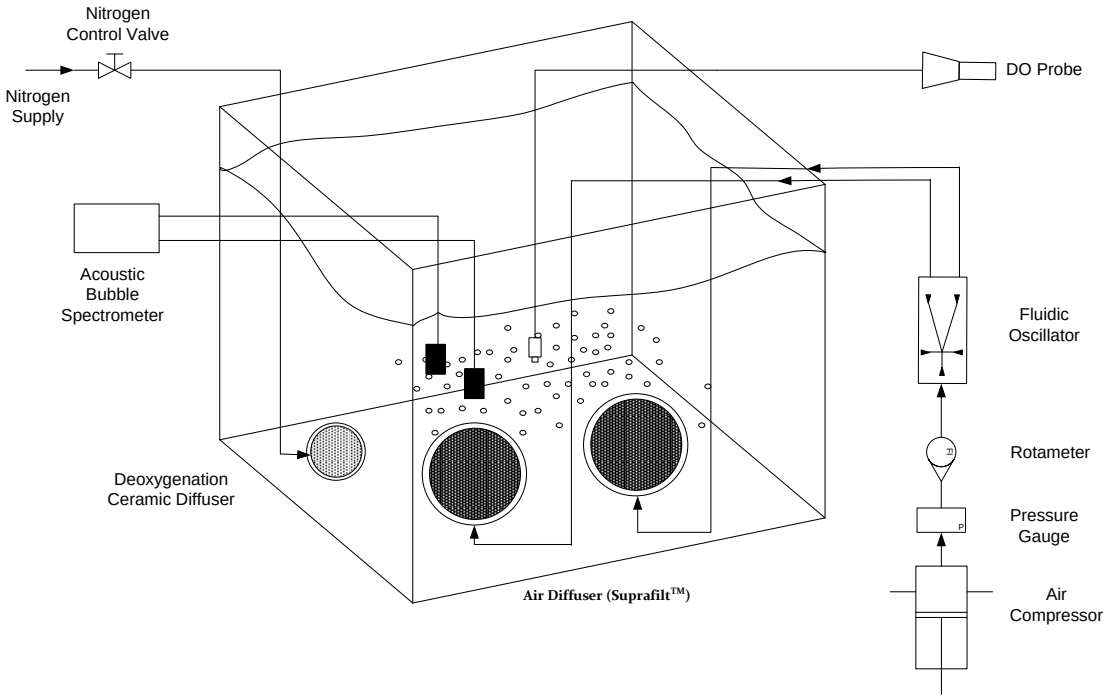

Figure 4-9 Experimental setup used for measurement of $K_l a$

A glass tank of dimensions (1.2 m x 0.5 m x 0.59 m) was used as water container. Approximately 0.30 m^3 (1.2m x 0.5m x 0.5m) was used in each experiment. A pair of Suprafilt™ 30 cm disks diffusers, widely used in industry, was used to bubble air in to the water. The diffuser material consists of ethylene propylene direne monomer membranes (EPDM).

A handheld YSI 556 DO probe was used to determine the DO concentration in the water over time. Water was first deoxygenated to a level well below 20% saturation.

For deoxygenation, N_2 was bubbled through a ceramic diffuser placed in the bottom of the water container. Oxygenation profiles were created between 20-80% saturation at a sample time interval of 30 seconds. Experiments were conducted at different flow rates ranging between 40-100 l min^{-1} with oscillatory flow and steady flow at same upstream pressure (4-17 psi*g* corresponding to each flow rate in the range of 40-100 l min^{-1}). The Fluidic oscillator was replaced with a Y-piece for the steady flow experiments. The DO probe was placed at the corner of the tank in order to avoid direct contact/attachment of bubbles with the sensor of the probe which could cause an error in $K_l a$ estimation.

In second set of experiments bubbles sizing was done using ABS. It consists of a pair of hydrophones which are placed in the liquid parallel to each other over the surface of the diffuser where bubbles are rising. Each hydrophone has a surface area of 5 x 5 cm^2 and hydrophones were placed at a distance of around 10 cm from each other. Hydrophones were placed in the mid depth of the tank. One of the hydrophones works as the emitter producing short bursts of sound waves at particular frequency (50-100 kHz) which are received by the other. The data was generated by the hydrophones and then analysed by the algorithms developed by Dynaflow INC. Bubble size distribution was measured at different flow rates ranging from 40-100 l min^{-1} for both oscillatory flow and steady flow.

4.2.4 Application of reactive separation on plasma-chemical process

Three different sets of experiment were conducted to assess the applicability of reactive separation on water vapour plasmolysis. In the first set of experiment $K_l a$ was measured for both oscillatory flow and steady flow at the same upstream pressure. The experimental rig used was same as used in section 4.2.3 and shown in **Figure 4-9**. However, the only difference was the use of MBD 600 diffusers-PointFour™ in these experiments instead of Suprafilt™ disk diffusers. MBD diffusers were chosen for two reasons. First, they are made with ceramic and plasma resistant. Secondly their ability to blow bubble at relatively lower flow rates. Considering the low flow rates used in plasma micro-reactors, a minimum flow rate of 1.1 l min^{-1} was used

to produce microbubble. Similar handheld DO probe (YSI 556), as used in previous section, was used to determine the amount of DO in the water.

Second set of experiments was conducted to measure the bubble size distribution using ABS for steady and oscillatory flows. The procedure adopted is the same to that described in section 4.2.3 for bubble sizing.

Third set of experiments was conducted to put the hypothesis of reactive separation to test. To assess the applicability of reactive separation on plasma-chemical processes, a reactor was designed with the plasma chamber directly below the diffuser as shown in **Figures 4-10 and 4-11**. This is to make an experimental arrangement such that the products emerging from plasma chamber can enter the water column in the form of microbubbles by passing through a diffuser as proposed is section 4.2.2. If it is assumed that the time lag for the gases to pass through the diffuser is negligible, the products coming out in the form of the bubbles could be separated by dissolving directly in the water. If the products are separated in the liquid phase at a quicker rate than they are formed in the plasma channel, an increased concentration of products should be produced by putting the plasma chamber directly below diffuser. It has been pointed out in section 2.4 in chapter 2 that ozone generation could be used instead of hydrogen production for optimisation studies (and the rationale for using ozone is given in section 5.3.1). In this set of experiments, ozone produced by air plasma was used to test the application of reactive separation on plasma-chemical process. Similar power supply, which was used previously in section 4.2.1 and 4.2.2 was used to ignite and sustain plasma. The concentration of ozone produced was monitored by indigo method (Bader and Hoigné, 1981) as described in section 4.2.2 using Hach Lange (DR 2800) spectrophotometer.

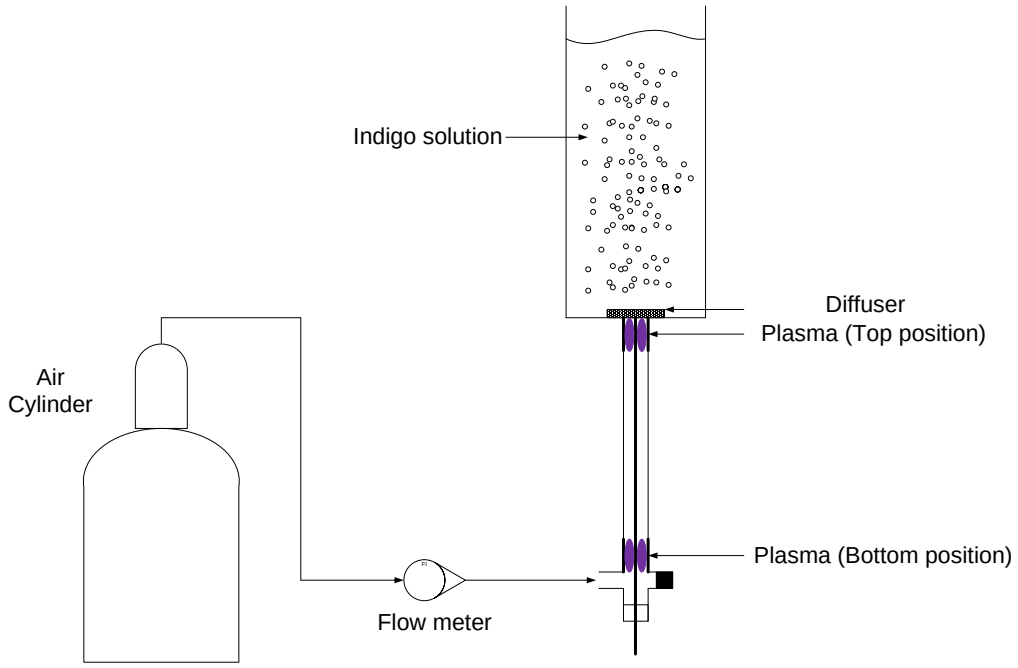

Figure 4-10 Experimental arrangement for application of reactive separation experiment

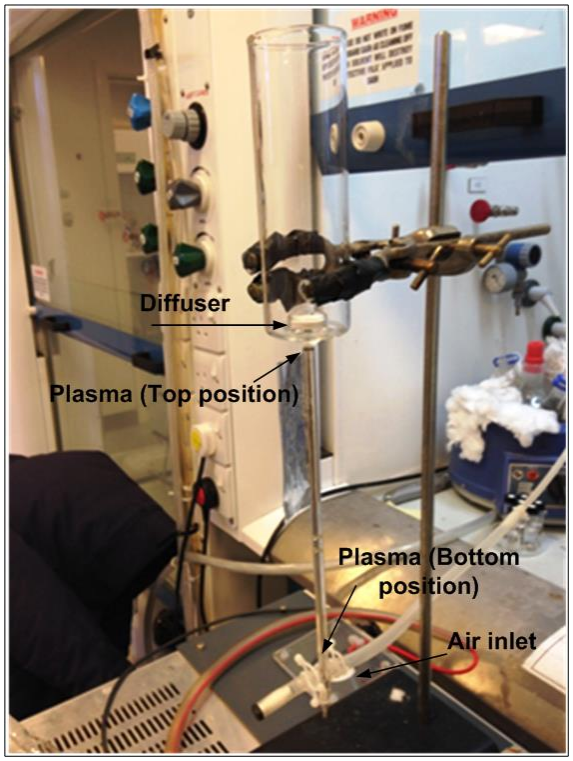

Figure 4-11 Modified DBD-corona hybrid discharge reactor used for reactive separation

The dimensions of the plasma micro-reactor are similar to what was used in section 4.2.2 producing a radial flow channel of 600 µm. The overall length of plasma micro-

reactor tube was 15 cm. A 2 cm long piece of Al tape was used as ground electrode. A sintered borosilicate diffuser of porosity >16 micrometer was attached at the outlet of the plasma micro-reactor. The diffuser was fused with a glass cylinder on top of it as shown in **Figure 4-11**. The current was allowed to settle according to the impedance of the plasma micro-reactor. The volume of indigo solution used was 150 ml. 4 kV was applied to ignite the plasma at a frequency of 37 kHz. The experiments were run at two different positions of external electrodes that is top and bottom. Experiments were run for an incremental interval of 3 seconds. For both positions, experiments were kept running until the indigo solution was completely decolourised (spectrophotometers showed 0 as absorbance reading). Air was blown for two minutes after the power was switched off at the end of each experiment in order for all the residual ozone to react with indigo solution. A sample was withdrawn at the end of each experiment for the spectrophotometric analysis.

Chapter 5

Results and Discussion

5.1 Preface

Results of the experiments, discussed in chapter 4 are presented and analysed in this chapter. The chapter is divided into six sections. The second section is dedicated for analysing the results of section 4.2.1. Water vapour plasma has been characterised for its fundamental properties. Feasibility of hydrogen production from water vapour plasmolysis at atmospheric pressure at relatively smaller inter-electrode distance has been demonstrated. Electron density, Debye length, electron, excitation, rotational and vibrational temperatures are calculated. Different types of energy yields are defined and calculated. Modelling work from chapter 3 is extended to observe the effect of addition of Ar along with water vapours as feed into the plasma micro-reactor. Results of experiments on the identification of optical emission spectral peaks between 317-400 nm are analysed. In the third section, results from section 4.2.2 have been analysed. Pressure and flow rate of the air, electrode material, length of external electrode and its configuration, applied power and frequency are optimised. In the fourth section, results from the section 4.2.3 have been analysed. $K_l a$ have been estimated for oscillatory and steady flows. In order to see the effects of oscillatory flow, results from the bubble sizing experiment have been analysed and oxygen transfer efficiency has been calculated. In the fifth section, results from section 4.2.4 have been analysed to assess its applicability on plasma-chemical reaction. Conclusions of the chapter are discussed in the sixth section.

5.2 Analysis of water vapour plasma

The residence time of water vapours in plasma chamber is a variable and is a function of total flow rate of water vapours and length of external electrode. Based on the 2 cm electrode length and gas flow rate, residence time in the current plasma reactor is in the order of 10^{-1} s. The time scale to reach steady state hydrogen production was found to be 10^{-2} s in chapter 3 by kinetic modelling. However, one of the objectives of this session is to show the feasibility of hydrogen production. A detailed analysis based on experimental investigations of optimum residence time has been carried out in section 5.3 which is entirely dedicated to optimisation of experimental parameters.

5.2.1 Electrical characterization

The plasma discharge has been characterised both electrically and optically. The voltage output signal, frequency spectrum and voltage-current (VI) characteristics have been plotted for AC powered DBD-corona hybrid discharge reactor. The voltage output signal of the power supply is shown in the **Figure 5-1**.

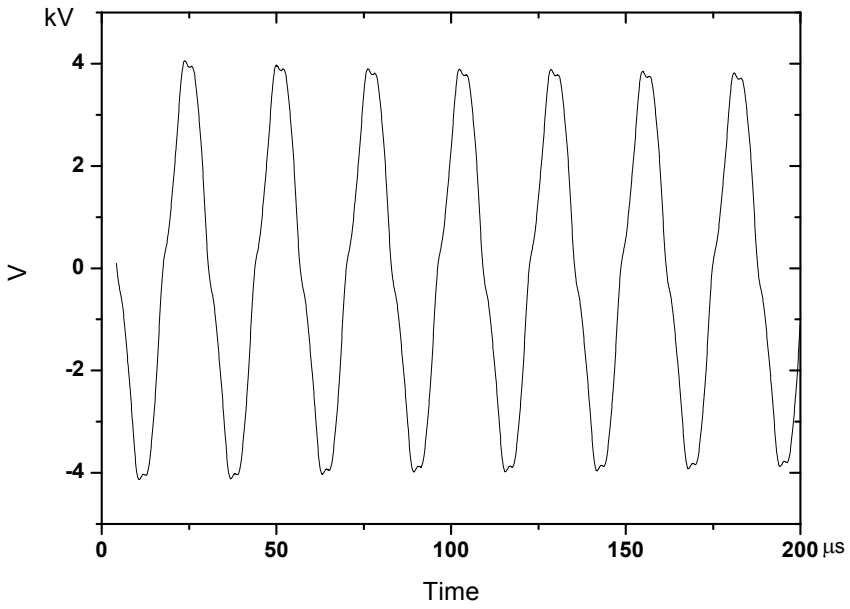

Figure 5-1 Voltage output signal of power supply

From **Figure 5-1**, it is evident that the source is providing a stable signal at 4 kV. **Figure 5-2** shows the frequency signal spectrum. The frequency signal spectrum was obtained using digital oscilloscope (ADC-212, Pico Technology Limited). On the y-axis, the

amplitude is in arbitrary units. The output signal mainly consisted of one main frequency of 36.74 kHz and two harmonics which are negligible; thus power goes into the reactor mainly at frequency of 36.74 kHz.

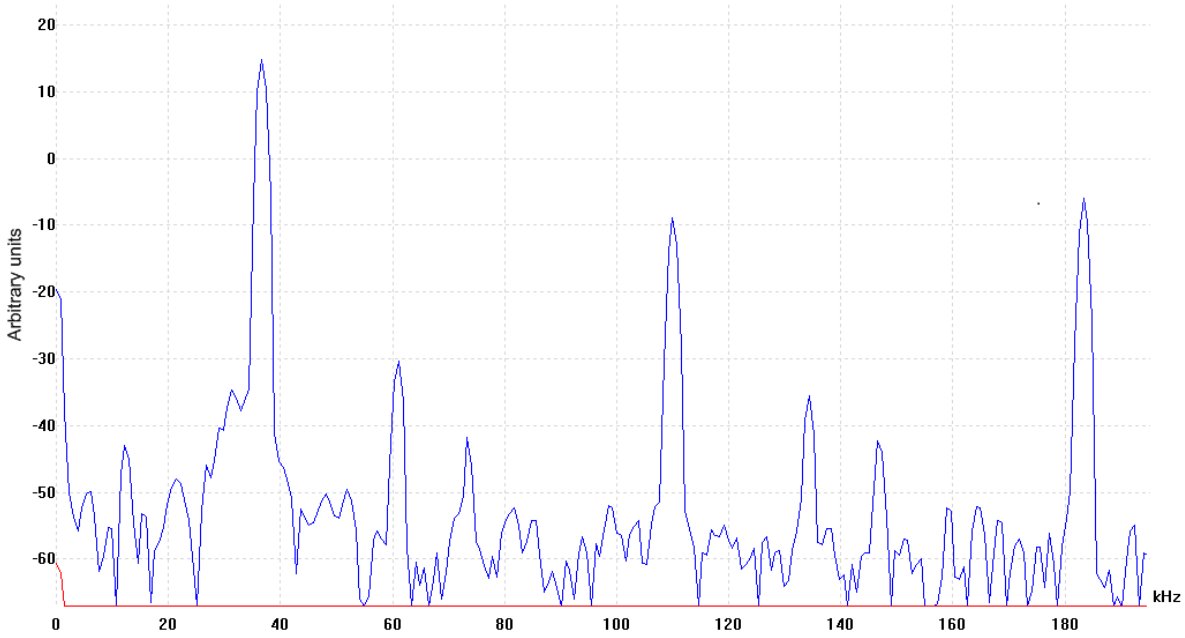

Figure 5-2 Frequency spectrum showing the output signal mainly at 36.74kHz

Figure 5-3 shows the VI characteristics for the DBD-corona hybrid discharge reactor used in this study.

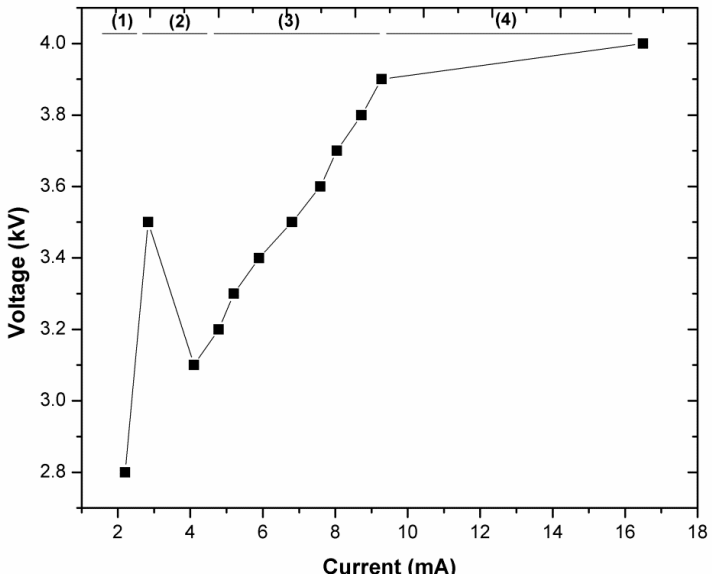

Figure 5-3 Current-voltage (VI) characteristics of AC powered DBD-corona hybrid discharge

It is subdivided in four different regions; 1- Townsend or pre-discharge, 2-normal glow, 3-abnormal glow and 4-discharge to arc transition (Schutze et al., 1998). The first region, namely, dark or Townsend discharge occurs prior to ignition. In the first region, a limited increase in the current proportional to the voltage is observed. In the second region, after the ignition of the plasma, the voltage drops immediately. This negative slope in **Figure 5-3** in region 2 shows voltage drop which usually appears in microdischarges (Sismanoglu and Amorim, 2008). At lower pressures (vacuum), Schutze et al., (1998) observed no voltage increase after region 2 with increase in current. The authors have reported rather a straight line parallel to increase in the current as shown in **Figure 2-3** in chapter 2. However, at higher pressure 2nd and 3rd region may shrink, (voltage starts increasing immediately after 2nd region) (Schutze et al., 1998) which is the case in the current study. In the third region, voltage starts to increase with the current until region 4 where a sharp decrease in the slope of line is observed which makes plasma highly conductive and can lead towards discharge to arc transition with further increase in voltage (Schutze et al., 1998). This discharge to arc transition can occur if the voltage was increased to more than 4kV as shown by sharp increase in the current in region 4 in **Figure 5-3**. Arcing is not desirable in the current study as it can break the reactor as shown in **Figure 5-4**, so, the voltage was only increased until 4 kV.

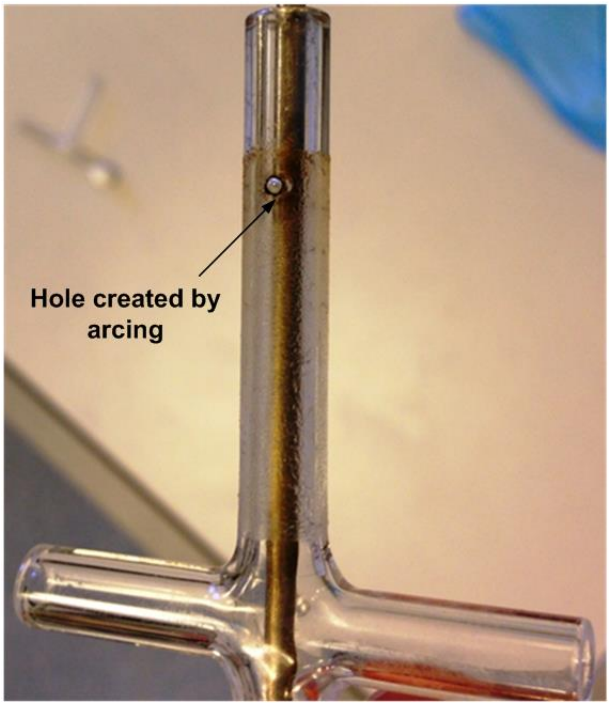

Figure 5-4 Hole created by arcing in DBD-corona hybrid discharge reactor

It is worth mentioning here that Schutze et al., (1998) used a DC glow discharge, however, an AC powered DBD plasma is discussed in the current study. From **Figure 5-3** it is also clear that the minimum breakdown voltage for steam flowing at 1 atm in a discharge gap of 1.24 mm is 3.5 kV at 3 mA. This corresponds to a power of 10.5 Watts. This breakdown voltage is in agreement with the discussion by Fridman (2008). Looking at the value of breakdown voltage of air, 30 kV cm^{-1} at 1 atm, it may be expected for water to breakdown at much greater voltage due to the density difference between air and water. However, a large number of studies (Fridman, 2008) have shown that the breakdown voltage of water is of the same order as for air. This is because of fast formation of gas channels in the body of water with imposed high electric field (Fridman, 2008). This essential and practically important effect could be elucidated on the basis of the process occurring at the electrode surface. The process occurring at the electrode surface can be further divided into two processes (Akiyama, 2000). The first process is subdivided in two phases as well; In the first phase a bubble is formed due to vaporisation of the liquid from local heating in the strong electric field regions at the tip of the electrode and in the second phase, electronic processes, the breakdown occurs due to ionising collision of electrons on their way across the breakdown gap. The first phase is not applicable in the current study as the water is already fed in vapour phase. Since water is fed in the vapour phase, which provides additional energy (latent heat of vaporisation of water) therefore overall energy for water vapour breakdown by plasmolysis is reduced. The second process is related to underwater electrical discharges and arc formation and hence not applicable on the current study. Although, experimentally determined minimum breakdown voltage is 3.5 kV with current of 3 mA, the analysis is conducted at 4 kV to obtain a better data set. The corresponding current at 4 kV was 16 mA.

5.2.2 Optical characterisation

Figure 5-5 shows the optical emission spectrum obtained by fibre optic probe from water vapour plasma. The spectrum shows an OH band between 302-317 nm.

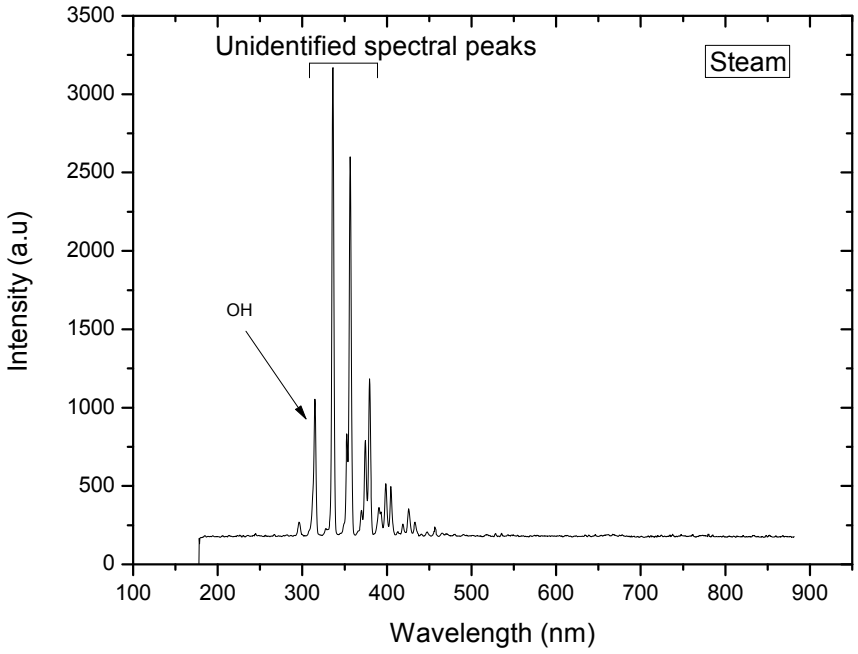

Figure 5-5 Optical emission spectrum of steam plasma

It was observed that some peaks occurring in the emission spectrum in the range of 300-400 nm, other than the peaks of OH band (302-317 nm), resemble nitrogen peaks (both second positive system of N_2 and first negative system of N_2^+) (Hong et al., 2008). However, these OES peaks appear in every experiment (spectral data of steam plasma, steam and argon plasma, and steam and nitrogen plasma), prompting an investigation of their identity which is discussed in section 5.2.11.

Figure 5-6 shows the optical emission spectrum of steam and argon plasma. A sharp increase in the OH band (302-317nm) is observed. The collision of Ar with the energetic electrons has also resulted in forming Ar atoms in various excited states, which is illustrated by the increased intensity of the argon emission lines at 696.5 nm, 750.38 nm and other Ar lines in the near IR region. Further details on the increased intensity of OH band (302-317) are discussed in section 5.2.9.

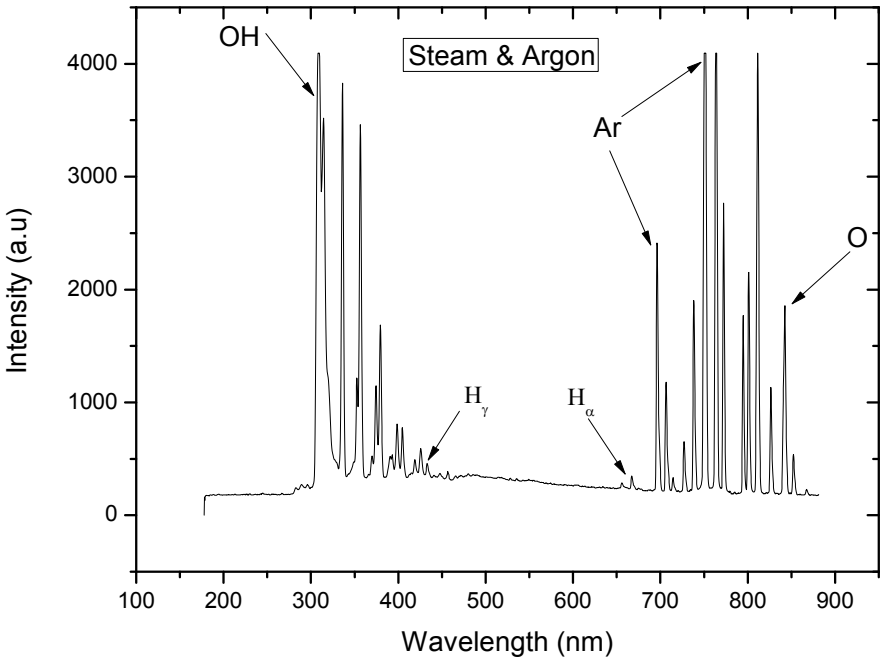

Figure 5-6 Steam and argon plasma spectrum

Figure 5-7 shows the emission spectrum of steam and nitrogen. Nitrogen was injected

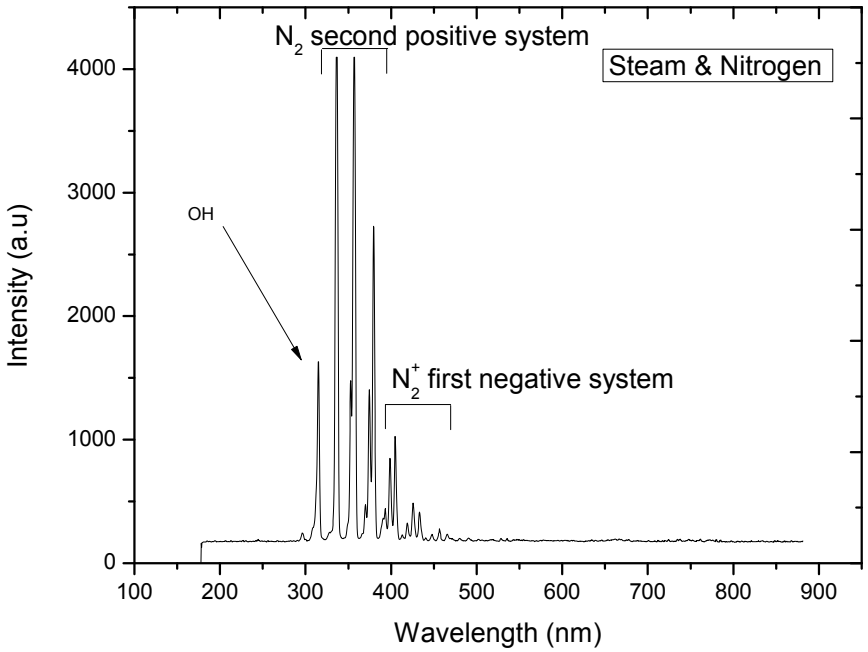

Figure 5-7 Optical emission spectrum of steam and nitrogen plasma

along with steam to determine the rotational temperature and vibrational temperature. Along with OH (302-317nm), nitrogen peaks are observed for both the second positive system of N_2 and first negative system of N_2^+ (Hong et al., 2008). Spectral data from Ar(I) lines, OH band (302-317 nm) and second positive system of N_2 are used to calculate T_e, T_{exc}, T_{rot}, and T_{vib}. The Ar lines shown in **Figure 5-6** between 690-815 nm have reliable published values of transition probabilities. Also, the energy gap between emitting upper levels is expanded within a range of more than 2 eV which is very important in choosing the lines for plasma diagnosis. The large number of available Ar lines (in the region of 690-815 nm) also give an additional advantage of choosing lines (at expense of lower intensity signal) with biggest energy difference between energy levels. This energy gap is essential to achieve higher accuracy for using the traditional Boltzmann plot (Gordillo-Vázquez et al., 2006).

5.2.3 Electron density

The electron density is calculated using $n_e = \frac{J}{e.v_d}$, where n_e, J, e and v_d represent the electron number density (m^{-3}), plasma current density (A m^{-2}), electron charge and electron drift velocity (m s^{-1}). The electron drift velocity was estimated by $v_d = \mu \times E$. Where, μ is the electron mobility and E is the average electric field. The electric field was estimated by measuring voltage using a high voltage probe and digital oscilloscope (ADC-212 from Pico Technology Limited). The voltage was measured to be 4 kV dissipating across a gap of 1.24 mm producing an electric field of 4.83 x 10^6 (V m^{-1}). Since the water vapours are following at atmospheric pressure, the electron mobility in atmospheric pressure plasmas, was taken as to be 0.01 m^2 s^{-1} (Abdul-Majeed et al., 2011). This produces a drift velocity of 4.83 x 10^4 m s^{-1}. The peak current was measured using digital current clamp meter (UNI-T, UT 201), where the current value was taken very near to the load and found to be 16 mA for the above given voltage value. The rationale for using peak current has been discussed later in section 5.2.9. The current density, 912 (A m^{-2}), was then calculated. Using the values of current density, electron charge and drift velocity, n_e was estimated to be 1.765 x $10^{17}m^{-3}$

which is in general agreement with studies (Nehra et al., 2008, Abdul-Majeed et al., 2011) using similar plasmas.

5.2.4 Electron temperature

OES has been used to determine electron, excitation, rotational and vibrational temperatures. In non- LTE plasmas, a normal Boltzmann plot is not permitted because the deviation from equilibrium may occur by a factor of 1000. However, there still exists information about the electron temperature in line intensities (Van der Sijde and Van der Mullen, 1990). It becomes very important to modify the Boltzmann plot for the calculation of T_e under non-LTE conditions. Electron temperature was calculated under non-LTE conditions by following equation (5-1) (Gordillo-Vázquez et al., 2006, Van der Sijde and Van der Mullen, 1990, Abdul-Majeed et al., 2011).

$$Ln\left(\frac{I_{ij}\sum A_{i>j}}{h\upsilon_{ij}A_{ij}b_{1i}}\right)=\frac{-E_i}{kT_e}+D \qquad (5\text{-}1)$$

Where, T_e is electron temperature, $h\nu_{ij}$ is the energy gap, k is the Boltzmann constant, A_{ij} is the transition probability and b_{1i} is a parameter determined by $b_{1i}=E_i^a\times p_i^b$. Where E_i is the excitation energy of excited state i, p_i is the effective quantum number for excited state, a and b are the fitting parameters obtained from (Gordillo-Vázquez et al., 2006). p_i for each level is given by the formula $pi=\sqrt{\frac{E_H}{E_\infty-E_i}}$. Where, E_H is the Rydberg constant (13.6 *eV*), E_∞ and E_i are the ionisation energy and excitation energy of the excited state i. The sum of transition probabilities ($A_{i>j}$) should contain all the excited energy level and number of radiative transitions starting in each considered argon energy level. **Figure 5-8** shows the modified Boltzmann plot used to determine the electron temperature.

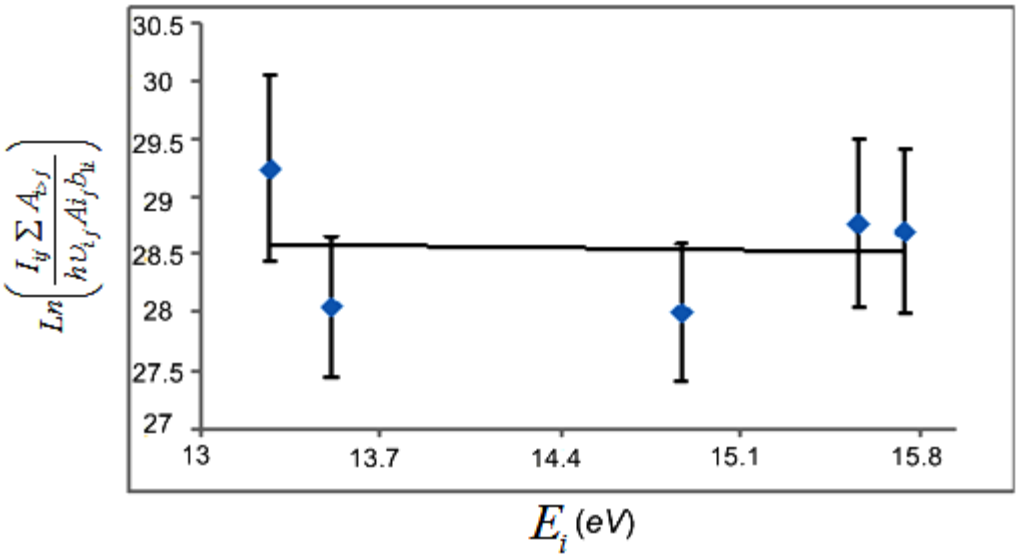

Figure 5-8 Modified Boltzmann plot for determination of electron temperature

T_e can be extracted from the slope of such modified Boltzmann plot. It is worth noting that strong emission lines are originated from a relatively small energy band and spectroscopic energy system which limits the energy difference between upper energy levels considered. This increases the errors in the determination of electron temperature. To avoid this, lines were chosen such that the gap between upper energy levels is greatest but at the cost of lower intensity signal. The data in the modified Boltzmann plot shows some inconsistency. Therefore error bars of $\pm$ 20% have been assigned to derive the electron temperature which is in agreement with (Gordillo-Vázquez et al., 2006). The line produces a slope of -7.0 x 10^{-5} which is equivalent to $\frac{-0.625}{T_e}$ which produces T_e = 8928.5 K = 7.7 x 10^{-1} $\pm$ 1.5 x 10^{-1} eV .

5.2.5 Debye length

The Debye length is the characteristic length scale in plasma. This parameter serves as a length scale to shield the Coulomb potential of individual charged particle when they collide. It can be calculated using equations (2-8) and (2-9). In the current study, the Debye length was calculated to be 3.24 µm which is in general agreement with (Bellan, 2006).

5.2.6 Excitation temperature

OES based temperature measurements such as T_e, T_{exc}, T_{vib} and T_{rot} which are derived from the emission spectrum, are based on the relative intensities of identical species at different excitation levels. These measurements can also be based on those of the ions of neighbouring ionisation stages on the relative continuum intensities and on the relative absolute intensities among others. T_{exc} depicts the population of the excited atomic states assuming that the population of excited atomic states follows Boltzmann distribution. It is a measure of the excitation capacity of atoms within the plasma. T_{exc} was measured in non-LTE conditions by the Boltzmann plot method (Pacheco et al., 2008). This method is considered good because it does not require a standard source of calibration, however, the peaks chosen to calculate T_{exc} should be selected carefully such that they cover the maximum possible range of EEDF to increase the accuracy. The Boltzmann plot method is expressed by the following equation (Ni et al., 2006, Pacheco et al., 2008).

$$\ln\left(\frac{I_{ij}\lambda_{ij}}{g_i A_{ij}}\right) = \ln K - \frac{E_i}{k_b T_{exc}} \qquad (5\text{-}2)$$

Where I_{ij} is the line intensity, λ_{ij} is the wave length, g_i is the statistical weight of the upper atomic state, A_{ij} is the transition probability, E_i is the excitation energy, k_b is the Boltzmann constant and K is a constant for all considered lines. The data used to obtain the Boltzmann plot has been taken from National Institute of Standards and Technology (NIST, 2012) and is presented in Rehman et al. (2012). A plot is drawn between $\ln\left(\frac{I_{ij}\lambda_{ij}}{g_i A_{ij}}\right)$ and E_i which produces a slope $(1/k_b T_{exc})$ which is equal to -0.625/T_{exc} and inversely proportional to the excitation temperature. **Figure 5-9** shows the typical Boltzmann plot which produced a slope of -1.0 x 10^{-4} hence producing T_{exc} = 6250 K= 5.3 x $10^{-1} \pm$ 6.4 x 10^{-2} eV .

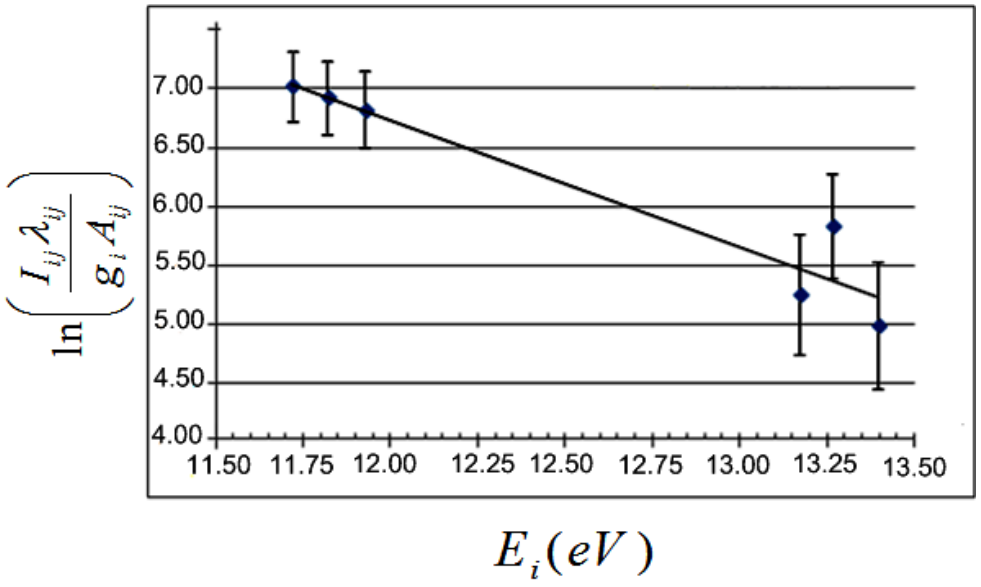

Figure 5-9 Boltzmann plot to determine excitation temperature

5.2.7 Rotational temperature

T_{rot} depicts the population of the rotational levels in molecular species present in discharge zone (Valdivia-Barrientos et al., 2008). Rotational temperature is considered to be the closest to the gas temperature as the rotational relaxation is fast at atmospheric pressure (Laux et al., 2003). The Boltzmann plot method could be applied in LTE plasma and also in non-LTE plasma to calculate rotational temperature, provided the pressure is sufficiently high (as in the current study) so that the collisional frequency of molecules is higher than that of the radioactive decay probability of excited state under consideration, which leads towards thermal equilibration of the state population (Kado et al., 2004). T_{rot} is measured by using rotational fine structure of electronic band such as $B^2\sum_u^+ - X^2\sum_g^+$, first negative system of N_2^+, and $A^2\sum^+ - X^2\prod$ for OH. The intensity of such rotational lines for a transition $(J'-J'')$, is expressed as a function of oscillator strength S_j or the transition probability, A_j:

$$I = DA_j h\upsilon \exp\left[\frac{-B_v hcJ'(J'+1)}{k_b T_{rot}}\right] \quad (5\text{-}3)$$

$$I = DS_j \upsilon^4 \exp\left[\frac{-B_v hcJ'(J'+1)}{k_b T_{rot}}\right] \quad (5\text{-}4)$$

Where, h is the Planck's constant, k_b is Boltzmann constant, B_v is the rotational constant which belongs to vibrational quantum number v and υ is the wave number associated to the emission line. Where, $S_j = K'+K''+1$. The practical values of S_j and $K'+K''+1$ are usually articulated as a function of the quantum number K'' (assigned to lower state). For N_2^+, two branches could be used, the P and the R branch (Hill, 2006). For the P branch it is expressed as $K' = K''-1$ and $K' = K''+1$ for the R branch. T_{rot}, can be calculated by plotting the intensity of the given line versus K'' (Hill, 2006).

For the P branch, $$Ln\frac{I}{2K''} = C - \frac{Bhc}{k_b T_{rot}} K''(K''-1) \quad (5\text{-}5)$$

For the R branch, $$Ln\frac{I}{2(K''+1)} = C - \frac{Bhc}{k_b T_{rot}} (K''+1)(K''+2) \quad (5\text{-}6)$$

Where C is a constant. The slope of such plot is equal to $\frac{-Bhc}{k_b T_{rot}}$ which is equal to $\frac{-2.983}{T_{rot}}$, thus T_{rot} can be estimated. The corresponding values of oscillator strength were taken from (Hill, 2006) and the R branch was used to calculate rotational temperature from first negative system of N_2^+. Optical emission spectrum of the first negative system of N_2^+ is shown in **Figure 5-10**. The data used for the calculation of T_{rot} has been taken from Hill (2006) and is presented in Rehman et al. (2012). **Figure 5-11** shows the graph between $(K''+1)(K''+2)$ and $Ln\left[\frac{I}{2(K''+1)}\right]$ which produced a slope of -4.0 x 10^{-3} resulting in 745.75 K = 6.4 x 10^{-2} ± 2.5 x 10^{-3} eV .

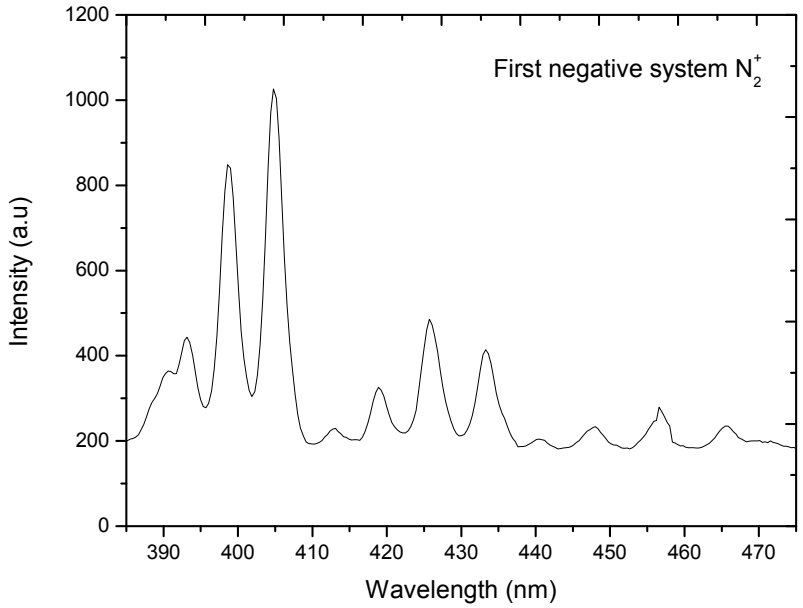

Figure 5-10 Optical emission spectrum of first negative system of N_2^+

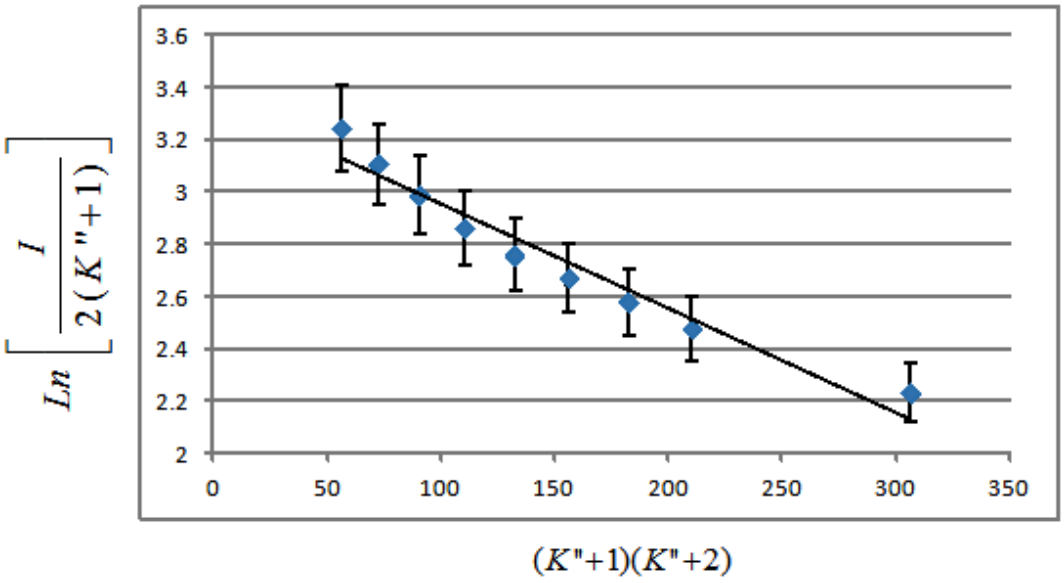

Figure 5-11 Linear fit between (K"+1)(K"+2) and Ln (1/2(K"+1)) to calculate rotational temperature by N_2^+ first negative system

The OH spectra could also be used for the determination of T_{rot}. However, it is more complex having five main branches O, P, Q, R and S. The whole band of $OH(A-X)$ transition could be used for determination of rotational temperature or more easily by utilising relative intensities of two groups of lines relating to the R and P branches

(Laux et al., 2003). Again, equation (5-7) can be used and T_{rot} can be calculated by plotting $Log\,(I\lambda / A)$ versus E_i.

$$Log(I\lambda / A) = \frac{-E_i}{kT_{rot}} + D \qquad (5\text{-}7)$$

Where D is a constant. The slope of such plot is given as $-0.625/T_{rot}$. The corresponding values of A and E_i was taken from Hill (2006) and presented in Rehman et al. (2012). **Figure 5-12** shows the plot of equation (5-7). The estimated value of the slope of line is -8x10^{-4} which produced T_{rot} = 781.2K = 6.7 x 10^{-2} ± 6.3x 10^{-3} eV.

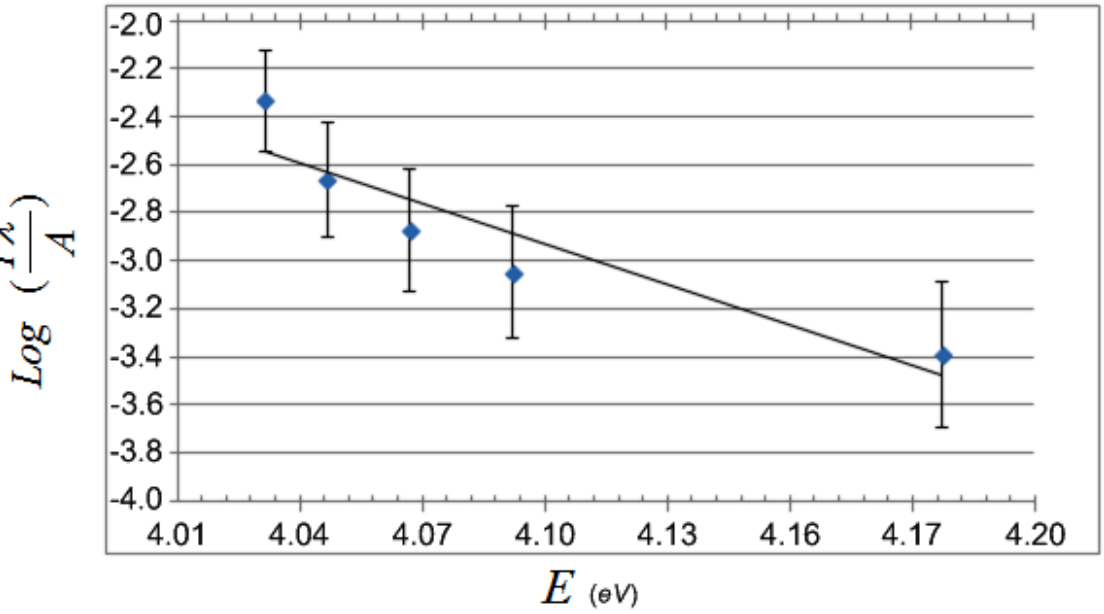

Figure 5-12 Linear fit to calculate the rotational temperature of OH

5.2.8 Vibrational temperature

The molecular band of second positive system of N_2 and first negative system of molecular ion of nitrogen N_2^+ can be utilised to calculate vibrational temperature T_{vib}. In the current study, T_{vib} is calculated using the second positive system of N_2 by considering nonthermal equilibrium conditions (Laux, 2002). The method to obtain T_{vib} is based on the emission process; $N_2^+(B^2\sum_u^+) \rightarrow (X^2\sum_g^+) + hv$ where the mechanism for the production of molecular ions in the state of $N_2^+(X^2\sum_g^+)$ is direct

ionisation by electronic impact of fundamental state $N_2(X^1\sum_g^+)$. Plotting a graph between $\ln\left[\frac{I_{v',v''}\lambda_{v',v''}}{A_{v',v''}hc}\right]$ against the vibrational term $G_{(v)}$ produces a slope of $-\frac{hc}{k_bT_{vib}}$, where $I_{v',v''}$ is intensity of the vibrational band (v',v''), $\lambda_{v',v''}$ is the corresponding wavelength, $A_{v',v''}$ is the Einstein's coefficient for spontaneous emission, $G_{(v)}$ is vibrational term, h is Planck's constant and c is the speed of light. This slope could be utilised to calculate T_{vib}. The data to calculate T_{vib} has been taken from (Lozano-Parada, 2007) and is presented in Rehman et al., (2012) . **Figure 5-13** shows the plot between $\ln\left[\frac{I_{v',v''}\lambda_{v',v''}}{A_{v',v''}hc}\right]$ and $G_{(v)}$ producing a slope of -2 x 10^{-5}, hence

$$-2.0\times10^{-5}=\frac{hc}{k_bT_{vib}}\Rightarrow T_{vib}\approx 720.2K = 6.20\,\text{x}\,10\text{-}2\;\;1.0\,\text{x}10\text{-}3\,.$$

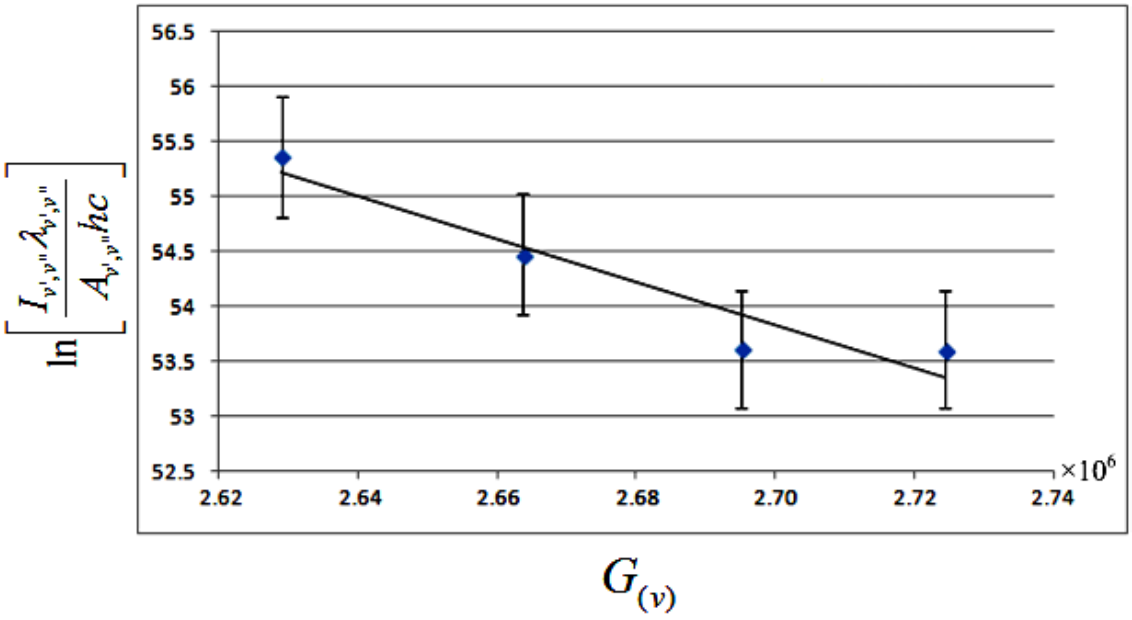

Figure 5-13 A linear fit to calculate vibrational temperature from N_2^+ second positive system

The results of the temperature measurement are summarised in **Table 5-1**. T_{rot} measured using the first positive systems of N_2 and OH band only differs by 4.5%.

Table 5-1 Summary of plasma characterization

Electron Density	1.765×10^{17} m^{-3}	
Debye length	3.24 (μm)	
Temperature	**K**	***eV***
Electron	8928.57	$7.7 \times 10^{-1} \pm 1.5 \times 10^{-1}$
Excitation	6250	$5.3 \times 10^{-1} \pm 6.4 \times 10^{-2}$
Vibrational	720.217	$6.2 \times 10^{-2} \pm 1 \times 10^{-3}$
Rotational (N_2^+ based) (OH based)	 745.75 781.21	 $6.4 \times 10^{-2} \pm 2.5 \times 10^{-3}$ $6.7 \times 10^{-2} \pm 6.3 \times 10^{-3}$

The value of the vibrational temperature lies between the gas temperature and the electron temperature (Stoffels et al., 2002). Often the gas temperature could be inferred from the rotational temperature of the excited molecules which have the time to equilibrate with the gas molecules of plasma before photon emission, hence their rotational distribution could reflect that of the gas molecules in the plasma (Masoud et al., 2005). However, it is interesting to note that, in the current study the rotational temperature is found to be slightly higher than the vibrational temperature. There could be a couple of explanations for this anomalous behaviour. Firstly, in the current study the plasma has been generated at atmospheric pressure. It is known that rotational temperature remains constant with the increase in the pressure, however, vibrational temperature is found to decrease with increasing pressure (Masoud et al., 2005, Kitamura et al., 2005). Secondly, the presence of even a small amount of oxygen in the plasma is known to lower the vibrational temperature at any point in the discharge zone. This could be explained on the basis of higher rate coefficients of relaxation between vibrational and rotational/translational motions of oxygen (O_2) than nitrogen (Kitamura et al., 2005). Since, in the current study O_2 has been evidently generated, it could possibly decrease the vibrational temperature. Both factors of having plasma at atmospheric pressure and generation of oxygen within plasma zone could explain this anomalous behaviour. Also, water vapours used as feedstock could give extra energy to the gas phase molecules in the plasma zone thereby increasing the rotational temperature.

5.2.9 Energy yield and cost

The amount of water vapour decomposed by plasmolysis was found by connecting two condensers to the outlet of the reactor. A second order central composite rotatable design was applied to monitor water vapour decomposition rate% (Y) as objective function. This was done to establish a statistical model correlating the water vapour decomposition rate with steam flow rate and argon flow rate. Steam flow rate and Ar flow rate were studied as two parameters affecting the water vapour decomposition rate according to the following model (Cochran and Cox, 1992);

$$Y = B_o + B_1 x_1 + B_2 x_2 + B_{11} x_1^2 + B_{22} x_2^2 + B_{12} x_1 x_2 \quad (5\text{-}8)$$

Where *Y* is the objective function (decomposition rate of water vapours) B_o, B_1, B_2, B_3, B_4 and B_5 are the constants, (x_1) and (x_2) are the code value for steam flow rate (ml min^{-1}) and argon flow rate (ml min^{-1}). These code values are tested in the range of (x_1 = -1.414, -1, 0, +1, +1.414) which is equivalent to the (1, 2, 3, 4, 5 ml min^{-1}) for steam and (x_2 = 10, 20, 30, 40, 50 ml min^{-1}) for argon. The data was fitted in the model equation (5-8) using multiple stepwise regression analysis which gave the following empirical model. The average absolute error of obtained model was estimated to be 1.32%.

$$Y = 9.64 - 0.16 x_1 + 0.28 x_2 - 0.51 x_1^2 - 0.11 x_2^2 + -0.025 x_1 x_2 \quad (5\text{-}9)$$

It was found that under current experimental conditions, the water vapour decomposition rate was decreased when steam flow rate was increased higher than 2 ml min^{-1}. However, an increase in the Ar flow rate enhances the decomposition rate and a maximum decomposition rate of 10% was found with 2 ml min^{-1} of steam and 50 ml min^{-1} of Ar.

Concentration of H_2O_2 was measured by a colorimetric method (Eisenberg, 1943) which is based on a specific reaction between H_2O_2 and titanyl ions giving stable yellow coloured complex of pertitanic acid which gives an absorption peak at $\lambda = 410$ nm.

$$Ti_4^+ + H_2O_2 + 2H_2O \longrightarrow TiO_2 + H_2O_2 + 4H^+ \quad (5\text{-}10)$$

A Hach Lange-DR 2800 spectrophotometer was used to determine the absorption of samples at 410 nm. Solution of a known concentration of titanium sulphate was added in the liquid condensate collected at the end of the experiment. There was no change in colour observed which showed there is no pertitanic acid and hence no H_2O_2 formation. **Figure 5-14 (A)** shows no yellow coloration while **Figure 5-14 (B)** shows the yellow formation of pertitanic acid when titanium sulphate was added to the standard solution of H_2O_2. The foggy colour in **Figure 5-14 (A)** may have been formed due to the dilution of titanium sulphate in the sample which is similar to colour change in **Figure 5-14 (C)** where titanium sulphate was dissolved in demineralised water. From the experiment it was clear that there was no H_2O_2 formation in the water vapour plasmolysis. Similar results have been observed by Givotov et al. (1981) where the only products of water vapour plasmolysis were H_2 and O_2 in stoichiometric ratios.

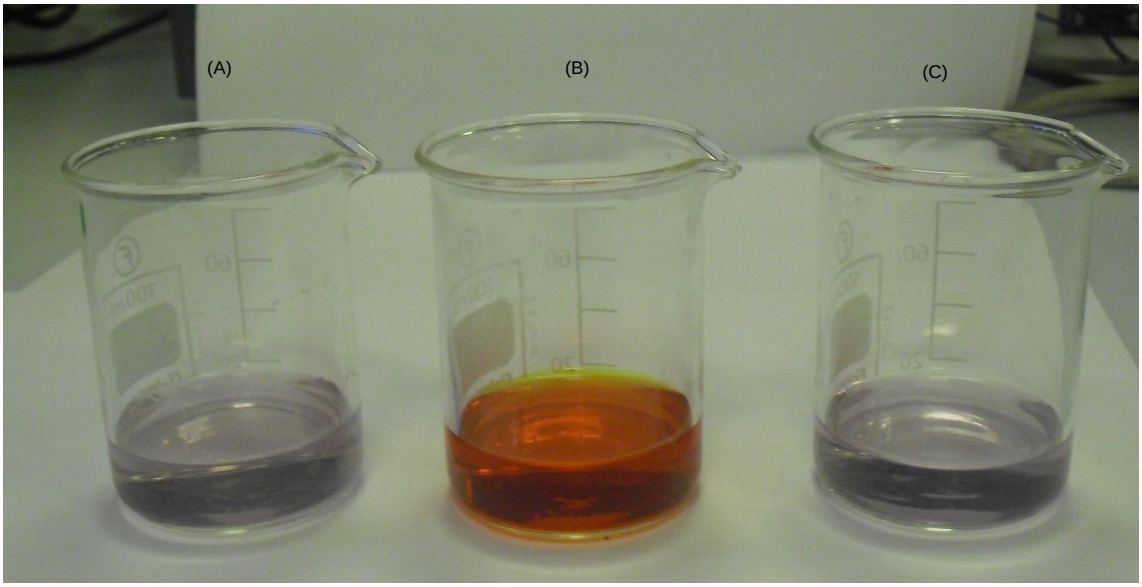

Figure 5-14 Formation of Pertitanic acid with addition of titanium sulphate in the sample (A) Demineralised water, (B) Standard solution (H_2O_2 0.0255 (Vol.%) and (C) steam condensate after steam plasmolysis

Both the vapour phase and liquid phase were analysed by GC. Liquid samples were collected at the end of the experiment and were analysed by head space analysis. The bottles containing liquid sample were kept in a water bath at 70 ^{o}C for half an hour before taking the sample from the bottle head space. A 10 ml standard plastic syringe was used to withdraw the samples from the head space of the bottle and injected into the GC, Varion cp3800, fitted with thermal conductivity detector (TCD), 2m HAYESEP C.

Argon gas was used as carrier gas. There was no peak observed for hydrogen or oxygen. Hence hydrogen and oxygen produced from the experiment were not dissolved in the water vapour condensate, i.e. negligible as the solubility of both oxygen and hydrogen in water at 100 ^{o}C is negligible.

It must be noted that the internal volume of the reactor (5.61 x 10^{-4} litres) is very small. Attaching any container directly at the outlet of the reactor is likely to increase the pressure inside the reactor and hence could change the kinetics of the plasmolysis. Considering this, gaseous samples were collected in number of ways. The steam leaving the reactor was condensed by the attaching two condensers (in series) with the outlet of plasma micro-reactor using flexible tubing. The gaseous (vapour phase) sample coming out of the outlet of the second condenser was calculated by attaching standard gas sampling bags. Samples collected were fed to the above mentioned GC. GC results showed significantly low percentages of H_2 (0.2306%) and O_2 (0.5195%). However, when the samples were withdrawn from top of the condensers (near the inlet), the oxygen concentration was raised to 5.6662% and hydrogen was 0.6251%. This could be explained on the availability of a large volume in the condensers section. Since there is a large volume available in condensers for the gases to occupy, they do not enter the gas sampling bag given the relative smallness of the inlet orifice. Also, the bag was unable to confine hydrogen, as shown by the continuous decrease in hydrogen content when samples from the same bag were analysed over time interval of half an hour. One of the reasons for hydrogen concentration being so low is its relatively low density. As it is lightest amongst the other product gases (O_2 and Ar), the analysis suggests, it might not flow with them at the same rate and would like to stay on the top parts of the condensers.

Bags (SKC^{TM} bags) which could contain hydrogen for longer periods of time were then used to collect gaseous samples. Bags were attached directly at the outlet of the plasma micro-reactor. This was done to collect all the gases and condense steam directly in the bag to eliminate the possibility of hydrogen or oxygen staying behind in the condenser section. The bag was submerged in a cold trap (thermal box containing ice, water and salt) to avoid overheating and help condensing the steam. The experiment was run for 3 minutes with 2 ml/min of steam and 50 ml/min of argon gas.

The gas samples from the bag were withdrawn and fed to GC. The percentage of oxygen was dropped 0.560%, however percentage of hydrogen remained similar. The bag has a small orifice as shown in **Figure 5-15** and only one turn opening was advised by the company so it leaves very little space for the gases to leave the reactor and fill the bag.

Figure 5-15 SKC-H_2 storage bad and inlet orifice

This smaller orifice has created pressure, by hindering the gas flow, inside the reactor which is likely to change the whole kinetics of reaction and hence percentage of oxygen was found to be very low. A sound of pressure relief could also be heard when SKC^{TM} bags were detached from the reactor at the end of the experiment. The other possibility, of the reduced percentage of the oxygen, could be the degree to which the inner surface of the bag is inert for oxygen. To monitor the inertness of the bag, it was filled with standard mixture (1% H_2, 5% O_2 and 94% Ar) and left for a day. GC results showed no decrease in the percentage of oxygen when analysed after 1 day. Repetition of the experiment with the bag three times showed similar results.

Considering the build-up of pressure in the reactor, a long glass tube (1.5"x 15") was used as a collection vessel. A rubber bung was used to seal the tube with a 8 mm hole in it serving as inlet. The tube was submerged in cold trap for condensing the steam. Experiment was run for 3 minutes. GC results showed 19.0532% oxygen, though hydrogen was dropped to 0.0799%. Experiment was repeated and similar results were achieved. Since, the size of the inlet of the glass tube was almost same to the outer diameter of reactor, gases would have flown easily without building any pressure in

the plasma micro-reactor. That may explain the higher percentage of oxygen obtained. However, the glass tube had a fixed volume and was air tight. It was difficult to withdraw samples from it. This led to the use of glass syringe which could be connected to the reactor directly and is likely to have little friction between its inner surface of the syringe and its plunger so it was thought it would not create any pressure inside the reactor. Two glass syringes of 20 ml and 100 ml were used to collect the gases. The experiment was finished when the glass syringe was full (15 seconds for 20 ml and 52 seconds for 100 ml). The gases did not fill very smoothly in the syringes; they were rather filled in time intervals creating pressure in the reactor. The GC results showed an average of 14.6500% oxygen and 0.3080% hydrogen. The percent of hydrogen and oxygen and overall volume gases collected is dependent on the methodology of collecting gases and hence it is difficult to quantitatively analyse the experiments. Snapshots of the results obtained when gas was collected by standard gas collection bags are shown in Appendix II in **Figure 7-5**, when sample was taken from top of the condenser in **Figure 7-6**, when the sample was collected in glass tube in **Figure 7-7** and when sample was collected in glass syringe in **Figure 7-8**.

For inline detection, the reactor was connected to GC through flexible tubing. The GC used was a Perkin Elmer Auto-system XL while the column is an RT-M sieve 5A (30m x 0.53mm id) by Restek. N_2 was used as a carrier gas meaning O_2 could not be detected due to its thermal conductivity being almost identical to N_2. However, the sensitivity towards H_2 became greater because the difference between thermal conductivity of carrier gas (N_2) and sample gas (H_2) was greater (Kirkpatrick and Locke, 2005). Calibration was done for 1%, 5%, 10% and 20% of hydrogen in N_2. The GC results showed about 0.9% of H_2 with no O_2 as stated above.

The GC analysis has shown different percentages of hydrogen and oxygen according to the different gas collection methods. It is suggested that different methods create different level of pressures inside the reactor which changes the kinetics and hence different percentages of hydrogen and oxygen shown by GC. Stoichiometrically, there should be half a mole of oxygen per every mole of hydrogen produced and hence similar volumetric ratios. The stoichiometric ratios between hydrogen and oxygen shown by GC analysis do not match with the theory. It could be explained on the basis

that hydrogen is produced in the experiments however, since H_2 is the smallest size molecule, it might have escaped though the materials (such as tubes and bags for sample collection) while collecting gaseous samples. This phenomenon is known as hydrogen embrittlement and causes reduction in the strength and ductility of materials (Cotterill, 1961, Oriani, 1978). Due to high temperature and pressure involved in the experiments, a significant amount of hydrogen gas produced might have escaped while collecting the sample. It is noted that hydrogen generation studies such as (Porter et al., 2009) and (Burlica et al., 2010) have successfully quantified hydrogen production by GC analysis. However their studies involved liquid water hence less pressure to deal with. Considering the above discussion, hydrogen was quantified using indirect methods, i.e. amount of hydrogen produced was determined by monitoring the decomposition rate of water vapours.

To find the water vapour decomposition rate the plasma was ignited with water vapour without Ar. The decomposition rate could be calculated by monitoring the difference of volume collected with and without plasma ignition over a total period of operational time.

$$Decomposition\ rate\ (\%) = \frac{Flow\ rate\ of\ \ water\ \ with\ \ plasma\ switched\ \ on}{Flow\ rate\ of\ \ water\ \ without\ \ plasma} \times 100 \qquad (5\text{-}11)$$

In DBDs the electrical power consumed (P) in plasma is different from the total power drawn from the mains (P_{total}). This is because the voltage and current are not in phase in the capacitive systems. The voltage is lagged the current by the phase angle (Zito et al., 2010). The power consumed in DBDs could be calculated by voltage-charge-cyclograms (Lissajous Figure) (Manley, 1943, Kriegseis et al., 2011) or from the knowledge of phase angle (Kostov et al., 2009). In a typical DBD configuration, for one oscillation period, the mean electric power could be calculated by using equations (5-12) to (5-14) (Kostov et al., 2009);

$$P = VI\cos\varphi \qquad (5\text{-}12)$$

$$I = \frac{V}{Z} \qquad (5\text{-}13)$$

$$P = \frac{1}{2}\frac{V^2}{|Z|}\cos\varphi \tag{5-14}$$

Where, *V* is the amplitude of ac voltage, *Z* is the impedance, φ is the phase angle between voltage and current. The impedance of DBDs could be calculated by the following relation:

$$Z = \frac{R}{(1+\omega^2 C_G^2 R^2)} - j\left(\frac{2}{\omega C_D} + \frac{\omega C_G R^2}{1+\omega^2 C_G^2 R^2}\right) \tag{5-15}$$

Where, *j* represents the imaginary part of the impedance, $C_D = \frac{k\varepsilon_0 A}{d}$ is the capacitance of the dielectric layer and $C_G = \frac{\varepsilon_0 A}{x}$ is the capacitance of the air gap *R* and is the equivalent resistance of the DBD discharge, ω is angular frequency, *A* is the electrode area, *d* is the thickness of dielectric layer, *k* is the dielectric constant and *x* is the discharge gap width.

Although the power consumed in the plasma is less than the total power, nevertheless, one has to pay for the total power utilised in the process. The total power (P_{total}) was estimated from the peak values of current and voltage.

$$P_{total} = V_{peak} \times I_{peak} \tag{5-16}$$

Considering the results from the statistical model (as discussed above), the water vapour flow rate was set to be 2 ml min^{-1} which produced a decomposition rate of 5%. Cost and energy yield have been calculated considering 5% decomposition rate of water vapour plasma (2 ml min^{-1}) and 10% with water vapours (2 ml min^{-1}) and argon (50 ml min^{-1}) plasma. The amount of hydrogen produced was calculated stoichiometrically by considering 5% decomposition in steam plasmolysis and 10% decomposition in steam and Ar plasmolysis. The power is measured to be 3.960 KJ min^{-1} (4 x 10^3 V x 16.5x10^{-3} A). The price (7.3 Pence kWh^{-1}) is taken under the category of "all consumers' average" from Quarterly Energy Prices (Department of Energy & Climate, 2012). The energy yield (g kWh^{-1}) and the cost of H_2 for hydrogen production (m^3 of H_2 produced/kWh and £ kWh^{-1} energy produced by H_2) is given in **Table 5-2**. It

can be seen from **Table 5-2** that in the presence of Ar, decomposition rate is doubled. The increase in the decomposition rate by addition of Ar has been observed by Burlica et al. (2010) as well.

Table 5-2 Amount of the H_2 produced, Energy yield and price of H_2 produced

Feed	Decomposition rate (%)	Amount of H_2 produced (gm/min)	Price (m^3 of H_2/kWh)	Price (£/kWh)
Steam	5	0.011	0.153	0.18
Argon + steam	10	0.022	0.306	0.09

The lower efficiency in case of steam plasmolysis, as given **Table 5-2** has been witnessed in a previous study as well (Givotov et al., 1981). The lower efficiency, 40% as compared to predicted efficiencies of 50-70%, in the work of Givotov et al, (1981) has been thought to be because of the ion-molecule reaction between **H_2O** and **H^-** ion produced by dissociative attachment of electron reaction, essential for a low degree of ionisation (as discussed in chapter 2).

$$H_2O + H^- \longrightarrow H_2 + OH^- \quad (5\text{-}17)$$

However, the efficiency was hypothesised to be 80% by the use of CO_2 which could work as catalyst in water vapour dissociation in a double stage plasma reactor. A similar catalytic affect could be achieved by using Ar. This catalytic affect is attributed to collisions of the Ar excited species (Ar^3P) with water molecule. Ar (^3P) is produced by electron impact collision with Ar atoms. Ar (^3P), hence produced, collides with water molecules as shown in reactions (5-18) and (5-19). These collisions lead to efficient dissociative excitation of the water molecules (Motret et al., 2000), which consequently produced extra OH radicals as demonstrated by the increased intensity of OH emission lines (302-317 nm) in **Figure 5-6**.

$$Ar + e \longrightarrow Ar(^3P) + e \quad (5\text{-}18)$$

$$Ar(^3P) + H_2O \longrightarrow H + OH + Ar \quad (5\text{-}19)$$

Energy efficiency of the process is defined as ratio of amount of energy produced by unit of fuel to the amount of energy required to produce the fuel.

$$\text{Energy efficiency} = \frac{\textit{Energy produced by unit amount of } H_2}{\textit{Energy consumed to produce unit amount of } H_2} \times 100 \quad (5\text{-}20)$$

The other type of efficiency usually defined as the thermodynamic efficiency which is the ratio of the theoretical amount of energy to produce a unit amount of fuel to the experimental amount of energy spent.

$$\text{Thermodynamic efficiency} = \frac{\textit{Theoretical amount of energy required to break } H_2O}{\textit{Experimental amount of energy used to break } H_2O} \times 100 \quad (5\text{-}21)$$

Considering 1.4 x 10^5 kJ/kg as gross calorific value (GCV) of H_2, energy efficiency was calculated by taking the ratio of amount of heat that would be generated by H_2 produced in the experiment to the amount of heat which was used to produce H_2. Experimental amount of energy used to break H_2O was calculated from the total power consumed in the process. The calculated energy yield and thermodynamic efficiency is presented in **Table 5-3**.

Table 5-3 Energy yield, energy efficiency and thermodynamic efficiency of H_2 production by plasmolysis

Feed	Energy Yield (g/kWh)	Energy Efficiency (%)	Thermodynamic Efficiency (%)
Steam	10	39.39	39.62
Argon + steam	20	78.77	79.16

Comparison of energy yields for hydrogen production for different types of plasma processes and other hydrogen producing technologies is given in **Table 5-4**. In the current study, the energy yield of water vapour plasmolysis in DBD-corona hybrid reactor is equal to the microwave discharge. It is worth noting that the energy yield of water vapour plasmolysis with Ar gas is equal to electrolysis. Ar used in the plasmolysis could be recycled. The recycling of Ar would depend on the use of hydrogen. If hydrogen is to be used on a plant as an intermediate energy storage then fuel cell conversion will result in the Ar in the off-gases along with water, hence naturally separated and recycled. If the hydrogen is to be used as a chemical intermediary, say for reducing biofuels to drop-in fuels, then if it is a liquid drop-in fuel, the Ar will stay in the gaseous phase and again recycled automatically.

Table 5-4 Energy yield for kinetic and thermodynamic limits for different types of plasmas processes and other technologies producing H_2 (Burlica et al., 2010)

Method	H_2 (g/kWh)	Reference
Thermodynamic limit	25-30	(Fridman, 2008)
Kinetic Limit		
Absolute Quenching	5.2	-
Ideal Quenching	10	-
Super ideal quenching	13	-
Electrolysis	20	(Burlica et al., 2010)
	14-18	-
Photocatalysis	0.01	-
Microwave plasma	10	(Fridman, 2008)
Corona	2	(Burlica et al., 2010)
AC gliding arc	1.3	-
Gliding arc spray (Ar as carrier gas)	13	-
DBD-Corona hybrid reactor		
Steam only	10	Current study
Steam and Ar	20	Current study (Best case)

The other high energy yield process is the gliding arc spray using Ar as a carrier gas (Burlica et al., 2010). The authors have used water droplets as feedstock. However, in the current study, low quality steam is used instead. In the current study, water vapour is produced by utilisation of waste heat which is widely available in the chemical engineering industries and power plants. Usually, the exhaust temperature from most industrial processes and power plants are lower than 370 ^{o}C. Recovering this heat by usual methods of waste heat recovery is economically infeasible and releasing this heat into the atmosphere causes heat pollution (Wei et al., 2007). Such heat could easily be recovered to produce low quality steam (Approx. 1 atm and 100 ^{o}C) thus increasing the process efficiency and preventing the heat pollution. This low quality steam could then be converted to hydrogen by plasmolysis.

$$H_2O \longrightarrow H_2 + \frac{1}{2} O_2 \qquad (5\text{-}22)$$

The thermodynamic limit for reaction-1 given in equation (5-22) is 28.7 g kWh^{-1} (2.6 *eV* molecule^{-1}) with kinetic limit of absolute quenching, ideal quenching and super ideal quenching are 5.2, 10, and 13 g kWh^{-1} respectively (Fridman, 2008). It is interesting to note that the hydrogen energy yield in the plasmolysis of water vapours with Ar has

exceeded the kinetic limits. This is possible because the theoretical kinetic limit of quenching process given in **Table 5-4** is for thermal plasmas (Fridman, 2008) which is different from the current plasmolysis conditions (non-thermal plasmolysis at atmospheric pressure) (Burlica et al., 2010). The logical explanation of high energy yield and higher efficiencies in the current study is the inclusion of latent heat of vaporisation (2257 kJ/kg) by the utilisation of the waste heat and relatively smaller flow channel which enables water vapours to breakdown at relatively low power. It is worth noting that the flow channel is 1.24 mm, however as mentioned earlier, (Lozano-Parada and Zimmerman, 2010) have reported production of ozone at 170V AC with a micro-channel plasma reactor of 800 μm diameter. Therefore, further reduction in the power requirement can be expected with the flow channel in micrometer range. This is because of the fact that only a small potential difference is required to maintain high electric field strength across the channel as there exists an inverse relation between electric field strength and discharge gap. Miniaturising plasma reactors also enhances the control over the plasma process because the use of microfluidics can tailor fluid dynamics (Zimmerman, 2011) and hence it can be concluded that further improvement in the efficiency is possible by better design and optimisation of reaction conditions.

It is worth nothing here that unlike large-scale plasma reactors, power supplies for such plasma micro-reactors are miniaturised as well and available commercially at very low price (~$10). These plasma micro-reactors can also be ignited with battery sources (Zhu et al., 2006). These power supplies can be coupled with such plasma micro-reactors to produce hydrogen locally instead of producing hydrogen at large scale and distributing it to consumers. Hydrogen can be produced and delivered to the fuel cell or combustor instantaneously for power generation. This becomes especially important for the use of hydrogen as transport fuel. In light and heavy vehicles, this solves the “hydrogen storage issues” one of the biggest barriers faced by hydrogen economy (Ross, 2006).

5.2.10 Effect of Ar injection on kinetic model of hydrogen production

Addition of Ar has a catalytic effect on water vapour plasmolysis as noticed in the current study and elsewhere in literature (Burlica et al., 2010, Shirafuji et al., 2009). As discussed above this catalytic affect could be attributed to the basic chemistry shown in reactions (5-18) and (5-19). To see if the kinetic model developed in chapter 3 could predict the effect of argon injection or not, reactions (5-18) and (5-19) were added in the kinetic scheme given in chapter 3 and analysed with REL 3.5a. As the model was 0 dimensional, the ratio of the concentrations of water vapour and Ar was used to infer the ratio of their flow rates in the experiments. The concentration ratio between water vapour and Ar was varied between 1 and 10 such that the total pressure of feed remained at 1 atm as shown in **Figure 5-16.** Maintaining atmospheric pressure is important as this was originally used in kinetic modelling in chapter 3.

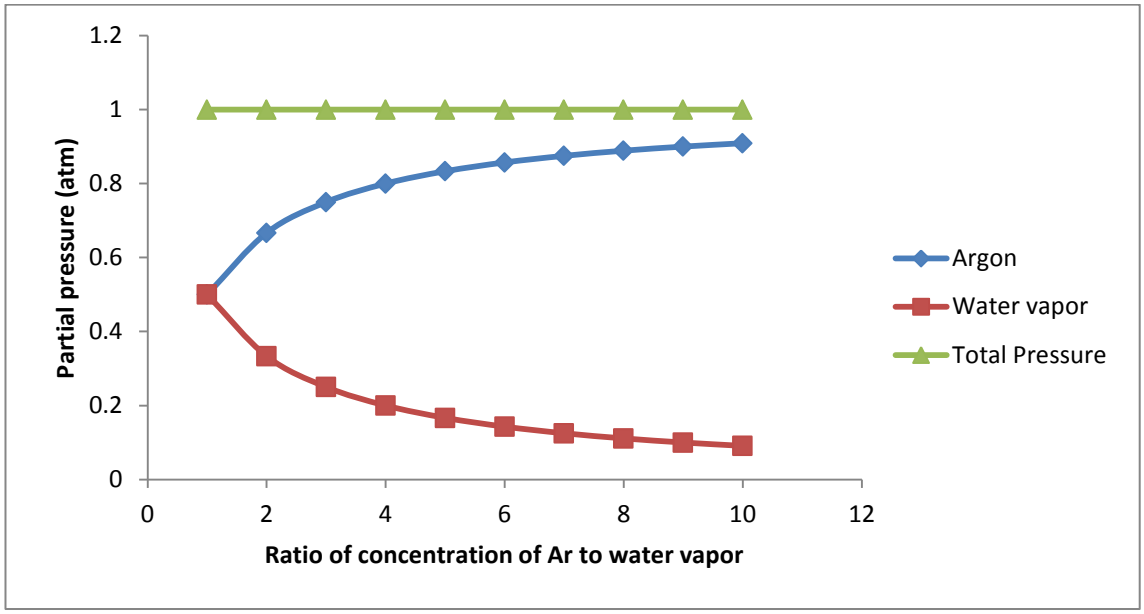

Figure 5-16 Variation in partial pressure of Ar and water vapours corresponding to concentration ratio

Figure 5-17 shows the results of adding Ar chemistry in the kinetic model. Along with other species, H_2, O_2, H_2O_2, OH, HO_2 and H, Ars (an excited species of Ar) can also be seen in **Figure 5-17**. However, the number density of Ars is very low (below $10^{18}m^{-3}$).

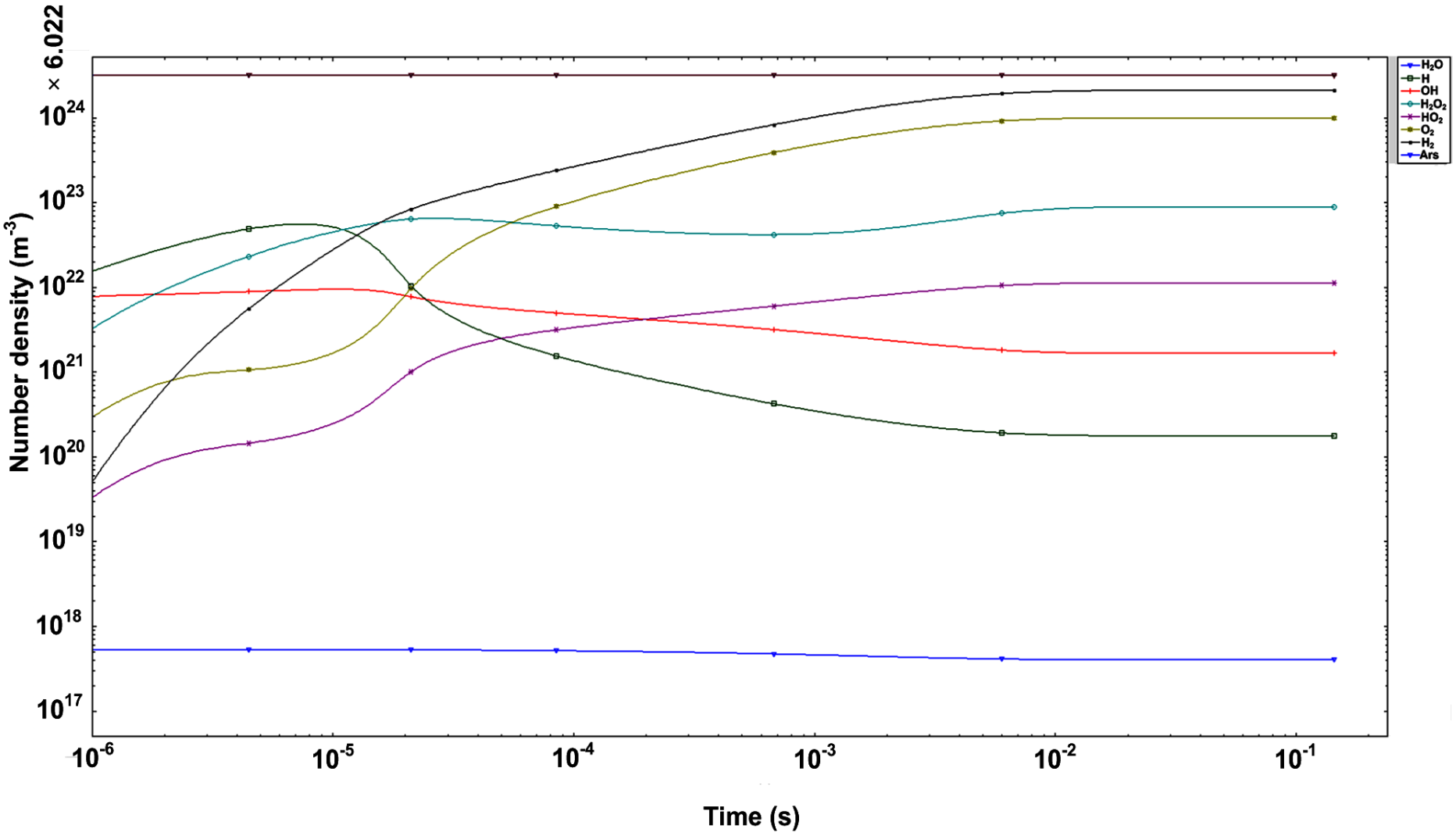

Figure 5-17 Number density of different species with Ar assisted water vapour plasmolysis at Ar to water concentration ratio of 10:1 at electron number density of 10^{21} m^{-3}

Figure 5-18 shows the number density of hydrogen with addition of Ar chemistry in the kinetic model. A gradual increase in the number density of hydrogen is observed with the increase in the ratio of concentration of Ar to water. However, a sharp change in the slope of line is expected at higher concentrations of Ar with the increase in hydrogen concentration becomes smaller and smaller before reaching to a steady state value. The trend seems to follow second order polynomial fit (Y = 3 x $10^{22}x^2$-2x10^9x + 1x10^{25}).

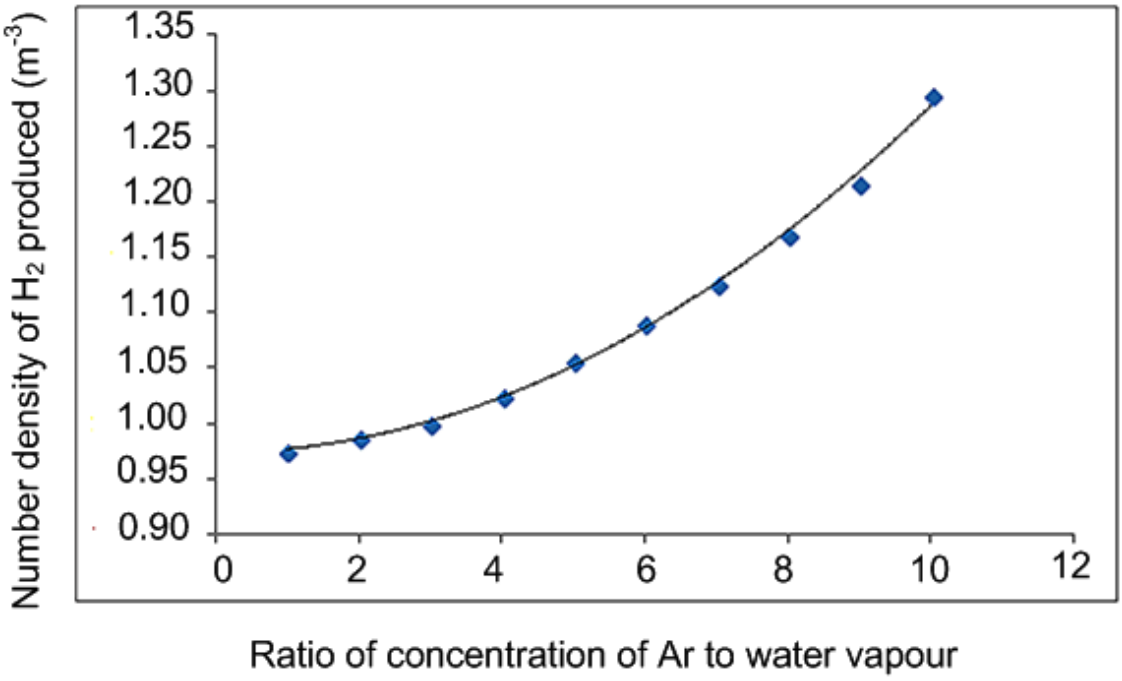

Figure 5-18 Predicted hydrogen concentration as a function of ratio of concentration of Ar and water vapours

5.2.11 Identification of optical emission peaks between 317-400nm

The following section is based on the discussion on the identity of optical emission peaks between 317-400 nm. As seen in **Figures 5-5, 5-6** and **5-7**, the optical emission peaks between 317-400 nm are always present irrespective of the gas or vapours in the flowing in the plasma micro-reactor. These optical emission peaks could simply because of the presence of N_2 in the system, interaction of the plasma with the glass surface or formation of NH in the system because of reaction between nitrogen present in the system and hydrogen formed in plasma micro-reactor. The NH radical in the mixture of N_2-H_2 glow discharge for metal surface nitriding has been shown to

form at 336 nm (Petitjean and Ricard, 1984). The NH signal dominated the spectrum at lower concentration of H_2 with highest signal achieved at about 10% concentration. Since in the current study, a similar/lower ratio between N_2 (if present in the system because of some leak) and H_2 could be expected, it may be possible that the peak at λ =336 nm in **Figures 5-5, 5-6** and **5-7** is because of formation of NH.

A test was devised to eliminate the interactions with the glass surface and remove N_2 from the system as discussed in section 4.2.1. Since no gas was flowing through the tube, nitrogen (from air) cannot enter in the system. The solubility of N_2 gas in water (0.02g of N_2/kg of H_2O) at room temperature is also very low so theoretically the amount of nitrogen present in the water is negligible. A plasma was ignited between the electrodes using 4kV at 37 kHz. and an optical emission spectra was recorded. A pathway was provided to push the water outside the tube when products (H_2 and O_2 etc.,) are formed due to water plasmolysis. Plasma generated, in this case, is localised in the inter-electrode gap thus avoiding the contact between plasma and glass surface. The optical emission spectrum is shown in **Figure 5-19**. It shows signal of H_α, H_β and *OH*. However, there are no optical emission peaks observed between 317-400 nm. There could be two reasons behind the disappearances of optical emission peaks between 317-400 nm. First, there was no contact of plasma with the glass surface and, secondly, the concentration of dissolved nitrogen in the water is negligible thus producing no signal.

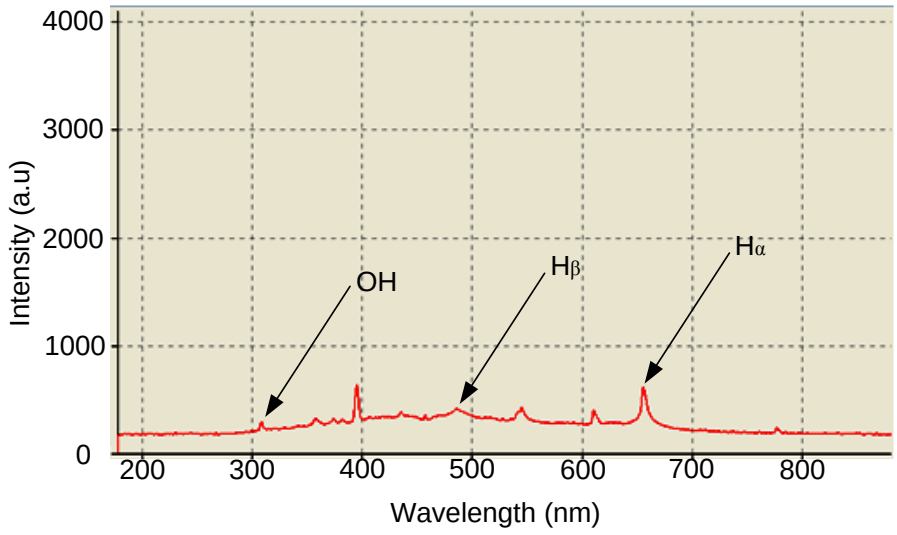

Figure 5-19 Optical emission spectrum of in-water plasma

In order to explore the possible changes on the glass layer properties upon being subjected to plasma, the contact angle of a demineralised water droplet was measured using the FTA tensiometer and applying the sessile drop technique. The contact angle of water on glass slides were measured before and after subjecting it to plasma. The flow of Ar was set to 105 ml/min at a gauge pressure of 0.35 bar*g*. The applied voltage was set to 4 kV at 37 kHz. The results, in **Figure 5-20,** show that the contact angle for the demineralised water droplet has increased from 56.3^{o} to 103.35^{o}. This indicates significant alterations on the surface properties due to the plasma treatment. The plasma treatment increases the free radicals on the surface of the glass slide and which could form polar compounds, which consequently causes significant changes in the glass properties as shown by the decrease in the surface wettability (Abdul-Majeed, 2012). This effect can change the nature of the glass surface from hydrophilic to hydrophobic. A rise in the level of water by 6 ml in a capillary tube after the plasma treatment has been demonstrated which shows the change of properties of glass from hydrophilic to hydrophobic (Li et al., 2009). After one minute of operation, there was a change of contact angle (38^{o}) between treated and untreated capillary. It is possible that one of the plasma the glass surface is causing these optical emission spectral peaks in the range of 300-400 nm. However, to confirm the identity of these optical emission spectral peaks a detailed study is required.

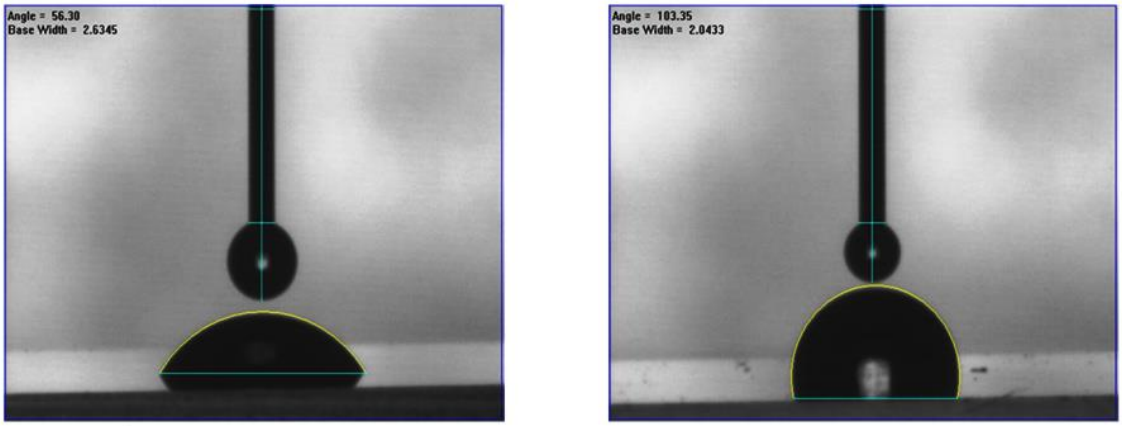

Figure 5-20 Water contact angle of the glass slide before and after treatment

5.3 Analysis of optimisation experiments

As discussed in section 5.2.9, detecting hydrogen in water vapour plasma flowing at atmospheric pressure in a plasma-micro-reactor by direct methods such gas GC is a difficult task (Rehman et al., 2013). In order to optimise the reaction conditions a method of direct measurement of the required species is generally required. Ozone can be detected by several direct methods. There are ozone detectors available commercially (ozone solutions AS-500). It could also be detected by chemical methods (Bader and Hoigné, 1981). Because of the ease and reliability of detection, ozone generation has been used for optimisation of operational parameters of plasmolysis. Also, due to the similar time scales for hydrogen and ozone formation, it can be assumed that ozone generation could be used to optimise operational parameters of water vapour plasmolysis. In the following section the rationale for using ozone generation has been studied in detail.

5.3.1 Rationale for using O_3 for optimisation of operational parameters

Kinetics of ozone formation has been discussed in section 2.4. Similar to ozone formation, it is interesting to see, that electron impact dissociation is the dominant pathway in kinetics of hydrogen formation as discussed in chapter 3 (Rehman et al., 2012). Also, the threshold energy required for electron impact reaction with H_2O (5.1 *eV*) (Kregar et al., 2009) is not very different from the threshold energy required for electron impact reaction with O_2 (6 *eV*) for O_3 generation (Kogelschatz, 2003). However, the ozone forming step is a three body reaction between O and O_2 while that in hydrogen formation is the reaction between H and HO_2. Again, in kinetics of formation of both hydrogen and ozone positive ions do not seem to have contributed significantly. The ozone formation is quenched by the presence of nitrogen and/or moisture at a higher power levels and oxygen atoms start recombining with each other to produce oxygen molecules or breakdown the already produced ozone. Similar behaviour is shown by water vapour plasma that hydrogen and hydroxide radicals produced in the plasma recombines to produce water (Fridman, 2008). The reaction is a three body reaction and has a small rate constant (3×10^{-33} cm^6 s^{-1}) which could start dominating the kinetics at higher power levels. **Figure 5-21** represents the kinetics of ozone formation in air plasmas (Kossyi et al., 1992). The red line has been drawn in

Figure 5-21 to show the time scales for hydrogen number density to reach of steady state and the blue line indicates the time scales for ozone number density to reach steady state. The most interesting observation is that the overall time scale to reach steady state formation of H_2 and O_3 is quite similar. Although the time to reach steady state production of O_3 is shorter than the time scale for hydrogen to reach steady state, it could be suggested that the overall kinetics would remain same. This might be explained by comparing time scales of reaching steady state formation of O_3 and H_2 in **Figure 5-21**. If an air plasma is tuned such that it is run only until the time scale to reach steady state H_2 instead of time scale to reach O_3 steady state formation, the only difference one can expect is slightly higher number density of NO_2. Since O_3 has already reached steady state, its concentration does not change. Similar time scales to what has been proposed by (Kossyi et al., 1992) for the ozone formation has been reported by (Eliasson and Kogelschatz, 1991) in air plasmas. However these kinetic studies (Eliasson and Kogelschatz, 1991, Kossyi et al., 1992) were carried out at higher electron density value (10^{25} m^{-3}) while, in chapter 3 hydrogen formation kinetics has been studied at lower electron density (10^{17}-10^{21} m^{-3}) (Nehra et al., 2008) .

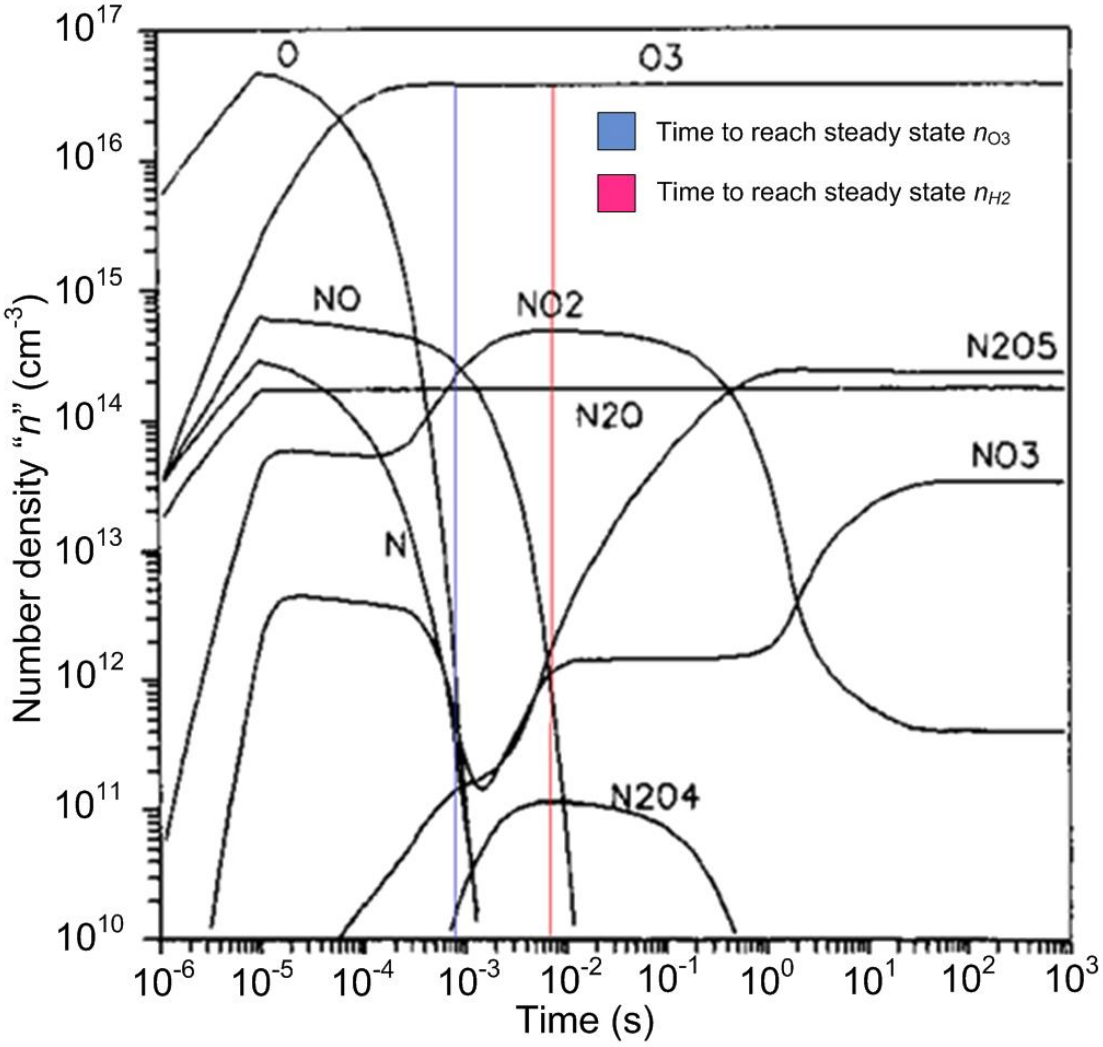

Figure 5-21 Kinetics of ozone formation in air plasma (Kossyi et al., 1992)

In **Figure 3-5** of chapter 3, the evolution time of species has been plotted against the electron density. It was observed that a decrease in evolution time of the species is expected as the electron density is increased. It has also been noticed (Kogelschatz, 2003) that time scales of ozone formation in air plasmas is an order of magnitude slower than the time scales of ozone formation in oxygen plasmas. The reason is the "*substantial fraction of electron energy initially lost*" in electron collision with nitrogen which is later recovered by reactions (2-36) and (2-37) given in section 2.4 (Eliasson and Kogelschatz, 1991). It is worth noting here that kinetic simulations run by Eliasson and Kogelsschatz (1991) did not have any moisture in it. However, air, even dried to have a dew point -60 ^{o}C, would contain 10 ppm of water vapour concentration (Yagi and Tanaka, 1979). The air used in the laboratories has a higher moisture content of

around 50 ppm (BOC, 2014). The presence of moisture, in a similar way to nitrogen in air plasma, could absorb energy from plasma and make reaction kinetics slow enough to make it comparable with the kinetics a of hydrogen formation. So in the light of discussion above, it could be assumed that as time scales for formation of hydrogen and ozone is similar and hence the overall kinetics of formation is also similar.

5.3.1 Calibration

The standard indigo solution was diluted with a known volume of water to make several diluted standard solutions. A calibration curve was plotted and is shown in **Figure 5-22**. The calibration curve shows the relation between concentration of indigo and corresponding absorption at 600 nm. The calibration curve was used to calculate the moles of indigo decomposed in each experiment and hence the concentration of ozone produced could be calculated.

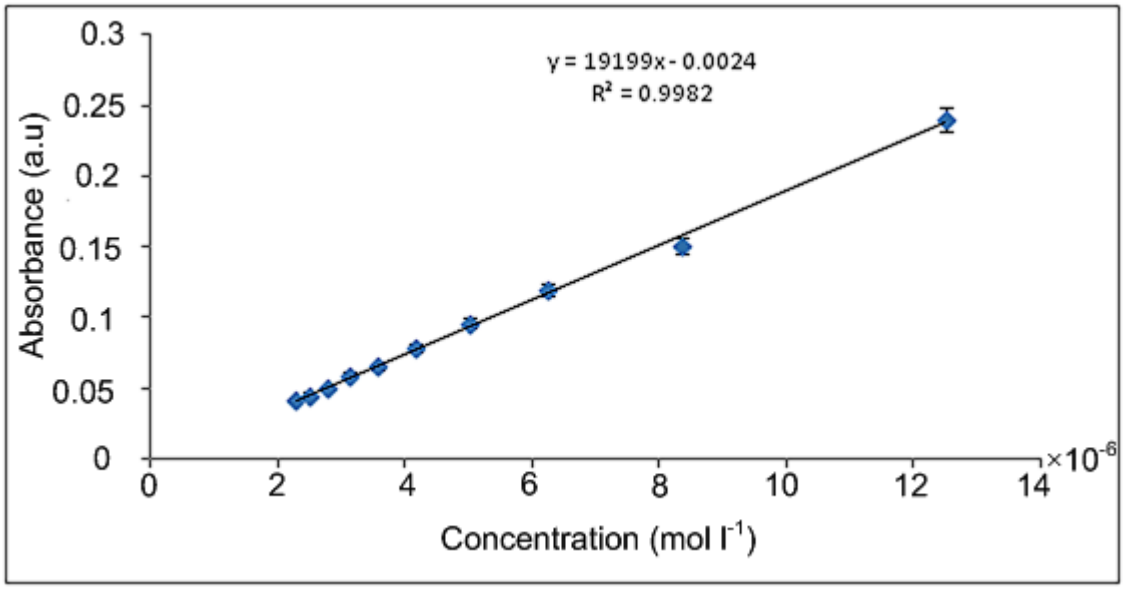

Figure 5-22 Calibration curve for Indigo solution

5.4.3 Effect of pressure

The effect of pressure on ozone production was monitored by increasing the pressure inside the plasma micro-reactor by putting a needle valve at the outlet. Pressure was varied between 0.2-1.0 bar*g*. The effects of increasing the pressure are shown in **Figure 5-23**.

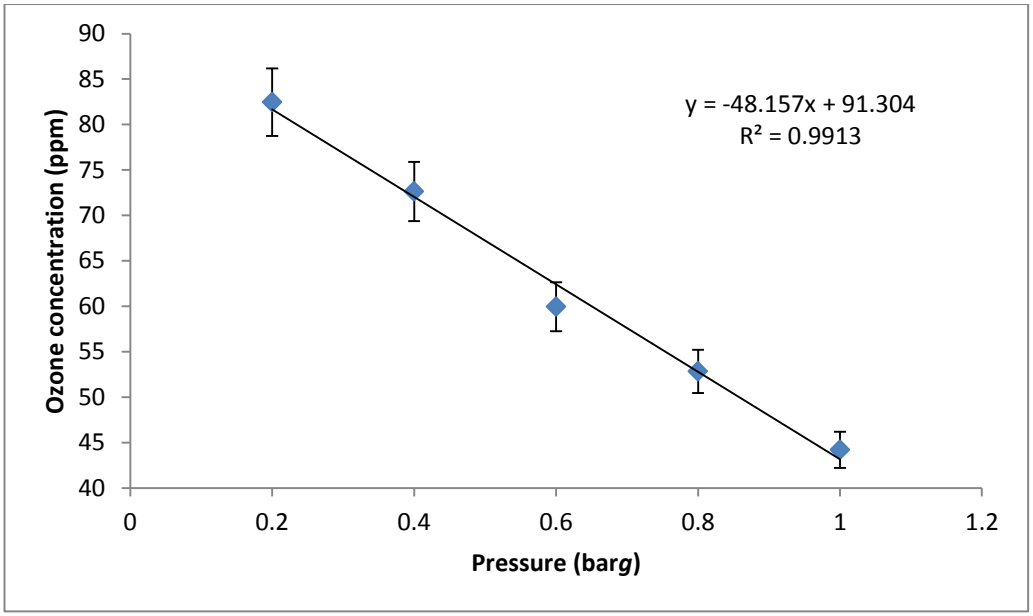

Figure 5-23 Effect of pressure on ozone formation

The standard error in absorbance was 4.5%. The pressure is found to decrease the ozone formation with an increase of 1 bar*g* reducing the ozone concentration by half. The reduction in concentration of ozone could be expected by increasing the pressure. With the increase in pressure, number density of gas particles in the plasma micro-reactor is increased as shown by ideal gas law. With an increase in the number density of gas particle, the electric field will be distributed over a larger number of particles lowering the energy level of each particle. Hence the number of effective collisions would decrease, eventually reducing the ozone formation. From the results, it could be stated that air flowing at 0.2 bar*g* would favour ozone formation.

5.4.4 Effect of flow rate

Flow rate was varied between 0.2 (l min^{-1}) to 5 l min^{-1}. The standard error in absorbance was 4.6%. The results are shown in **Figure 5-24**. The trend line could be divided into two main parts. Ozone concentration reaches a point of maximum formation before reducing back to a steady state condition. Further increase in the flow rate of air (at a constant pressure of 0.2 bar*g*) would result in quenching plasma (Yagi and Tanaka, 1979).

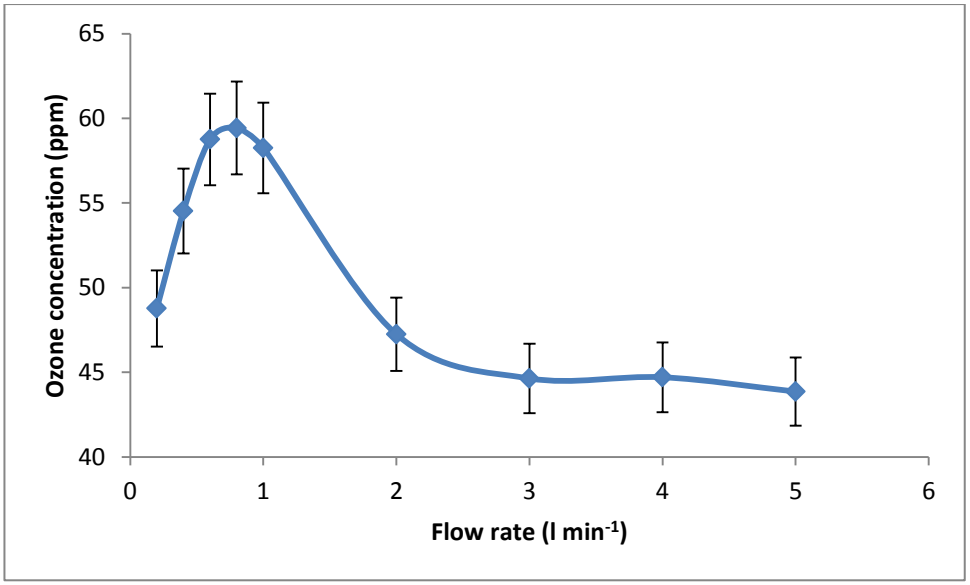

Figure 5-24 effect of flow rate on ozone formation at 4.8 kV, 37 kHz, 3 cm electrode length and atmospheric pressure

Initially, an increase in the ozone concentration is observed as the flow rate is varied from 0.2 l min^{-1} to 1 l min^{-1}. However, it could be seen that 0.6, 0.8 and 1 l min^{-1} flow results in similar concentration of ozone. A sharp decrease in the concentration of ozone is observed from 1-2 l min^{-1}. From 2-5 l min^{-1} a steady ozone concentration is obtained. The results shown in **Figure 5-24** could be explained on the basis of phenomenon occurring both in plasma and mass transfer on the skin of the bubble/gas-liquid interface.

Increase in ozone formation could be attributed to a relatively smaller ratio of oxygen atoms to oxygen molecules $[O]/[O_2]$. As discussed earlier in chapter 2 in section 2.4, a higher concentration of oxygen atoms has a poisoning effect on ozone formation by reacting with O_3 and /or O_3*, as shown in reactions (2-26)-(2-28), where an optimised ratio of concentration $[O]/[O_2]$ of an order of 10^{-3} has been proposed to be optimum (Eliasson and Kogelschatz, 1991). Increasing the flow rate from 0.2 to 1 l min^{-1} would have increased the concentration of oxygen molecules $[O_2]$ in plasma and hence the quenching effect of oxygen atoms [O] might be reduced causing ozone formation to be increased. Since, applied power was same in all experiments, increasing the flow rate from 1-5 l min^{-1} would have reduced the specific energy (*eV* $molecule^{-1}$) to an extent where ozone formation is decreased.

Since ozone solubility in water (5 x 10^{-5} mol l^{-1}) (Sotelo et al., 1989) is low (compared to 3.78 x 10^{-4} mol l^{-1} at 20^{o}C) (Nixon and Pauley, 2014), mass transfer of ozone from bubble (gas phase) to liquid could be assumed to be controlled by the liquid phase transfer coefficient (Caprio et al., 1982, Konsowa, 2003). The initial increase in the ozone concentration could be attributed to an increase in mass transfer from the bubble (gas phase-a mixture of ozone and air) to liquid. This enhancement in mass transfer could be explained on the basis of relatively increased turbulence at higher flow rate, hence mixing, and increase in gas holdup (ε_G) with increasing flow rate as depicted by $\varepsilon_G \propto Q^n$. Where Q is the air flow rate and n ranges from 0.7 to 1.2 under bubbly flow conditions which prevails at relatively smaller gas flow rates (Konsowa, 2003). As a result of increased gas holdup, liquid-gas interfacial area is increased and hence the mass transfer from bubble to liquid increases. The increase in mass transfer and consequently an increase in ozone concentration because of its dilution in water is observed until the bubble flow regime is replaced by a heterogeneous regime (at relatively larger bubbles). At this point the bubbles start growing big because of frequent collisions and coalescence. Additionally, the increased bubble size reduces the surface area and hence the overall mass transfer is reduced. The bubbly flow regime and heterogeneous regime are shown in Appendix III (**Figure 7-6** and **Figure 7-7**).

Experimental results shown in **Figure 5-24** could be used to calculate the residence time of air in the plasma chamber. **Figure 5-25** shows the concentration of ozone produced at different residence times. It is worth noting that the maximum ozone concentration is produced at around 2 x 10^{-2} s which is time assumed for the ozone to reach maximum concentration (Eliasson and Kogelschatz, 1991, Kossyi et al., 1992).

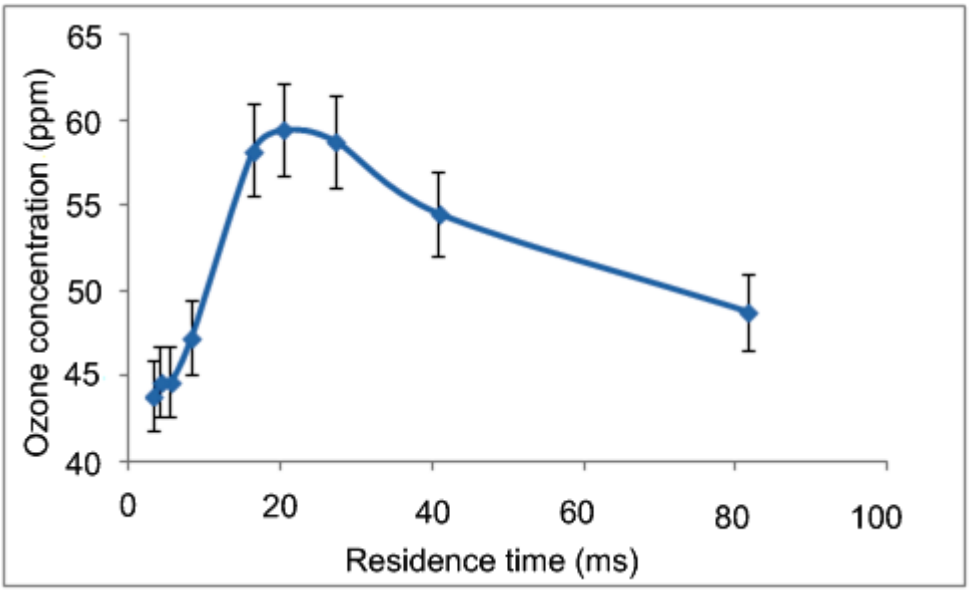

Figure 5-25 Effect of residence time on ozone formation

It also validates the assumption that the timescale for both hydrogen and ozone production is similar and hence the kinetics of formation are similar. With further increase in the residence time, formation of NO_x dominates and the ozone concentration is reduced (Yagi and Tanaka, 1979).

5.4.5 Effect of power

The effect of power on ozone formation is observed by changing the power from ~ 20-80 W by varying the voltage between 3.4-4.8 kV at 37 kHz The lower limit of the applied voltage was set corresponding to the minimum breakdown voltage of air and the upper limit was set to avoid arcing in the system. The current was allowed to adjust itself according to impedance of the system. The standard error in absorbance was 10%. Ozone concentration is found to increase with the power input. The experimental results are depicted in **Figure 5-26**. Two different slopes could be observed in **Figure 5-26**. From 20-50 W the slope looks steeper than the slope from 60-80 W. Higher power density leads to the stronger microdischarges which eventually start supporting side reactions either by recombination of O atoms to produce O_2 or break down the O_3* and/or O_3 by collision with O atoms as shown in reactions (2-26)-(2-28) given in section 2.4. Also as discussed above the formation of NO and NO_2 could start dominating ozone production at higher power densities.

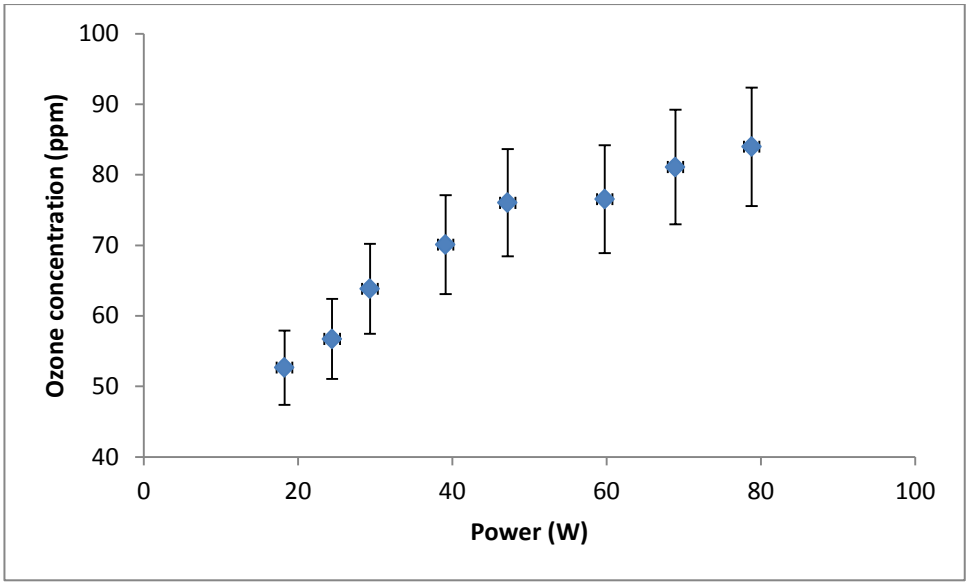

Figure 5-26 Effect of power on ozone formation at 1 l min^{-1}, 37 kHz, 3 cm electrode length and 1.01 bar

However, the trend indicates that the plasma is still not power saturated in which case a decrease in the ozone concentration at higher power levels would have been observed. The results, however indicate that some other dielectric material with higher dielectric strength could be used instead of borosilicate glass in order to conduct the experiments at higher voltages (>5 kV) like mica (7) or alumina (9.3-11.5) (ToolBox, 2014). From the results it could be concluded that higher powers would favour formation of ozone in the range of 3.4-4.8 kV with 37 kHz using 3cm long electrode.

5.4.6 Material and geometry of electrode

Electrodes used in plasma-micro reactors deteriorate as they are used over longer period of times. It becomes important to test the behaviour of electrode material over longer period of time. However, because of the scale of the study it was not possible to run the experiment for longer periods of time (over a period of days). As discussed above three different internal electrodes and four different external electrodes were used to see the effect of properties (such as electrical conductivity) of materials on the ozone formation. Aluminium, brass and stainless steel were chosen as internal electrodes because they present inexpensive options to be used as electrodes compared with Pt. For longer period of time, the change in structural properties of inner electrodes and the corresponding effect on ozone concentration could not be tested because of the requirement of large amounts or indigo solution for it. Other

than type of material used for external electrodes, two different configurations of material used were sheet and mesh. Al sheet and Al tape are sheet electrodes and two stainless steel made meshes were used as well. The electrodes are shown in Appendix III (**Figure 7-8**). The meshes were used to monitor the effect of different configuration of electrode on ozone concentration as it is reported that meshes can make plasma more homogenous (Ye et al., 2012). Also, the electrical conductivity of the external electrodes would govern how much current they can conduct and hence can affect the plasma efficiency by limiting the power supplied to the it. More power will be dissipated as heat if a poor conductor is used. The standard error in the experiments was found to be 3.13%. The results are shown in **Figure 5-27**. No significant difference was observed by using different combinations of internal and external electrodes, although, Al tape seems to produce slightly higher concentration of ozone but the effect was not significant.

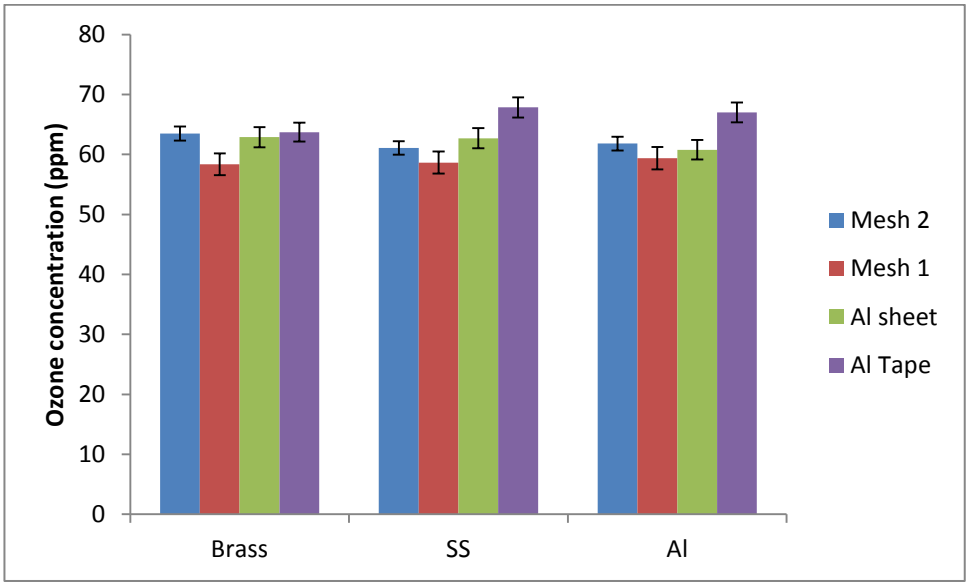

Figure 5-27 Effect of different material type and configuration of electrode

From **Table 5-6** it is evident that there is a significant difference between electrical and thermal conductivities of the material used in the experiment. However, the difference in these properties does not seem to affect ozone concentration. This indicates that the plasma impedance is controlling the overall power flow through the reactor and electrical conductivity of materials does not play a significant role in ozone formation.

Table 5-5 Electrical and Thermal conductivities of Aluminium, Brass and Stainless steel (ToolBox, 2014)

Material	Electrical Conductivity (Siemens/m))	Thermal Conductivity (W/m-K)
Aluminium	3.77×10^6	205
Brass	15.9×10^6	109
Stainless steel	1.0×10^6	16

5.4.7 Electrode length

The length of external electrode was varied in order to optimise the length of plasma reactor. The standard error in absorbance was 7%. The results of variation in ozone formation are shown in **Figure 5-28**. A gradual increase in the ozone formation is seen with an increase in the length of the plasma chamber.

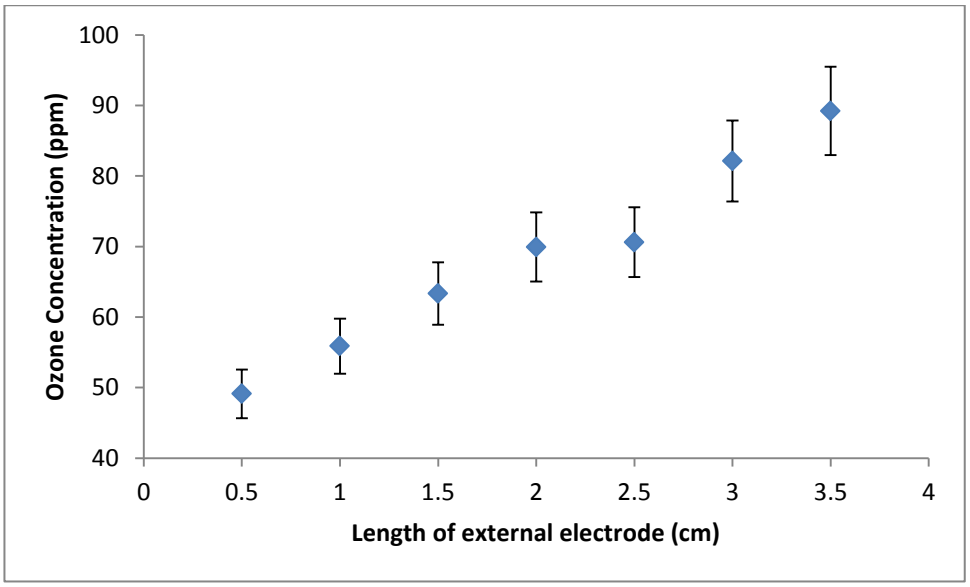

Figure 5-28 effect of variation in electrode length (Al-Tape) on ozone formation at 4.8 kV, 37 kHz, 1 l min^{-1} and at 0.2 bar*g*

By increasing the length of electrode the residence time for which air is passing through active plasma zone has increased causing an increase in ozone concentration.

5.4.8 Effect of frequency

The frequency was varied between 26-40 kHz to see its effect on ozone concentration. 40 kHz was the maximum value which could be achieved by the present power supply. The lower limit was set in order to prevent arcing. The standard error in absorbance was 6% in case of 3 kV and 34 kHz while in all other experiments the percentage error was around 1%. As mentioned above the current was allowed to settle at a value according to the impedance of the system. However, at different frequencies at given

voltages the current drawn by the plasma micro-reactor varies. **Figure 5-29** shows peak current drawn at different frequencies. Also, it could be seen that it is not possible to conduct the experiments at 4.2-4.8 kV at 28 kHz because of arcing. Only at 3 kV it was possible to lower the frequency to 26.3 kHz. The peak current drawn in the plasma micro-reactor increases as the frequency is decreased from 40 kHz.

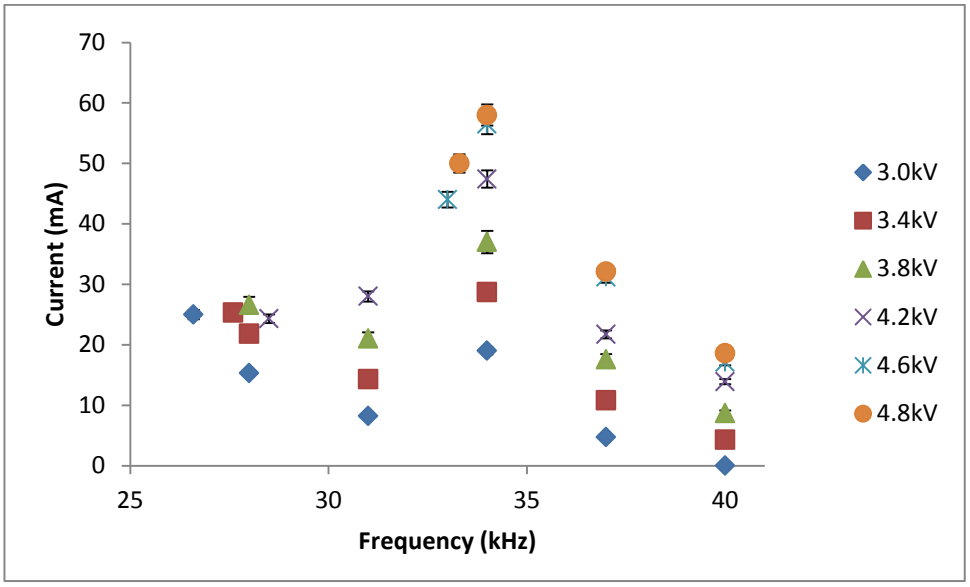

Figure 5-29 Peak current drawn by plasma at different frequencies

For every applied voltage the maximum current is absorbed at 34 kHz. The current then decreases as the frequency is further lowered to 31 kHz and starts rising again as the frequency is further reduced to 28 kHz and keeps rising as frequency is further reduced to 26 kHz in case of 3.0 kV. **Figure 5-30** shows the power consumed by the plasma reactor. The trends shown are similar to **Figure 5-29**.

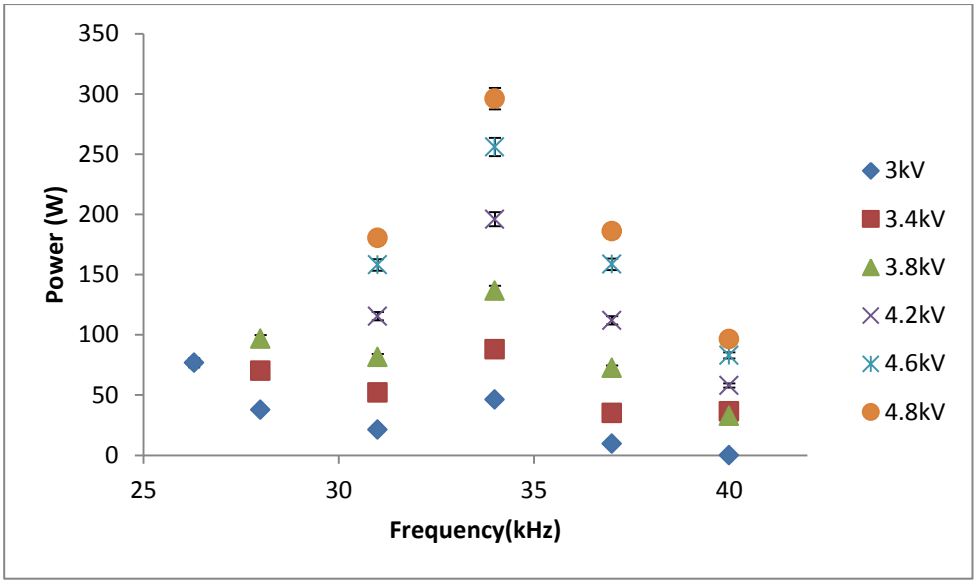

Figure 5-30 Variation in absorbed power at different frequencies

Figure 5-31 Effect of varying the frequency on ozone concentration. It can be noted that ozone formation is favoured at lower frequencies.

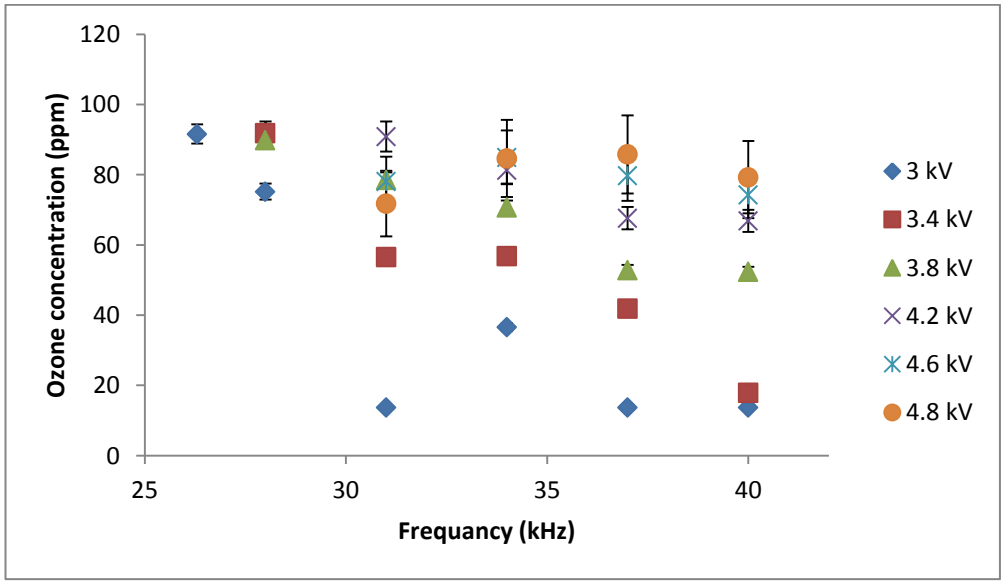

Figure 5-31 Effect of frequency on ozone formation

Except for 4.6 kV and 4.8 kV the concentration of ozone produced increases with a decrease in the frequency. It could be seen that maximum ozone concentration is obtained at 3 kV at 26.3 kHz, 3.4 kV and 3.8 kV at 28 kHz. In an AC powered plasma reactor, at lower frequency, it takes more time for polarity to shift from one electrode to the other. This means charge is felt by the air for longer period of time and hence higher concentration of ozone is obtained. As mentioned above, it was not possible to

lower the frequency to 28 kHz for higher voltages (4.2-4.8 kV) so the exact effect of smaller frequencies at higher applied voltages cannot be found.

Figure 5-32 shows the effect of power on ozone formation at different frequencies. The maximum concentration of ozone (~90 ppm) is produced utilising 60 W at 28 kHz. It is also interesting to see that similar ozone concentration is produced at 26 kHz. Further analysis could not be performed as there is only one data point available at 26 kHz and 3.0 kV. In the current experimental setup higher concentrations of ozone are produced at low power (~70 W) at low frequency (26 and 28 kHz) than at higher power (~300 W) at higher frequency (40 kHz).

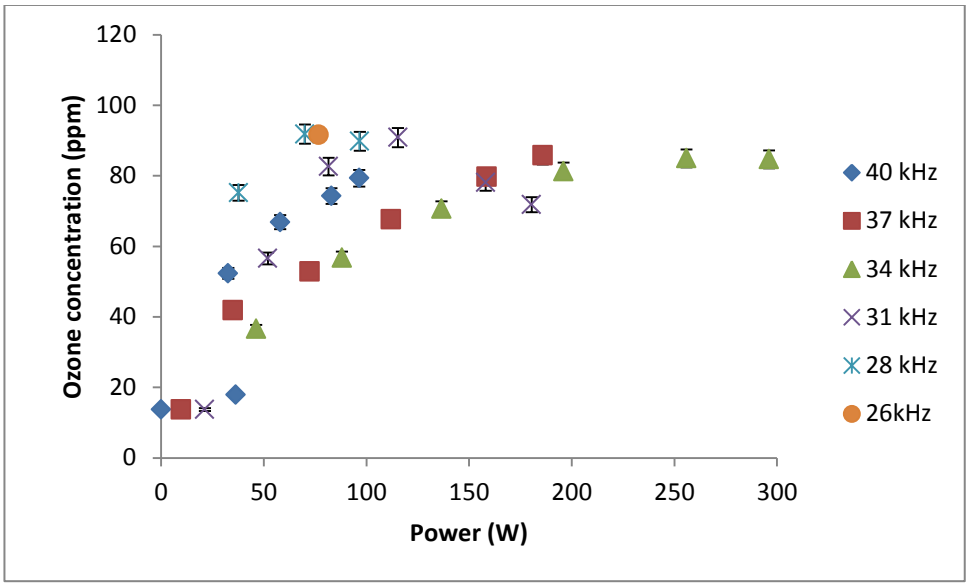

Figure 5-32 Effect of frequency variation over ozone formation

It is interesting to compare results shown in **Figure 5-32** to the results shown in the section 5.4.5. Similar trends to **Figure 5-26** are observed. At a specific frequency, increasing power produces higher ozone concentration except 31 kHz where ozone concentration is found to decrease with an increase in power. As discussed above higher power density could lead to the stronger microdischarges which eventually start supporting side reactions either by recombination of O atoms to produce O_2 or break down the O_3* and/or O_3 by collision with O atoms as shown in reactions (2-26)-(2-28). Ozone formation using plasma micro-reactors, thus, requires much lower frequencies (~28 kHz) at lower applied voltages (~34 kHz). Values of optimised variables are given in **Table 5-7**.

Table 5-6 Summary of optimised operational parameters

Parameters	**Optimised Values**
Pressure	Atmospheric pressure
Flow rate	~ 1 l min^{-1}
Power	80 W at 37kHz
Electrode (internal)	Aluminium rod (not significant difference though)
Electrode length	3.5 cm
Frequency	28 kHz at 3.4 kV

5.4 Separation of hydrogen from product gas

5.4.1 Rationale for using air-water system for separation process

The efficiency of hydrogen separation can be measured by measuring the mass transfer from product gases to liquid phase e.g., oxygen from microbubbles. However, it must be noted that the current study is utilising plasma micro-reactors. The flow of gases used in the study is in the order of millilitres as discussed in sections 4.2.1 and 5.2.9. The amount of hydrogen and oxygen produced could not affect the concentration of dissolved gases in water significantly to be detected by conventional detection equipment such as a DO probe. Additionally, the fluidic oscillator used in this study requires 40 l min^{-1} as a threshold value to start oscillating the fluid. In order to identify the potential use of oscillatory flow as a separation technique, however, a distinctive air-water system could be used. The air-water system will allow working at higher flow rates, measure $K_l a$ and hence an efficient and cost effective method of microbubble generation could be identified for hydrogen separation process.

5.4.2 Measurement of $K_l a$

$K_l a$ can be found by using unsteady state method i.e., fitting the data to the following equation (Kawahara et al., 2009).

$$\frac{dC}{dt} = K_l a\left(C_s - C\right) \tag{5-23}$$

Where C_s is saturation concentration of water at test temperature as given by Henry's law and C is the concentration of oxygen in water during experiment measured at

different time intervals. The experimental data obtained was analysed for $K_l a$ using the equation below (Gray, 1990).

$$E = \frac{C_s - C_t}{C_s - C_o} = e^{-(Kla)t} \quad (5\text{-}24)$$

Where , C_t is DO concentration (mg/l) at time t, C_s is as described above, C_o is initial DO concentration (mg l^{-1}) and $K_l a$ is volumetric mass transfer coefficient. Temperature adjustment was done following the equation 5-25;

$$(K_l a)_{20} = \frac{(K_l a)_T}{\theta^{T-20}} \quad (5\text{-}25)$$

Where, θ = Temperature correction factor for oxygen transfer coefficient taken as 1.024, T= Average temperature of the experiment-considered 20°C in the current study. All experiments were repeated three times to estimate the standard error. Here an average error of 12.12% in oscillated flow and 11.96% in steady state flow is reported. **Figure 5-33** shows the graph plotted for the measurement of $K_l a$ for steady state flow and oscillatory flow respectively. It is clear from the **Figure 5-33** that $K_l a$ is higher for oscillatory flow than that of steady state flow.

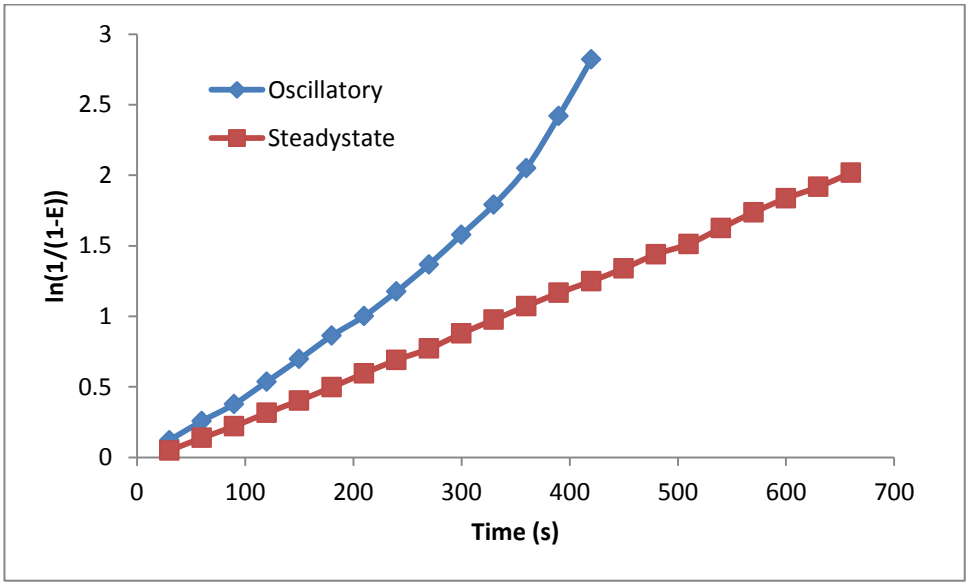

Figure 5-33 k_la model used for oscillatory flow and steady state flow

Figure 5-34 shows the bar chart for $K_l a$ values for the oscillatory flow and steady state flow. It is clear that at each flow rate $K_l a$ for oscillatory flow is higher than the steady state flow.

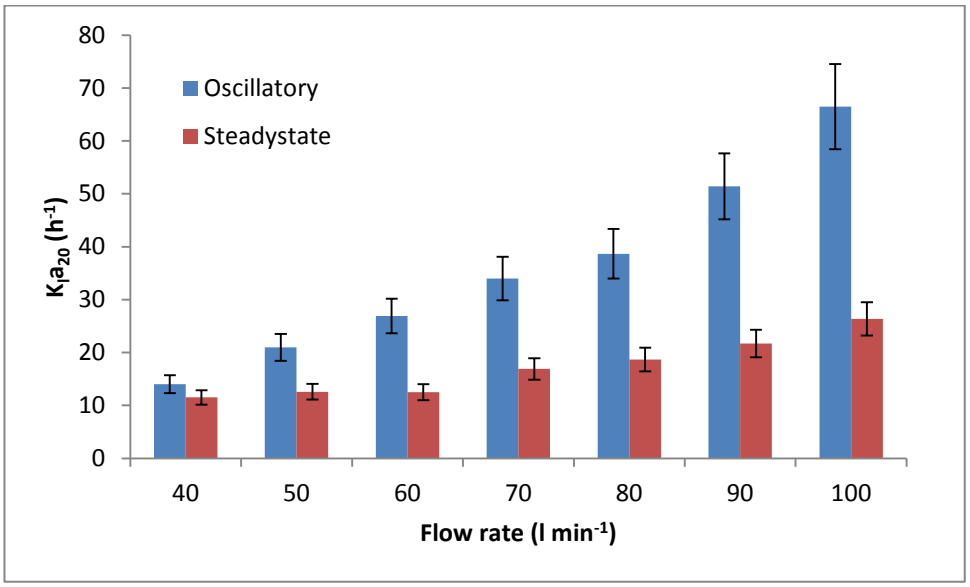

Figure 5-34 Comparison between $K_l a20$ measured under oscillatory flow and steady state flow

It is interesting to note in **Figure 5-35** that with increase in flow rate from 40-60 l min^{-1}, improvement in $K_l a$ by oscillatory flow has increased gradually.

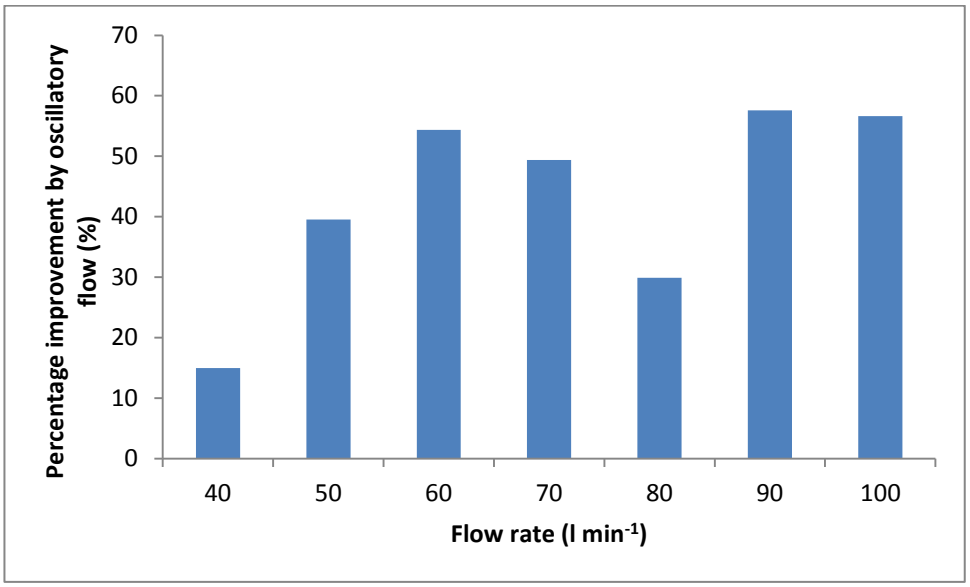

Figure 5-35 Percentage improvement for 40-100 l min^{-1}

However, for 70 and 80 l min^{-1} the improvement in $K_l a$ is less than that seen in 40-60 l min^{-1}. For 90 and 100 l min^{-1}, similar level of improvement is seen with 55% being the

highest observed for 60, 90 and 100 l min^{-1}. It is very interesting to notice that $K_l a$ for oscillatory flow at 60 l min^{-1} is approximately equal to $K_l a$ for 100 l min^{-1} under steady state conditions which means same amount of mass transfer could be achieved using oscillated flow at much lower gas flow rates. This shows the increase in mass transfer using fluidic oscillator and its potential application in separation process. Since all other operational parameters were kept constant, the increase in $K_l a$ for oscillatory flow could be attributed towards the presence of larger number density of microbubbles in the system. Also, one of the reasons explaining higher efficiencies at higher flow rate is the higher frequency of oscillation at higher flow rates. Frequency of oscillation is inversely proportional to the feedback loop length. Since, the feedback loop length used in the experiment was the shortest one, frequency of oscillation would be higher and hence higher density of microbubbles will be produced at higher flow rates.

Increase in mass transfer at higher flow rates has been explained on the basis of reduction in diffusion layer thickness of the bubbles by the wake of the rising bubbles from eddy current. The gas hold up increases at high flow rates hence increasing the gas-liquid interfacial area as well as the rate of mass transfer (Konsowa, 2003). The diffuser membrane material used in this study could have also helped in the bubble break off mechanism. Since it is constructed from a flexible membrane with pore size of approximately 600 µm when fully inflated, it could cause opening and closing of the pore to help pinch the bubble off at smaller size than the steady state flow.

In **Figure 5-36,** it is interesting to observe that, to the naked eye, the bubble size and turbulence generated by both oscillatory and steady flow appeared to be the same. However when bubble sizing was carried out using ABS, it clearly shows that the density of microbubbles is high in oscillatory flow compared to steady flow. This could prove to be doubly advantageous when process is to upgrade to industrial scale. Higher turbulence will maintain high degree of mixing and hence homogenous conditions throughout the liquid column/container and yet full advantages from higher mass transfer could be exploited.

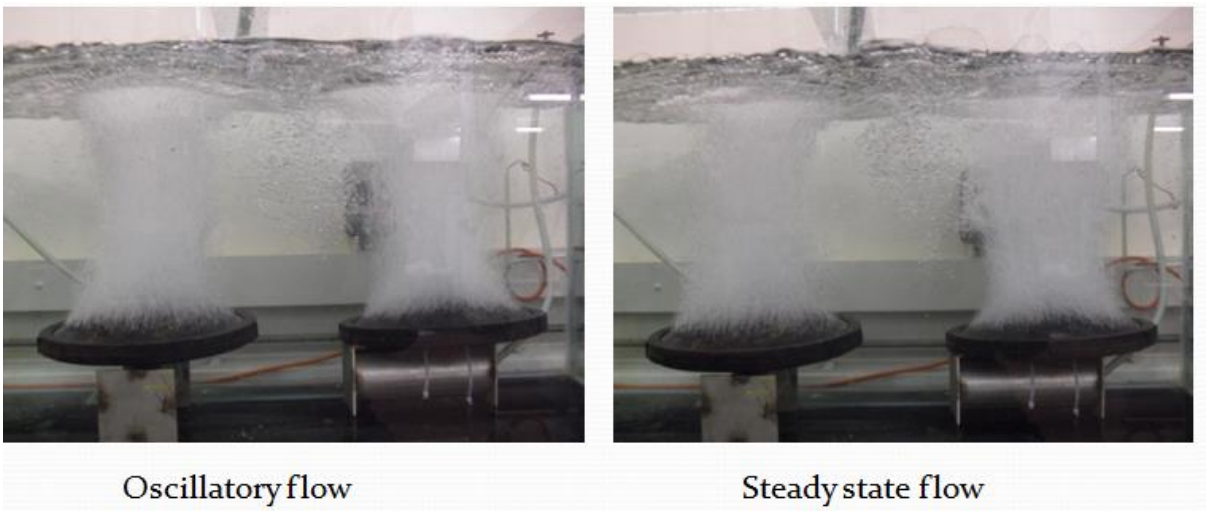

Figure 5-36 Gas flow through diffusers under oscillatory flow and steady state flow

5.4.3 Bubble size distribution

Bubble sizing was carried out in the flow range of 40-100 l min^{-1} to measure the bubble size distribution. It was done to observe any reduction in the bubble size with the oscillatory flow which could validate the enhancement in mass transfer and hence higher $K_l a$. Hydrophones would measure the size of the cloud of bubbles passing between them. Bubbles were seen coming out from the whole surface of the membrane. However, bubbles converged to the centre as they rise in the water. Two competing mechanisms, at this point, are involved on the surface of the bubble. As the bubble rise, oxygen inside the bubble would transfer from the bubble to the surrounding liquid causing the bubble to shrink. Also, hydrostatic head is reduced with the bubble rise causing bubble to expand. The final size of the bubble is determined by the equilibrium point between these two forces.

Bubble size distribution was measured by ABS. ABS measures bubble size density and void fraction in real time in a single capture or continuous mode. One of the advantages of using this technique is its insensitivity to particulate matter in the liquid phase which might interfere with the actual measurements. **Figure 5-37** and **Figure5-38** show the bubble size distribution measurement at different flow rates. It was found that the bubble density for oscillatory flow is higher than that for the steady flow. However, at 40 l min^{-1}, the difference between the bubble densities for two types of flow is not significant compared to the other flows used in the current study as shown in **Figure 5-37 (A)**. This is because 40 l min^{-1} is the minimum flow rate at which the

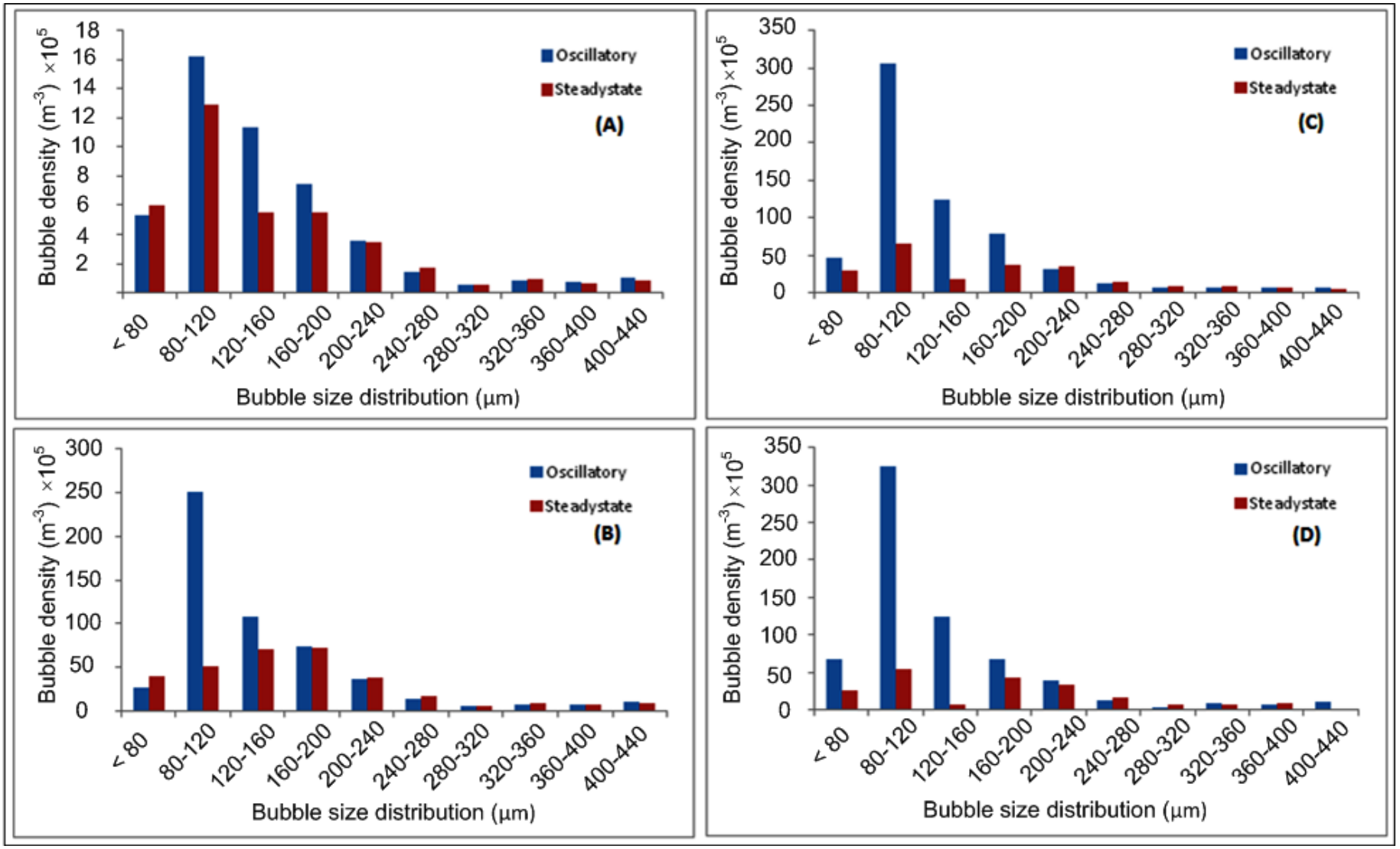

Figure 5-37 Bubble size distribution for (A) 40 l min^{-1} (B) 50 l min^{-1} (C) 60 l min^{-1} (D) 70 l min^{-1}

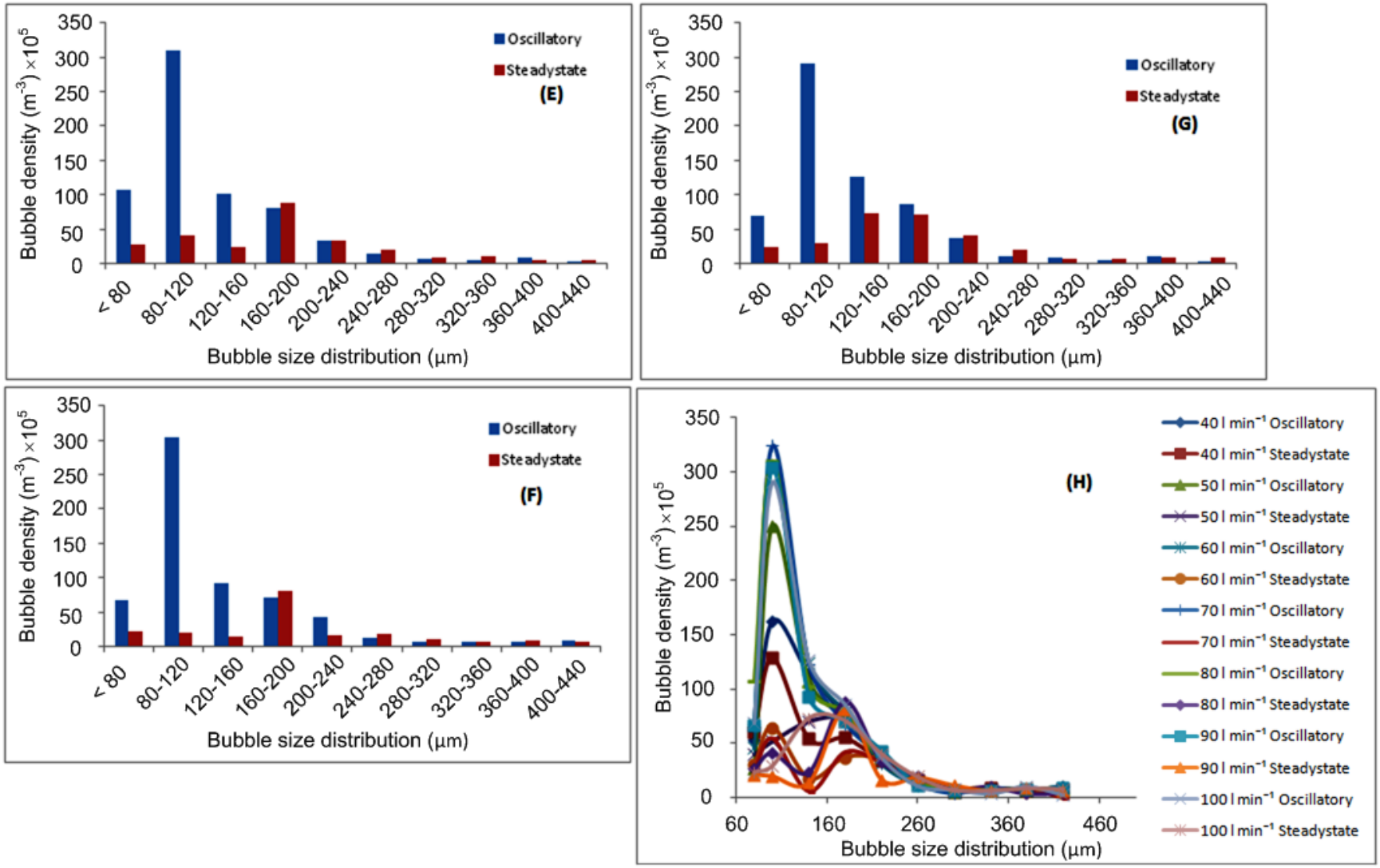

Figure 5-38 Bubble size distribution for (E) 80 l min^{-1} (F) l min^{-1} (G) l min^{-1} (H) combined result

fluidic oscillator starts oscillating the fluid and hence the difference between the bubble densities is not considerable. As the flow rate is increased, the bubble density for oscillatory flow becomes higher as seen in **Figure 5-37 (B, C and D)**. It is also noticeable that highest density for microbubbles lies between the range of 80-120 µm which is shown in **Figure 5-38 (H).** It could be based on the fact that single feedback loop length was used in all experiments. As mentioned earlier frequency of oscillation is a function of feedback loop length, so it is expected that highest bubble density would peak for a particular size distribution which is favoured at that frequency of oscillation.

It could also be noted that total volume of all bubbles (as shown in **Figures (5-37 and 5-38)** does not match with corresponding air flow rates (40-100 l min^{-1}) used in the experiments because this study is focused on the production of microbubbles so frequency of ABS was set such that bubbles between the size distribution of >80-450 µm could be monitored. However, more hydrophones for different frequency ranges could be utilised to measure fine bubbles as well.

Experiments for both measurement of $K_l a$ and bubble size distribution indicate that microbubbles could reliably be generated by the use of fluidic oscillator. As shown in chapter 2 in **Figure 2-6** in section 2.5.2 dissociation products from plasma micro-reactors would come out in the form of microbubbles. Using oscillatory flow, along with microbubble generation, enough mixing could be obtained to keep level of oxygen same in the water column. Hence oxygen from the microbubble could be assumed to constantly transfer from microbubble to water outside at steady rate. The bubble bursting at the water surface would then release hydrogen rich gas. Using a fluidic oscillator, a very conservative estimate of improvement of mass transfer coefficient of 55% could be expected. Additionally, fluidic oscillators can be retrofitted in any industrial mass transfer limited process such is the simplicity of its installation.

5.4.4 Oxygen removal efficiency

Utilising the same data used to calculate $K_l a$, oxygen separation efficiency can be calculated as shown in **Figure 5-39**. The maximum oxygen removal efficiency is found to be 24%. It seems from **Figure 5-39**, that the efficiency of oxygen removal is decreasing with the increasing flow rate from 40 to 100 l min^{-1}. However, it was noted

in section 5.4.2 that increasing flow rate results in higher value of $K_l a$. The contradiction between the two results can be explained on the basis of the fixed volume of water used in the experiments. It must be noted that in all experiments volume of water was kept constant. However, the air flow rate was varied from 40-100 l min^{-1}. Only a certain amount of oxygen can be dissolved in water (saturation concentration of oxygen in water) which is a function of water temperature.

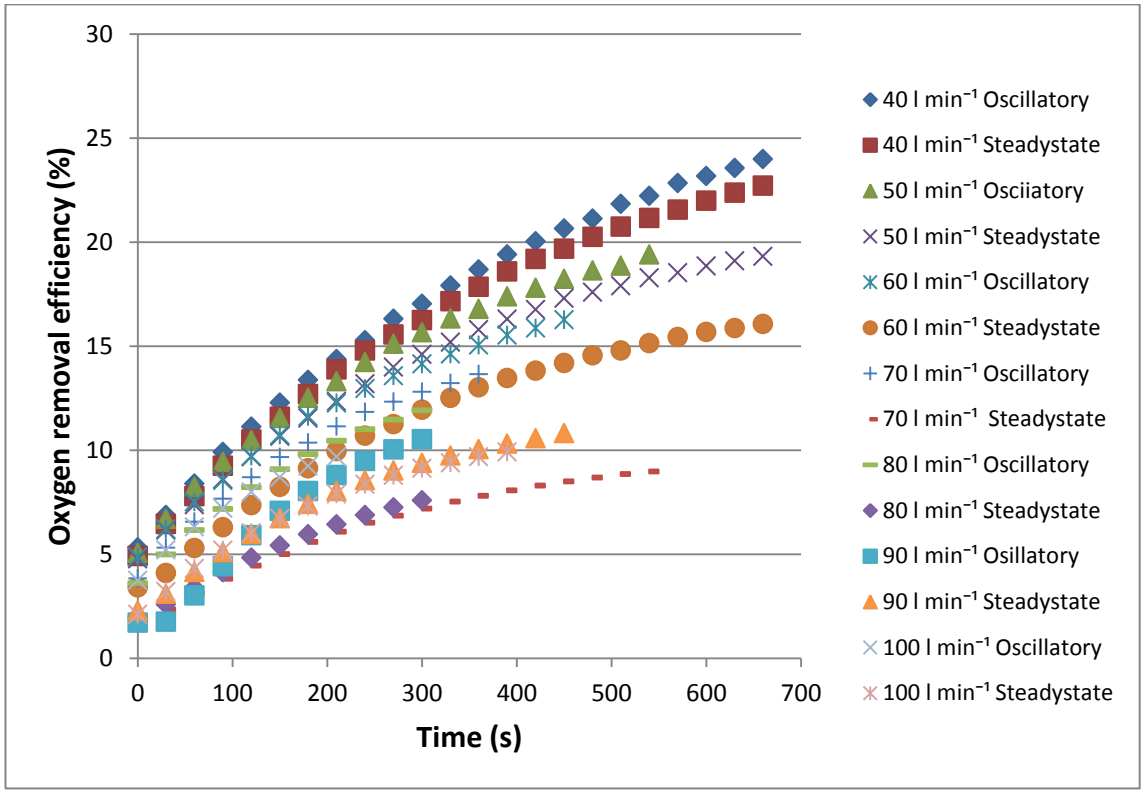

Figure 5-39 Oxygen removal efficiency at different flow rates for Oscillatory and steady state flow

Since volume of water was kept constant, oxygen removal efficiency is a function of saturation concentration of oxygen in that volume of water at that particular temperature. However, with increase in flow rate of air from 40-100 l min^{-1}, the amount of oxygen coming in the water has increased so oxygen removal seems to have diminished. A better representation of the results can be shown as **Figure 5-40**. Again, at each flow rate only a certain amount of oxygen can be removed. However, with increase in flow rate from 40-100 l min^{-1}, the saturation limit has been reached quickly. For 100 l min^{-1}, the saturation has been achieved below 200 s. However, it has taken more than 800 s for the water to get saturated. Also, at every value of flow rate,

saturation concentration has been reached quicker with oscillatory flow than with steady state flow.

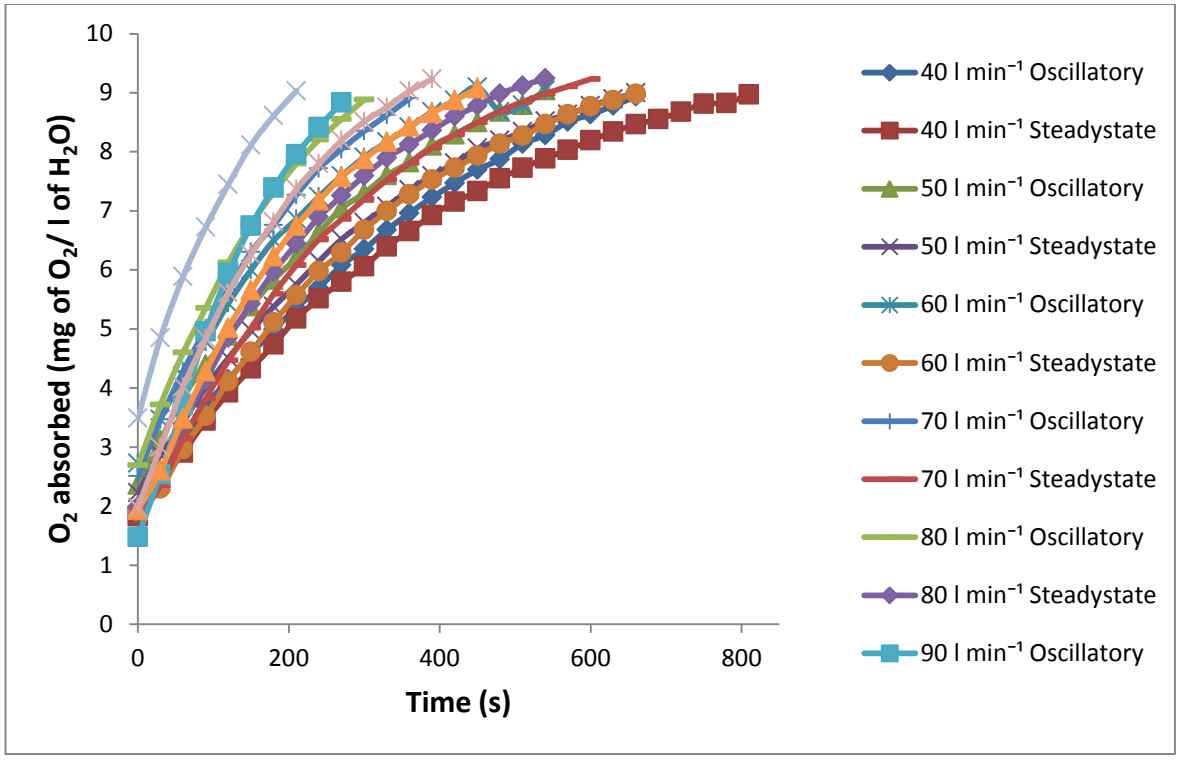

Figure 5-40 Oxygen absorbed at different flow rates under oscillatory and steady state flow conditions

5.5 Application of reactive separation on plasma-chemical process

5.5.1 Measurement of $K_l a$

Similar procedure as discussed in section 5.4.2 was used to measure $K_l a$. The value of $K_l a$ has been measured for both oscillatory and steady flow using MBD-600 diffusers. A standard error of 3% was observed in experiments measuring $K_l a$. The results are shown in **Figure 5-41**. The value of $K_l a$ has been reported in s^{-1} units to compare with reaction time scale (τ) calculated in chapter 3.

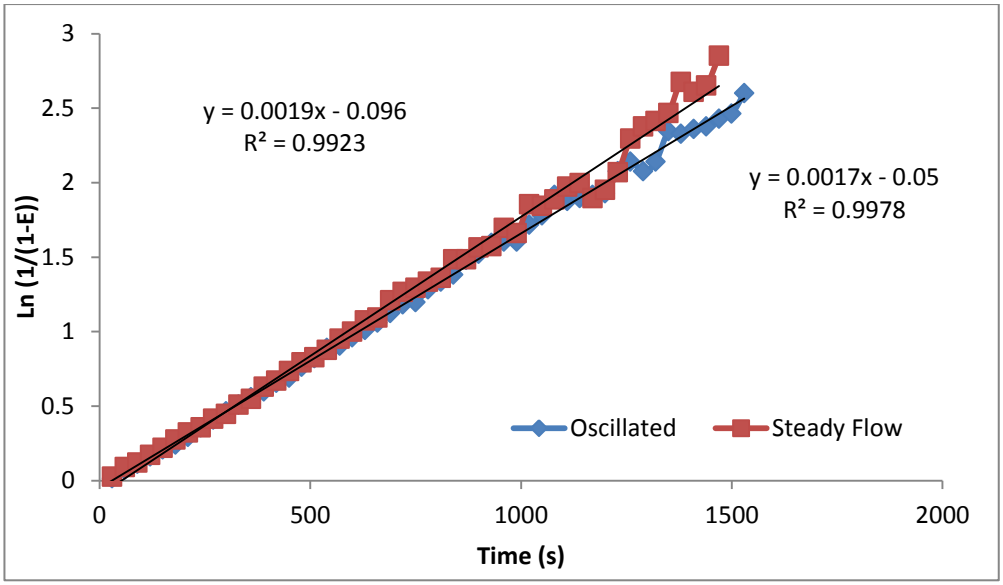

Figure 5-41 $K_l a$ for oscillatory and steady flow

It was assumed and has been noted in section 5.3.1 that the time scale for producing steady state concentration of hydrogen and ozone is in the order of 10^{-2}s. **Figure 5-41** shows $K_l a$ values for both oscillatory and steady flow is in the order of 10^{-3}s which indicates oxygen is dissolving in water an order of magnitude quicker than at what hydrogen is being produced in plasma micro-reactor making reactive separation possible on plasmo-chemical reaction. This higher separation rate should drive the equilibrium towards production of more hydrogen and oxygen, hence, higher yield of products could be expected. However, there are two possible barriers needed to be overcome before this approach could be applied. First is the flow rates of the water vapours and Ar gas (reactants in general) should be such that the residence time of the products in diffuser section is higher than both rate of formation of products in the plasma micro-reactor and also separation time scale of gases in water. This would, essentially, require multiplexing the plasma micro-reactors into one relatively larger unit where higher flow rates could be utilised. Multiplexing micro plasma reactors, in addition to solving this problem, yield higher concentration. It is worth noting that multiplexing of plasma micro-reactors has already been shown in literature (Zimmerman et al., 2010). The other barrier to overcome is selection of proper material to be used as a diffuser. The diffuser section has to be very thin such that the residence time of products in the diffuser is negligible compared to the reaction time scale (τ) and separation time scale ($K_l a$). Diffuser material needs to have very fine

pores, be homogenously distributed, plasma resistant and commercially available. However, reactive separation will only be truly applicable if production and separation could occur simultaneously. There should not exists an intermediate stage between production (plasma micro-reactor) and separation (diffuser and water column) processes. An ideal plasma micro-reactor would have very fine pores at the outlet such that products coming out from the reactor could enter into the water column without have to pass through the diffuser. Plasma filled micro-bubbles, in this case, will enter into the water column. At the bubble interface, oxygen (products) will start dissolving in the water column and since the rate at which it is dissolving in water is faster than the reaction time scale of plasmolysis occurring inside the microbubble, the equilibrium will be shifted in the forward direction.

The other important result shown in **Figure 5-41,** is similar values of $K_l a$ for oscillatory and steady flow. This result is unexpected and also contradictory to establish theory of enhanced mass transfer by higher surface area offered by microbubbles. This can be explained by comparing the residence time of microbubbles in the water tank with the time required for microbubbles to transfer oxygen to water and reach mass transfer equilibrium. Since microbubbles have very high surface area, they start transferring the oxygen as soon as emerge out of diffuser and reach mass transfer equilibrium. This mass transfer equilibrium could be achieved at a length scale of approximately 3 diameter lengths of microbubbles (Private communication with Professor William Zimmerman of Department of chemical & Biological Engineering, The University of Sheffield, UK). Since the microbubbles reach equilibrium very quickly, they spend rest of their time in the tank without transferring oxygen to the water. However, fine bubbles being large in the size (>1 mm), having small surface area transfer oxygen slowly to the water and reach mass transfer equilibrium near water surface later than the microbubbles. Hence, similar values of $K_l a$ are achieved for both oscillatory and steady flow. This effect is very predominant in smaller flow rates like what has been used in the current section (5.5.1). On the other hand, at larger flow rates (40-100 l min^{-1}) used in section 5.4.2 the fine bubbles have high velocity and thus very little residence time. They rise quickly and reach surface without reaching equilibrium causing a significant reduction in mass transfer as was observed in section 5.4.2.

5.5.2 Bubble size distribution

Figure 5-42 shows bubble size distribution for steady and oscillatory flow. It can be observed that the number density of microbubbles produced under oscillatory condition is significantly higher for 20 micron diameter. The higher number density of microbubbles is a function of frequency of oscillation which is governed by length of feedback loop as discussed in section 5.4.3. Efficient generation of microbubbles by fluidic oscillation has already been discussed. However it is worth noting that density of microbubbles produced by oscillatory flow is similar to steady state flow for the size distribution of 20-40 µm and 40-60 µm.

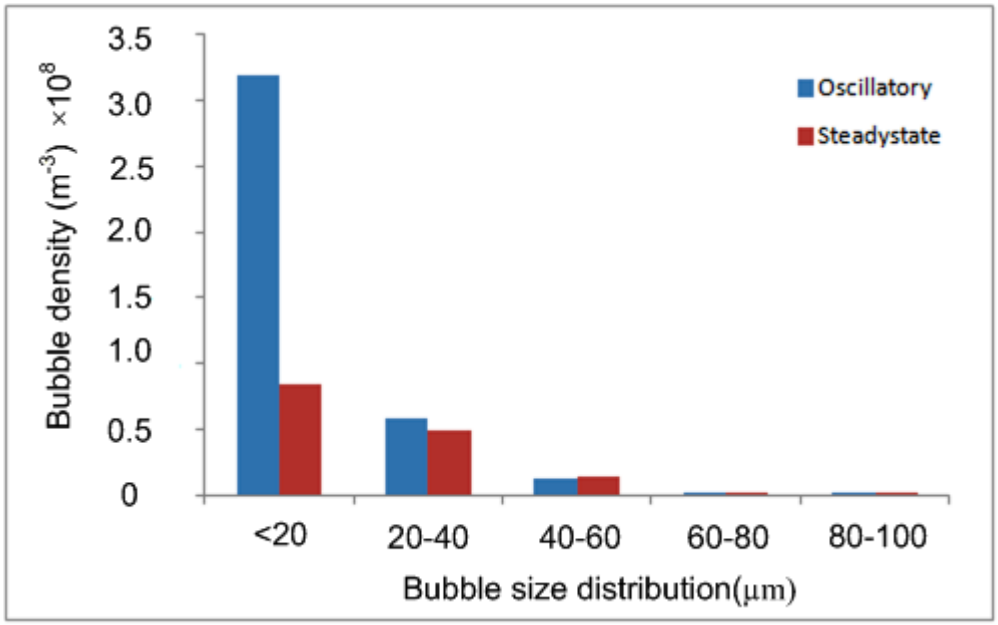

Figure 5-42 Bubble size density distribution for MBD 600 diffuser under oscillatory and steady flow

This result could be attributed to the hydrophilic nature of the diffuser used in the experiment. As discussed in section 2.5.3, hydrophilic surfaces assist the bubble formation mechanism. Hence it could be concluded that using oscillatory flow by fluidic oscillator is a cost effective method to generate microbubbles by using ceramic and membrane diffusers which is a key step in applying separation approach in the current study.

5.5.3 Ozone generation experiments

Figure 5-43 shows the results of ozone generation by changing the positions of external electrode to generate plasma at different position along the length of plasma micro-reactor. Indigo solution was decolourised (spectrophotometer showed zero

absorbance reading) in 18 seconds when external electrode was placed below the diffuser section. However, it took 36 seconds to completely decolourise the indigo solution when external electrode was placed at the bottom position. The result could be attributed to few reasons. Firstly, placing the external electrode below the diffuser would have given a chance for ozone to react instantaneously with indigo solution. If the reaction between ozone and indigo solution is faster than the rate of production of ozone in plasma channel, this would shift the equilibrium of reaction in plasma channel in the direction of ozone production.

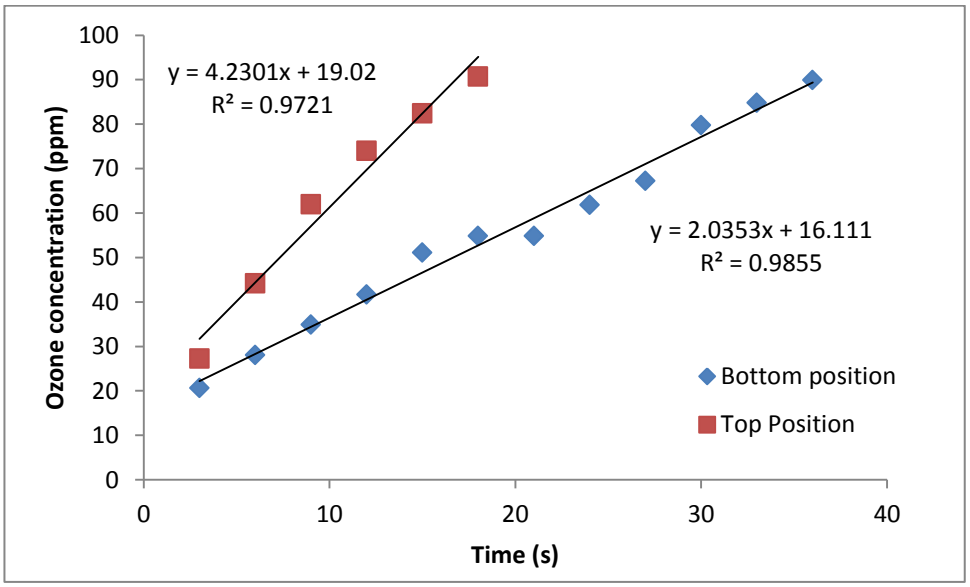

Figure 5-43 Ozone concentration produced by placing electrode at top and bottom position of plasma micro-reactor

Hence, it could be concluded that reactive separation could have occurred as hypothesised in chapter 1. However, at 1 l min^{-1} of air used in the experiment the residence time of products in diffuser section is 6.6 x 10^{-2} s. Looking into the flow rate analysis done in section 5.4, flow rate of 1 l min^{-1} was chosen. Higher flow rates, though would have increased residence time, were not chosen as significant reduction in ozone concentration has been observed at higher flow rates. At lower ozone concentration it would have been difficult to compare the data for two different positions of plasma ignition. The residence time is of similar order to reaction time scale and separation time scale. So the extent to which reactive separation has a role play in producing an increased ozone concentration could not be quantified.

Secondly, there exists other oxidizing species in air plasma such as OH radicals because of the presence of moisture in it. As discussed above, air even dried to have a dew point of -60^{o}C would still have 10 ppm (Yagi and Tanaka, 1979). Along with OH radicals, other species like O could also exist in air plasma. These species have a very short life spans. Putting electrodes below the diffuser might have given enough time for these species to react with indigo and cause more oxidation. However the life span of excited radicals like OH and O is of the order of less than a microsecond. Considering the residence time of gases in plasma chamber and in diffuser section, these radicals would not have enough time to reach the indigo solution and decolourise it. Also, diffusers have significantly high surface area so the chances of OH, O or any other ionic or excited species reaching indigo solution are very limited. Again, an increased concentration of produced ozone could not be solely attributed to the existence of these species. A third reason could be the dissociation of ozone by colliding with wall of reactor and/or by colliding with another molecule of ozone. Again it is difficult to assume that half of the ozone produced at lower position (13 cm away from diffuser) of plasma channel being destroyed by colliding with the walls of the plasma micro-reactor or with another ozone molecule. Industrial scale ozone generators are equipped with cooling system to control the temperature. Ozone production has been known to decrease with increasing temperature. Since no cooling system was used in the experiment to control the temperature of outer electrode, a reduction in ozone concentration could be attributed to an increase in temperature. However, reaction conditions are the same in both experiments so temperature would have effected in similar fashion. Also, each experiment was only run for 3s, hence no significant increase in the temperature of the electrode is expected. However, a definite conclusion could be made that igniting plasma below the diffuser (top position in **Figure 4-10**) has produced twice as much ozone as it did when plasma was ignited away (bottom position in **Figure 4-10**) from the diffuser.

5.6 Summary

Minimum breakdown voltage for water vapours flowing at 1 atm was found to be 3.5 kV, 3 mA at 36.73 kHz. Water vapour plasma was characterized by optical emission spectroscopy. An electron density, 1.765 x 10^{17} m^{-3} and Debye length 3.24 μm has been estimated. Electron, excitation, rotational and vibrational temperatures was calculated. The temperatures calculated showed the order T_e(0.77eV)> T_{exc}(0.53*eV*)> T_{rot}(0.067*eV*) which confirms the non-LTE environment of the plasma. Analysis based on the decomposition rate suggests an energy yield of 10 g/kWh for water vapour and 20 g/kWh for water vapour and Ar which is on a par with electrolysis. Energy efficiency and thermodynamic efficiency for water vapour plasmolysis along with Argon was found to be 78.77% and 79.16%. This shows that hydrogen could potentially be produced by water vapour plasmolysis, as hypothesised in chapter 1. A discussion is presented on the identification of optical emission spectral peaks in the region between 317-400 nm.

It is identified that the O_3 generation could be used instead of H_2 generation to optimise the operational parameters of plasmolysis. The rationale for this assumption has been discussed. Pressure and flow rate of the air, electrode material, length of external electrode and its configuration, applied power and frequency have been optimised. It was found that at higher pressure, raising the pressure to 1 *barg*, ozone concentration is reduced to half. The optimum flow rate is found to be around 1 l min^{-1} . It was found experimentally that ozone formation is favoured at around time scale of order of 10^{-2}s hence validating the assumption that time scale for ozone formation and time scale for hydrogen formation is similar. This time scale is in agreement to the time scale found in chapter 3 by kinetic modelling. Both electrode materials for internal and external electrodes and two configurations (sheet and mesh) were not found to affect ozone formation significantly. At constant frequency of 37 kHz, ozone concentration was found to increase with the increase in voltage from 3.4 kV to 4.8kV. However, when frequency was varied between 28-40 kHz, the maximum ozone was produced at frequency ~ 28 kHz and voltage ~3.4 kV.

A novel approach has been presented to separate hydrogen produced by water vapour plasmolysis by exploiting the difference between solubilities of hydrogen and oxygen in water. For all values of flow rate $K_l a$ has been found to be higher for oscillatory flow than steady flow with highest improvement of ~55% observed at 60, 90 and 100 l min^{-1}. Bubble sizing was done using acoustic bubble spectrometer for 40-100 l min^{-1}. At every flow rate, the bubble density for microbubbles was higher under oscillatory flow conditions which validate the production of microbubbles using fluidic oscillator. It has been identified that the fluidic oscillator could be used to produce oscillatory flow for the separation of hydrogen from the products.

For application of reactive separation on plasma-chemical reaction, $K_l a$ has been measured for the MBD-600 diffuser to measure the separation time scale. The value of $K_l a$ for steady state and oscillatory flow was found to be 0.0017 s^{-1} and 0.0019 s^{-1} respectively. Comparison of reaction time scale τ from chapter 3 and $K_l a$ shows that using an ideal plasma micro-reactor, reactive separation could be used to change the reaction equilibrium and improve reaction efficiency. Experiments were conducted to observe any change in ozone formation by air plasma by changing the position of plasma micro-reactor relative to diffuser section. Experiments showed twice as much ozone as is produced when plasma was ignited near the diffuser.

Chapter 6

Conclusions and Recommendations for Future Study

6.1 General conclusions

Energy plays a pivotal role in socio-economic development by raising standard of living. It is becoming gradually accepted that current energy systems, networks encompassing everything from primary energy sources to final energy services, are becoming unsustainable. Currently, energy-related GHG emissions, mainly from fossil fuel combustion for heat supply, electricity generation and transport, account for around 70% of total emissions including carbon dioxide, methane and some traces of nitrous oxide. During the past two decades, the risk and reality of environmental degradation have become more apparent. In recent years, public and political sensitivities to environmental issues and energy security have led to the promotion of alternative energy resources. Realizing the exigency of reducing emissions and simultaneously catering to energy needs of society, researchers foresee the alternative energy resources, which are independent of fossil fuel, as the promising entrant to overcome these challenges. Hydrogen as a fuel could contribute significantly towards reduction in both the consumption of fossil fuel and in the reduction of greenhouse gases.

The objective of this study was to develop a method for simultaneous production and separation of hydrogen by integrating micro-plasma technology with fluidic oscillation for microbubble generation. Hydrogen production by water plasmolysis has been considered as an expensive method so far. In this study, a method of simultaneous production and separation of hydrogen has been proposed and developed.

Literature has been surveyed to develop basic understanding of the related subjects, make a basis for further modelling and experimental work and identify the needs of production of hydrogen by a cost effective method. Conventional hydrogen production techniques like steam methane reforming, pyrolysis and gasification are dependent on fossil fuel. Plasma fundamentals have been studied in detail. Applied principles and plasma chemistry in the current project have been reviewed in the chapter two. A detailed discussion on plasmolysis of water vapour has been carried out identifying the major mechanisms involved in water plasmolysis. Recent studies on hydrogen production using plasma from different feed stocks have been reported. Finally, a brief

comparison between plasmolysis and electrolysis has been carried out as both technologies utilise electricity. It was concluded that there exists a need to develop a method for simultaneous production and separation of hydrogen. It was identified that ozone generation could be used to optimise the operational parameters of plasmolysis. The rationale for this assumption is discussed in detail in analysis and discussion chapter. However, to understand the assumption kinetics of ozone formation and its decomposition in aqueous phase has been studied. Different technologies for hydrogen separation have been discussed briefly. Microbubble mediated mass transfer produced by fluidic oscillation has been identified a cost effect method to separate hydrogen from the product gases. Reactive separation has been studied and its application on plasma-chemical process has been identified.

I. Kinetic modelling

A kinetic model has been formulated to understand the kinetics of hydrogen formation from water vapour plasmolysis under nonthermal plasma conditions. A pure stream of water vapours was considered as feedstock. The concentration of water vapours was calculated using the ideal gas law. A kinetic scheme of one hundred and seventy six reaction pathways with thirty six different species was identified for kinetic modelling. Kinetics was studied using reaction engineering laboratories-COMSOL 3.5a. Different pathways of decomposition such as, dissociation reactions, electron dissociative attachment of electrons, dissociative ionisation reactions, ionisation reactions and dissociative excitation reactions were included along with the other pathways for different species produced and consumed in water vapour plasmolysis. Dissociation reactions were found to dominate the water vapour plasmolysis followed by dissociative attachment of electron reaction being the other important kinetic step. Reaction time scales and concentrations of hydrogen and the other species were found to be in direct relation with electron density and reached their respective highest values n_{H_2} = 9.64 x 10^{24} m^{-3} at $\tau_{reaction}$~ 10 ms. The time scale for reaching 99% of hydrogen production (steady state concentration of H_2) was found to be around 10^{-2} s. Recombination reactions of H-H atoms were not found to be significant for the production of H_2. The key step for the generation of H_2 was the reaction between H and HO_2. Finally, a mechanism consistent with the kinetically important steps is

proposed. Reaction time scales indicate that hydrogen could be produced at lower power if plasma is tuned according to the kinetics of formation of hydrogen. Reactions time scales found by kinetic modelling were used to determine applicability of reactive separation in chapter 5.

II. Experimental work

After gaining the understanding of kinetics of formation of hydrogen production, a DBD-corona hybrid discharge reactor was designed and fabricated. Experimental work was carried out to:

a) Feasibility of hydrogen production by water vapour plasmolysis

Experiments were conducted to find out the feasibility of hydrogen production by water vapour plasmolysis and to characterise the water vapour plasma by optical emission spectroscopy. Voltage-current (VI) characteristic has been plotted and discussed in detail. Different parameters measured were electron density, 1.765 x 10^{17} m^{-3}, Debye length 3.24 µm and electron, excitation, rotational and vibrational temperatures**.** Rotational temperatures were calculated from both the first positive system of N_2 (0.640 *eV*) and the OH (*A-X*) band (0.067 *eV*). The temperature calculated showed the order T_e(0.77eV)> T_{exc}(0.53*eV*)> T_{rot}(0.067*eV*) which confirms the non-LTE environment of the plasma. No H_2O_2 was produced in the experiment. An effort was made to detect hydrogen by online and offline GC. The analysis suggests that a pressure is built up in the reactor by attachment of gas collection bags which changes the reaction chemistry and hence the percentage of hydrogen and oxygen was found to vary with the type of sampling vessel attached. Head space analysis showed no DO or hydrogen in the liquid phase. The energy yield was calculated to be 10 g of H_2 kWh^{-1} for water vapour plasmolysis and 20 g of H_2 kWh^{-1} for plasmolysis of water vapour and Ar. The energy yield for plasmolysis of water and Ar is equal to that of electrolysis. The energy efficiency and thermodynamic efficiency for water vapour plasmolysis along with Ar was found to be 78.77% and 79.16% respectively. A discussion is presented on the identification of emission lines in the region 317-400 nm. Lastly, water contact angle with glass slides was increased by 42.9^0 after plasma treatment which shows significant alteration in the surface properties of glass with plasma treatment.

b) Optimisation of plasmolysis

The objective of optimising the reaction condition has been achieved by using ozone generation. It is identified that the time scale to reach steady state ozone production and hydrogen production is similar hence it could be assumed that if a reactor is optimised for ozone production, similar values of operational parameters could be used to produce hydrogen. The ozone was produced in a plasma micro-reactor using air at room temperature. The ozone concentration was measured using the standard indigo method. The pressure and flow rate of the air, electrode material, length of external electrode and its configuration, applied power and frequency were optimised. It was found that at a higher pressure (1 bar*g*) ozone concentration is reduced to half. The optimum flow rate is found to be around 1 l min^{-1}. Both electrode materials used as internal and external electrodes and configuration of external electrodes were not found to affect ozone formation significantly. The ozone concentration was found to increase with higher power at 37 kHz using 3 cm of electrode. However, when frequency was varied, maximum ozone was produced at lower frequency (~28 kHz) and low voltage (3.4 kV).

c) Separation of hydrogen from product gases

A novel approach to separate hydrogen and oxygen based on microbubble dynamics is presented. The approach utilises the difference between solubilities to separate mixtures of gases. A fluidic oscillator containing no moving parts was used to generate microbubbles for the separation processes. $K_l a$ has been calculated for oscillatory flow and steady state flow in the range of 40-100 l min^{-1}. At every flow rate $K_l a$ was found to be higher for oscillatory flow with highest improvement of ~55% observed at 60, 90 and 100 l min^{-1}. Bubble sizing was done using ABS for 40-100 l min^{-1}. At every flow rate, the bubble density for microbubbles was higher under oscillatory flow conditions which validate the production of microbubbles using a fluidic oscillator. The results suggest that fluidic oscillators could be used for providing sufficient mixing in order to keep conditions homogenous, having better mass transfer coefficient which in turn could be used to separate hydrogen and oxygen efficiently.

d) Assessment of reactive separation on plasma-chemical process

A ceramic based diffuser- MBD 600 was used to measure $K_l a$. Comparison of reaction time scale τ and $K_l a$ shows that reactive separation could be used to change

the reaction equilibrium and improve reaction efficiency. However, an ideal plasma micro-reactor to achieve this objective will have to be designed. The ozone was produced using air plasma. The plasma was ignited at two different positions to observe the effect of reactive separation. Experiments showed that concentration of ozone produced was twice when plasma was ignited below the diffuser. Finally, a discussion is done on possible factors causing an increased ozone concentration when plasma was generated below diffuser.

It has been identified by modelling and experiments that hydrogen could be produced by water vapour plasmolysis using lower power than what was previously thought. A power supply designed to give specific range of optimised value of power and frequency would reduce both its cost and the size. Hydrogen produced could be separated by the difference between the solubility of hydrogen and oxygen. Fluidic oscillation was used to generate microbubbles for a separation process. Better design of a plasma micro-reactor, it's multiplexing, with careful selection of materials for and diffuser can make reactive separation applicable on plasma-chemical processes.

8.2 Recommendation of future studies

The current study proves that hydrogen could be produced from water vapour plasmolysis at competitive prices. However, there still remains a margin of improvement in the techniques.

A direct method for identification of hydrogen could not be identified in the current study. The fact, that attaching gas sampling bag or any other gas collection container creates pressure and alters the kinetics of plasmolysis, hindered hydrogen detection by direct methods for instances gas chromatography. So, there still remains a need to establish/identify a direct method for hydrogen detection in the current experimental set-up. This could be done by changing the reactor design to avoid pressure build-up in the reactor. One of the solutions is to multiplex plasma micro-reactor. The multiplexed plasma micro-reactor would be able to generate significant amount of hydrogen. This design should avoid any pressure build-up when gas sampling bags or any other vessel is attached so that hydrogen could be detected by a hydrogen sensor or gas chromatography.

The experimental investigations are necessary to identify a better dielectric material for the plasma micro-reactors. Experiments for optimisation of plasmolysis parameters could not be conducted below 20 kHz and above 4.8 kV because of the limited dielectric strength of dielectric material used in the current study. It is important to highlight that the optimum value of different parameters may exist below 20 kHz or above 4.8 kHz. So, it is very important to identify better dielectric material and an extended experimental investigation regarding optimisation of plasmolysis parameters is recommended.

In the current study, the focus was on the identification of cheaper electrode material e.g., brass and stainless steel etc., However, a more detailed experimental investigation involving conventional electrode material such as platinum is required to compare the effect of electrode material on plasmolysis efficiency.

Based on experimental results from optimisation experiments, a model could be proposed which could correlate the variables studied (pressure and flow rate of air, voltage and frequency of power used, length, material and configuration of electrodes) and predict the effect of varying them on plasmolysis efficiency.

This study identifies fluidic oscillation as cost effective method to produce microbubbles for hydrogen separation from product stream. However, further experiments could be conducted with a standard mixture of hydrogen, oxygen and argon to analyse separation performance. Although, the experiment would require safety precautions but it could be conducted while remaining within the flammability limits of hydrogen (4-75%).

The kinetics of water vapour plasmolysis has been studied in detail in chapter 3 using a homogenous kinetics model. However, a more robust model considering spatial effects on plasmolysis is recommended. The model should incorporate the effects of walls of the reactor in order to simulate quenching effect of wall and the extent to which it can affect plasmolysis. The model should help in monitoring the changes in plasma properties such as electron density or surface charge density by varying parameters like voltage or frequency on water vapour plasmolysis. Eventually a simulation of water vapour plasmolysis could help in optimising the operational parameters.

The reaction time scale calculated by kinetic modelling and volumetric mass transfer coefficient by bubbling air in water indicates reactive separation can occur in plasma-chemical reaction. Also, ozone concentration was found to increase when plasma was ignited below the diffuser. However, in order to draw a firm conclusion on the application of reactive separation process, more detailed experimental investigation is required. An ideal reactor needs to be designed in which plasma micro-reactor for hydrogen production and water column for separation could be integrated into one stage.

Based on the results from direct detection and measurement of hydrogen and optimisation studies a small sized hydrogen generator could be built such that it could be used in small scale applications.

References

ABDUL-MAJEED, W. S. 2012. *Development of online, continuous heavy metals detection and monitoring sensors based on microfluidic plasma reactors.* PhD, The Univeristy of Sheffield.

ABDUL-MAJEED, W. S., PARADA, J. H. L. & ZIMMERMAN, W. B. 2011. Optimization of a miniaturized DBD plasma chip for mercury detection in water samples. *Analytical and bioanalytical chemistry,* 401**,** 2713-2722.

ADHIKARI, S. & FERNANDO, S. 2006. Hydrogen membrane separation techniques. *Industrial & Engineering Chemistry Research,* 45**,** 875-881.

AKIYAMA, H. 2000. Streamer discharges in liquids and their applications. *Dielectrics and Electrical Insulation, IEEE Transactions on,* 7**,** 646-653.

AL-MASHHADANI, M. K., BANDULASENA, H. H. & ZIMMERMAN, W. B. 2011. CO2 mass transfer induced through an airlift loop by a microbubble cloud generated by fluidic oscillation. *Industrial & Engineering Chemistry Research,* 51**,** 1864-1877.

ALEKSANDROV, N., KINDYSHEVA, S., KIRPICHNIKOV, A., KOSAREV, I., STARIKOVSKAIA, S. & STARIKOVSKII, A. Y. 2007. Plasma decay in N2, CO2 and H2O excited by high-voltage nanosecond discharge. *Journal of Physics D: Applied Physics,* 40**,** 4493.

AVTAEVA, S., GENERAL, A. & KEL'MAN, V. 2010a. Kinetic model for low-density non-stationary gas discharge in water vapour. *Journal of Physics D: Applied Physics,* 43**,** 315201.

AVTAEVA, S., GENERAL, A. & KEL'MAN, V. 2010b. Kinetic model for low-density non-stationary gas discharge in water vapour. *Journal of Physics D: Applied Physics,* 43**,** 315201.

BABARITSKII, A., BARANOV, I., BIBIKOV, M., DEMKIN, S., ZHIVOTOV, V., KONOVALOV, G., LYSOV, G., MOSKOVSKII, A., RUSANOV, V. & SMIRNOV, R. 2004. Partial hydrocarbon oxidation processes induced by atmospheric-pressure microwave-discharge plasma. *High Energy Chemistry,* 38**,** 407-411.

BADER, H. & HOIGNÉ, J. 1981. Determination of ozone in water by the indigo method. *Water Research,* 15**,** 449-456.

BALAT, H. & KıRTAY, E. 2010. Hydrogen from biomass–present scenario and future prospects. *International Journal of Hydrogen Energy,* 35**,** 7416-7426.

BALAT, M. 2006. Biomass energy and biochemical conversion processing for fuels and chemicals. *Energy Sources, Part A,* 28**,** 517-525.

BALAT, M., BALAT, M., KıRTAY, E. & BALAT, H. 2009. Main routes for the thermo-conversion of biomass into fuels and chemicals. Part 2: Gasification systems. *Energy conversion and Management,* 50**,** 3158-3168.

BARNI, R., ESENA, P. & RICCARDI, C. 2005. Chemical kinetics simulation for atmospheric pressure air plasmas in a streamer regime. *Journal of Applied Physics,* 97**,** 073301-073301-7.

BASU, P. & KAUSHAL, P. 2009. Modeling of pyrolysis and gasification of biomass in fluidized beds: a review. *Chemical Product and Process Modeling,* 4.

BASU, S., KHAN, A. L., CANO-ODENA, A., LIU, C. & VANKELECOM, I. F. 2010. Membrane-based technologies for biogas separations. *Chemical Society Reviews,* 39**,** 750-768.

BEENAKKER, C., HEER, F. J. D., KROP, H. & MÖHLMANN, G. 1974. Dissociative excitation of water by electron impact. *Chemical Physics,* 6**,** 445-454.

BELLAN, P. M. 2006. *Fundamentals of plasma physics*, Cambridge Univ Pr.

BOC. 2014. *Industrial gases, A member of the Linde Group UK* [Online]. [Accessed 28-02-14 2014].

BOCKRIS, J. M., DANDAPANI, B., COCKE, D. & GHOROGHCHIAN, J. 1985. On the splitting of water. *International Journal of Hydrogen Energy,* 10**,** 179-201.

BOUTOT, T., BUCKLE, K., COLLINS, F., FLETCHER, D., FRONTAIN, E., KOZINSKI, J., LISTER, D., LIN, H., LIU, Z. & MENDOZA, G. 2004. High-Concentration Hydrogen Production from

Natural Gas Using a Pulsed Dielectric Barrier Discharge. *Proceedings Hydrogen and Fuel Cells*.

BP 2013. Statistical Review of World Energy

BUEHLER, R. E., STAEHELIN, J. & HOIGNÉ, J. 1984. Ozone decomposition in water studied by pulse radiolysis. 1. Perhydroxyl (HO2)/hyperoxide (O2-) and HO3/O3-as intermediates. *The Journal of Physical Chemistry,* 88**,** 2560-2564.

BURLICA, R., SHIH, K. Y. & LOCKE, B. 2010. Formation of H2 and H2O2 in a Water-Spray Gliding Arc Nonthermal Plasma Reactor. *Industrial & Engineering Chemistry Research*.

BUTTERWORTH, T. 2010. *Effect of volumetric flow rate on decontamination efficiency of a microplasma ozonation system.* MSc, The University of Sheffield.

CAPRIO, V., INSOLA, A., LIGNOLA, P. & VOLPICELLI, G. 1982. A new attempt for the evaluation of the absorption constant of ozone in water. *Chemical Engineering Science,* 37**,** 122-124.

CHAFFIN, J. H., BOBBIO, S. M., INYANG, H. I. & KAANAGBARA, L. 2006. Hydrogen production by plasma electrolysis. *Journal of energy engineering,* 132**,** 104-108.

CHENG, Y., PENA, M., FIERRO, J., HUI, D. & YEUNG, K. 2002. Performance of alumina, zeolite, palladium, Pd–Ag alloy membranes for hydrogen separation from Towngas mixture. *Journal of Membrane Science,* 204**,** 329-340.

CLAYTON, S. T., STIEGEL, G. J. & WIMER J.G. 2002. Gasification Markets and Technologies-Present and Future *In:* ENERGY, U. S. D. O. (ed.).

COCHRAN, W. C. & COX, G. M. 1992. *Experimental Design* Wiley.

COLLOT, A.-G. 2006. Matching gasification technologies to coal properties. *International Journal of Coal Geology,* 65**,** 191-212.

COTTERILL, P. 1961. The hydrogen embrittlement of metals. *Progress in Materials Science,* 9**,** 205-301.

DAS, D. & VEZIROĞLU, T. N. 2001. Hydrogen production by biological processes: a survey of literature. *International Journal of Hydrogen Energy,* 26**,** 13-28.

DEMIRBAŞ, A. 2002a. Gaseous products from biomass by pyrolysis and gasification: effects of catalyst on hydrogen yield. *Energy Conversion and Management,* 43**,** 897-909.

DEMIRBAŞ, A. 2002b. Hydrogen production from biomass by the gasification process. *Energy Sources,* 24**,** 59-68.

DEPARTMENT OF ENERGY & CLIMATE, U. 2012. A National Statistics Publication, Quarterly Energy Prices *In:* ENERGY PRICE ANALYSIS TEAM , D. O. E. C., UK (ed.).

DIXON-LEWIS, G., SUTTON, M. & WILLIAMS, A. 1962. The kinetics of hydrogen atom recombination. *Discuss. Faraday Soc.,* 33**,** 205-212.

DIXON, R. K. 2007. Advancing towards a hydrogen energy economy: status, opportunities and barriers. *Mitigation and Adaptation Strategies for Global Change,* 12**,** 325-341.

DOLAN, T. 1993. Electron and ion collisions with water vapour. *Journal of Physics D: Applied Physics,* 26**,** 4.

EISENBERG, G. 1943. Colorimetric determination of hydrogen peroxide. *Industrial & Engineering Chemistry Analytical Edition,* 15**,** 327-328.

ELIASSON, B. & KOGELSCHATZ, U. 1991. Modeling and applications of silent discharge plasmas. *Plasma Science, IEEE Transactions on,* 19**,** 309-323.

FORNI, L., BAHNEMANN, D. & HART, E. J. 1982. Mechanism of the hydroxide ion-initiated decomposition of ozone in aqueous solution. *The Journal of Physical Chemistry,* 86**,** 255-259.

FREIRE, A. P. S., MIRANDA, D. D. E., LUZ, L. & FRANÇA, G. F. 2002. Bubble plumes and the Coanda effect. *International journal of multiphase flow,* 28**,** 1293-1310.

FRIDMAN, A. 2008. *Plasma chemistry*, Cambridge University Press.

FRIDMAN, A., CHIROKOV, A. & GUTSOL, A. 2005. Non-thermal atmospheric pressure discharges. *J. Phys. D: Appl. Phys,* 38**,** R1-R24.

FRIDMAN, A. A. & KENNEDY, L. A. 2004. *Plasma physics and engineering*, CRC.

GIBALOV, V. I. & PIETSCH, G. J. 2000. The development of dielectric barrier discharges in gas gaps and on surfaces. *Journal of Physics D: Applied Physics,* 33**,** 2618.

GIVOTOV, V., FRIDMAN, A., KROTOV, M., KRASHENINNIKOV, E., PATRUSHEV, B., RUSANOV, V. & SHOLIN, G. 1981. Plasmochemical methods of hydrogen production. *International Journal of Hydrogen Energy,* 6**,** 441-449.

GORDILLO-VÁZQUEZ, F. J., CAMERO, M. & GOMEZ-ALEIXANDRE, C. 2006. Spectroscopic measurements of the electron temperature in low pressure radiofrequency Ar/H2/C2H2 and Ar/H2/CH4 plasmas used for the synthesis of nanocarbon structures. *Plasma Sources Science and Technology,* 15**,** 42.

GRAY, N. F. 1990. *Activated sludge: theory and practice*, Oxford University Press.

GRIGORIEV, S., POREMBSKY, V. & FATEEV, V. 2006. Pure hydrogen production by PEM electrolysis for hydrogen energy. *International Journal of Hydrogen Energy,* 31**,** 171-175.

GUOXIN, H., HAO, H. & YANHONG, L. 2009. Hydrogen-Rich Gas Production from Pyrolysis of Biomass in an Autogenerated Steam Atmosphere. *Energy & Fuels,* 23**,** 1748-1753.

HADJ-ZIANE, S., HELD, B., PIGNOLET, P., PEYROUS, R. & COSTE, C. 1992. Ozone generation in an oxygen-fed wire-to-cylinder ozonizer at atmospheric pressure. *Journal of Physics D: Applied Physics,* 25**,** 677.

HAGELAAR, G., KROESEN, G., VAN SLOOTEN, U. & SCHREUDERS, H. 2000. Modeling of the microdischarges in plasma addressed liquid crystal displays. *Journal of Applied Physics,* 88**,** 2252.

HARTGERS, A., VAN DER HEIJDEN, H., BEKS, M., VAN DIJK, J. & VAN DER MULLEN, J. 2005. An elemental diffusion description for LTE plasma models. *Journal of Physics D: Applied Physics,* 38**,** 3422.

HERRON, J. T. 2001. Modeling studies of the formation and destruction of NO in pulsed barrier discharges in nitrogen and air. *Plasma chemistry and plasma processing,* 21**,** 581-609.

HILL, S. J. 2006. *Inductively coupled plasma spectrometry and its applications*, Wiley-Blackwell.

HOIGNÉ, J. 1998. Chemistry of aqueous ozone and transformation of pollutants by ozonation and advanced oxidation processes. *Quality and Treatment of Drinking Water II.* Springer.

HOIGNE, J. & BADER, H. 1976. The role of hydroxyl radical reactions in ozonation processes in aqueous solutions. *Water Research,* 10**,** 377-386.

HOLLADAY, J. D., HU, J., KING, D. L. & WANG, Y. 2009. An overview of hydrogen production technologies. *Catalysis Today,* 139**,** 244-260.

HONG, Y. C., UHM, H. S. & YI, W. J. 2008. Atmospheric pressure nitrogen plasma jet: Observation of striated multilayer discharge patterns. *Applied Physics Letters,* 93**,** 051504-051504-3.

ITIKAWA, Y. & MASON, N. 2005. Cross sections for electron collisions with water molecules. *Journal of physical and chemical reference data,* 34**,** 1-22.

JASINSKI, M., DORS, M. & MIZERACZYK, J. 2008. Production of hydrogen via methane reforming using atmospheric pressure microwave plasma. *Journal of Power sources,* 181**,** 41-45.

JOENSEN, F. & ROSTRUP-NIELSEN, J. R. 2002. Conversion of hydrocarbons and alcohols for fuel cells. *Journal of Power Sources,* 105**,** 195-201.

JOHANNA, I. 2004. Summary of electrolytic hydrogen production *In:* NATIONAL RENEWABLE ENERGY LABORATORIES, U. S. (ed.). Colorado

KADO, S., SEKINE, Y., NOZAKI, T. & OKAZAKI, K. 2004. Diagnosis of atmospheric pressure low temperature plasma and application to high efficient methane conversion. *Catalysis Today,* 89**,** 47-55.

KAWAHARA, A., SADATOMI, M., MATSUYAMA, F., MATSUURA, H., TOMINAGA, M. & NOGUCHI, M. 2009. Prediction of micro-bubble dissolution characteristics in water and seawater. *Experimental Thermal and Fluid Science,* 33**,** 883-894.

KIM, D. B., RHEE, J., MOON, S. & CHOE, W. 2006. Study of geometrical and operational parameters controlling the low frequency microjet atmospheric pressure plasma characteristics. *Applied Physics Letters,* 89**,** 061502.

KIRKPATRICK, M. J. & LOCKE, B. R. 2005. Hydrogen, oxygen, and hydrogen peroxide formation in aqueous phase pulsed corona electrical discharge. *Industrial & Engineering Chemistry Research,* 44**,** 4243-4248.

KITAMURA, N., SAKAMOTO, T., MATSUURA, H. & AKATSUKA, H. Year. Dependence of Vibrational and Rotational Temperatures of Microwave Discharge Nitrogen-Oxygen Mixed Discharge on their Mixture Ratio. *In:* 27th International Conference Phenomena in Ionised Gases, CD-ROM Proceedings, 2005. 03-080.

KOGELSCHATZ, U. 2003. Dielectric-barrier discharges: their history, discharge physics, and industrial applications. *Plasma chemistry and plasma processing,* 23**,** 1-46.

KOGELSCHATZ, U., ELIASSON, B. & EGLI, W. 1997. Dielectric-barrier discharges. Principle and applications. *Journal de Physique IV,* 7.

KOGELSCHATZ, U., ELIASSON, B. & EGLI, W. 1999. From ozone generators to flat television screens: history and future potential of dielectric-barrier discharges. *Pure and Applied Chemistry,* 71**,** 1819-1828.

KONSOWA, A. 2003. Decolorization of wastewater containing direct dye by ozonation in a batch bubble column reactor. *Desalination,* 158**,** 233-240.

KOO, I. G. & LEE, W. M. 2007. Hydrogen generation by plasma-assisted electrochemical pumping. *Electrochemistry Communications,* 9**,** 2325-2329.

KOSAREV, I. & STARIKOVSKII, A. Y. 2000. Mechanism for electric breakdown in a chemically nonequilibrium system and the influence of the chain oxidation reaction in an H2-air mixture on the breakdown threshold. *Plasma Physics Reports,* 26**,** 701-709.

KOSSYI, I., KOSTINSKY, A. Y., MATVEYEV, A. & SILAKOV, V. 1992. Kinetic scheme of the non-equilibrium discharge in nitrogen-oxygen mixtures. *Plasma Sources Science and Technology,* 1**,** 207.

KOSTOV, K., HONDA, R., ALVES, L. & KAYAMA, M. 2009. Characteristics of dielectric barrier discharge reactor for material treatment. *Brazilian Journal of Physics,* 39**,** 322-325.

KOTHARI, R., BUDDHI, D. & SAWHNEY, R. 2004. Sources and technology for hydrogen production: a review. *International journal of global energy issues,* 21**,** 154-178.

KREGAR, Z., KRSTULOVIĆ, N., VUKELIĆ, N. G. & MILOŠEVIĆ, S. 2009. Space and time resolved optical emission spectroscopy characterization of inductively coupled RF water vapour plasma. *Journal of Physics D: Applied Physics,* 42**,** 145201.

KRIEGSEIS, J., GRUNDMANN, S. & TROPEA, C. 2011. Power consumption, discharge capacitance and light emission as measures for thrust production of dielectric barrier discharge plasma actuators. *Journal of applied physics,* 110**,** 013305.

KROPOSKI, B., LEVENE, J., HARRISON, K., SEN, P. K. & NOVACHEK, F. 2006. Electrolysis: Information and Opportunities for Electric Power Utilities *In:* NATIONAL RENEWABLE ENERGY LABORATORIES, U. S. (ed.). Colorado

LANGMUIR, I. 1929. The interaction of electron and positive ion space charges in cathode sheaths. *Physical Review,* 33**,** 954.

LARKIN, F. & THRUSH, B. Year. The kinetics of hydrogen-atom recombination. *In*, 1965. Elsevier, 397-402.

LARMINIE, J., DICKS, A. & MCDONALD, M. S. 2003. *Fuel cell systems explained*, Wiley Chichester.

LAROUSSI, M. 2002. Nonthermal decontamination of biological media by atmospheric-pressure plasmas: Review, analysis, and prospects. *Plasma Science, IEEE Transactions on,* 30**,** 1409-1415.

LAUX, C., SPENCE, T., KRUGER, C. & ZARE, R. 2003. Optical diagnostics of atmospheric pressure air plasmas. *Plasma Sources Science and Technology,* 12**,** 125.

LAUX, C. O. Year. Radiation and non-equilibrium collisional radiative models, in Physico-chemical Models for High Enthalpy and Plasma Flows *In:* D. G. FLETCHER ET AL., ed. VKI LS, (2002-2007) 2002 Genese, Belgium

LEE, Y. & VON GUNTEN, U. 2010. Oxidative transformation of micropollutants during municipal wastewater treatment: comparison of kinetic aspects of selective (chlorine, chlorine dioxide, ferrate VI, and ozone) and non-selective oxidants (hydroxyl radical). *Water research,* 44**,** 555.

LI, S. Z., HUANG, W. T., ZHANG, J. & WANG, D. 2009. Optical diagnosis of an argon/oxygen needle plasma generated at atmospheric pressure. *Applied Physics Letters,* 94**,** 111501.

LIEBERMAN, M. A. & LICHTENBERG, A. J. 2005. *Principle of Plasma Discharge and Material Processing*, John Wiley & Sons, Inc.

LIU, X., LIU, C. J. & ELIASSON, B. 2003. Hydrogen production from methanol using corona discharges. *Chinese Chemical Letters,* 14**,** 631-633.

LOCKE, B., SATO, M., SUNKA, P., HOFFMANN, M. & CHANG, J. S. 2006. Electrohydraulic discharge and nonthermal plasma for water treatment. *Industrial & Engineering Chemistry Research,* 45**,** 882-905.

LOZANO-PARADA, J. H. 2007. *Design simulation and fabrication of microchannel plasma rector.* PhD, The University of Sheffield

LOZANO-PARADA, J. H. & ZIMMERMAN, W. B. 2010. The role of kinetics in the design of plasma microreactors. *Chemical Engineering Science,* 65**,** 4925-4930.

LUKES, P., CLUPEK, M., BABICKY, V., SIMEK, M., TOTHOVA, I., JANDA, V., MOUCHA, T. & & KORDAC, M. 2008a. Role of solution conductivity in the electron impact dissociation of H2O induced by plasma processes in the pulsed corona discharge in water. *HAKONE XI, 11th International Symposium on High Pressure, Low Temperature Plasma Chemistry, Contributed Papers.* . Oléron Island.

LUKES, P., CLUPEK, M., BABICKY, V. & SUNKA, P. 2008b. Ultraviolet radiation from the pulsed corona discharge in water. *Plasma Sources Science and Technology,* 17**,** 024012.

LUMANAUW, D. 2000. Hydrogen bubble characterization in alkaline water electrolysis. *A thesis submitted in conformity with the requirements for the degree of Master of Applied Science Gnduate Department of Metailurgy and Materiais Science. University of Toronto, Copyright by Daniel Lumanauw*.

MAEHARA, T., TOYOTA, H., KURAMOTO, M., IWAMAE, A., TADOKORO, A., MUKASA, S., YAMASHITA, H., KAWASHIMA, A. & NOMURA, S. 2006. Radio frequency plasma in water. *Jpn J Appl Phys,* 45**,** 8864-8868.

MANLEY, T. 1943. The electric characteristics of the ozonator discharge. *Transactions of the electrochemical society,* 84**,** 83-96.

MASOUD, N., MARTUS, K., FIGUS, M. & BECKER, K. 2005. Rotational and Vibrational Temperature Measurements in a High-Pressure Cylindrical Dielectric Barrier Discharge (C-DBD). *Contributions to Plasma Physics,* 45**,** 32-39.

MEDEDOVIC, S., FINNEY, W. C. & LOCKE, B. R. 2008. Electrical discharges in mixtures of light and heavy water. *Plasma Processes and Polymers,* 5**,** 76-83.

MEDODOVIC, S. & LOCKE, B. 2009. Primary chemical reactions in pulsed electrical discharge channels in water. *Journal of Physics D: Applied Physics,* 42**,** 049801.

MIZUNO, T., AKIMOTO, T. & OHMORI, T. Year. Confirmation of anomalous hydrogen generation by plasma electrolysis. *In:* Proc. 4th meeting JCF research Soc., ed. H. Yamada, 2002. 27-31.

MORAVEJ, M., YANG, X., NOWLING, G., CHANG, J., HICKS, R. & BABAYAN, S. 2004. Physics of high-pressure helium and argon radio-frequency plasmas. *Journal of applied physics,* 96**,** 7011-7017.

MOTRET, O., HIBERT, C., PELLERIN, S. & POUVESLE, J. 2000. Rotational temperature measurements in atmospheric pulsed dielectric barrier discharge-gas temperature and molecular fraction effects. *Journal of Physics D: Applied Physics,* 33**,** 1493.

MUELLER-LANGER, F., TZIMAS, E., KALTSCHMITT, M. & PETEVES, S. 2007. Techno-economic assessment of hydrogen production processes for the hydrogen economy for the short and medium term. *International Journal of Hydrogen Energy,* 32**,** 3797-3810.

MUKASA, S., NOMURA, S., TOYOTA, H., MAEHARA, T. & YAMASHITA, H. 2011. Internal conditions of a bubble containing radio-frequency plasma in water. *Plasma Sources Science and Technology,* 20**,** 034020.

MURADOV, N. & VEZIROĞLU, T. 2005. From hydrocarbon to hydrogen–carbon to hydrogen economy. *International Journal of Hydrogen Energy,* 30**,** 225-237.

MURADOV, N. Z. 1998. CO2-free production of hydrogen by catalytic pyrolysis of hydrocarbon fuel. *Energy & Fuels,* 12**,** 41-48.

MUTAF-YARDIMCI, O., SAVELIEV, A., FRIDMAN, A. & KENNEDY, L. 1998. Employing plasma as catalyst in hydrogen production. *International Journal of Hydrogen Energy,* 23**,** 1109-1111.

NEHRA, V., KUMAR, A. & DWIVEDI, H. 2008. Atmospheric non-thermal plasma sources. *International Journal of Engineering (IJE),* 2**,** 53.

NGUYEN, S. V. T., FOSTER, J. E. & GALLIMORE, A. D. 2009. Operating a radio-frequency plasma source on water vapor. *Review of Scientific Instruments,* 80**,** 083503.

NI, M., LEUNG, D. Y. C., LEUNG, M. K. H. & SUMATHY, K. 2006. An overview of hydrogen production from biomass. *Fuel Processing Technology,* 87**,** 461-472.

NIST 2011. National Institute of standard and technology

NIST 2012. National Institute of Standards and Technology 2011 ed.

NIXON, J. & PAULEY, S. P. 2014. *Missouri Department of Natural resources* [Online]. Missouri [Accessed 26-02-14 2014].

NREL 2004. 2003 Research Review *In:* NATIONAL RENEWABLE ENERGY LABORATORIES, U. S. (ed.). Colorado

ORIANI, R. 1978. Hydrogen embrittlement of steels. *Annual review of materials science,* 8**,** 327-357.

PACHECO, M., PACHECO, J., MORENO, H., MERCADO, A., VALDIVIA, R. & SANTANA, A. 2008. OES analysis in a nonthermal plasma used for toxic gas removal: Rotational and excitation temperature estimation. *Laser physics,* 18**,** 303-307.

PAPAGIANNAKIS, I. 2005. Studying and improving the efficiency of water electrolysis using a proton exchange membrane electrolyser. *The Energy Systems Research Unit (ESRU)*.

PAULMIER, T. & FULCHERI, L. 2005. Use of non-thermal plasma for hydrocarbon reforming. *Chemical engineering journal,* 106**,** 59-71.

PETITJEAN, L. & RICARD, A. 1984. Emission spectroscopy study of N2-H2 glow discharge for metal surface nitriding. *Journal of Physics D: Applied Physics,* 17**,** 919.

PETITPAS, G., ROLLIER, J.-D., DARMON, A., GONZALEZ-AGUILAR, J., METKEMEIJER, R. & FULCHERI, L. 2007. A comparative study of non-thermal plasma assisted reforming technologies. *International Journal of Hydrogen Energy,* 32**,** 2848-2867.

PINART, J., SMIRDEC, M., PINART, M.-E., AARON, J., BENMANSOUR, Z., GOLDMAN, M. & GOLDMAN, A. 1996. Quantitative study of the formation of inorganic chemical species following corona discharge—I. Production of HNO< sub> 2</sub> and HNO< sub> 3</sub> in a composition-controlled, humid atmosphere. *Atmospheric Environment,* 30**,** 129-132.

PORTER, D., POPLIN, M. D., HOLZER, F., FINNEY, W. C. & LOCKE, B. R. 2009. Formation of hydrogen peroxide, hydrogen, and oxygen in gliding arc electrical discharge reactors with water spray. *Industry Applications, IEEE Transactions on,* 45**,** 623-629.

PRINS, M. J., PTASINSKI, K. J. & JANSSEN, F. J. 2007. From coal to biomass gasification: Comparison of thermodynamic efficiency. *Energy,* 32**,** 1248-1259.

RAJVANSHI, A. K. 1986. Biomass gasification. *Alternative energy in agriculture,* 2**,** 83-102.

REBA, I. 1966. Applications of the Coanda effect. *Scientific American,* 214**,** 84-92.

REHMAN, F., ABDUL-MAJEED, W. & ZIMMERMAN, W. B. 2013. Hydrogen production from water vapour plasmolysis using DBD-Corona hybrid reactor. *Energy & Fuels*.

REHMAN, F., LOZANO-PARADA, J. H. & ZIMMERMAN, W. B. 2012. A kinetic model for H_2 production by plasmolysis of water vapours at atmospheric pressure in a dielectric barrier discharge microchannel reactor. *International Journal of Hydrogen Energy,* 37**,** 17678-17690.

RICO, V. J., COTRINO, J., GALLARDO, V., SARMIENTO, B., BREY, J. J. & GONZÁLEZ-ELIPE, A. R. 2009. Hybrid catalytic-DBD plasma reactor for the production of hydrogen and preferential CO oxidation (CO-PROX) at reduced temperatures. *Chemical Communications***,** 6192-6194.

ROSS, D. 2006. Hydrogen storage: The major technological barrier to the development of hydrogen fuel cell cars. *Vacuum,* 80**,** 1084-1089.

ROSTRUP-NIELSEN, J. R. & ROSTRUP-NIELSEN, T. 2002. Large-scale hydrogen production. *Cattech,* 6**,** 150-159.

RUBIN, M. B. 2001. The history of ozone. The Schönbein period, 1839–1868. *Bull. Hist. Chem,* 26**,** 40-56.

SALABAS, A., MARQUES, L., JOLLY, J., GOUSSET, G. & ALVES, L. 2004. Systematic characterization of low-pressure capacitively coupled hydrogen discharges. *Journal of applied physics,* 95**,** 4605-4620.

SARMIENTO, B., BREY, J. J., VIERA, I. G., GONZALEZ-ELIPE, A. R., COTRINO, J. & RICO, V. J. 2007. Hydrogen production by reforming of hydrocarbons and alcohols in a dielectric barrier discharge. *Journal of Power sources,* 169**,** 140-143.

SATO, M. 2008. Environmental and biotechnological applications of high-voltage pulsed discharges in water. *Plasma Sources Science and Technology,* 17**,** 024021.

SCHEMBECKER, G. & TLATLIK, S. 2003. Process synthesis for reactive separations. *Chemical Engineering and Processing: Process Intensification,* 42**,** 179-189.

SCHÖNBEIN, C. Year. On the Odour Accompanying Electricity, and on the Probability of Its Dependence on the Presence of a New Substrate.[Abstract]. *In:* Abstracts of the Papers Printed in the Philosophical Transactions of the Royal Society of London, 1837. JSTOR, 226-226.

SCHUTZE, A., JEONG, J. Y., BABAYAN, S. E., PARK, J., SELWYN, G. S. & HICKS, R. F. 1998. The atmospheric-pressure plasma jet: A review and comparison to other plasma sources. *Plasma Science, IEEE Transactions on,* 26**,** 1685-1694.

SHIH, K. Y. & LOCKE, B. R. 2010a. Chemical and physical characteristics of pulsed electrical discharge within gas bubbles in aqueous solutions. *Plasma Chemistry and Plasma Processing,* 30**,** 1-20.

SHIH, K. Y. & LOCKE, B. R. 2010b. Optical and Electrical Diagnostics of the Effects of Conductivity on Liquid Phase Electrical Discharge. *Plasma Science, IEEE Transactions on***,** 1-10.

SHIRAFUJI, T., MORITA, T., SAKAI, O. & TACHIBANA, K. 2009. Enhancement of of OH production rate in plasma on water by mixing Ar. *International symposium on plasma chemistry* Bochum, Germany.

SIEMENS 1857. *Poggendorf's Ann. Phys. Chem.,* 102.

SIMPSON, A. P. & LUTZ, A. E. 2007. Exergy analysis of hydrogen production via steam methane reforming. *International Journal of Hydrogen Energy,* 32**,** 4811-4820.

ŠINGLIAR, M. 2007. Solar energy using for hydrogen production. *Petroleum & Coal,* 49**,** 40-47.

SISMANOGLU, B. & AMORIM, J. 2008. Microhollow cathode discharge and breakdown in micron separations. *The European Physical Journal- Applied Physics,* 41**,** 165-172.

SOBACCHI, M., SAVELIEV, A., FRIDMAN, A., KENNEDY, L. A., AHMED, S. & KRAUSE, T. 2002. Experimental assessment of a combined plasma/catalytic system for hydrogen production via partial oxidation of hydrocarbon fuels. *International Journal of Hydrogen Energy,* 27**,** 635-642.

SOLOMON, S., QIN, D., MANNING, M., ALLEY, R., BERNTSEN, T., BINDOFF, N., CHEN, Z., CHIDTHAISONG, A., GREGORY, J. & HEGERL, G. 2007. Climate change 2007: The physical science basis, contribution of working group 1 to the fourth assessment report of the Intergovernmental Panel on Climate Change. Cambridge University Press.

SOTELO, J., BELTRAN, F., BENITEZ, F. & BELTRAN-HEREDIA, J. 1989. Henry's law constant for the ozone-water system. *Water Research,* 23**,** 1239-1246.

STAEHELIN, J. & HOIGNE, J. 1982. Decomposition of ozone in water: rate of initiation by hydroxide ions and hydrogen peroxide. *Environmental Science & Technology,* 16**,** 676-681.

STEFANIDIS, G. D. & VLACHOS, D. G. 2010. Intensification of steam reforming of natural gas: Choosing combustible fuel and reforming catalyst. *Chemical Engineering Science,* 65**,** 398-404.

STOFFELS, E., FLIKWEERT, A., STOFFELS, W. & KROESEN, G. 2002. Plasma needle: a non-destructive atmospheric plasma source for fine surface treatment of (bio) materials. *Plasma Sources Science and Technology,* 11**,** 383.

TENDERO, C., TIXIER, C., TRISTANT, P., DESMAISON, J. & LEPRINCE, P. 2006. Atmospheric pressure plasmas: A review. *Spectrochimica Acta Part B: Atomic Spectroscopy,* 61**,** 2-30.

TESAŘ, V. 2012. MICROBUBBLE GENERATION BY FLUIDICS. PART I: DEVELOPMENT OF THE OSCILLATOR. *Colloquim Fluid Dynamics* Institute of Thermomechanics AS CR, v.v.vi., Paragues, Czech Republic.

TOMIYASU, H., FUKUTOMI, H. & GORDON, G. 1985. Kinetics and mechanism of ozone decomposition in basic aqueous solution. *Inorganic Chemistry,* 24**,** 2962-2966.

TOOLBOX, T. E. 2014. *Resistivity, Conductivity and Temperature coefficients for some common materials* [Online]. [Accessed 26-02-14 2014].

UDAGAWA, J., AGUIAR, P. & BRANDON, N. 2007. Hydrogen production through steam electrolysis: model-based steady state performance of a cathode-supported intermediate temperature solid oxide electrolysis cell. *Journal of Power sources,* 166**,** 127-136.

VALDIVIA-BARRIENTOS, R., PACHECO-SOTELO, J., PACHECO-PACHECO, M., MERCADO-CABRERA, A., JIMÉNEZ-LÓPEZ, M. L., CRUZ-AZOCAR, V., RAMOS-FLORES, F., DURÁN-GARCÍA, M. & HIDALGO-PÉREZ, A. M. 2008. Temperature Evaluation of the Nonthermal Equilibrium of Plasma Discharges by OES Analysis. *Laser Physics-Nonlinear optics and spectroscopy* 18**,** 298-302.

VAN DER SIJDE, B. & VAN DER MULLEN, J. 1990. Temperature determination in non-LTE plasmas. *Journal of Quantitative Spectroscopy and Radiative Transfer,* 44**,** 39-46.

VON GUNTEN, U. 2003. Ozonation of drinking water: Part I. Oxidation kinetics and product formation. *Water Research,* 37**,** 1443-1467.

WANG, H., PAUL, D. R. & CHUNG, T.-S. 2013. Surface modification of polyimide membranes by diethylenetriamine (DETA) vapor for H< sub> 2</sub> purification and moisture effect on gas permeation. *Journal of Membrane Science,* 430**,** 223-233.

WANG, W., ZHU, C. & CAO, Y. 2010. DFT study on pathways of steam reforming of ethanol under cold plasma conditions for hydrogen generation. *International Journal of Hydrogen Energy,* 35**,** 1951-1956.

WEI, D., LU, X., LU, Z. & GU, J. 2007. Performance analysis and optimization of organic Rankine cycle (ORC) for waste heat recovery. *Energy conversion and Management,* 48**,** 1113-1119.

XI ZHEN, L., LIU, C. J. & ELIASSON, B. 2003. Hydrogen Production from Methanol Using Corona Discharges. *Chinese Chemical Letters,* 14**,** p631-633.

YAGI, S. & TANAKA, M. 1979. Mechanism of ozone generation in air-fed ozonisers. *Journal of Physics D: Applied Physics,* 12**,** 1509.

YAN, Z., CHEN, L. & WANG, H. 2008. Hydrogen generation by glow discharge plasma electrolysis of ethanol solutions. *Journal of Physics D: Applied Physics,* 41**,** 155205.

YE, Q., WU, Y., LI, X., CHEN, T. & SHAO, G. 2012. Uniformity of dielectric barrier discharges using mesh electrodes. *Plasma Sources Science and Technology,* 21**,** 065008.

ZENG, K. & ZHANG, D. 2010. Recent progress in alkaline water electrolysis for hydrogen production and applications. *Progress in Energy and Combustion Science,* 36**,** 307-326.

ZHANG, Y., WEN, X. H. & YANG, W. H. 2007. Excitation temperatures of atmospheric argon in dielectric barrier discharges. *Plasma Sources Science and Technology,* 16**,** 441.

ZHU, Z., ZHANG, S., LV, Y. & ZHANG, X. 2006. Atomization of hydride with a low-temperature, atmospheric pressure dielectric barrier discharge and its application to arsenic speciation with atomic absorption spectrometry. *Analytical chemistry,* 78**,** 865-872.

ZIMMERMAN, W. B. 2011. Electrochemical microfluidics. *Chemical Engineering Science,* 66**,** 1412-1425.

ZIMMERMAN, W. B., LOZANO-PARADA, J. H. & BANDULASENA, H. H. 2010. Ozone regenerated: low power consumption and high dispersal rates with microbubbles. *J. Sewerage & Water*.

ZIMMERMAN, W. B., TESAR, V., BUTLER, S. & BANDULASENA, H. C. 2008. Microbubble generation. *Recent Patents on Engineering,* 2**,** 1-8.

ZIMMERMAN, W. B., ZANDI, M., HEMAKA BANDULASENA, H., TESAŘ, V., JAMES GILMOUR, D. & YING, K. 2011. Design of an airlift loop bioreactor and pilot scales studies with fluidic oscillator induced microbubbles for growth of a microalgae< i> Dunaliella salina</i>. *Applied Energy,* 88**,** 3357-3369.

ZIMMERMAN, W. B. J. & TESAR, V. 2013. BUBBLE GENERATION FOR AERATION AND OTHER PURPOSES. US Patent 20,130,092,626.

ZITO, J. C., ARNOLD, D. P., DURSCHER, R. J. & ROY, S. Year. Investigation of Impedance Characteristics and Power Delivery for Dielectric Barrier Discharge Plasma Actuators. *In:* 48th AIAA Aerospace Sciences Meeting, 2010.

List of Appendices

Appendix-I

The model is checked by running the model with initial water number density of 1 x10^{25} m^{-3} calculated at 1000 ^{o}C by Van der Vaal's instead of 1.93 x 10^{25} m^{-3} using ideal gas law. The number density of H_2 produced was dropped from 9.64 x 10^{24} m^{-3} to 6.62 x 10^{24} to m^{-3}. However, more importantly, the behaviour of the concentration profiles doesn't change. A snapshot of the concentration profiles is shown in **Figure 7-1**.

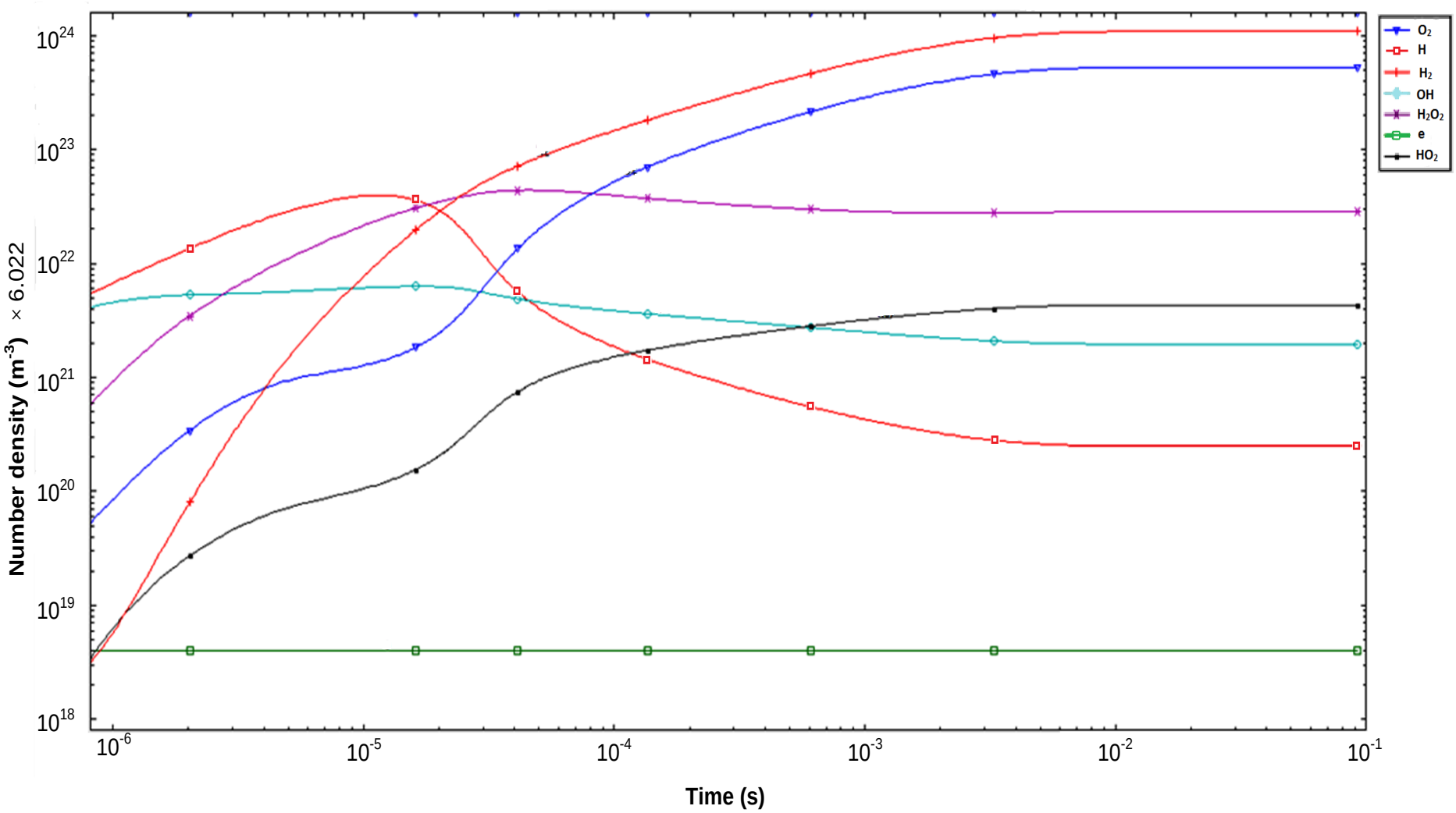

Figure 0-1 Concentration profiles of species using water vapour concentration at 1000C using Van der Waal's equation of state

Appendix-II

Print Date: Mon Dec 16 09:39:11 2013 Page 1 of 1

Title :
Run File : C:\Star\keith\270412388.run
Method File : C:\Star\GR Series Bypass +HCs.mth
Sample ID : Fahad110213_2

Injection Date: 2/11/13 3:10 PM Calculation Date: 2/11/13 3:15 PM

Operator : M.Jones Detector Type: 0800 (1 Volt)
Workstation: C Bus Address : 80
Instrument : E55 GC Sample Rate : 10.00 Hz
Channel : 1 = TCD Run Time : 5.002 min

** Star Chromatography Workstation Version 5.52 ** 00123-7691-66A-4051 **

Run Mode : Analysis
Peak Measurement: Peak Area
Calculation Type: External Standard

Peak No.	Peak Name	Result ()	Ret. Time (min)	Time Offset (min)	Area (counts)	Sep. Code	Width 1/2 (sec)	Status Codes
1	Helium/H2	0.2306	0.792	-0.004	11261	BV	1.6	
2	O2	0.5195	0.980	-0.005	11723	VB	0.0	
	Totals:	0.7501		-0.009	22984			

Total Unidentified Counts : 0 counts

Detected Peaks: 6 Rejected Peaks: 4 Identified Peaks: 2

Multiplier: 1 Divisor: 1 Unidentified Peak Factor: 0

Baseline Offset: -13032 microVolts

Noise (used): 14 microVolts - monitored before this run

Manual injection

****

Figure 0-2 GC analysis of one of the samples collected in standard gas collection bags

Print Date: Thu Dec 12 13:29:23 2013 Page 1 of 1

Title :
Run File : C:\Star\keith\270412418.run
Method File : C:\Star\GR Series Bypass +HCs.mth
Sample ID : Fahad180212_C

Injection Date: 2/18/13 3:10 PM Calculation Date: 2/18/13 3:11 PM

Operator : K.Penny Detector Type: 0800 (1 Volt)
Workstation: C Bus Address : 80
Instrument : E55 GC Sample Rate : 10.00 Hz
Channel : 1 = TCD Run Time : 1.317 min

** Star Chromatography Workstation Version 5.52 ** 00123-7691-66A-4051 **

Run Mode : Analysis
Peak Measurement: Peak Area
Calculation Type: External Standard

Peak No.	Peak Name	Result ()	Ret. Time (min)	Time Offset (min)	Area (counts)	Sep. Code	Width 1/2 (sec)	Status Codes
1	Helium/H2	0.6251	0.834	0.010	36984	BV	1.6	
2	O2	5.6662	1.038	0.012	54061	VB	1.8	C
	Totals:	6.2913		0.022	91045			

Status Codes:
C - Out of calibration range

Total Unidentified Counts : 0 counts

Detected Peaks: 2 Rejected Peaks: 0 Identified Peaks: 2

Multiplier: 1 Divisor: 1 Unidentified Peak Factor: 0

Baseline Offset: -10743 microVolts

Noise (used): 53 microVolts - monitored before this run

Manual injection

Calib. out of range; No Recovery Action Specified

****

Figure 0-3 GC analysis of one of the samples collected from the top of the condenser

Print Date: Thu Dec 12 12:46:20 2013 Page 1 of 1

Title :
Run File : C:\Star\Fahad Decomp\270412402.run
Method File : C:\Star\GR Series Bypass +HCs.mth
Sample ID : Fahad120213_5

Injection Date: 2/12/13 11:10 AM Calculation Date: 2/12/13 11:11 AM

Operator : M.Jones Detector Type: 0800 (1 Volt)
Workstation: C Bus Address : 80
Instrument : E55 GC Sample Rate : 10.00 Hz
Channel : 1 = TCD Run Time : 1.763 min

** Star Chromatography Workstation Version 5.52 ** 00123-7691-66A-4051 **

Run Mode : Analysis
Peak Measurement: Peak Area
Calculation Type: External Standard

Peak No.	Peak Name	Result ()	Ret. Time (min)	Time Offset (min)	Area (counts)	Sep. Code	Width 1/2 (sec)	Status Codes
1	Helium/H2	0.0799	0.793	-0.012	3201	BV	1.7	
2	O2	19.0532	0.988	-0.007	217814	VP	1.7	C
	Totals:	19.1331		-0.019	221015			

Status Codes:
C - Out of calibration range

Total Unidentified Counts : 0 counts

Detected Peaks: 5 Rejected Peaks: 3 Identified Peaks: 2

Multiplier: 1 Divisor: 1 Unidentified Peak Factor: 0

Baseline Offset: -10938 microVolts

Noise (used): 11 microVolts - monitored before this run

Manual injection

Calib. out of range; No Recovery Action Specified

****

Figure 0-4 GC analysis of one of the samples collected in glass tube

Print Date: Thu Dec 12 13:03:42 2013 Page 1 of 1

Title :
Run File : C:\Star\keith\270412410.run
Method File : C:\Star\GR Series Bypass +HCs.mth
Sample ID : Fahad150213glass

Injection Date: 2/15/13 3:30 PM Calculation Date: 2/15/13 3:31 PM

Operator : K.Penny Detector Type: 0800 (1 Volt)
Workstation: C Bus Address : 80
Instrument : E55 GC Sample Rate : 10.00 Hz
Channel : 1 = TCD Run Time : 1.327 min

** Star Chromatography Workstation Version 5.52 ** 00123-7691-66A-4051 **

Run Mode : Analysis
Peak Measurement: Peak Area
Calculation Type: External Standard

Peak No.	Peak Name	Result ()	Ret. Time (min)	Time Offset (min)	Area (counts)	Sep. Code	Width 1/2 (sec)	Status Codes
1	Helium/H2	0.3059	0.821	0.008	18521	VV	1.6	
2	O2	14.4548	1.021	0.001	115803	VB	1.7	C
	Totals:	14.7607		0.009	134324			

Status Codes:
C - Out of calibration range

Total Unidentified Counts : 0 counts

Detected Peaks: 3 Rejected Peaks: 1 Identified Peaks: 2

Multiplier: 1 Divisor: 1 Unidentified Peak Factor: 0

Baseline Offset: -10019 microVolts

Noise (used): 14 microVolts - monitored before this run

Manual injection

Calib. out of range; No Recovery Action Specified

****

Figure 0-5 GC analysis of one of the samples collected in glass syringes

Appendix-III

Figure 0-6 Bubble flow regime at relatively lower flow rates (1 l min^{-1}) in the current study

Figure 0-7 Heterogeneous flow regime at higher flow rates (2-5 l min^{-1}) in the current study

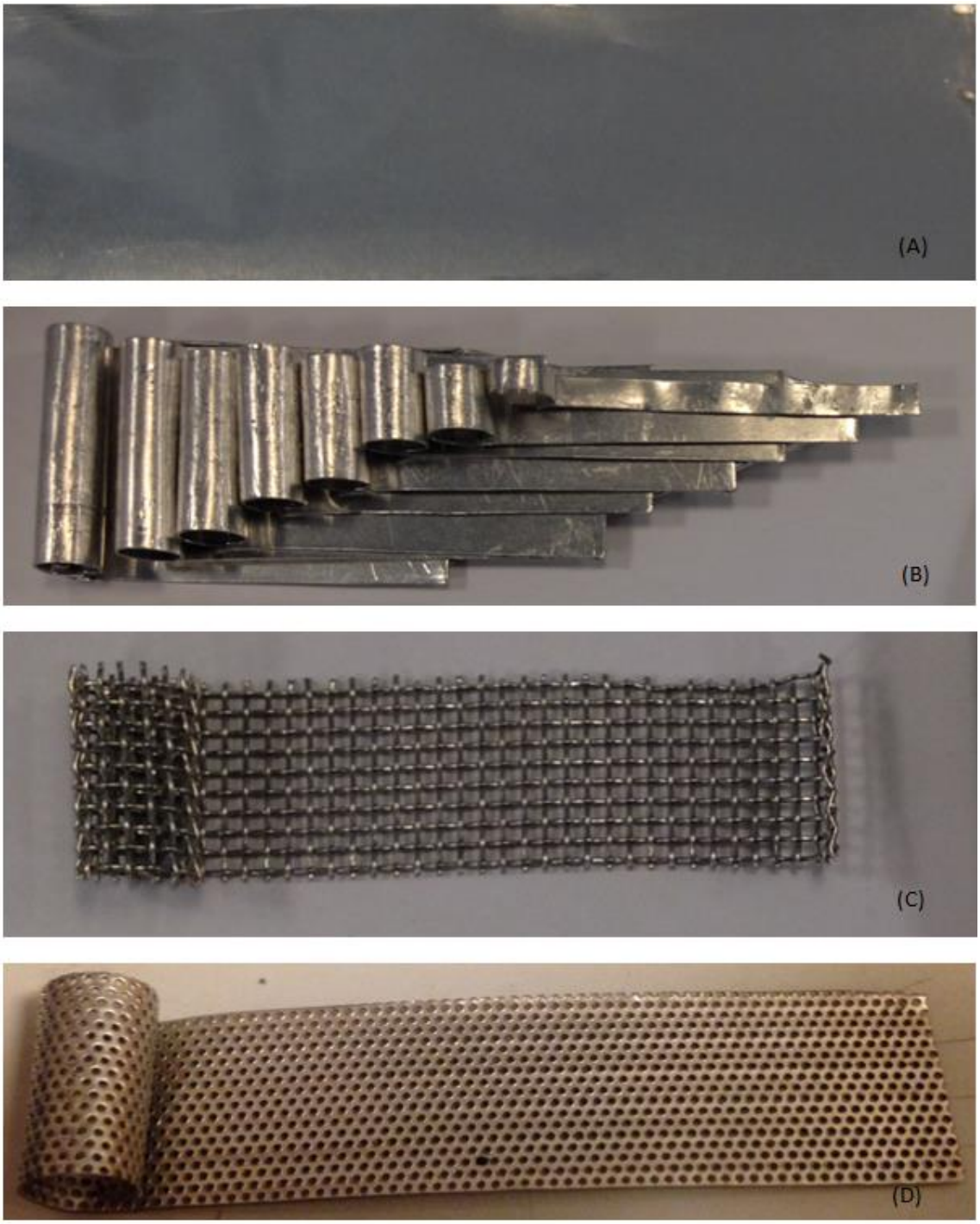

Figure 0-8 Different types of electrode (A) Aluminium Tape, (B) Aluminium sheet, (C) Mesh 1 (squared hole mesh) and (D) mesh 2 (punched hole mesh)

Appendix-IV

Other Achievements

- The author has published three journal articles cited in reference sections and two manuscripts are under preparation stage.
- Served as referee for two scientific articles upon invitation for fuel and energy
- Served as mentor for the following research projects (MSc. Dissertations):
  1. Enhancement of hydrogen production by the addition of different gases with steam into plasma micro reactor, 2012
  2. Value addition to biodiesel: Production of allyl alcohol from glycerol and formic acid, 2012
  3. The optimization of ozone sterilization system using plasma micro-reactors in dosing lance, 2013